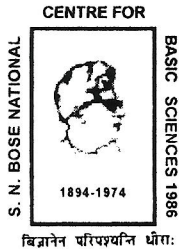


# **Synthesis and Characterization of Multifunctional Nanoparticles and their interaction with biological Macromolecules**

**THESIS  
SUBMITTED FOR THE DEGREE OF  
DOCTOR OF PHILOSOPHY (SCIENCE)  
OF  
JADAVPUR UNIVERSITY  
2013**

**BY  
ANUPAM GIRI**

**DEPARTMENT OF CHEMICAL, BIOLOGICAL AND  
MACROMOLECULAR SCIENCES,  
S. N. BOSE NATIONAL CENTRE FOR BASIC SCIENCES,  
BLOCK JD, SECTOR III, SALT LAKE,  
KOLKATA 700 098, INDIA**



सत्येन्द्र नाथ बसु राष्ट्रीय मौलिक विज्ञान केन्द्र  
SATYENDRA NATH BOSE NATIONAL  
CENTRE FOR BASIC SCIENCES

**CERTIFICATE FROM THE SUPERVISOR**

This is to certify that the thesis entitled "Synthesis and Characterization of Multifunctional Nanoparticles and their interaction with biological Macromolecules" submitted by Mr. Anupam Giri, who got his name registered on June 23, 2010 for the award of **Ph.D. (Science) degree of Jadavpur University**, is absolutely based upon his own work under the supervision of Dr. Samir Kumar Pal and that neither this thesis nor any part of it has been submitted for any degree/diploma or any other academic award anywhere before.



25<sup>th</sup> November 2013

(Signature of Supervisor/date with official seal)

**Dr. SAMIR KUMAR PAL**  
Professor  
S. N. Bose National Centre For Basic Sciences  
Government of India  
Block-JD, Sector-III, Salt Lake  
Kolkata-700098

ब्लॉक जे० डी०, सेक्टर-३, साल्ट लेक, कोलकाता ७०००९८, BLOCK-JD, SECTOR III, SALT LAKE, KOKATA - 700 098

दूरभाष/ Phones : 0091-(0)33-2335 5705-8, 2335 3057/61, 2335 0312/1313

इ-मेल/ E-mail : root@bose.res.in

Webpage : <http://www.bose.res.in>

Fax : 0091-(0)33-2335 3477

FUNDED BY THE DEPARTMENT OF SCIENCE & TECHNOLOGY, GOVT. OF INDIA

निष्ठिवद्ध विज्ञान और प्रौद्योगिकी विभाग भारत सरकार द्वारा

*To My Parents  
and Sister*

## *Acknowledgements*

*First of all I take this opportunity to express my sincere gratitude to my advisor Dr. Samir Kumar Pal, whom I am extremely grateful for being an exceptional mentor for me. His instrumental expertises, insight into various experimental problems, wisdom, and inspiration have allowed my research skills to develop, my creativity to flourish along with getting shaped as a working researcher. He has provided me with many opportunities to gain scientific experience, allowing me to explore new areas of research, interact and collaborate with talented researchers from a number of different national and international institutes. If it weren't for his ideas, constant support, guidance, motivation and patience, none of this work would have been possible. He has taught me so much, inspired me to work hard, always taken time to listen to my crazy ideas, and made these years so enjoyable. I could not have wished for a better advisor. Thank you Sir, for everything you have done for me.*

*I would also like to thank Prof. Thalappil Pradeep of Department of Chemistry, IIT Madras, India; Prof. Joydeep Dutta of Sultan Qaboos University, Sultanate of Oman; Prof. Arup Kumar Raychaudhuri of S. N. Bose Centre; Dr. Barnali Ghosh of S. N. Bose Centre, India; Prof. Peter Lemmens of Institute for Condensed Matter Physics, Technical University of Braunschweig, Germany; Dr. Nguyen T. K. Thanh of Department of Physics and Astronomy, University College London, London; Dr. Achintya Singha of Bose Institute, Kolkata, India; Dr. Mrinal Pal of Department of Physics, The University of Burdwan, Golapbag, Burdwan, India, Prof. Aanjana Kumar Dasgupta of Department of Biochemistry, University of Calcutta, India and Dr. Sambhu Nath Bandyopadhyay, Institute of Post Graduate Medical Education and Research (IPGME&R), India, for fruitful collaboration.*

*I am thankful to the lab members of my collaborating research groups: Paulrajpillai Lourdu Xavier, Megalamane Siddaramappa Bootharaju, Robin John, Soumik Sarkar and Chandan Sasmal, for insightful discussions.*

*I am also obliged to the director of S. N. Bose National Centre for Basic Sciences, Prof. Arup Kumar Raychaudhuri for his great effort in increasing the experimental facility at the centre, which has proved to be a boon for our research work. I am also thankful to all those faculty members of the centre whose activities at several instances have promoted our progress. I thank all the staff members of this institute for their sincere cooperation and help.*

*Because of the research environment sustained by Dr. Pal, I have crossed paths with a number of Ph.D. students (Dr. Pramod Kumar Verma, Dr. Abhinandan Makhal) who have influenced and enriched my research. The members of the Pal group have contributed immensely to my personal and professional time at S. N. Bose Centre. The direction of my Ph.D. work has been strongly influenced by the members of the Pal group, notably Nirmal, Pramod da and (Abhinandan) Makhal da. I would like to acknowledge my other colleagues (Surajit, Subrata, Ranajay, Tanumoy, Soumik, Soma, Siddhi, Samim, Nabarun, Susobhan, Prasenjit and Dilip) for providing me a homely and*

*cheerful environment. They have been a great source of knowledge, expertise, and technical assistance. We have learned a great deal from each other and I thank them for their patience. I am, especially, thankful to Nirmal, Surajit and Subrata who shared glorious moments over a long period of time, supported my work annoyances, and also for the good moments of fun!*

*My time at S. N. Bose Centre was made enjoyable in large part due to the many friends and groups that became a part of my life. I am also thankful to all my friends at this centre for providing company at several instances. I gratefully acknowledge the University Grants Commission (UGC) of India for providing me a fellowship. My work was also supported by the DST.*

*I must name Mr. Rabindra Nath Jana and Mr. Kartik Chandra Pradhan as two of the most influential teacher during my schooldays. Thanks is due to Mr. Kartik Chandra Pradhan (from my higher secondary school), in whom I found an excellent teacher and a source of motivation towards chemistry.*

*And lastly, I express my gratitude to my parents, my sister and brother. A career in science would not have been possible without the great support from my parents, who have always encouraged me to chart my own path in life. Without their sacrifices, moral supports and blessings the thesis would not have taken its shape. My close friends Tarun, Soham, Sambhu, Tuhin, Sumanda and Bishuda also need to be mentioned for being a great source of strength; they always lent an ear to the hassles in my life and encouraged me to pursue research. I must thank all my other extended family members for being extremely supportive and providing me with an environment which enabled me to do research.*

Dated: 25/11/2013  
Department of Chemical, Biological  
and Macromolecular Sciences,  
S. N. Bose National Centre for Basic Sciences,  
Salt Lake, Kolkata 700098,  
India.

Anupam Giri  
(Anupam Giri)

# CONTENTS

	<b>Page</b>
<b>Chapter 1: Introduction</b>	
1.1. Nanoparticles	1
1.2. Classification of Nanoparticles	1
1.2.1. Metal Nanoparticles	1
1.2.2. Metal Nanoclusters	2
1.2.3. Magnetic Nanoparticles	3
1. 2. 3. 1.    Iron Oxides	3
1. 2. 3. 2.    Manganese Oxides	4
1.2.4. Quantum Dots	5
1.3. Synthesis of Nanoparticles	6
1.4. Surface Modification of Nanoparticles	7
1.5. Multifunctional Nanoparticles	7
1.6. Scope and Objective	8
1.7. Summary of the Work Done	11
1.7.1. Surface Modification of Nanoparticles for their New Functionality and Better Acceptability in the Biophysical Studies	11
1.7.1.1.    Emergence of Multicolor Photolumines- cence in $\text{La}_{0.67}\text{Sr}_{0.33}\text{MnO}_3$ Nanoparticles	11
1.7.2. Synthesis of Biocompatible Nanoparticles with Novel Optical & Magnetic Properties and their Characterization	12
1.7.2.1.    Rational Surface Modification of $\text{Mn}_3\text{O}_4$ Nanoparticles to Induce Multiple Photoluminescence and Room Temperature Ferromagnetism	12

1.7.3.	Surface Functionalization of Nanoparticles and their Interaction with Small Organic Molecules	13
1.7.3.1.	Functionalization of Manganite Nanoparticles and their Interaction with Biologically Relevant Small Ligands: Picosecond Time-Resolved FRET Studies	13
1.7.4.	Synthesis of Amino Acid Modified Fluorescent Quantum Dots in Aqueous Solution and their Interaction with Biological Macromolecules	13
1.7.4.1.	Preparation of Water Soluble L-Arginine Capped CdSe/Zns QDs and their Interaction with Synthetic DNA: Picosecond-Resolved FRET Study	13
1.7.5.	Novel Synthesis of Biocompatible and Highly Luminescent Metal Cluster and their Characterization	14
1.7.5.1.	Atomically Precise Luminescent Iron Clusters in Solution	14
1.8.	Plan of Thesis	14
	References	16

## **Chapter 2: Overview of Spectroscopic Tools and Systems**

2.1.	Steady-State and Dynamical Tools	21
2.1.1.	Förster Resonance Energy Transfer (FRET)	21
2.1.2.	Tachiya Model	24
2.2.	Systems	25
2.2.1.	Molecular Probes	25
2.2.1.1.	4-nitrophenyl anthranilate (4-NPA)	25
2.2.1.2.	[3,8-diamino-5-ethyl-6-phenylphenanthridinium bromide], Ethidium Bromide (EtBr)	25
2.2.1.3.	2'-(4-hydroxyphenyl)-5-[5-(4-methylpiperazine-1-yl)-benzimidazo-2-yl-benzimidazole],	

	Hoechst 33258 (H258)	25
2.2.1.4.	2-aminopurine (2-AP)	26
2.2.1.5.	4',6-diamidino-2-phenylindole (DAPI)	26
2.2.1.6.	Methylene blue (MB)	26
2.2.2.	Protein	27
2.2.2.1.	Human Serum Albumin (HSA)	27
2.2.2.2.	Hemoglobin	30
2.2.3.	Deoxyribonucleic Acid (DNA)	30
	References	32

### **Chapter 3: Instrumentation and Sample Preparation**

3.1.	Instrumental Setup	35
3.1.1.	Steady-State Absorption and Fluorescence Spectroscopy	35
3.1.2.	Circular Dichroism Spectroscopy	36
3.1.3.	Time Correlated Single Photon Counting	38
3.1.4.	X-Ray Diffractometer	39
3.1.5.	Fourier Transform Infrared Spectroscopy	40
3.1.6.	Vibrating-Sample Magnetometer (VSM)	42
3.1.7.	Superconducting Quantum Interference Device (SQUID)	43
3.1.8.	Transmission Electron Microscope	45
3.1.9.	Scanning Electron Microscope	46
3.1.10.	Fluorescence Microscope	47
3.1.11.	X-Ray Photoelectron Spectroscopy	48
3.1.12.	Refractive Indices Measurement	50
3.1.13.	Thermogravimetric-Differential Thermal Analyzer	51
3.1.14.	Laser Raman Spectroscopy	52
3.1.15.	Matrix-Assisted Laser Desorption Ionization-Time of Flight (MALDI-TOF) Mass Spectrometry	53
3.1.16.	Electrospray Ionization Mass Spectrometry (ESI-MS)	55
3.2.	Sample Preparation	56
3.2.1.	Synthesis of $\text{La}_{0.67}\text{Sr}_{0.33}\text{MnO}_3$ Nanoparticles (LSMO NPs)	57

3.2.2. Functionalization and Further Surface Modification of LSMO NPs	57
3.2.3. Incorporation of Tartrate-LSMO NPs into Human Oral Squamous Epithelial Cells	57
3.2.4. Synthesis of Bulk Mn <sub>3</sub> O <sub>4</sub> NPs	58
3.2.5. Functionalization of As-Prepared Mn <sub>3</sub> O <sub>4</sub> NPs by Different Ligands to Prepare Ligand Functionalized-Mn <sub>3</sub> O <sub>4</sub> NPs	58
3.2.6. Further Surface Modification of Tartrate-Mn <sub>3</sub> O <sub>4</sub> (T-Mn <sub>3</sub> O <sub>4</sub> ) NPs to Impart High Photoluminescence	58
3.2.7. Preparation of Water Soluble Arginine Capped QDs	58
3.2.8. Preparation of DNA Samples	59
3.2.9. Synthesis of the Protein-Incorporated Fe Quantum Clusters (Fe <sub>QC</sub> s)	59
3.2.10. Ligand Exchange and Phase Transfer from Water to Chloroform	59
3.2.11. Evidence of “Zero Oxidation State” of Fe <sub>QC</sub> in Hb Matrix, Detection Procedure Using Chemiluminescence	59
3.2.12. Quantum Yield Calculation	60
References	61

**Chapter 4: Surface Modification of Nanoparticles  
for their New Functionality and Better  
Acceptability in the Biophysical Studies**

4.1.	Introduction	63
4.2.	Result and Discussion	64
4.2.1.	Emergence of Multicolor Photoluminescence in La <sub>0.67</sub> Sr <sub>0.33</sub> MnO <sub>3</sub> Nanoparticles	64
4.3.	Conclusion	83
	References	84

**Chapter 5: Synthesis of Biocompatible Nanoparticles with  
Novel Optical & Magnetic Properties and their  
Characterization**

5.1.	Introduction	88
5.2.	Result and Discussion	90
5.2.1.	Rational Surface Modification of Mn <sub>3</sub> O <sub>4</sub> Nanoparticles to Induce Multiple Photoluminescence and Room Temperature Ferromagnetism	90
5.3.	Conclusion	105
	References	106

**Chapter 6: Surface Functionalization of Nanoparticles  
and their Interaction with Small Organic  
Molecules**

6.1.	Introduction	111
6.2.	Result and Discussion	112
6.2.1.	Functionalization of Manganite Nanoparticles and their Interaction with Biologically Relevant Small Ligands: Picosecond Time-Resolved FRET Studies	112

6.3.	Conclusion	120
	References	122

**Chapter 7: Synthesis of Amino-Acid Modified Fluorescent  
Quantum Dots in Aqueous Solution and their  
Interaction with Biological Macromolecules**

7.1.	Introduction	126
7.2.	Result and Discussion	128
	7.2.1. Preparation of Water Soluble L-Arginine Capped CdSe/Zns QDs and their Interaction with Synthetic DNA: Picosecond-Resolved FRET Study	128
7.3.	Conclusion	135
	References	136

**Chapter 8: Novel Synthesis of Biocompatible and  
Highly Luminescent Metal Cluster and their  
Characterization**

8.1.	Introduction	141
8.2.	Result and Discussion	142
	8.2.1. Atomically Precise Luminescent Iron Clusters in Solution	142
8.3.	Conclusion	163
	References	164

<b>LIST OF PUBLICATIONS</b>	168
-----------------------------	-----

# Chapter 1

## Introduction

### 1.1. Nanoparticles

The term 'nanoparticle' is used to describe a particle with size in the range of 1 to 100 nm, at least in one of the three dimensions. Because of this very small size scale, they possess an immense surface area per unit volume, a high proportion of atoms in the surface and near surface layers, and the ability to exhibit quantum effects. In this size range, the physical, chemical and biological properties of the nanoparticle change in fundamental ways from the properties of both individual atoms/molecules and of the corresponding bulk material. Nanoparticles exist with great chemical diversity in the form of metals, metal oxides, semiconductors, polymers, carbon materials, organics or biological. They also exhibit great morphological diversity with shapes such as spheres, cylinders, disks, platelets, hollow spheres and tubes, etc. Depending on the material they consist of, nanoparticles can possess a number of different properties such as high electron density and strong optical absorption (e.g. metal particles, in particular Au), photoluminescence (semiconductor quantum dots, e.g. CdSe or CdTe) or phosphorescence (doped oxide materials, e.g.  $Y_2O_3$ ), or magnetic moment (e.g. iron or manganese oxide nanoparticles). The unique properties of these various types of nanoparticles give them novel electrical, catalytic, magnetic, mechanical, thermal, or imaging features that are highly desirable for applications in catalysis, biomedicines, and electronics, and environmental sectors.

### 1.2. Classification of Nanoparticles

Nanoparticles can be classified based upon their sizes, shapes, and materials, and with various chemical and surface properties. There is a constant and rapid growth in this field which adds to the basis of classification. However, the classes of nanoparticles listed below are mainly based upon their constituent materials, and some of their basic properties and current known uses are also described here.

#### 1.2.1. Metal Nanoparticles

Noble metal nanoparticles, such as gold (Au), silver (Ag) and Cu nanoparticles and nanorods, exhibits unique electric, photonic and catalytic properties like local surface

plasmon resonance (LSPR) [1, 2], surface-enhanced Raman scattering (SERS) [3] and surface-enhanced fluorescence (SEF) [4]. The strong plasmon resonance band of the noble metal NPs in the visible region has been used in the development of biosensors for use in colorimetric detection of analytes [5-7]. The light absorption by NPs is related to the incident light interaction with the surface of the nanoparticle. When light of a specific energy interacts with the surface of noble metal NP, an intense localized field is induced. The coupling of the NPs conduction band electrons with the electric field of incident light, at a resonant frequency, generates a localized plasmonic oscillation on the surface of the NPs, designated by surface plasmon resonance (SPR) or localized SPR (LSPR) [8].

### **1.2.2. Metal Nanoclusters**

Similar to metal nanoparticles, study of metal nanoclusters has also received considerable attention in recent years because they bridge the evolution of properties from isolated atoms to nanoparticles and even to the bulk [9, 10]. Providing the “missing link” between atomic and nanoparticles behaviour in noble metals, the fluorescent, water-soluble metal nanoclusters offer complementary transition energy size scalings at smaller dimensions. Their robust, discrete, size-dependent emission makes them ideal fluorophores for single-molecule spectroscopic studies. Their transition energies have been found to scale with the inverse of the cluster radius based on the spherical jellium model [11], valid for metals with free electrons such as gold and silver. Due to the similarity in electronic structure of metal clusters and single atoms, the metal clusters are also called “multi-electron artificial atoms” [12, 13].

According to the spherical jellium model, a metal cluster is represented as uniform, positively charged sphere with electronic shells filled with free electrons. These free electrons are provided by the valence electrons of metal atoms, and they delocalize and form spherical electron shells surrounding the positively charged core. Due to a strong electron screening effect, valence electrons of noble metal atoms are considered free after neglecting electron-electron and electron-ion interactions [14]. Distinct from the electronic structure of single atoms, cluster electron density is independent of the number of free electrons in the metal clusters. However, analogous to single atoms, free electrons in metal clusters are also delocalized for electronic shells surrounding the atoms and subject to the Pauli Exclusion Principle. The jellium model predicts that the emission energy of metallic

nanoclusters follow a power law of the number of atoms in the nanoclusters with no adjustable parameters by the simple scaling relation of  $E_{\text{fermi}}/N^{1/3}$  in which  $E_{\text{fermi}}$  is the Fermi energy of bulk metal and  $N$  is the number of atoms in the nanoclusters. It has been successfully applied to small gold nanoclusters [15], describing accurately the size-dependent electronic structure and relative electronic transitions of the small clusters [11].

### **1.2.3. Magnetic Nanoparticles**

Magnetic nanoparticles are of great interest for researchers from a wide range of disciplines, including magnetic fluids [16], catalysis [17], biotechnology/biomedicine [18], magnetic resonance imaging [19], data storage [20], and environmental remediation [21]. Two key issues dominate the magnetic properties of nanoparticles: finite-size effects and surface effects which give rise to various special features. Finite-size effects result, for example, from the quantum confinement of the electrons, whereas typical surface effects are related to the symmetry breaking of the crystal structure at the boundary of each particle. Magnetic nanoparticles can be utilized in versatile ways, very similar to those of nanoparticles in general. However, the magnetic properties of these particles add a new dimension where they can be manipulated upon application of an external magnetic field. This property opens up new applications where drugs that are attached to a magnetic particle to be targeted in the body using a magnetic field. Here, we briefly introduce different kinds of magnetic nanoparticles.

#### **1. 2. 3. 1. Iron Oxides**

Iron oxides have received increasing attention due to their extensive applications, such as magnetic recording media, catalysts, pigments, gas sensors, optical devices, and electromagnetic devices [22]. By definition, superparamagnetic iron oxide particles are generally classified with regard to their size into superparamagnetic iron oxide particles (SPIO), displaying hydrodynamic diameters larger than 30 nm, and ultra small superparamagnetic iron oxide particles (USPIO), with hydrodynamic diameters smaller than 30 nm. Among several crystalline modifications of anhydrous ferric oxides there are two magnetic phases, namely, rhombohedral hematite ( $\alpha$ -Fe<sub>2</sub>O<sub>3</sub>) and cubic maghemite ( $\gamma$ -Fe<sub>2</sub>O<sub>3</sub>). In the  $\alpha$ -structure, all Fe<sup>3+</sup> ions have an octahedral coordination, whereas in  $\gamma$ -Fe<sub>2</sub>O<sub>3</sub> having the structure of a cation-deficient AB<sub>2</sub>O<sub>4</sub> spinel, the metal atoms A and B occur in tetrahedral and octahedral environments, respectively. The oxide  $\alpha$ -Fe<sub>2</sub>O<sub>3</sub> is

antiferromagnetic at temperatures below 950 K, while above the Morin point (260 K) it exhibits so-called weak ferromagnetism. Among all iron oxides, magnetite  $\text{Fe}_3\text{O}_4$  possess the most interesting properties because of the presence of iron cations in two valence states,  $\text{Fe}^{2+}$  and  $\text{Fe}^{3+}$ , in the inverse spinel structure. The cubic spinel  $\text{Fe}_3\text{O}_4$  is ferrimagnetic at temperatures below 858 K. This inverse spinel structure for magnetite was first suggested to explain the fast electron hopping-continuous exchange of electrons between  $\text{Fe}^{2+}$  and  $\text{Fe}^{3+}$  in the octahedral positions at room temperature, rendering magnetite an important class of half metallic material.

### **1. 2. 3. 2. Manganese Oxides**

During the past few decades, manganese oxides have been widely exploited because of their promising applications in many fields, such as catalysis [23], molecular adsorption [24, 25], ion exchange [26], supercapacitors [27], magnetic applications [28], and secondary batteries. Among the manganese oxides, the hausmannite  $\text{Mn}_3\text{O}_4$  is the most stable oxide at high temperature relative to other manganese oxides, such as  $\text{MnO}_2$  and  $\text{Mn}_2\text{O}_3$ . The compound is known to be an active catalyst for the oxidation of methane and carbon monoxide [29], decomposition of waste gases, the selective reduction of nitrobenzene [30], and the combustion of organic compounds at temperatures of the order of 373-773 K. These catalytic applications provide a powerful method of controlling air pollution. Most recently, hollow  $\text{Mn}_3\text{O}_4$  nanoparticles have been utilized as positive MRI contrast agent (exploiting their room temperature paramagnetism) with enhanced relaxivity attributed to an increased water-accessible surface area and the flexibility of further functional surface modifications [31, 32].  $\text{Mn}_3\text{O}_4$  is also a starting material in the preparation of soft magnetic materials, such as manganese ferrite for dioxy-magnetic cores in transformers for power supplies [33], in the lithiation of Li-Mn-O electrode materials for rechargeable lithium batteries [34], and in a corrosion-inhabiting pigment for epoxy-polyamide-based and epoxy-ester-based primers and top coatings.

In recent years, mixed-valent perovskite manganese oxides of general formula  $\text{Ln}_{1-x}\text{A}_x\text{MnO}_3$  (Ln and A are lanthanide and alkaline-earth cations, respectively) have attracted much attention for their remarkable interrelated structural, magnetic and transport properties induced by the mixed valence (3+ and 4+) of the Mn ions. In particular, they exhibit very large negative magnetoresistance, called colossal magnetoresistance (CMR),

in the vicinity of metal–insulator transition for certain compositions. In the perovskite structure, the  $\text{MnO}_3$  network of corner-shared  $\text{MnO}_6$  octahedra is at the origin of an incredible amount of spectacular physical properties which are driven by competition between double-exchange ferromagnetism (DE-F) [35] and a natural tendency towards orbital and charge ordering phenomena [36]. The Jahn–Teller (J-T)  $\text{Mn}^{3+}\text{O}_6$  octahedra, with a  $t_{2g}^3e_g^1$  electronic configuration for  $\text{Mn}^{3+}$ , can be either flattened or elongated depending on the  $e_g$  orbital filling,  $d_x^2-y^2$  or  $d_z^2$ , respectively. According to the super exchange rules [37], depending on the orbital configurations,  $\text{Mn}^{3+}\text{–O–Mn}^{3+}$  is either antiferromagnetic (AF) or ferromagnetic (F). Starting from  $\text{LaMnO}_3$ , the creation of  $\text{Mn}^{4+}$  cations ( $t_{2g}^3e_g^0$ ), which lie in much less distorted  $\text{MnO}_6$  octahedra than  $\text{Mn}^{3+}\text{O}_6$ , can be induced by  $\text{Ln}^{3+}_{1-x}\text{A}^{2+}_x$  divalent substitution. This is responsible for the ferromagnetic double-exchange,  $\text{Mn}^{3+}\text{–O–Mn}^{4+}$ . In the  $\text{La}_{1-x}\text{Sr}_x\text{MnO}_3$  series, the ferromagnetism becomes metallic as soon as  $x > 0.15$ , [38] i.e. as the 3D percolation threshold is reached, and the Curie temperature reaches a maximum  $T_C = 371\text{K}$  value for  $x = 0.40$  [38].

#### 1.2.4. Quantum Dots

An important field of research, for the past fifteen years, quantum dots are typically composed of combinations of Group II and IV elements or Group III and V elements of the periodic table. They have been developed in the form of semiconductors, insulators, metals, magnetic materials or metallic oxides. Semiconductor quantum dots (QDs) are tiny light-emitting particles on the nanometer scale, and are emerging as a new class of fluorescent labels for biology and medicine. QDs are nearly spherical semiconductor particles with diameters on the order of 2–10 nanometers, containing roughly 200–10,000 atoms. The semiconducting nature and the size-dependent fluorescence of these nanocrystals have made them very attractive for use in optoelectronic devices, biological detection, and also as fundamental prototypes for the study of colloids and the size-dependent properties of nanoparticles [39]. Bulk semiconductors are characterized by a composition-dependent bandgap energy, which is the minimum energy required to excite an electron to an energy level above its ground state, commonly through the absorption of a photon of energy greater than the bandgap energy. Relaxation of the excited electron back to its ground state may be accompanied by the fluorescent emission of a photon. Small nanocrystals of semiconductors are characterized by a bandgap energy that is

dependent on the particle size, allowing the optical characteristics of a QD to be tuned by adjusting its size. In comparison with organic dyes and fluorescent proteins, QDs are about 10–100 times brighter, mainly due to their large absorption cross sections, 100–1000 times more stable against photobleaching, and show narrower and more symmetric emission spectra. In addition, a single light source can be used to excite QDs with different emission wavelengths, which can be tuned from the ultraviolet [40], throughout the visible and near-infrared spectra [41], and even into the mid-infrared [42]. The group II-VI QD nanocrystals such as CdSe, CdTe, CdS [43], ZnS [44], and ZnSe have been studied extensively over the past decade, and QDs with a CdSe core and ZnS shell are currently commercially available.

### **1.3. Synthesis of Nanoparticles**

Nanoparticles can be synthesized by a variety of methods using gas, liquid or solid phase processes. These include gas phase processes of flame pyrolysis, high temperature evaporation, and plasma synthesis; microwave irradiation; physical and chemical vapor deposition synthesis; colloidal or liquid phase methods in which chemical reactions in solvents lead to the formation of colloids, molecular self-assembly, and, mechanical processes of size reduction including grinding, milling and alloying.

Gas phase synthesis approaches are based on homogeneous nucleation of a supersaturated vapour and subsequent particle growth by condensation, coagulation and capture. The supersaturated vapour can be generated in many ways depending on the chemical nature of the material, but typically by heating a solid and evaporating it into a carrier gas phase.

Vapour deposition methods are based on forming a vapour by pyrolysis, followed by reduction, oxidation and allowing the deposition of the vapour on a surface. Starting from initial nuclei existing as islands on a surface, the growth is controlled by various ways to produce nanoparticles. An important example of this approach is the production of carbon nanotubes.

Colloidal methods are based on precipitation processes in solution. For example, solutions of different ions can be mixed under controlled conditions of temperature and pressure to form insoluble precipitates. By controlling the nucleation and growth kinetics, particles of various sizes and morphologies can be produced. The method has been

implemented in bulk solutions and also in confined systems such as reverse micelles. To control the process of nucleation, ultrasonic or sonochemical effects have also been employed. A wide range of metal, metal oxide and organic nanoparticles have been produced by colloidal wet chemical approach.

All of the above synthesis approaches start at the molecular level to build up or create the nanoparticles. In the opposite direction, mechanical size reduction methods such as grinding and milling have also been employed to generate nanoparticles. These methods are the traditional approaches to produce fine particles and they have been able to generate nanoparticles from minerals such as clay, coal and metals. To avoid particle aggregation in the course of the size reduction process, the grinding and milling operations are often carried out with colloidal stabilizers.

#### **1.4. Surface Modification of Nanoparticles**

Once the nanoparticles are produced and purified to a satisfactory level it is often necessary to introduce surface modifications. The surface modifications can be for the purposes of (a) passivating a very reactive nanoparticle, (b) stabilizing a very aggregative nanoparticle in a medium (which may be a solvent or a polymer melt) where the nanoparticles are to be dispersed, (c) functionalizing the nanoparticle for applications such as molecular recognition, or (d) promoting the assembly of nanoparticles. Most commonly used surface modification methods include grafting thiolated surfactants or polymers, adsorption of charged surfactants, charged ligands or polymer brushes, attachment of biological molecules such as DNA, peptides, proteins, antigens, streptavidin or coating a continuous polymer film on nanoparticles.

#### **1.5. Multifunctional Nanoparticles**

The emerging fields of nanotechnology and nanoengineering provide a path to design and fabricate nanoparticles for their diverse applications. Particularly, nanotechnology offers tremendous potential for future biomedical technology. Due to their unique characteristics including superparamagnetic or fluorescent properties, and small size comparable to biomolecules, nanostructured materials have emerged as novel bio-imaging, diagnostic, and therapeutic agents for the future medical field. The use of combinations of different nanostructured materials will allow the development of novel multifunctional nanomedical

platforms for multimodal imaging, and simultaneous diagnosis and therapy. For example, the combination of magnetic resonance imaging (MRI) contrast agent and fluorescent organic dye can allow the detection of cancer through non-invasive MRI and the optical guide of surgery. The encapsulation of MRI contrast agent and anti-cancer drug in a nanostructured matrix has the potential to allow for simultaneous diagnosis and targeted chemotherapy. There are many possible combinations of the various imaging and therapeutic modalities, which make it possible to accomplish multimodal imaging, and simultaneous diagnosis and therapy. Moreover, the conjugation of targeting moieties on the surface of these multifunctional nanoparticles gives them specific targeted imaging and therapeutic properties.

## **1.6. Scope and Objective**

The interface of biology and inorganic nanoparticles represents one of the fastest growing and most promising areas of nanotechnology. The innovative use of engineered nanoparticles in medicine, be it in therapy or diagnosis, is growing dramatically. This is motivated by the current extraordinary control over the synthesis of complex nanoparticles with a variety of biological functions (e.g. contrast agents, drug-delivery systems, transducers, amplifiers, etc.). Engineered nanoparticles are found in the bio-context with a variety of applications in fields such as sensing, imaging, therapy or diagnosis [45]. As the degree of control to fabricate customized novel nanoparticles evolves, new applications, devices with enhanced performance or unprecedented sensing limits can be achieved. The major applications of nanoparticles in the biomedical field can be mainly divided into imaging and therapy. Most of the clinically used imaging and therapeutic modalities are small molecules, such as the gadolinium complexes used as T<sub>1</sub> MRI contrast agents and anticancer chemical drugs. The limitations of these small molecules are their very short blood circulation time and non-specific biodistribution, which causes many unwanted side effects. Nanostructured materials can be employed to overcome these limitations [46]. For example, the blood circulation times can be increased significantly by the size control and surface modification of nanoparticles and by conjugating targeting molecules, such as antibodies and peptides, on their surface. However, several challenging issues still circumvent widespread biomedical uses of advanced nanotechnology. For example, novel multifunctional nanoparticles and improved treatment strategies are required to meet the

needs of real-time, non-invasive imaging in living subjects or humans, and those of satisfactory drug delivery and therapeutic efficiency *in vivo*. Secondly, standardized nanoplatforms to be applied to diagnostic or therapeutic investigations of various diseases still have to be developed and formulated. The development of multifunctional nanoparticles with precise biological/chemical functions having economic, healthcare and environmental benefits are a key focus in nanobiotechnology and could have profound impact on many research areas, ranging from molecular imaging to medical diagnostics/therapeutics, chemical conversion and energy production. Several novel nanoparticles have recently been described for their unique optical, magnetic, electronic and structural properties. Considerable efforts have also been directed towards rational surface modifications to modulate their complicated surface chemistry, high-specificity and efficient targeting. However, despite recent advancement, much works still need to be done in order to achieve, (i) hydrophilic and biocompatible nanoparticles that are intrinsically luminescent, with surface chemistry adaptable to varied biological/chemical applications, (ii) selective and specific labeling of live cells and biomolecules. Since, nanoparticles can display distinct biological effects compared to bulk materials of the same chemical composition, the physico-chemical characterization of nanoparticles and the understanding of their interaction with biological media are essential for optimizing the properties of nanoparticles. The ‘nano-bio’ interface comprises the dynamic physicochemical interactions, kinetics and thermodynamic exchanges between nanoparticles surfaces and the surfaces of biological components (for example small biomolecule, protein, DNA etc.). Moreover, nanotechnology-based approaches are being explored for a variety of biomedical applications such as for drug delivery, bioimaging, tissue engineering, and biosensors. A substantial number of these approaches employ nanoscale materials or bio-nanoparticles for developing unique functionalities required by the biomedical systems. For this field to evolve, it is necessary to understand the dynamic forces and molecular components that shape these interactions. The key focus of this thesis is (a) to explore how the interactions between nanoparticles and biological systems modify the fundamental forces that govern nanoparticle properties as well as their interactions, (b) development of ligand functionalization approaches to control the surface chemistry of nanoparticles in order to gain a better understanding of the origin of surface-induced

optical, magnetic and catalytic properties, since, subtle differences in ligand functional groups or the structural position of the functional groups can dramatically change the optical, magnetic and catalytic responses of the nanoparticles, (c) development of multifunctional nanoprobos with precise biological functions along with novel reactivity and selectivity towards a desired chemical transformation having direct biological and medical significance.

In this thesis, we will present a molecular functionalization strategy to solubilize one of the promising manganite nanoparticles  $\text{La}_{0.67}\text{Sr}_{0.33}\text{MnO}_3$  (LSMO) in aqueous environments. The electronic structural modification of the NPs imparted through functionalization and subsequent water solubilization reveals multiple absorption bands in the UV-vis region. Using the absorption band of the functionalized nanoparticles, we have monitored their interaction with other biologically important ligands such as 4-nitrophenylanthranilate (NPA) and a DNA base mimic, 2-aminopurine (2AP). Förster resonance energy transfer (FRET) of the covalently attached probe NPA with the capped NPs confirm their attachment with the surface functional group ( $-\text{OH}$ ) of the citrate ligand, whereas, the FRET of 2AP, with the nanoparticles confirm the surface adsorption of the 2AP molecules. In another work, we have observed that surface treatment of the tartrate/citrate functionalized highly water soluble LSMO nanoparticles, lead to the emergences of multi-color photoluminescence (from blue to red region of the spectrum) when it is addressed with different excitation wavelengths, where the respective excitation wavelengths have a direct correlation with the observed UV-vis absorption bands. Using a multitude of spectroscopic tools we have investigated the mechanistic insight behind the origin of different absorption bands and emergence of multicolor photoluminescence from the functionalized nanoparticles.

In the study on  $\text{Mn}_3\text{O}_4$  nanoparticles, we have demonstrated their surface modification induced multiple photoluminescence and room temperature ferromagnetic activation. Moreover, employing a systematic variation of the ligands, their functional groups and the structural position of the functional groups, we have identified the necessary and sufficient structural requirement of the surface co-ordinating ligands, to induce such unprecedented optical/magnetic responses from the nanoparticles.

One of the challenges for using nanoparticles in biological studies is to design nanoparticles which are water-soluble with surface chemistry adaptable to varied biological applications. For this purpose, different ligands have been exploited to impart biocompatibility and bioactive functionalities to nanoparticles through surface modification with biomolecules. In this direction, in one of our studies, we have exchanged TOPO (trioctylphosphine oxide) ligand of CdSe/ZnS core/shell quantum dots (QDs) with an amino acid L-arginine (Arg) at the toluene/water interface and eventually rendered the QDs from toluene to aqueous phase. We have studied the interaction of the water soluble Arg-capped QDs (energy donor) with ethidium bromide (EB) labeled synthetic dodecamer DNA (energy acceptor) using picosecond resolved FRET technique.

With respect to bulk materials, clusters are of fundamental interest due to their own intrinsic properties but also because of their intermediate position between molecular and materials science. Compared with common fluorophores such as organic dyes and semiconductor quantum dots, where practical deployment can be limited by relatively poor photostability (for organic fluorophores) or toxicity concerns (e.g., quantum dots), fluorescent metal clusters are promising alternatives for the design of novel bioimaging probes because of their ultrafine size, excellent photostability, and low toxicity. So, there is a strong interest in the development of synthesis methods for highly fluorescent metal clusters. In this regard, in one of our studies, we have demonstrated the synthesis and characterization of novel super-paramagnetic iron clusters in hemoglobin matrix that are highly luminescent, having quantum yield of ~10% at 565 nm. Using mass spectrometry, we have tentatively assigned that the clusters synthesized in solution consist of 8, 10 and 13 number of Fe atoms. We believe that this new material holds promise for fundamental applications like catalysis, imaging and sensing.

## **1.7. Summary of the Work Done:**

### **1.7.1. Surface Modification of Nanoparticles for their New Functionality and Better Acceptability in the Biophysical Studies:**

#### **1.7.1.1. Emergence of Multicolor Photoluminescence in $\text{La}_{0.67}\text{Sr}_{0.33}\text{MnO}_3$ Nanoparticles [47]:** In the present study, we report the emergence of multicolor

photoluminescence in a mixed valence manganite nanoparticle  $\text{La}_{0.67}\text{Sr}_{0.33}\text{MnO}_3$  (LSMO NP), achieved through electronic structural modification of the nanoparticles upon functionalization with a biocompatible organic ligand, sodium tartrate. From UV-vis absorption, X-ray photoelectron spectroscopy (XPS), time-resolved photoluminescence study and Raman spectroscopic measurements, it is revealed that ligand-to-metal charge transfer transitions from highest occupied molecular orbital (HOMO, centered in tartrate ligand) to lowest unoccupied molecular orbital (LUMO, centered in  $\text{Mn}^{3+/4+}$  of the NPs), and d-d transitions involving Jahn-Teller sensitive  $\text{Mn}^{3+}$  ions in the nanoparticles plays the central role behind the origin of multiple photoluminescence from the ligand functionalized LSMO nanoparticles.

## **1.7.2. Synthesis of Biocompatible Nanoparticles with Novel Optical & Magnetic Properties and their Characterization:**

**1.7.2.1. Rational Surface Modification of  $\text{Mn}_3\text{O}_4$  Nanoparticles to Induce Multiple Photoluminescence and Room Temperature Ferromagnetism [48]:** Surface modification can have a significant influence on the materials behavior at the nanoscale and can lead to nanostructures with novel properties. In the present contribution, we demonstrate surface modification induced multiple photoluminescence and room temperature ferromagnetic activation of  $\text{Mn}_3\text{O}_4$  nanoparticles (NPs). Employing a systematic variation of the ligands, their functional groups and the structural position of the functional groups, we have identified the necessary and sufficient structural requirement of the surface co-ordinating ligands, to induce such unprecedented optical/magnetic responses from the NPs. Using a multitude of spectroscopic techniques, we have investigated the mechanistic insight behind this emergence of multiple photoluminescence (PL), and it is revealed that, the presence of a  $\alpha$ -hydroxy carboxylate moiety in the ligands is necessary to activate the Jahn-Teller (J-T) splitting of  $\text{Mn}^{3+}$  ions on the NPs surface and the corresponding d-d transitions along with ligand-to-metal charge transfer transitions (LMCT, associated with  $\text{Mn}^{2+/3+}$ -ligand interactions) plays the deciding role. Whereas, the presence of a carboxylate group in the surface coordinating ligands is sufficient to activate the room temperature ferromagnetism of the NPs. Moreover, it has been observed that the ligands induce smallest crystal field splitting energy (CFSE) resulted in the strongest ferromagnetic activation of the NPs. Finally, the functionalized material has been

identified as an efficient catalyst for the photo-degradation of a model cationic organic dye. Apart from the fundamental scientific interest, these results represent a promising route for the rational designing of  $\text{Mn}_3\text{O}_4$  NPs adaptable to diverse applications.

### **1.7.3. Surface Functionalization of Nanoparticles and their Interaction with Small Organic Molecules:**

#### **1.7.3.1. Functionalization of Manganite Nanoparticles and their Interaction with Biologically Relevant Small Ligands: Picosecond Time-Resolved FRET Studies [49]:**

In this study, we report molecular functionalization of one of the promising manganite nanoparticles  $\text{La}_{0.67}\text{Sr}_{0.33}\text{MnO}_3$  (LSMO) for their solubilization in aqueous environments. The functionalization of individual NPs with biocompatible citrate ligand as confirmed by fourier transform infrared (FTIR) spectroscopy, reveals that citrates are covalently attached to the surface of the NPs. UV-vis spectroscopic studies on the citrate functionalized NPs revealing an optical band in the visible region. Uniform size selectivity (2.6 nm) of the functionalization process is confirmed from high resolution transmission electron microscope (HRTEM). In the present study we have used the optical band of the functionalized NPs to monitor their interaction with other biologically important ligands. Förster resonance energy transfer (FRET) of a covalently attached probe 4-nitrophenyl anthranilate (NPA) with the capped NPs confirm the attachment of the NPA ligands with the surface functional group (-OH) of the citrate ligand. The FRET of a DNA base mimic, 2-aminopurine (2AP), with the NPs confirms the surface adsorption of 2AP. Our study may find its relevance to study interaction of the individual manganite NPs with the drug/ligand molecules.

#### **1.7.4. Synthesis of Amino Acid Modified Fluorescent Quantum Dots in Aqueous Solution and their Interaction with Biological Macromolecules:**

##### **1.7.4.1. Preparation of Water Soluble L-Arginine Capped CdSe/Zns QDs and their Interaction with Synthetic DNA: Picosecond-Resolved FRET Study [50]:**

In the present contribution, we have exchanged TOPO (trioctylphosphine oxide) ligand of CdSe/ZnS core/shell quantum dots (QDs) with an amino acid L-arginine (arg) at the toluene/water interface and eventually rendered the QDs from toluene to aqueous phase. We have studied the interaction of the water soluble arg-capped QDs (energy donor) with ethidium (EB) labeled synthetic dodecamer DNA (energy acceptor) using picoseconds

resolved Förster resonance energy transfer (FRET) technique. Furthermore, we have applied a kinetic model developed by M. Tachiya to understand the kinetics of energy transfer and the distribution of acceptor (EB-DNA) molecules around the donor QDs. Circular dichroism (CD) studies revealed a negligible perturbation in the native B-form structure of the DNA upon interaction with arg-capped QDs. The melting and the rehybridization pathways of the DNA attached to the QDs have been monitored by the CD which reveals hydrogen bonding is the associative mechanism for interaction between arg-capped QDs and DNA.

### **1.7.5. Novel Synthesis of Biocompatible and Highly Luminescent Metal Cluster and their Characterization:**

**1.7.5.1. Atomically Precise Luminescent Iron Clusters in Solution [51]:** Metal clusters, composed of a few atoms at the core, exhibit unique properties and have potential applications. Although atomically precise clusters of noble metals have been synthesized, analogous systems of reactive metals, such as iron, have not been realized in solution due to high reactivity. Here we report the synthesis and characterization of novel iron clusters in hemoglobin matrix that are highly luminescent (quantum yield 10% at 565 nm). The super-paramagnetic iron clusters, after successful ligand exchange from protein and phase transfer from water to chloroform using tri-octylphosphineoxide (TOPO), were detected as  $[\text{Fe}_{10}(\text{TOPO})_3(\text{H}_2\text{O})_3]^+$ ,  $[\text{Fe}_{13}(\text{TOPO})_2(\text{H}_2\text{O})]^+$  and  $[\text{Fe}_8(\text{TOPO})(\text{H}_2\text{O})_2]^+$  by mass spectrometry. This study lays the groundwork for exploiting unique properties of soluble iron clusters.

### **1.8. Plan of Thesis:**

The plan of the thesis is as follows:

**Chapter 1:** This chapter gives a brief introduction to the various kinds of nanoparticles, their synthesis and surface functionalization, as well as the scope and motivation behind the thesis work. A brief summary of the work done is also included in this chapter.

**Chapter 2:** This chapter provides an overview of the dynamical and steady-state tools, the structural aspects of biologically important systems (proteins, DNAs) and probes used in the research.

**Chapter 3:** Details of instrumentation, data analysis and experimental procedures have been discussed in this chapter.

**Chapter 4:** This chapter demonstrate the possibility of electronic structural modifications of manganite nanoparticles ( $\text{La}_{0.67}\text{Sr}_{0.33}\text{MnO}_3$ , and thus the resulting novel optical properties) by charge transfer through functionalization with small organic ligands.

**Chapter 5:** Rational surface modification strategy to induce multiple photoluminescence, room temperature ferromagnetism and novel photocatalytic property to a transition metal oxide nanoparticle has been discussed in this chapter.

**Chapter 6:** This chapter deals with the molecular functionalization of a promising manganite nanoparticle  $\text{La}_{0.67}\text{Sr}_{0.33}\text{MnO}_3$  (LSMO) and their interaction with biologically relevant small ligands.

**Chapter 7:** A convenient approach for preparing water-soluble, biocompatible QDs following a liquid-liquid interfacial ligand exchange method has been discussed in this chapter.

**Chapter 8:** This chapter offers the synthesis of highly luminescent and water-soluble Fe quantum clusters, starting from Hemoglobin (Hb), a Fe-containing metalloprotein which acts as the iron source as well as the protecting agent.

## References

- [1] F.N. Crespilho, F.C.A. Lima, A.B.F. da Silva, O.N. Oliveira Jr, V. Zucolotto, The origin of the molecular interaction between amino acids and gold nanoparticles: A theoretical and experimental investigation, *Chem. Phys. Lett.* 469 (2009) 186.
- [2] T. Endo, K. Kerman, N. Nagatani, E. Tamiya, Excitation of localized surface plasmon resonance using a core-shell structured nanoparticle layer substrate and its application for label-free detection of biomolecular interactions, *J. Phys. Condens. Matter* 19 (2007) 215201.
- [3] X. Zhang, M.A. Young, O. Lyandres, R.P. Van Duyne, Rapid detection of an anthrax biomarker by surface-enhanced raman spectroscopy, *J. Am. Chem. Soc.* 127 (2005) 4484.
- [4] D.J. Maxwell, J.R. Taylor, S. Nie, Self-assembled nanoparticle probes for recognition and detection of biomolecules, *J. Am. Chem. Soc.* 124 (2002) 9606.
- [5] P.C. Lee, D. Meisel, Adsorption and surface-enhanced raman of dyes on silver and gold sols, *J. Phys. Chem.* 86 (1982) 3391.
- [6] J.J. Storhoff, A.A. Lazarides, R.C. Mucic, C.A. Mirkin, R.L. Letsinger, G.C. Schatz, What controls the optical properties of DNA-linked gold nanoparticle assemblies?, *J. Am. Chem. Soc.* 122 (2000) 4640.
- [7] T.A. Taton, C.A. Mirkin, R.L. Letsinger, Scanometric DNA array detection with nanoparticle probes, *Science* 289 (2000) 1757.
- [8] S. Eustis, M.A. El-Sayed, Why gold nanoparticles are more precious than pretty gold: Noble metal surface plasmon resonance and its enhancement of the radiative and nonradiative properties of nanocrystals of different shapes, *Chem. Soc. Rev.* 35 (2006) 209.
- [9] L.A. Peyser, A.E. Vinson, A.P. Bartko, R.M. Dickson, Photoactivated fluorescence from individual silver nanoclusters, *Science* 291 (2001) 103.
- [10] G.A. Ozin, H. Huber, Cryophotoclustering techniques for synthesizing very small, naked silver clusters  $Ag_n$  of known size (where  $n = 2-5$ ). The molecular metal cluster-bulk metal particle interface, *Inorg. Chem.* 17 (1978) 155.
- [11] J. Zheng, P.R. Nicovich, R.M. Dickson, Highly fluorescent noble-metal quantum dots, *Annu. Rev. Phys. Chem.* 58 (2007) 409.

- [12] W.D. Knight, K. Clemenger, W.A. de Heer, W.A. Saunders, M.Y. Chou, M.L. Cohen, Electronic shell structure and abundances of sodium clusters, *Phys. Rev. Lett.* 52 (1984) 2141.
- [13] W.A. Deheer, The physics of simple metal-clusters -experimental aspects and simple-models, *Rev. Mod. Phys.* 65 (1993) 611.
- [14] A. Henglein, Physicochemical properties of small metal particles in solution: "Microelectrode" reactions, chemisorption, composite metal particles, and the atom-to-metal transition, *J. Phys. Chem.* 97 (1993) 5457.
- [15] J. Zheng, C. Zhang, R.M. Dickson, Highly fluorescent, water-soluble, size-tunable gold quantum dots, *Phys. Rev. Lett.* 93 (2004) 077402.
- [16] S. Chikazumi, S. Taketomi, M. Ukita, M. Mizukami, H. Miyajima, M. Setogawa, Y. Kurihara, Physics of magnetic fluids, *J. Magn. Magn. Mater.* 65 (1987) 245.
- [17] A.-H. Lu, W. Schmidt, N. Matoussevitch, H. Bönnemann, B. Spliethoff, B. Tesche, E. Bill, W. Kiefer, F. Schüth, Nanoengineering of a magnetically separable hydrogenation catalyst, *Angew. Chem. Int. Ed.* 43 (2004) 4303.
- [18] A.K. Gupta, M. Gupta, Synthesis and surface engineering of iron oxide nanoparticles for biomedical applications, *Biomaterials* 26 (2005) 3995.
- [19] Z. Li, L. Wei, M.Y. Gao, H. Lei, One-pot reaction to synthesize biocompatible magnetite nanoparticles, *Adv. Mater.* 17 (2005) 1001.
- [20] T. Hyeon, Chemical synthesis of magnetic nanoparticles, *Chem. Commun.* (2003) 927.
- [21] M. Takafuji, S. Ide, H. Ihara, Z. Xu, Preparation of poly(1-vinylimidazole)-grafted magnetic nanoparticles and their application for removal of metal ions, *Chem. Mater.* 16 (2004) 1977.
- [22] A.-H. Lu, E.L. Salabas, F. Schüth, Magnetic nanoparticles: Synthesis, protection, functionalization, and application, *Angew. Chem. Int. Ed.* 46 (2007) 1222.
- [23] H. Einaga, S. Futamura, Catalytic oxidation of benzene with ozone over alumina-supported manganese oxides, *J. Catal.* 227 (2004) 304.
- [24] Y.F. Shen, R.P. Zerger, R.N. DeGuzman, S.L. Suib, L. McCurdy, D.I. Potter, C.L. O'Young, Manganese oxide octahedral molecular sieves: Preparation, characterization, and applications, *Science* 260 (1993) 511.

- [25] Y. Lvov, B. Munge, O. Giraldo, I. Ichinose, S.L. Suib, J.F. Rusling, Films of manganese oxide nanoparticles with polycations or myoglobin from alternate-layer adsorption, *Langmuir* 16 (2000) 8850.
- [26] O. Giraldo, S.L. Brock, W.S. Willis, M. Marquez, S.L. Suib, S. Ching, Manganese oxide thin films with fast ion-exchange properties, *J. Am. Chem. Soc.* 122 (2000) 9330.
- [27] M. Toupin, T. Brousse, D. Bélanger, Charge storage mechanism of MnO<sub>2</sub> electrode used in aqueous electrochemical capacitor, *Chem. Mater.* 16 (2004) 3184.
- [28] A.R. Armstrong, P.G. Bruce, Synthesis of layered LiMnO<sub>2</sub> as an electrode for rechargeable lithium batteries, *Nature* 381 (1996) 499.
- [29] E.R. Stobbe, B.A. de Boer, J.W. Geus, The reduction and oxidation behaviour of manganese oxides, *Catal. Today* 47 (1999) 161.
- [30] E.J. Grootendorst, Y. Verbeek, V. Ponec, The role of the mars and van krevelen mechanism in the selective oxidation of nitrosobenzene and the deoxygenation of nitrobenzene on oxidic catalysts, *J. Catal.* 157 (1995) 706.
- [31] J. Shin, R.M. Anisur, M.K. Ko, G.H. Im, J.H. Lee, I.S. Lee, Hollow manganese oxide nanoparticles as multifunctional agents for magnetic resonance imaging and drug delivery, *Angew. Chem. Int. Ed.* 48 (2009) 321.
- [32] T.-L. Ha, H.J. Kim, J. Shin, G.H. Im, J.W. Lee, H. Heo, J. Yang, C.M. Kang, Y.S. Choe, J.H. Lee, I.S. Lee, Development of target-specific multimodality imaging agent by using hollow manganese oxide nanoparticles as a platform, *Chem. Commun.* 47 (2011) 9176.
- [33] R. Ramachandran, Preparation and characterization of manganous manganic oxide (Mn<sub>3</sub>O<sub>4</sub>), *J. Mater. Sci. - Mater. Electron.* 13 (2002) 257.
- [34] L. Sanchez, J. Farcy, J.-P. Pereira-Ramos, L. Hernan, J. Morales, J.L. Tirado, Low-temperature mixed spinel oxides as lithium insertion compounds, *J. Mater. Chem.* 6 (1996) 37.
- [35] C. Zener, Interaction between the d-shells in the transition metals. II. ferromagnetic compounds of manganese with perovskite structure, *Phys. Rev.* 82 (1951) 403.
- [36] J.B. Goodenough, Theory of the role of covalence in the perovskite-Type manganites [La,M(II)]MnO<sub>3</sub>, *Phys. Rev.* 100 (1955) 564.

- [37] P.W. Anderson, New approach to the theory of superexchange interactions, *Phys. Rev.* 115 (1959) 2.
- [38] A. Urushibara, Y. Moritomo, T. Arima, A. Asamitsu, G. Kido, Y. Tokura, Insulator-metal transition and giant magnetoresistance in  $\text{La}_{1-x}\text{Sr}_x\text{MnO}_3$ , *Phys. Rev. B* 51 (1995) 14103.
- [39] A.P. Alivisatos, Semiconductor clusters, nanocrystals, and quantum dots, *Science* 271 (1996) 933.
- [40] S.-W. Kim, J.P. Zimmer, S. Ohnishi, J.B. Tracy, J.V. Frangioni, M.G. Bawendi, Engineering  $\text{InAs}_x\text{P}_{1-x}/\text{InP}/\text{ZnSe}$  III–V alloyed core/shell quantum dots for the near-infrared, *J. Am. Chem. Soc.* 127 (2005) 10526.
- [41] R.E. Bailey, S. Nie, Alloyed semiconductor quantum dots: Tuning the optical properties without changing the particle size, *J. Am. Chem. Soc.* 125 (2003) 7100.
- [42] J.M. Pietryga, R.D. Schaller, D. Werder, M.H. Stewart, V.I. Klimov, J.A. Hollingsworth, Pushing the band gap envelope: Mid-infrared emitting colloidal PbSe quantum dots, *J. Am. Chem. Soc.* 126 (2004) 11752.
- [43] S. Foglia, L. Suber, M. Righini, Size tailoring of CdS nanoparticles by different colloidal chemical techniques, *Colloid Surf., A* 177 (2001) 3.
- [44] R. Kho, C.L. Torres-Martínez, R.K. Mehra, A simple colloidal synthesis for gram-quantity production of water-soluble ZnS nanocrystal powders, *J. Colloid Interface Sci.* 227 (2000) 561.
- [45] P.K. Jain, X. Huang, I.H. El-Sayed, M.A. El-Sayed, Noble metals on the nanoscale: Optical and photothermal properties and some applications in imaging, sensing, biology, and medicine, *Acc. Chem. Res.* 41 (2008) 1578.
- [46] D. Peer, J.M. Karp, S. Hong, O.C. Farokhzad, R. Margalit, R. Langer, Nanocarriers as an emerging platform for cancer therapy, *Nat. Nanotech.* 2 (2007) 751.
- [47] A. Giri, N. Goswami, M.S. Bootharaju, P.L. Xavier, R. John, N.T.K. Thanh, T. Pradeep, B. Ghosh, A.K. Raychaudhuri, S.K. Pal, Emergence of multicolor photoluminescence in  $\text{La}_{0.67}\text{Sr}_{0.33}\text{MnO}_3$  nanoparticles, *J. Phys. Chem. C* 116 (2012) 25623.
- [48] A. Giri, N. Goswami, M. Pal, M.T. Zar Myint, S. Al-Harathi, A. Singha, B. Ghosh, J. Dutta, S.K. Pal, Rational surface modification of  $\text{Mn}_3\text{O}_4$  nanoparticles to induce multiple

photoluminescence and room temperature ferromagnetism, *J. Mater. Chem. C* 1 (2013) 1885.

[49] A. Giri, A. Makhal, B. Ghosh, A.K. Raychaudhuri, S.K. Pal, Functionalization of manganite nanoparticles and their interaction with biologically relevant small ligands: Picosecond time-resolved FRET studies, *Nanoscale* 2 (2010) 2704.

[50] A. Giri, N. Goswami, P. Lemmens, S.K. Pal, Preparation of water soluble l-arginine capped CdSe/ZnS QDs and their interaction with synthetic DNA: Picosecond-resolved FRET study, *Mater. Res. Bull.* 47 (2012) 1912.

[51] N. Goswami, A. Baksi, A. Giri, P.L. Xavier, G. Basu, T. Pradeep, S.K. Pal, Atomically precise luminescent iron clusters in solution, *Nanoscale* (2013) (In press).

## Chapter 2

### Overview of Spectroscopic Tools and Systems

In order to investigate the various processes involved in course of study on ultrafast spectroscopy, synthesis, functionalization and potential application of the nanocrystals, the different steady-state and dynamical tools that have been used are Förster Resonance Energy Transfer (FRET) theory and kinetic model of Tachiya in donor-acceptor systems. In this chapter, a brief discussion about these tools has been provided. A brief overview of the various systems used has also been discussed.

#### 2.1. Steady-State and Dynamical Tools

**2.1.1. Förster Resonance Energy Transfer (FRET):** Förster Resonance Energy Transfer [1] is an electrodynamic phenomenon involving the non-radiative transfer of the excited state energy from the donor dipole (D) to an acceptor dipole (A) (Figure 2.1a). FRET has got wide uses in all fluorescence applications including medical diagnostics, DNA analysis and optical imaging. Since FRET can measure the size of a protein molecule or the thickness of a membrane, it is also known as “spectroscopic ruler” [2]. FRET is very often used to measure the distance between two sites on a macromolecule. Basically, FRET is of two types: (a) Homo-molecular FRET and (b) Hetero-molecular FRET. In the former case the same fluorophore acts both as energy donor and acceptor, while in the latter case two different molecules act as donor and acceptor.

Each donor-acceptor (D-A) pair participating in FRET is characterized by a distance known as Förster distance ( $R_0$ ) i.e., the D-A separation at which energy transfer is 50% efficient. The  $R_0$  value ranges from 20 to 60 Å. The rate of resonance energy transfer ( $k_T$ ) from donor to an acceptor is given by [3],

$$k_T = \frac{1}{\tau_D} \left( \frac{R_0}{r} \right)^6 \quad (2.1)$$

where  $\tau_D$  is the lifetime of the donor in the absence of acceptor,  $R_0$  is the Förster distance and  $r$  is the donor to acceptor (D-A) distance. The rate of transfer of donor energy depends upon the extent of overlap of the emission spectrum of the donor with the absorption spectrum of the acceptor ( $J(\lambda)$ ), the quantum yield of the donor ( $Q_D$ ), the relative

orientation of the donor and acceptor transition dipoles ( $\kappa^2$ ) and the distance between the donor and acceptor molecules ( $r$ ) (Figure 2.1b). In order to estimate FRET efficiency of the donor and hence to determine distances of donor-acceptor pairs, the methodology described below is followed [3]. The Förster distance ( $R_0$ ) is given by,

$$R_0 = 0.211[\kappa^2 n^{-4} Q_D J(\lambda)]^{1/6} \text{ (in \AA)} \quad (2.2)$$

where  $n$  is the refractive index of the medium,  $Q_D$  is the quantum yield of the donor and  $J(\lambda)$  is the overlap integral.  $\kappa^2$  is defined as,

$$\kappa^2 = (\cos\theta_T - 3\cos\theta_D \cos\theta_A)^2 = (\sin\theta_D \sin\theta_A \cos\varphi - 2\cos\theta_D \cos\theta_A)^2 \quad (2.3)$$

where  $\theta_T$  is the angle between the emission transition dipole of the donor and the absorption transition dipole of the acceptor,  $\theta_D$  and  $\theta_A$  are the angles between these dipoles and the vector joining the donor and acceptor and  $\varphi$  is angle between the planes of the donor and acceptor (Figure 2.1b).  $\kappa^2$  value can vary from 0 to 4. For collinear and parallel transition dipoles,  $\kappa^2 = 4$ ; for parallel dipoles,  $\kappa^2 = 1$ ; and for perpendicularly oriented dipoles,  $\kappa^2 = 0$ . For donor and acceptors that randomize by rotational diffusion prior to energy transfer, the magnitude of  $\kappa^2$  is assumed to be  $2/3$ .  $J(\lambda)$ , the overlap integral, which expresses the degree of spectral overlap between the donor emission and the acceptor absorption, is given by,

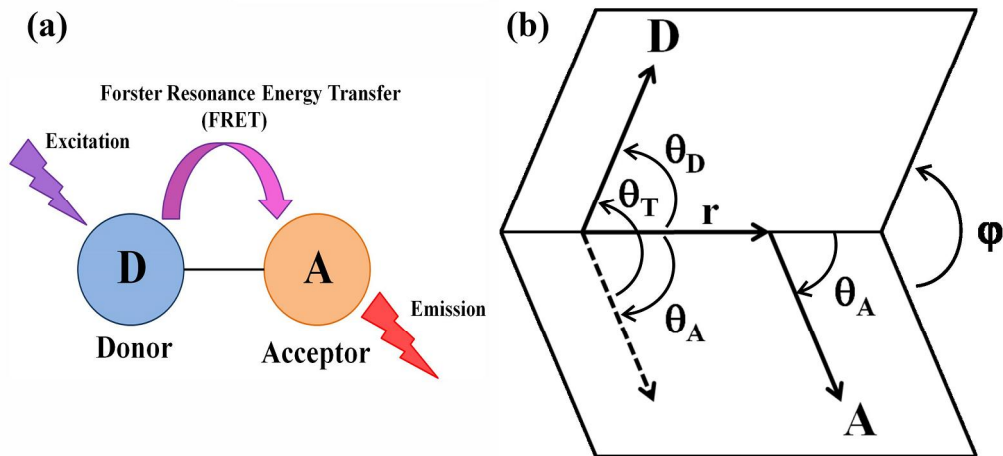


**Figure 2.1.** (a) Schematic illustration of the Förster Resonance Energy Transfer (FRET) process. (b) Dependence of the orientation factor  $\kappa^2$  on the directions of the emission and absorption dipoles of the donor and acceptor, respectively.

$$J(\lambda) = \frac{\int_0^{\infty} F_D(\lambda) \varepsilon_A(\lambda) \lambda^4 d\lambda}{\int_0^{\infty} F_D(\lambda) d\lambda} \quad (2.4)$$

where,  $F_D(\lambda)$  is the fluorescence intensity of the donor in the wavelength range of  $\lambda$  to  $\lambda + d\lambda$  and is dimensionless.  $\varepsilon_A(\lambda)$  is the extinction coefficient (in  $M^{-1}cm^{-1}$ ) of the acceptor at  $\lambda$ . If  $\lambda$  is in nm, then  $J(\lambda)$  is in units of  $M^{-1} cm^{-1} nm^4$ .

Once the value of  $R_0$  is known, the efficiency of energy transfer can be calculated. The efficiency of energy transfer ( $E$ ) is the fraction of photons absorbed by the donor which are transferred to the acceptor and is defined as,

$$E = \frac{k_T(r)}{\tau_D^{-1} + k_T(r)} \quad (2.5)$$

or

$$E = \frac{R_0^6}{r^6 + R_0^6} \quad (2.6)$$

The transfer efficiency is measured using the relative fluorescence intensity of the donor, in absence ( $F_D$ ) and presence ( $F_{DA}$ ) of the acceptor as,

$$E = 1 - \frac{F_{DA}}{F_D} \quad (2.7a)$$

For D-A systems decaying with multiexponential lifetimes,  $E$  is calculated from the amplitude weighted lifetimes  $\langle \tau \rangle = \sum_i \alpha_i \tau_i$  [3] of the donor in absence ( $\tau_D$ ) and presence ( $\tau_{DA}$ ) of the acceptor as,

$$E = 1 - \frac{\tau_{DA}}{\tau_D} \quad (2.7b)$$

The D-A distances can be measured using equations (2.6), (2.7a) and (2.7b). The distances measured using Eq. 2.7a and 2.7b are revealed as  $R^S$  (steady state measurement) and  $R^{TR}$  (time-resolved measurement), respectively. In one of recent studies from our group [4], we have reported the potential danger of using Eq. 2.7a to conclude the nature of energy transfer as Förster type. The study shows that the energy transfer efficiency  $E$ , calculated from steady state experiment (Eq. 2.7a) might be due to re-absorption of donor emission, but not due to dipole-dipole interaction (FRET).

**2.1.2. Tachiya Model:** The excited state decay of the donor may be described by the following kinetic model assuming a competition of the energy transfer with unimolecular decay processes:



where  $P_n^*$  stands for excited state donor with n number of acceptor molecules attached, while  $P_n$  stands for ground state donor with n number of acceptor molecules attached.  $k_0$  is the total decay constant of the donor in excited state in absence of the acceptor molecule.  $k_q$  is the rate constant for energy transfer for one donor molecule. In this model, it is assumed that the distribution of the number of acceptor molecules attached to one donor follows a Poisson distribution, [5] namely:

$$p(n) = (m^n / n!) \exp(-m) \quad (2.10)$$

where m is the mean number of acceptor molecules attached to one donor and

$$m = k_+[A] / k_- \quad (2.11)$$

where  $k_+$  is the rate constant for attachment of a acceptor molecule to a donor, while  $k_-$  is the rate constant for detachment of a acceptor molecule from the donor.  $[A]$  stands for the concentration of acceptor molecule in the aqueous phase. Based upon the above model, the equation for the total concentration  $P^*(t)$  of excited state donor at time t is given by [5]:

$$P^*(t) = P^*(0) \exp\left[-\left(k_0 + \frac{k_0 k_+[A]}{k_- + k_q}\right)t - \frac{k_q^2 k_+[A]}{k_-(k_- + k_q)^2} \{1 - \exp[-(k_- + k_q)t]\}\right] \quad (2.12)$$

If  $k_-$  is much smaller than  $k_q$ , Eq. (2.12) reduces to:

$$P^*(t) = P^*(0) \exp\{-k_0 t - m[1 - \exp(-k_q t)]\} \quad (2.13)$$

In one of our study, we have used the Tachiya kinetic model where QDs nanocrystals and EB-DNA molecules have been used as donor and acceptor respectively. In our system, along with the acceptor EB-DNA molecules, there exist some unidentified traps on the surface of the QDs and these are also taken into account. If the distribution of the number of unidentified traps on the surface of the QDs follows a Poisson distribution with the average number ( $m_t$ ), the decay curves of the excited state of QDs in the absence and presence of dye molecules are described by [6]:

$$P^*(t,0) = P^*(0) \exp\{-k_0 t - m_t[1 - \exp(-k_{qt}t)]\} \quad (2.14)$$

$$\text{and } P^*(t,m) = P^*(0) \exp\{-k_0 t - m_t[1 - \exp(-k_{qt}t)] - m[1 - \exp(-k_q t)]\} \quad (2.15)$$

where the quenching rate constant ( $k_{qt}$ ) by unidentified traps may be different from that ( $k_q$ ) by acceptor EB-DNA molecules. We have determined the values of the parameters  $m_t$ ,  $k_{qt}$ ,  $k_0$ ,  $m$ , and  $k_q$  by fitting Eq. 2.14 and 2.15 to the decay curves in the absence and presence of acceptor EB-DNA molecules.

## 2.2. Systems:

**2.2.1. Molecular Probes:** In this section, we will discuss about the different probe molecules that have been used in the course of study.

**2.2.1.1. 4-nitrophenyl anthranilate (4-NPA):** 4-NPA (Figure 2.2A) is a well-known probe having an anthranilate group as fluorescence moiety. 4-NPA, also has an active p-nitro-phenyl ester group that can react with nucleophiles [7].

**2.2.1.2. [3,8-diamino-5-ethyl-6-phenylphenanthridinium bromide], Ethidium Bromide (EtBr):** EtBr is a well known fluorescent probe for DNA, which readily intercalates into the DNA double helix [8]. Its structure is given in Figure 2.2B. Compared to the case of bulk water, the emission intensity and lifetime of EtBr increase nearly 11 times when EtBr intercalates into the double helix of DNA. This remarkable fluorescence enhancement of EtBr is utilized to study the motion of DNA segments, quenching of DNA bound EtBr by various agents, and the interaction of DNA with surfactants and drugs [9]. The photophysical processes of the fluorescence enhancement have recently been explored. The emission intensity of EtBr is low in highly polar, protic solvents, such as alcohol and water, compared to polar, aprotic solvents, e.g., acetone or pyridine. EtBr is insoluble in nonpolar, aprotic solvents like alkanes or dioxane. Compared to the case of water, the emission intensity and lifetime of EtBr increase nearly 5 times in acetone. Addition of water to acetone is found to quench fluorescence of EtBr, while deuterated solvents enhance emission of EtBr.

**2.2.1.3. 2'-(4-hydroxyphenyl)-5-[5-(4-methylpiperazine-1-yl)-benzimidazo-2-yl-benzimidazole], Hoechst 33258 (H258):** The commercially available probe H258 (Figure 2.2C) is widely used as fluorescent cytological stain of DNA. Since it has affinity for the double stranded DNA, H258 can affect transcription/translation, and block

topomerase/helicase activities. The dye is also used as a potential antihelminthic drug. X-ray crystallographic and NMR studies of the dye bound to a dodecamer DNA shows that the dye is bound to A-T rich sequence of the DNA minor groove. The binding constant of the dye [10] to double stranded DNA at low [dye]:[DNA] ratio is found to be  $5 \times 10^5 \text{ M}^{-1}$ . The solvchromic properties of the dye can be used to report the hydration dynamics as well as the dynamics of restricted systems [11].

**2.2.1.4. 2-aminopurine (2-AP):** 2-AP (Figure 2.2D), an analog of guanine and adenine, is a fluorescent molecular marker used in nucleic acid research [12]. It most commonly pairs with thymine as an adenine-analogue, but can also pair with cytosine as a guanine-analogue [13]. For this reason it is sometimes used in the laboratory for mutagenesis.

**2.2.1.5. 4',6-diamidino-2-phenylindole (DAPI):** The dye DAPI (Figure 2.2E) is another commercially available fluorescent cytological stain for DNA. Studies on the DAPI-DNA complexes show that the probe exhibits a wide variety of interactions of different strength and specificity with DNA [14]. The dye exhibits intramolecular proton transfer as an important mode of excited state relaxation at physiological pH,[15] which takes place from the amidino to the indole moiety. Suppression of this excited state pathway leads to enhancement of fluorescence quantum yield and hence the fluorescence intensity in hydrophobic restricted environments.

**2.2.1.6. Methylene blue (MB):** MB is a heterocyclic aromatic chemical compound with molecular formula:  $\text{C}_{16}\text{H}_{18}\text{ClN}_3\text{S}$ . It has many uses in a range of different fields. At room-temperature it appears as a solid and is odourless and a dark green powder, which yields a blue solution when dissolved in water. They are widely used as model water contaminant [16]. Its structure is given in Figure 2.2F. When dissolved in water, the UV-vis spectrum of MB showed three absorption maxima. The first band was observed at 246 nm and then 291 nm and more intensely 663 nm. The absorption maxima wavelength of MB ( $\lambda_{\text{max}} = 663 \text{ nm}$ ) was used for the analysis during decolorization of MB dye.

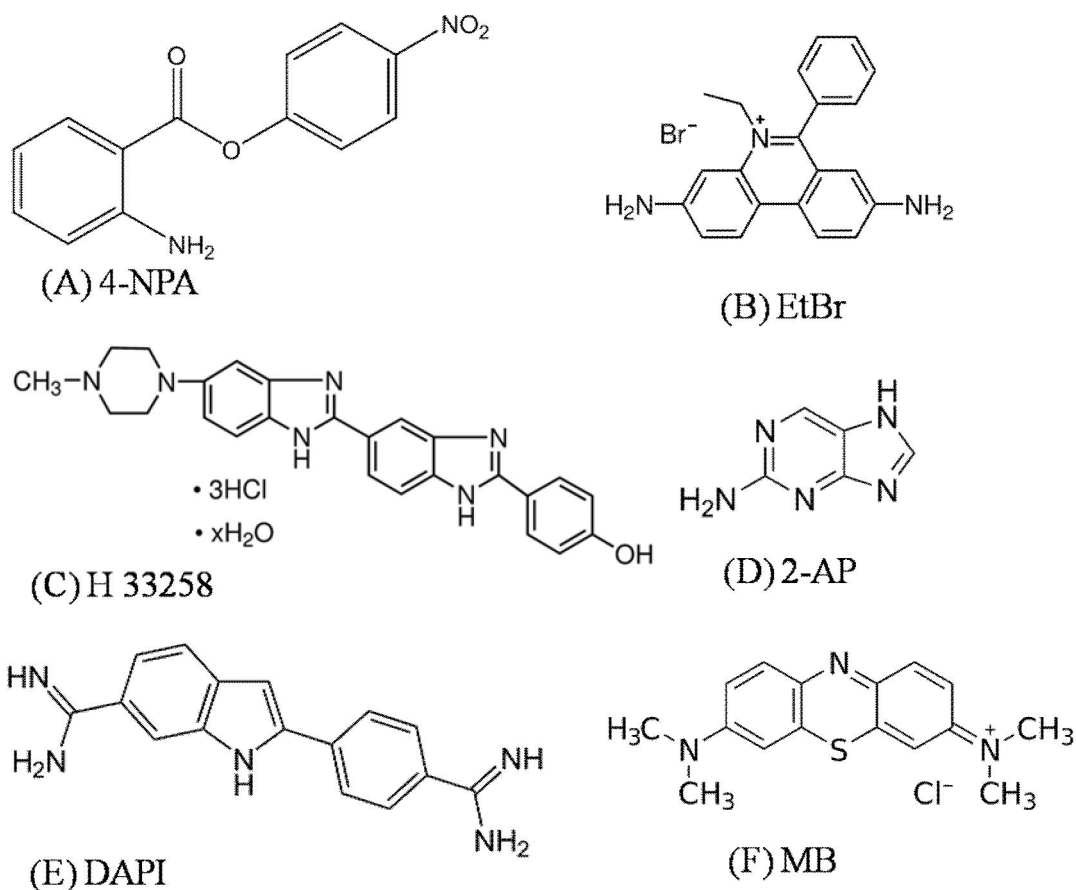


**Figure 2.2.** Molecular structure of the probes: (A) 4-NPA, (B) EtBr, (C) H 33258, (D) 2-AP, (E) DAPI and (F) MB.

### 2.2.2. Protein:

**2.2.2.1. Human Serum Albumin (HSA):** Serum albumins are multi-domain proteins forming the major soluble protein constituent (60% of the blood serum) of the circulatory system [17]. Human Serum Albumin (HSA) (molecular weight 66,479 Da) is a heart-shaped tridomain protein (Figure 2.3) with each domain comprising of two identical subdomains A and B with each domain depicting specific structural and functional characteristics [18]. HSA having 585 amino acid residues assumes solid equilateral triangular shape with sides  $\sim 80$  Å and depth  $\sim 30$  Å [19]. Its amino acid sequence comprises of 17 disulfide bridges distributed over all domains, one free thiol (Cys34) in domain-I and a tryptophan residue (Trp214) in domain-IIA. About 67% of HSA is  $\alpha$ -helical while the rest of the structure being turns and extended polypeptides [19]. Each domain contains 10 principle helices (h1-h10). Subdomains A and B share a common

motif that includes h1, h2, h3 and h4 for subdomain-A, and h7, h8, h9, h10 for subdomain-B. The non-existence of disulfide linkage connecting h1 and h3 in subdomain-IA is an exception. HSA is engaged with various physiological functions involving maintenance of osmotic blood pressure, transportation of a wide variety of ligands in and out of the physiological system. The protein binds various kinds of ligands [20] including photosensitizing drugs [21]. The principal binding regions are located in subdomains IIA and IIIA of which IIIA binding cavity is the most active one [19] and binds digitoxin, ibuprofen and tryptophan. Warfarin, however, occupies a single site in domain-IIA. It is known that HSA undergoes reversible conformational transformation with change in pH of the protein solution [17, 22], which is very essential for picking up and releasing the drugs at sites of differing pH inside the physiological system.

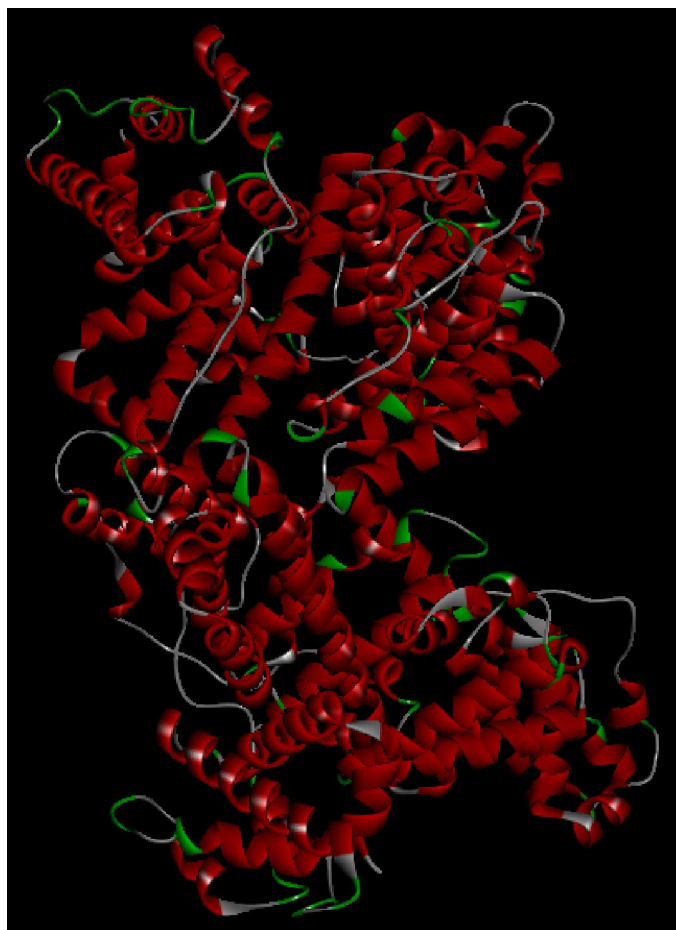


**Figure 2.3.** Schematic structure of Human Serum Albumin (HSA). Protein Data Bank ID-4K2C.

At normal pH (pH = 7), HSA assumes the normal form (N) which abruptly changes to fast migrating form (F) at pH values less than 4.3, as this form moves “fast” upon gel electrophoresis [22]. Upon further reduction in pH to less than 2.7 the F-form changes to the fully extended form (E). On the basic side of the normal pH (above pH = 8), the N-form changes to basic form (B) and above pH = 10, the structure changes to the aged form (A). Serum albumin undergoes an ageing process when stored at low ionic strength and alkaline pH. The ageing process is catalyzed by the free sulfhydryl group and involves sulfhydryl-disulfide interchange that results in the conservation of the sulfhydryl at its original position.

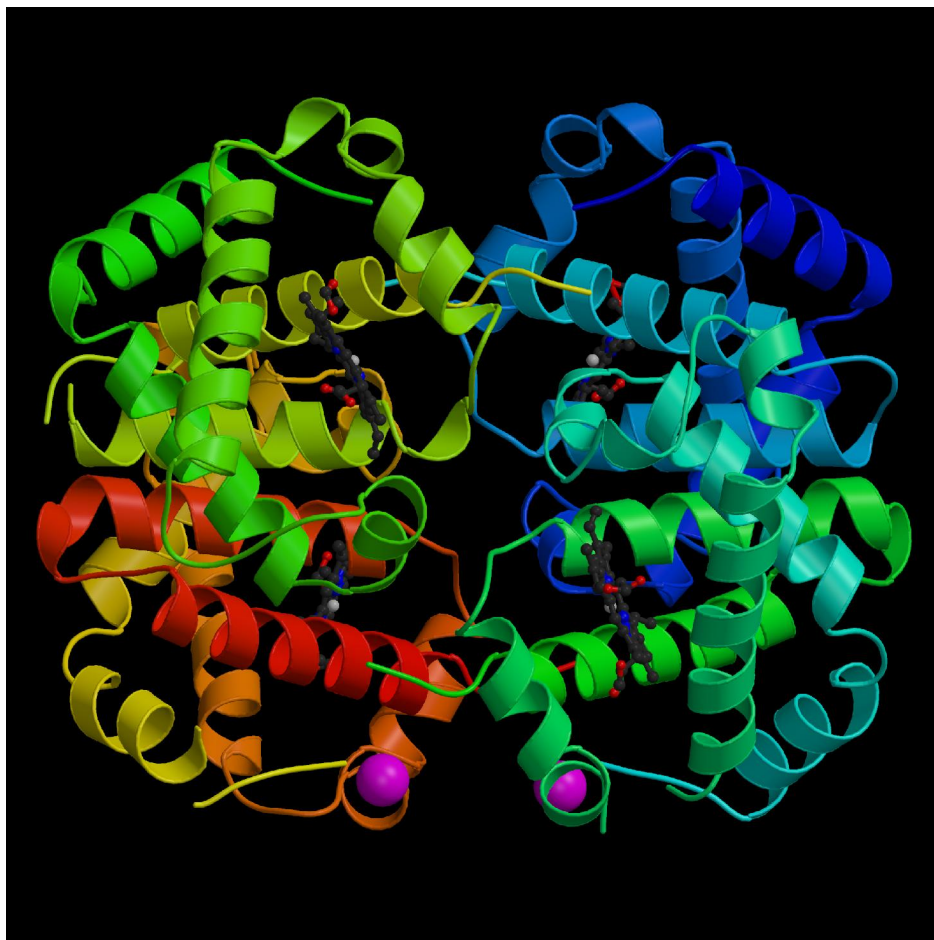


**Figure 2.4.** Structure of hemoglobin. There are four subunits as shown by the various colors. The heme groups are shown in predominantly gray. Protein Data Bank ID-4hbb.

**2.2.2.1. Hemoglobin:** Found in red blood cells, hemoglobin (Figure 2.4) is globular protein that ferry oxygen (O<sub>2</sub>) molecules and carbon dioxide (CO<sub>2</sub>) molecules throughout the body. Each hemoglobin protein structure consists of four polypeptide subunits, which are held together by ionic bonds, hydrogen bonds, hydrophobic interactions, and van der Waals forces, as well as four heme pigments, one in each of the subunits [23, 24]. These heme groups contain positively-charged iron (Fe<sup>2+</sup>) molecules which can reversibly bind to oxygen molecules and transport them to various areas of the body [23, 24]. As the heme groups bind or release their oxygen loads, the overall hemoglobin undergoes conformational changes which alters their affinity for oxygen. Hemoglobin tetramers are comprised of the four subunits, two  $\alpha$ -globin chains and two  $\beta$ -globin chains all of which take the form of alpha helices [23]. Found in each chain is a non-protein heme group, which is an assembly of cyclic ring structures surrounding an iron ion that is tethered by nitrogen atoms. The heme group, which is typically hidden within the various subunits, is covalently bound to yet a different nitrogen atom that belongs to a nearby histidine group. This histidine chain, combined with other hydrophobic interactions, stabilize the heme group within each subunit. Oxygen molecules bind to the side of the iron ion that is opposite of the proximal histidine. Located near this opposite side is a different histidine chain, which serves two important function even though it is not directly bound to the heme group [25].

**2.2.3. Deoxyribonucleic Acid (DNA):** Nucleic acids form the central molecules in transmission, expression and conservation of genetic information. DNA serves as carrier of genetic information [26]. The classic example of how biological function follows from biomolecular structure comes from the elucidation of double helical structure of DNA by Watson and Crick [27]. DNAs are polynucleotides with each nucleotide comprising of deoxyribose sugar, purine and pyrimidine bases and phosphate groups. The main bases whose intermolecular hydrogen bonding holds the DNA strands together are adenine, guanine, thymine and cytosine. There are generally three forms of DNA: the A, B and Z-form. Native DNA, however, exists in B-form. Native DNA is about a metre long and comprises of hundreds of base pairs. The distance between two base pairs in B-DNA is 3.4 Å [28]. In about 4 M NaCl, B-form is converted into Z-form. DNA structures consist of

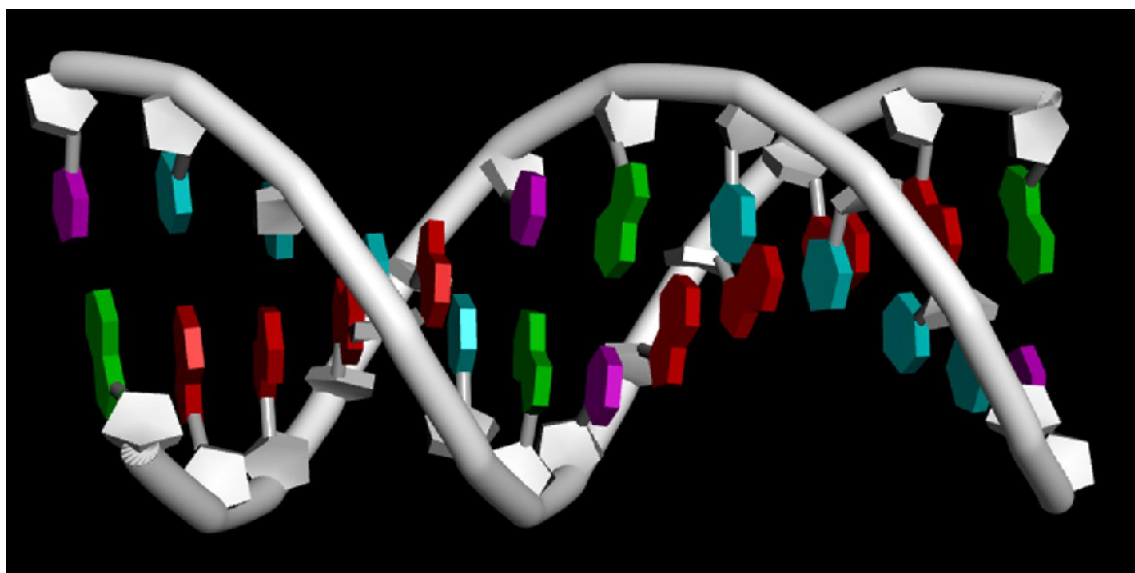


**Figure 2.5.** Schematic representation of a double stranded DNA. The DNA structure having sequence CTTTTGCAAAAG was made by employing the WEBLAB VIEWERLITE program.

major and minor grooves and intercalation spaces through which DNA interacts with ligands. There are two modes of interaction of DNA with ligands: (i) intercalation, where the planar polycyclic heteroaromatic ligands occupy the space in between the base pairs of DNA (Figure 2.5) and interact through  $\pi$ - $\pi$  interaction [29, 30], and (ii) groove binding where the ligands bind in the major and minor grooves of DNA [31]. The water molecules at the surface of DNA are critical to the structure and to the recognition by other molecules, proteins and drugs. In one of our study, a synthetic DNA oligomer having sequence CTTTTGCAAAAG was used.

## References

- [1] T. Förster, Intramolecular energy migration and fluorescence, *Ann. Phys.* 2 (1948) 55.
- [2] L. Stryer, Fluorescence energy transfer as a spectroscopic ruler, *Annu. Rev. Biochem.* 47 (1978) 819.
- [3] J.R. Lakowicz, Principles of Fluorescence Spectroscopy, 3<sup>rd</sup> ed., Springer, New York, 2006.
- [4] P. Majumder, R. Sarkar, A.K. Shaw, A. Chakraborty, S.K. Pal, Ultrafast dynamics in a nanocage of enzymes: Solvation and fluorescence resonance energy transfer in reverse micelles, *J. Colloid Interface Sci.* 290 (2005) 462.
- [5] M. Tachiya, Kinetics of quenching of luminescent probes in micellar systems. II, *J. Chem. Phys.* 76 (1982) 340.
- [6] S. Sadhu, K.K. Haldar, A. Patra, Size dependent resonance energy transfer between semiconductor quantum dots and dye using FRET and kinetic model, *J. Phys. Chem. C* 114 (2010) 3891.
- [7] J. Broos, A.J.W.G. Visser, J.F.J. Engbersen, W. Verboom, A. Van Hoek, D.N. Reinhoudt, Flexibility of enzymes suspended in organic solvents probed by time-resolved fluorescence anisotropy. Evidence that enzyme activity and enantioselectivity are directly related to enzyme flexibility, *J. Am. Chem. Soc.* 117 (1995) 12657.
- [8] D.P. Millar, R.J. Robbins, A.H. Zewail, Torsion and bending of nucleic acids studied by subnanosecond time-resolved fluorescence depolarization of intercalated dyes, *J. Chem. Phys.* 76 (1982) 2080.
- [9] S.K. Pal, D. Mandal, K. Bhattacharyya, Photophysical processes of ethidium bromide in micelles and reverse micelles, *J. Phys. Chem. B* 102 (1998) 11017.
- [10] R. Jin, K.J. Breslauer, Characterization of the minor groove environment in a drug-DNA complex: Bisbenzimidazole bound to the poly[d(AT)].poly[d(AT)]duplex, *Proc. Natl. Acad. Sci.* 85 (1988) 8939.
- [11] S.K. Pal, L. Zhao, A.H. Zewail, Water at DNA surfaces: Ultrafast dynamics in minor groove recognition, *Proc. Natl. Acad. Sci.* 100 (2003) 8113.
- [12] J.M. Jean, K.B. Hall, 2-aminopurine fluorescence quenching and lifetimes: Role of base stacking, *Proc. Natl. Acad. Sci.* 98 (2001) 37.

- [13] L.C. Sowers, G.V. Fazakerley, R. Eritja, B.E. Kaplan, M.F. Goodman, Base pairing and mutagenesis: Observation of a protonated base pair between 2-aminopurine and cytosine in an oligonucleotide by proton NMR, *Proc. Natl. Acad. Sci.* 83 (1986) 5434.
- [14] W.D. Wilson, F.A. Tanious, H.J. Barton, R.L. Jones, K. Fox, R.L. Wydra, L. Streckowski, DNA sequence dependent binding modes of 4',6-diamidino-2-phenylindole (DAPI), *Biochemistry* 29 (1990) 8452.
- [15] M.L. Barcellona, E. Gratton, A molecular approach to 4',6-diamidino-2-phenylindole (DAPI) photophysical behaviour at different pH values, *Biophys. Chem.* 40 (1991) 223.
- [16] N. Xu, Z. Shi, Y. Fan, J. Dong, J. Shi, M.Z.C. Hu, Effects of particle size of TiO<sub>2</sub> on photocatalytic degradation of methylene blue in aqueous suspensions, *Ind. Eng. Chem. Res.* 38 (1999) 373.
- [17] J.F. Foster, Some aspects of the structure and conformational properties of serum albumin, Oxford, Pergamon, 1977.
- [18] M. Dockal, D.C. Carter, F. Rümer, The three recombinant domains of human serum albumin: Structural characterization and ligand binding properties, *J. Biol. Chem.* 274 (1999) 29303.
- [19] X.M. He, D.C. Carter, Atomic structure and chemistry of human serum albumin, *Nature* 358 (1992) 209.
- [20] J. Ghuman, P.A. Zunszain, I. Petitpas, A.A. Bhattacharya, M. Otagiri, S. Curry, Structural basis of the drug-binding specificity of human serum albumin, *J. Mol. Biol.* 353 (2005) 38.
- [21] M. Wardell, Z. Wang, J.X. Ho, J. Robert, F. Rümer, J. Ruble, D.C. Carter, The atomic structure of human methemalbumin at 1.9 Å, *Biochem. Biophys. Res. Commun.* 291 (2002) 813.
- [22] J.F. Foster, The plasma proteins, 1st ed., Academic Press, New York, 1960.
- [23] D.E. Sadava, H. Craig Heller, D.M. Hillis, M. Berenbaum, Life: The science of biology, 8<sup>th</sup> ed., Sinauer Associates Inc. and W.H. Freeman and Company, Massachusetts and Virginia, 2008.
- [24] E.J. Neer, W. Konigsberg, G. Guidotti, The interactions between  $\alpha$  and  $\beta$  chains of human hemoglobin, *J. Biol. Chem.* 243 (1968) 1971.

- [25] M.F. Perutz, Mechanisms regulating the reactions of human hemoglobin with oxygen and carbon monoxide, *Annu. Rev. Physiol.* 52 (1990) 1.
- [26] A.D. Hershey, M. Chase, Independent functions of viral protein and nucleic acid in growth of bacteriophage, *J. Gen. Physiol.* 36 (1952) 39.
- [27] J.D. Watson, F.H.C. Crick, Molecular structure of nucleic acids: A structure for deoxyribose nucleic acid, *Nature* 171 (1953) 737.
- [28] D.L. Nelson, M.M. Cox, *Lehninger principles of biochemistry*, 3rd ed., Worth, New York, 2000.
- [29] L.S. Lerman, The structure of the DNA-acridine complex, *Proc. Natl. Acad. Sci.* 49 (1963) 94.
- [30] M.B. Lyles, I.L. Cameron, Interactions of the DNA intercalator acridine orange, with itself, with caffeine, and with double stranded DNA, *Biophys. Chem.* 96 (2002) 53.
- [31] P.B. Dervan, Molecular recognition of DNA by small molecules, *Bioorg. Med. Chem.* 9 (2001) 2215.

# Chapter 3

## Instrumentation and Sample Preparation

In this chapter we will describe the details of instrumental setup and sample preparation techniques used in our studies.

### 3.1. Instrumental Setup:

**3.1.1. Steady-State Absorption and Fluorescence Spectroscopy:** Steady-state UV-vis absorption and emission spectra of the probe molecules were measured with Shimadzu UV-2450 spectrophotometer and Jobin Yvon Fluoromax-3 fluorimeter, respectively. Schematic ray diagrams of these two instruments are shown in Figures 3.1 and 3.2.

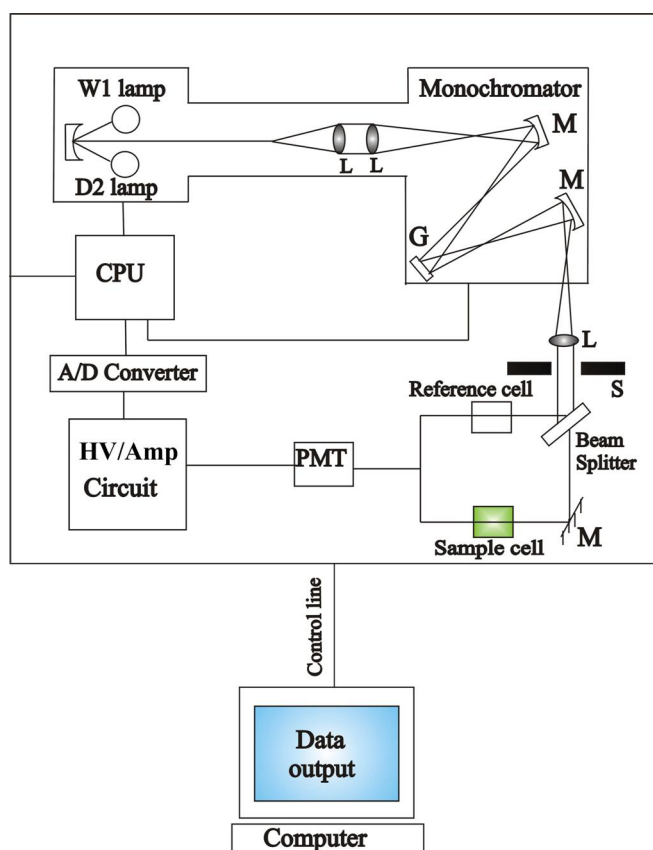


**Figure 3.1.** Schematic ray diagram of an absorption spectrophotometer. Tungsten halogen (W1) and Deuterium lamps (D2) are used as light sources in the visible and UV regions, respectively. M, G, L, S, PMT designate mirror, grating, lens, shutter and photomultiplier tube, respectively. CPU, A/D converter and HV/Amp indicate central processing unit, analog to digital converter and High-voltage/Amplifier circuit, respectively.

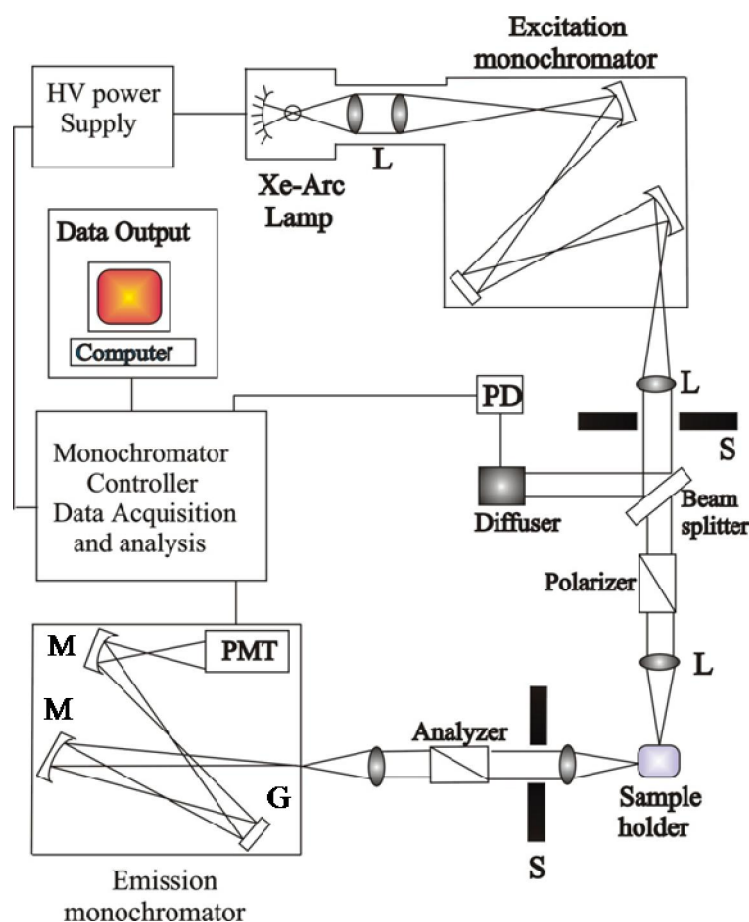


**Figure 3.2.** Schematic ray diagram of an emission spectrofluorimeter. M, G, L, S, PMT and PD represent mirror, grating lens, shutter, photomultiplier tube and reference photodiode, respectively.

**3.1.2. Circular Dichroism (CD) Spectroscopy:** Circular Dichroism (CD) is a form of spectroscopy based on the differential absorption of left and right-handed circularly polarized light. It can be used to determine the structure of macromolecules (including the secondary structure of proteins and the handedness of DNA). The CD measurements were done in a JASCO spectropolarimeter with a temperature controller attachment (Peltier) (Figure 3.3). The CD spectra were acquired using a quartz cell of 1 cm path length. For proteins, the typical concentration used for CD measurements were within 10  $\mu\text{M}$  while that for DNA were about 20  $\mu\text{M}$ . The secondary structural data of the CD spectra were analyzed using CDNN deconvolution program.

The working principle of CD measurement is as follows: when a plane polarized light passes through an optically active substance, not only do the left (L) and right (R) circularly polarized light rays travel at different speeds,  $c_L \neq c_R$ , but these two rays are absorbed to a different extent, i.e.  $A_L \neq A_R$ . The difference in the absorbance of the left and right circularly polarized light, i.e.,  $\Delta A = A_L - A_R$ , is defined as Circular Dichroism (CD). CD spectroscopy follows Beer-Lambert law. If  $I_0$  is the intensity of light incident on the cell, and  $I$ , that of emergent light, then absorbance is given by,

$$A = \log_{10} \left( \frac{I_0}{I} \right) = \epsilon cl \quad (3.1)$$

i.e.,  $A$  is proportional to concentration ( $c$ ) of optically active substance and optical path length ( $l$ ). If ' $c$ ' is in moles/litre and ' $l$ ' is in cm, then  $\epsilon$  is called the molar absorptivity or molar extinction coefficient. In an optically active medium, two absorbances,  $A_L$  and  $A_R$  are considered, where  $A_L = \log_{10}(I_0/I_L)$  and  $A_R = \log_{10}(I_0/I_R)$ . At the time of incidence on the sample, intensity of left and right circularly polarized light are same, i.e.  $I_0 = I_L = I_R$ . Any micrograph passes periodically changing light through the medium, oscillating between left and right circular polarization, and the difference in absorbances are recorded directly.

$$\Delta A = A_L - A_R = \log_{10} \left( \frac{I_0}{I_L} \right) - \log_{10} \left( \frac{I_0}{I_R} \right) = \log_{10} \left( \frac{I_R}{I_L} \right) \quad (3.2)$$

$$\text{or} \quad \Delta A = (\Delta \epsilon) cl \quad (3.3)$$

As seen from Eq. 3.2,  $I_0$  does not appear in this final equation, so there is no need for a reference beam. The instruments are, therefore, of single beam type. Most of the CD spectropolarimeters, although they measure differential absorption, produce a CD spectrum in units of ellipticity ( $\theta$ ) expressed in millidegrees versus  $\lambda$ , rather than  $\Delta A$  versus  $\lambda$ . The relation between ellipticity and CD is given by,

$$\theta = \frac{2.303 \times 180 \times (A_L - A_R)}{4\pi} \text{ degrees} \quad (3.4)$$

To compare the results from different samples, optical activity is computed on a molar or residue basis. Molar ellipticity,  $[\theta]$  is defined as,

$$[\theta] = \frac{\theta}{cl} \quad (3.5)$$

where ‘ $\theta$ ’ is in degrees, ‘ $c$ ’ is in moles per litre and ‘ $l$ ’ is in cm. The unit of molar ellipticity is  $\text{deg M}^{-1} \text{cm}^{-1}$ .

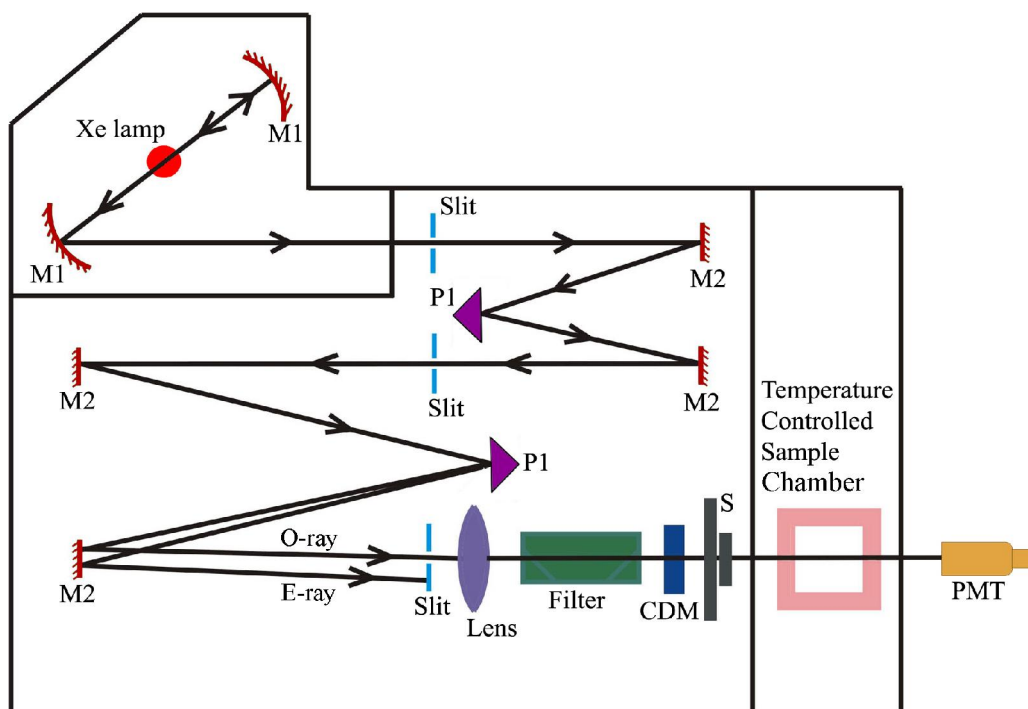


**Figure 3.3.** Schematic ray diagram of a circular dichroism (CD) spectropolarimeter. M1, M2, P1, S, PMT, CDM, O-ray and E-ray represent concave mirror, plain mirror, reflecting prism, shutter, photomultiplier tube, CD-modulator, ordinary ray and extraordinary ray, respectively.

**3.1.3. Time Correlated Single Photon Counting (TCSPC):** All the picosecond-resolved fluorescence transients were recorded using time correlated single photon counting (TCSPC) technique. The schematic block diagram of a TCSPC system is shown in Figure 3.4. TCSPC setup from Edinburgh instruments, U.K. was used during fluorescence decay acquisitions. The instrument response functions (IRFs) of the laser sources at different excitation wavelengths have been mentioned in our original published articles [1, 2]. The fluorescence from the sample was detected by a photomultiplier after dispersion through a grating monochromator. For all transients, the polarizer in the emission side was adjusted to be at  $54.7^\circ$  (magic angle) with respect to the polarization axis of excitation beam. In order to measure fluorescence anisotropy decay, the fluorescence decays were taken with

emission polarizer aligned in parallel and perpendicular directions with respect to vertical polarization of excitation light.

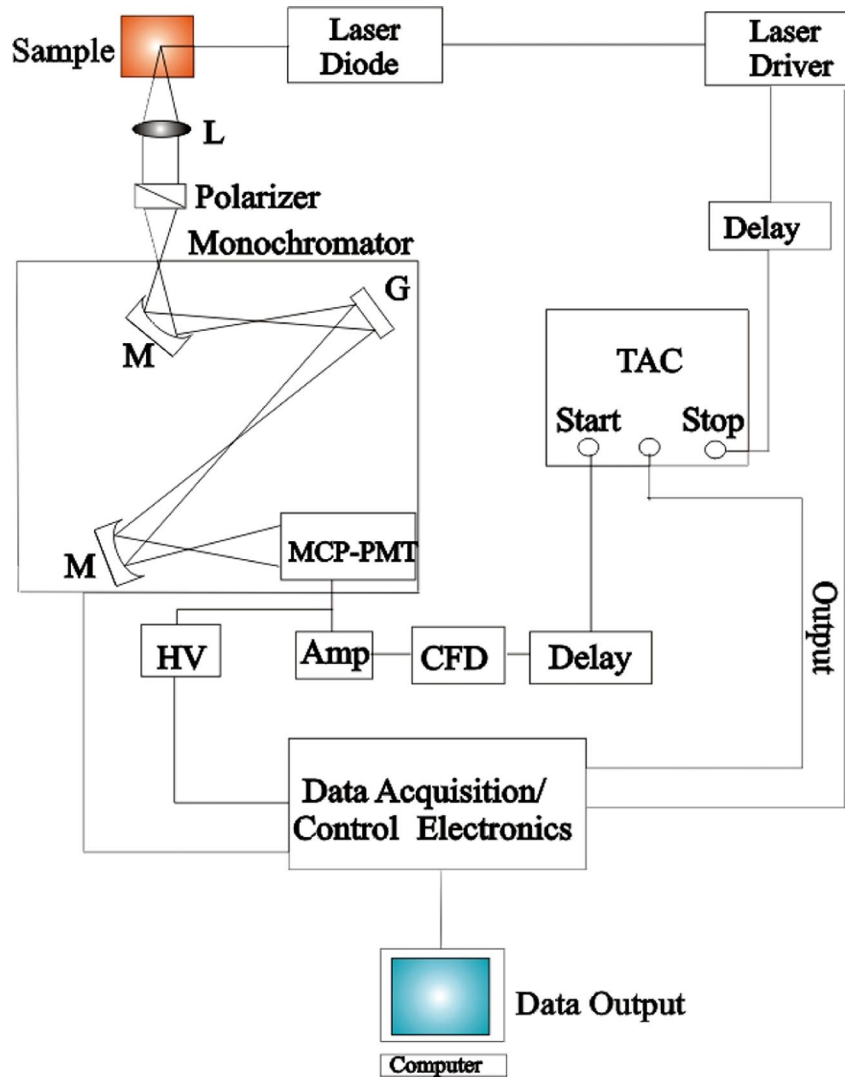


**Figure 3.4.** Schematic ray diagram of a time correlated single photon counting (TCSPC) spectrophotometer. A signal from microchannel plate photomultiplier tube (MCP-PMT) is amplified (Amp) and connected to start channel of time to amplitude converter (TAC) via constant fraction discriminator (CFD) and delay. The stop channel of the TAC is connected to the laser driver via a delay line. L, M, G and HV represent lens, mirror, grating and high voltage source, respectively.

**3.1.4. X-Ray Diffractometer (XRD):** It is a popular and powerful technique for determining crystal structure of crystalline materials. By examining the diffraction pattern, one can identify the crystalline phase of the material. Small angle scattering is useful for evaluating the average inter particle distance while wide-angle diffraction is useful for

refining the atomic structure of nanoclusters. The widths of the diffraction lines are closely related to strain and defect size and distribution in nanocrystals. As the size of the nanocrystals decrease, the line width is broadened due to loss of long-range order relative to the bulk.

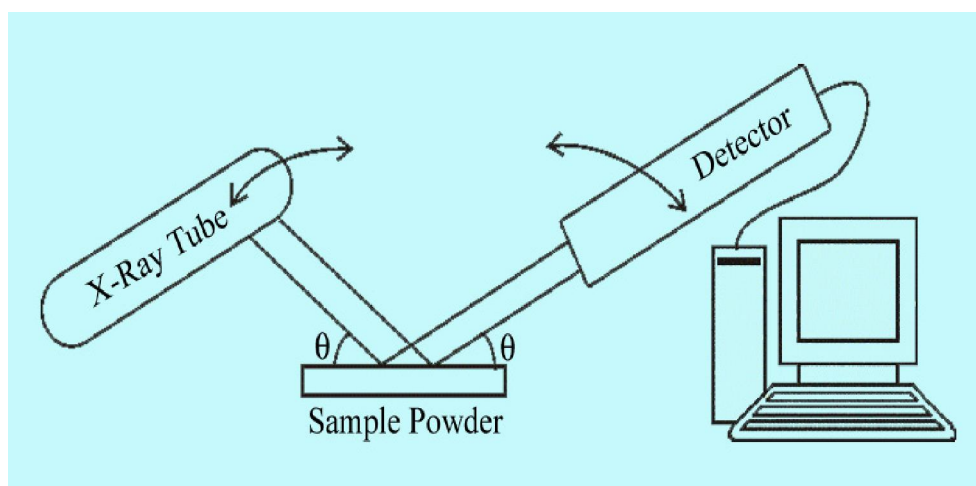


**Figure 3.5.** Schematic diagram of X-ray diffraction (XRD) instrument. By varying the angle  $\theta$ , the Bragg's Law conditions,  $n\lambda = 2d\sin\theta$  are satisfied by different d-spacings in polycrystalline materials. Plotting the angular positions and intensities of the resultant diffracted peaks of radiation produces a pattern, which is characteristic of the sample.

This XRD line width can be used to estimate the size of the particle by using the Debye-Scherrer formula,

$$D = \frac{0.9\lambda}{\beta \cos\theta} \quad (3.6)$$

where  $D$  is the nanocrystal diameter,  $\lambda$  is the wavelength of light,  $\beta$  is the full width half-maximum (fwhm) of the peak in radians, and  $\theta$  is the Bragg angle. XRD measurements were performed on a PANalytical XPERT-PRO diffractometer (Figure 3.5) equipped with Cu  $K\alpha$  radiation ( $\lambda = 1.5418 \text{ \AA}$  at 40 mA, 40 kV). XRD patterns were obtained by employing a scanning rate of  $0.02^\circ \text{ s}^{-1}$  in the  $2\theta$  range from  $20^\circ$  to  $80^\circ$ .

**3.1.5. Fourier Transform Infrared (FTIR) Spectroscopy:** It is a technique that can provide very useful information about functional groups in a sample. An infrared spectrum represents the fingerprint of a sample with absorption peaks which correspond to the

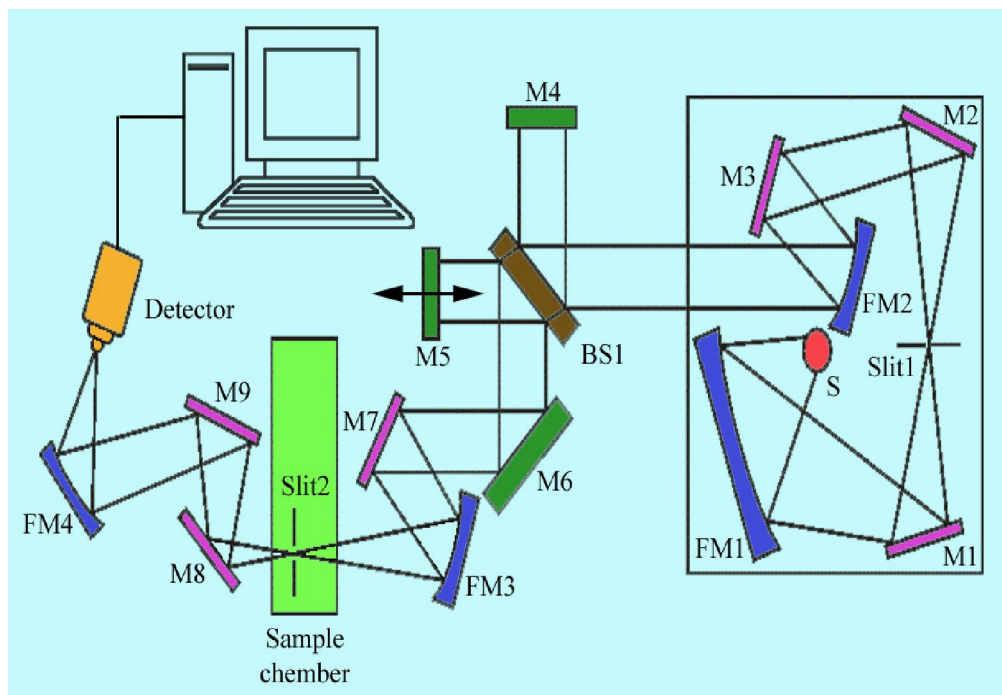


**Figure 3.6.** Schematic of Fourier transform infrared (FTIR) spectrometer. It is basically a Michelson interferometer in which one of the two fully-reflecting mirrors is movable, allowing a variable delay (in the travel-time of the light) to be included in one of the beams. M, FM and BS1 represent the mirror, focusing mirror and beam splitter, respectively. M5 is a moving mirror.

frequencies of vibrations between the bonds of the atoms making up the material. Because each different material is a unique combination of atoms, no two compounds produce the exact same infrared spectrum.

Therefore, infrared spectroscopy can result in a positive identification (qualitative analysis) of every different kind of material. In addition, the size of the peaks in the spectrum is a direct indication of the amount of material present. The two-beam Michelson interferometer is the heart of FTIR spectrometer. It consists of a fixed mirror (M4), a moving mirror (M5) and a beamsplitter (BS1), as illustrated in Figure 3.6. The beamsplitter is a laminate material that reflects and transmits light equally. The collimated IR beam from the source is partially transmitted to the moving mirror and partially reflected to the fixed mirror by the beamsplitter. The two IR beams are then reflected back to the beamsplitter by the mirrors. The detector then sees the transmitted beam from the fixed mirror and reflected beam from the moving mirror simultaneously. The two

combined beams interfere constructively or destructively depending on the wavelength of the light (or frequency in wavenumbers) and the optical path difference introduced by the moving mirror. The resulting signal is called an interferogram which has the unique property that every data point (a function of the moving mirror position) which makes up the signal has information about every infrared frequency which comes from the source. Because the analyst requires a frequency spectrum (a plot of the intensity at each individual frequency) in order to make identification, the measured interferogram signal cannot be interpreted directly. A means of “decoding” the individual frequencies is required. This can be accomplished via a well-known mathematical technique called the Fourier transformation. This transformation is performed by the computer which then presents the user with the desired spectral information for analysis. FTIR measurements were performed on a JASCO FTIR-6300 spectrometer (transmission mode). For the FTIR measurements, powdered samples were mixed with KBr powder and pelletized. The background correction was made using a reference blank of KBr pellet.

**3.1.6. Vibrating-Sample Magnetometer (VSM):** A vibrating-sample magnetometer measures the magnetic moment of a sample when it is vibrated perpendicularly to a uniform magnetizing field. With this instrument, changes as small as  $10^{-5}$  to  $10^{-6}$  emu can be detected, and a stability of one part in  $10^4$  can be attained [3]. The novel features of this magnetometer are: first, sample motion perpendicular to the applied field; and second, detection coil configurations, with effective area-turns non-symmetrically distributed about the axis of vibrations, which permit this oscillating dipole field to be observed. The sample is subjected to a sinusoidal motion (of frequency  $\nu$ ) and the corresponding voltage is induced in suitably located stationary pickup coils. The electrical output signals of these pickup coils have the same frequency  $\nu$ . The schematic diagram of the set-up is shown in Figure 3.7. The sample to be measured is centered in the region between the poles of an electromagnet which can generate a uniform magnetic field  $H_0$ . A thin vertical nonmagnetic sample rod connects the sample holder with a transducer assembly located above the magnet. The transducer converts a sinusoidal signal as drive signal (generated by an oscillator/amplifier circuit) into a sinusoidal vertical vibration of the sample rod. The sample is thus subjected to a sinusoidal motion in the magnetic field  $H_0$ . Pickup coils made of copper and mounted on the poles of the magnet which pickup

the signal resulting from the motion of the sample. However, though the pickup coil signal at the vibration frequency  $\nu$  is proportional to the magnitude of the moment of the sample, it is also proportional to the vibration amplitude and frequency. Thus the moment readings taken simply by measuring the amplitude of the signal are subjected to errors due to variation in amplitude and frequency of vibration. In order to avoid this difficulty, a nulling technique is introduced employing a vibrating capacitor for generating a reference signal that varies with moment, vibration amplitude and frequency, in the same manner as the signal from the pickup coils. When these two signals are processed in an appropriate manner, it is possible to eliminate the effects of vibration amplitude and frequency shifts. In that case one obtains readings that vary only with the moment of the samples.

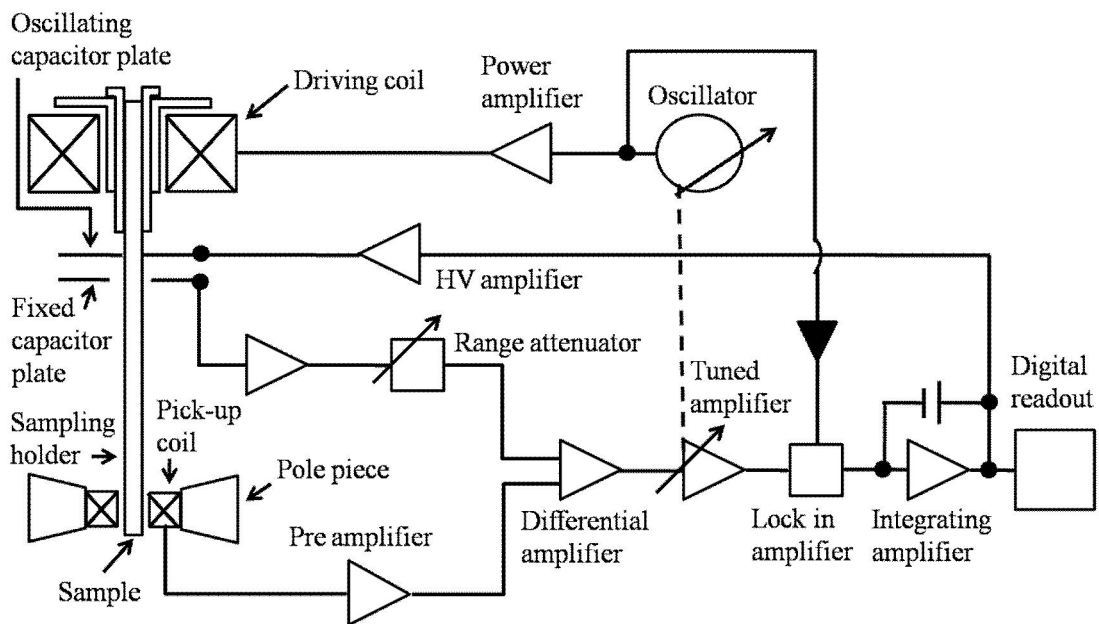


**Figure 3.7.** Schematic diagram of the working principle of vibrating-sample magnetometer.

**3.1.7. Superconducting Quantum Interference Device (SQUID):** Superconducting Quantum Interference Device (SQUID) magnetometry is one of the most effective and sensitive ways of measuring magnetic properties. In particular, it is the only method which allows to directly determine the overall magnetic moment of a sample in absolute units. Following the equations established by Brian David Josephson in 1962, the electrical current density through a weak electric contact between two superconductors

depends on the phase difference  $\Delta\phi$  of the two superconducting wave functions[4]. Moreover, the time derivative of  $\Delta\phi$  is correlated with the voltage across this weak contact. In a superconducting ring with two (Figure 3.8a, blue) weak contacts,  $\Delta\phi$  is additionally influenced by the magnetic flux  $\Phi$  through this ring. Therefore, such a structure can be used to convert magnetic flux into an electrical voltage. This is the basic working principle of a SQUID magnetometer.

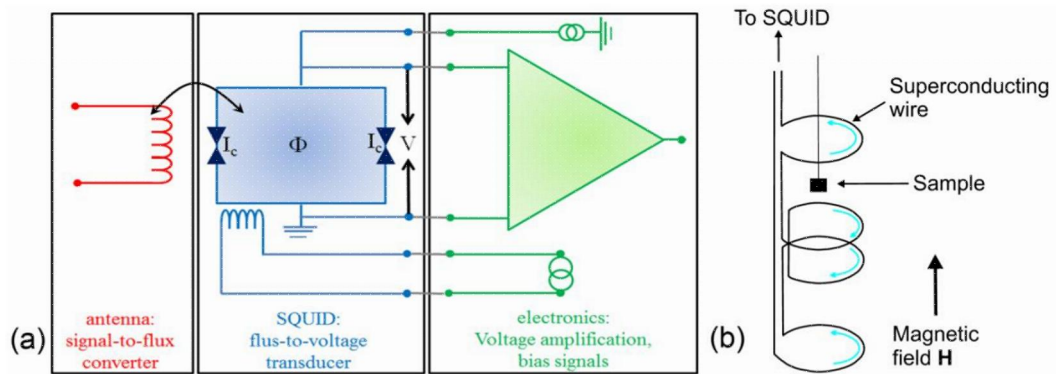


**Figure 3.8.** (a) Schematic diagram of the working principle of SQUID (flux to voltage converter). (b) The detection coils of the SQUID.

To measure the magnetization of a sample, a field must be applied to the sample to induce a net moment in the sample. The net moment induced in the sample induces a current in the detector coils which are made from superconducting wire, the detector coils are connected to the SQUID and the output voltage of the SQUID is directly proportional to the current induced by the magnetization of the sample. Hence the SQUID acts as current-to-voltage convertor and magnetization is measured from the induced voltage. In Figure 3.8b the setup of the detection coils is shown. There are coils at the top and bottom that are wound anti-clockwise and two central coils wound clockwise. This arrangement of detection coils means that variations of the magnetic field induce opposing current in the clockwise and anti-clockwise coils which cancel each other out, thus minimizing noise in the detection circuit. The magnetization produced by the sample would not be uniform across the sample space, with the detection coils measuring the local changes in the magnetic flux density, in this way a current is induced in the detection coils by the sample's net magnetization. A cutaway view of the Quantum Design MPMS XL7 SQUID

magnetometer used for the measurement of magnetization of T-LSMO NPs is shown in Figure 3.9.

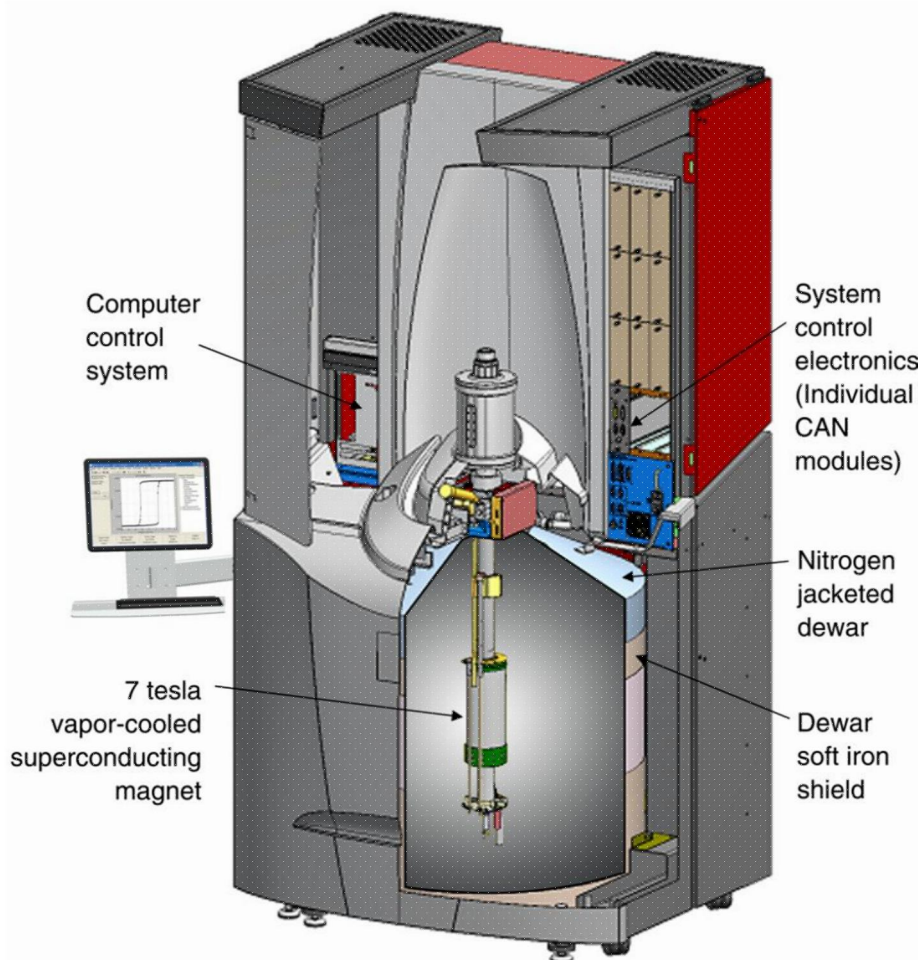


**Figure 3.9.** Cutaway view of the MPMS SQUID VSM.

**3.1.8. Transmission Electron Microscope (TEM):** An FEI TecnaiTF-20 field-emission high-resolution transmission electron microscope (HRTEM) (Figure 3.10) equipped with an Energy Dispersive X-ray (EDAX) spectrometer was used to characterize the microscopic structures of samples and to analyze their elemental composition. The size of the nanoparticles was determined from the TEM images obtained at 200 kV. Samples for TEM were prepared by placing a drop of the colloidal solution on a carbon-coated copper grid and allowing the film to evaporate overnight at room temperature.

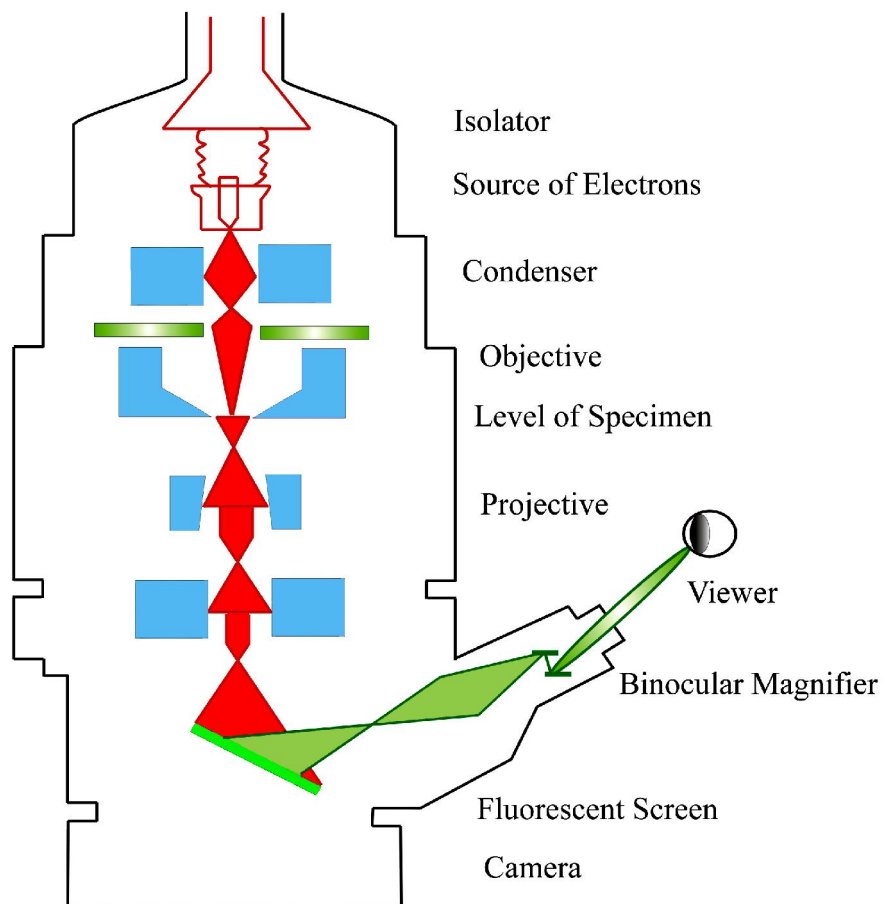


**Figure 3.10.** Schematic diagram of a typical transmission electron microscope (TEM). After the transmission of electron beam through a specimen, the magnified image is formed either in the fluorescent screen or can be detected by a CCD camera.

**3.1.9. Scanning Electron Microscope (SEM):** Surface characteristics of Porous silicon samples were done by scanning electron microscope FE-SEM; JEOL. Ltd., JSM-6500F. A electron-gun is attached to SEM and the electrons from filament triggered by 0 KV to 30 KV. These electrons go first through a condenser lens and then through a objective lens, then through a aperture and finally reach to the specimen. The high energy electrons go a bit in the sample and back again give secondary electrons. The signal from secondary electrons are detected by detector and amplified. The ray diagram of the SEM setup is shown in Figure 3.11.

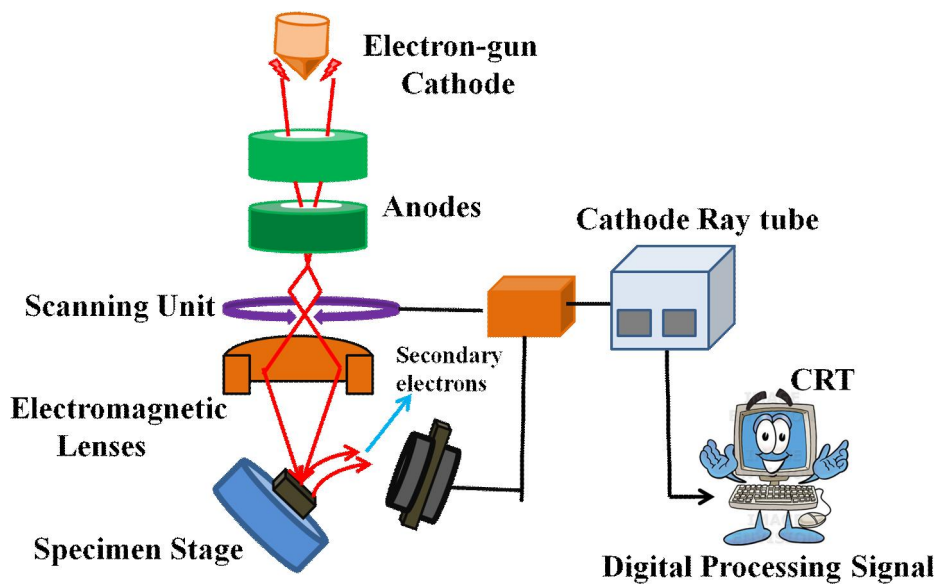


**Figure 3.11.** Schematic diagram of typical scanning electron microscope (SEM).

**3.1.10. Fluorescence Microscope:** A fluorescence microscope is much the same as a conventional light microscope with added features to enhance its capabilities. The conventional microscope uses visible light (400-700 nanometers) to illuminate and produce a magnified image of a sample. A fluorescence microscope, on the other hand, uses a much higher intensity light source which excites a fluorescent species in a sample of interest. This fluorescent species in turn emits a lower energy light of a longer wavelength that produces the magnified image instead of the original light source. In most cases the sample of interest is labelled with a fluorescent substance known as a fluorophore and then illuminated through the lens with the higher energy source. The illumination light is absorbed by the fluorophores (now attached to the sample specimen) and causes them to emit a longer lower energy wavelength light. This fluorescent light can be separated from the surrounding radiation with filters designed for that specific wavelength allowing the viewer to see only that which is fluorescing. The basic task of the fluorescence microscope is to let excitation light radiate the specimen and then sort out the much weaker emitted light from the image. First, the microscope has a filter that only lets through radiation with the specific wavelength that matches your fluorescing material. The radiation collides with the atoms of the sample specimen and electrons are excited to a higher energy level. When

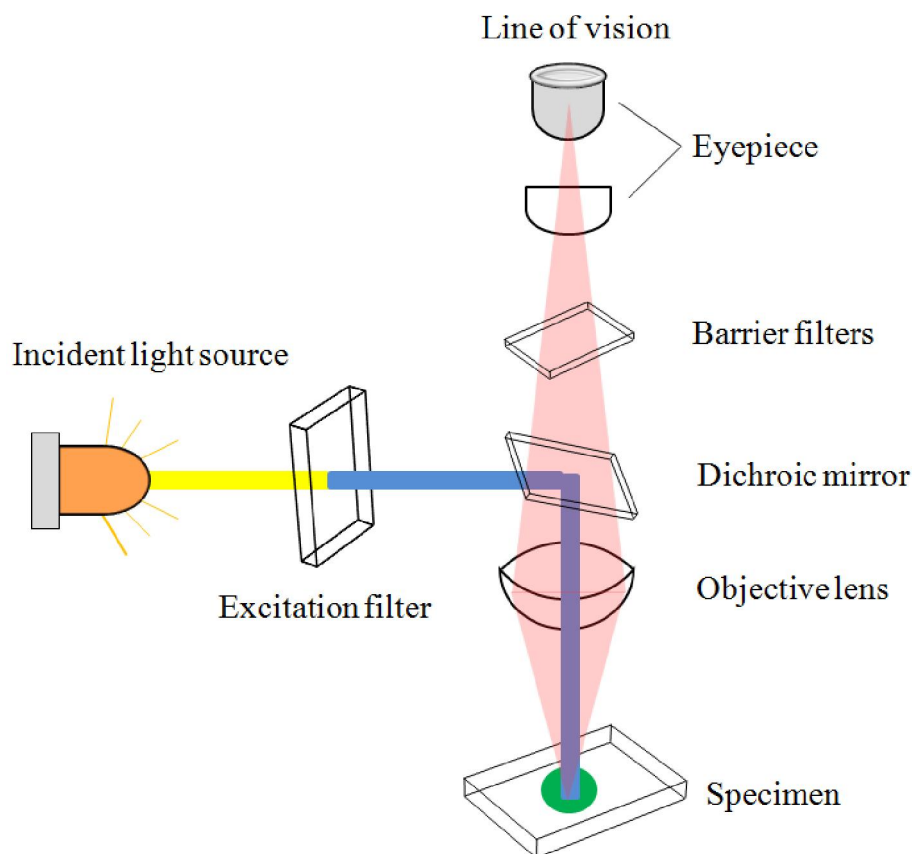


**Figure 3.12.** Optical system of a fluorescence microscope.

they relax to a lower level, they emit light. To become detectable (visible to the human eye) the fluorescence emitted from the sample is separated from the much brighter excitation light in a second filter (Figure 3.12). This works because the emitted light is of lower energy and has a longer wavelength than the light that is used for illumination. Most of the fluorescence microscopes used in biology today are epi-fluorescence microscopes, meaning that both the excitation and the observation of the fluorescence occur above the sample. Most use a Xenon or Mercury arc-discharge lamp for the more intense light source.

**3.1.11. X-Ray Photoelectron Spectroscopy (XPS):** XPS works on the principle of photoelectric effect discovered by Heinrich Hertz in 1887. Upon radiation of appropriate energy incident, electrons are emitted from the surface of the metal. The relation between the energy of the excitation radiation, work function of the metal and the maximum kinetic energy of the emitted electron as proposed by Einstein in 1905 is:

$$h\nu = \phi + KE_{\max} \quad (3.7)$$

‘ $\Phi$ ’ is the work function of the metal, ‘ $h\nu$ ’ is the energy of the radiation, ‘ $KE_{\max}$ ’ is the maximum kinetic energy of the emitted electron. For analysing the core electronic structure (0 – 1300 eV) of elements, radiation of high energy were used like X-rays, hence the corresponding spectroscopy is termed X-ray Photoelectron Spectroscopy (XPS) (Figure 3.13).

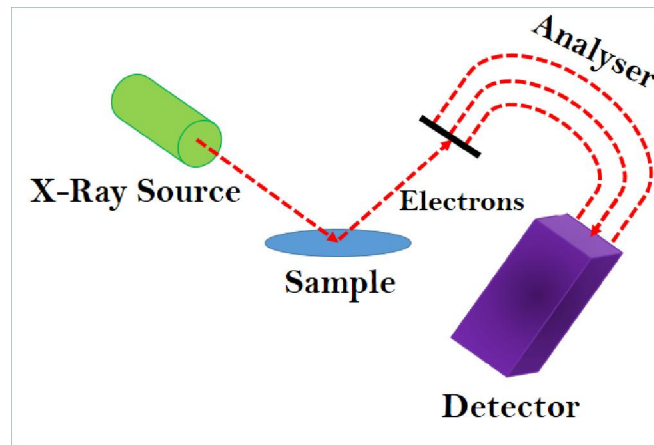


**Figure 3.13.** Schematic diagram of a typical X-ray photoelectron spectroscopy (XPS).

Surface analysis by XPS is accomplished by irradiating a sample with monoenergetic soft X-rays and analysing the energy of the detected electrons. Mg  $K\alpha$  (1253.6 eV), Al  $K\alpha$  (1486.6 eV), or monochromatic Al  $K\alpha$  (1486.7 eV) X-rays are usually used. These photons have limited penetrating power in a solid of the order of 1 – 10  $\mu\text{m}$ . They interact with atoms in the surface region, causing electrons to be emitted by the photoelectric effect. The emitted electrons have measured kinetic energies given by:

$$KE = h\nu - BE - \phi_s \quad (3.8)$$

where ‘ $h\nu$ ’ is the energy of the photon, ‘ $BE$ ’ is the binding energy of the atomic orbital from which electron originates, ‘ $\Phi_s$ ’ is the work function of the spectrometer. The binding energy may be regarded as the energy difference between the initial and final states after the photoelectron has left the atom. Because there are a variety of possible final states of the ions from each type of atom, there is a corresponding variety of kinetic energies of the

emitted electrons. Moreover there is a different probability or cross section for each final state.

Because each element has unique set of binding energies, XPS can be used to identify and determine the concentration of the elements in the surface. Variation in the elemental binding energies (the chemical shifts) arise from differences in the chemical potential and polarizability of compounds. These chemical shifts can be used to identify the chemical state of the material being analysed. In our studies, XPS were performed on a Omicron ESCA probe spectrometer with polychromatic Mg K $\alpha$  X-rays ( $h\nu = 1253.6$  eV).

**3.1.12. Refractive Indices Measurement:** Refractive indices of the solutions were measured by using a Rudolph J357 automatic refractometer. The instruments measures the refractive indices using sodium D-line of wavelength 589.3 nm with accuracies  $\pm 0.00004$ . The measurement of the refractive index of the sample is based on the determination of the critical angle of total reflection. A light source, usually a long-life LED, is focused onto a prism surface via a lens system. Due to the focusing of light to a spot at the prism surface, a wide range of different angles is covered. As the measured sample is in direct contact with the measuring prism. Depending on its refractive index, the incoming light below the critical angle of total reflection is partly transmitted into the sample, whereas for higher angles of incidence the light is totally reflected. This dependence of the reflected light intensity from the incident angle is measured with a high-resolution sensor array. From the video signal taken with the CCD sensor the refractive index of the sample can be calculated.

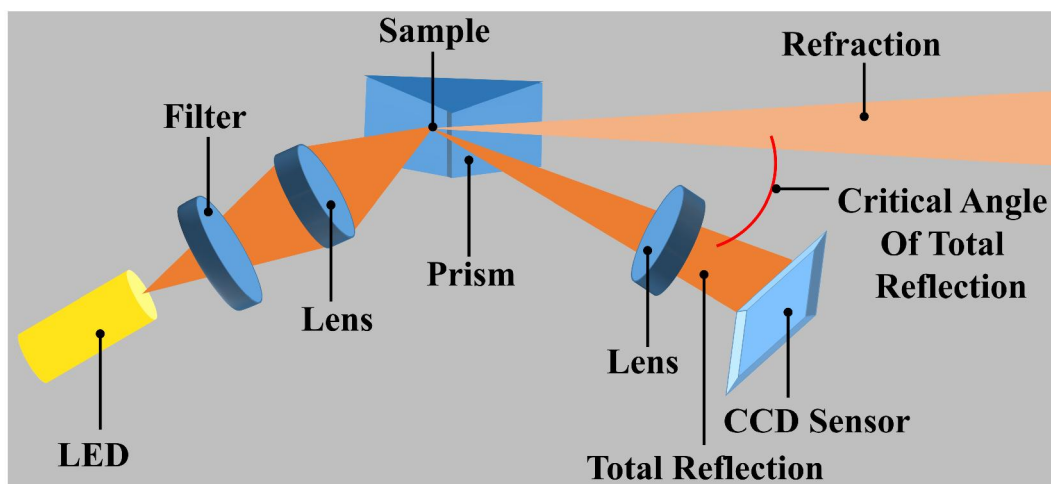


**Figure 3.14.** Schematic representation of the refractometer.

**3.1.13. Thermogravimetric-Differential Thermal Analyzer (TG-DTA) Setup:** The thermogravimetric (TG) analysis was carried out using Diamond thermogravimetric (TG)-differential thermal analyzer (DTA) from Perkin Elmer. The TG determines the weight change of a sample whereas the DTA measures the change in temperature between a sample and the reference as a function of temperature and/or time. The schematic of the TG-DTA setup is shown in Figure 3.15. When a weight change occurs on the sample side, the beam holding the platinum pans is displaced. This movement is detected optically and the driving coil current is changed to return the displacement to zero. The detected driving coil current change is proportional to the sample weight change and the output is the TG signal. The DTA detects the temperature difference between the sample holder and the reference holder using the electromotive force of thermocouples, which are attached to the holders. This difference is measured as the DTA signal.

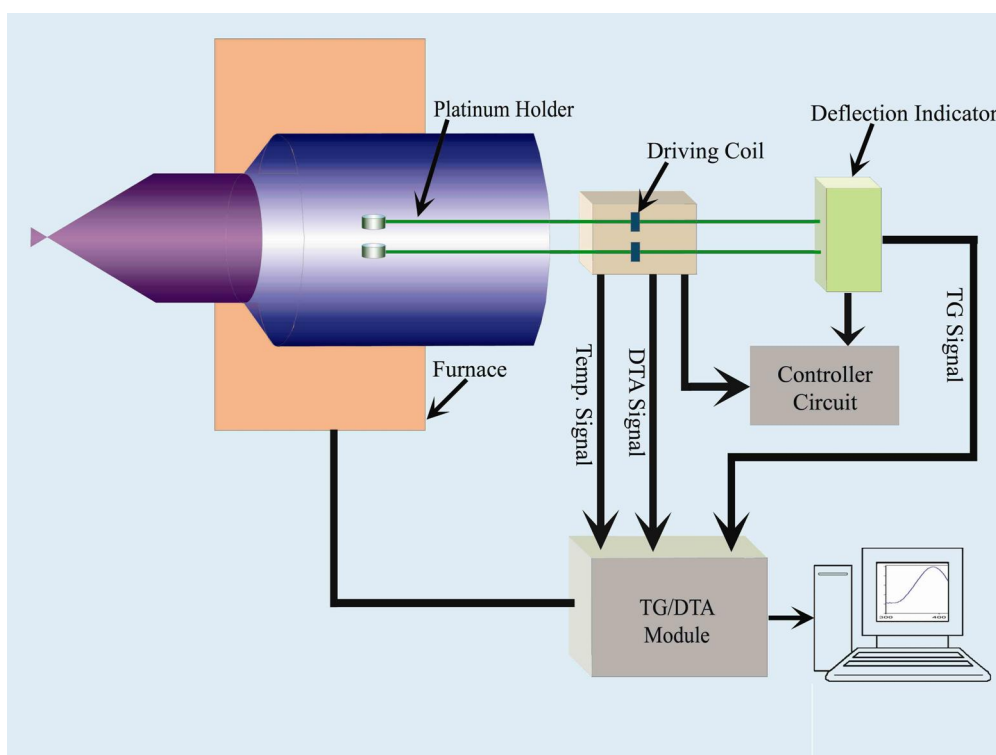


**Figure 3.15.** The schematic representation of thermogravimetric-differential thermal analyzer (TG-DTA) setup.

**3.1.14. Laser Raman Spectroscopy:** Raman spectroscopy is a useful technique for the identification of a wide range of substances: solids, liquids, and gases. It is a straightforward, non-destructive technique requiring no sample preparation. Raman spectroscopy involves illuminating a sample with monochromatic light and using a spectrometer to examine light scattered by the sample.

At the molecular level photons can interact with matter by absorption or scattering processes. Scattering may occur either elastically, or inelastically. The elastic process is termed Rayleigh scattering, whilst the inelastic process is termed Raman scattering. The electric field component of the scattering photon perturbs the electron cloud of the molecule and may be regarded as exciting the system to a ‘virtual’ state. Raman scattering occurs when the system exchanges energy with the photon, and the system subsequently decays to vibrational energy levels above or below that of the initial state. The frequency shift corresponding to the energy difference between the incident and scattered photon is termed the Raman shift. Depending on whether the system has lost or gained vibrational energy, the Raman shift occurs either as an up or down-shift of the scattered photon frequency relative to that of the incident photon. The down-shifted and up-shifted components are called, respectively, the Stokes and anti-Stokes lines. A plot of detected number of photons versus Raman shift from the incident laser energy gives a Raman spectrum. Different materials have different vibrational modes, and therefore characteristic Raman spectra. This makes Raman spectroscopy a useful technique for material identification. There is one important distinction to make between the Raman spectra of gases and liquids, and those taken from solids-in particular, crystals. For gases and liquids it is meaningful to speak of the vibrational energy levels of the individual molecules which make up the material. Crystals do not behave as if composed of molecules with specific vibrational energy levels, instead the crystal lattice undergoes vibration. These macroscopic vibrational modes are called phonons.

In modern Raman spectrometers (LabRAM HR, Jobin Yvon), lasers are used as a photon source due to their highly monochromatic nature, and high beam fluxes (Figure 3.16). This is necessary as the Raman effect is weak, typically the Stokes lines are  $\sim 10^5$  times weaker than the Rayleigh scattered component. In the visible spectral range, Raman spectrometers use notch filters to cut out the signal from a very narrow range centred on

the frequency corresponding to the laser radiation. Most Raman spectrometers for material characterization use a microscope to focus the laser beam to a small spot (<1–100  $\mu\text{m}$  diameter). Light from the sample passes back through the microscope optics into the spectrometer. Raman shifted radiation is detected with a charge-coupled device (CCD) detector, and a computer is used for data acquisition and curve fitting. These factors have helped Raman spectroscopy to become a very sensitive and accurate technique.

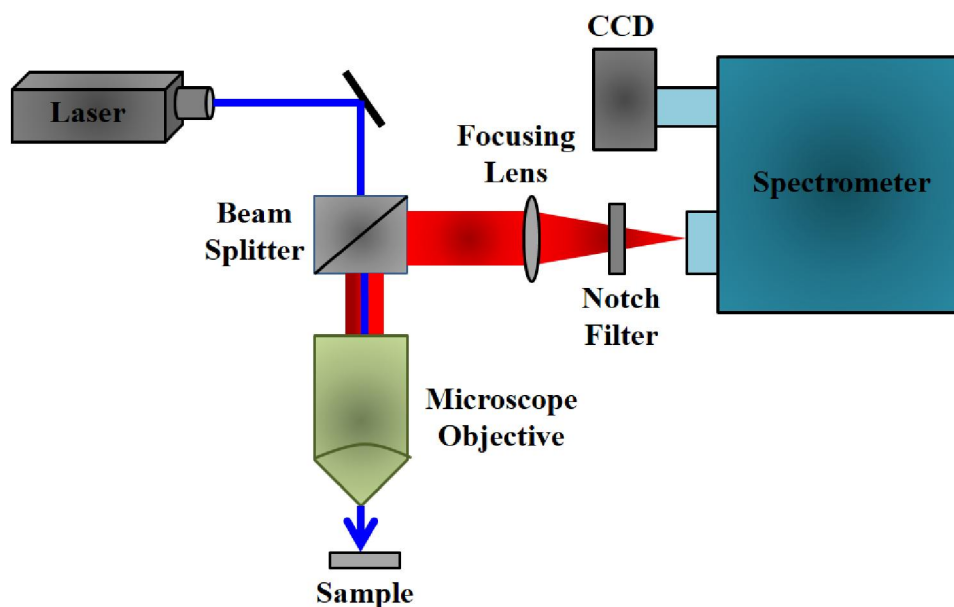


**Figure 3.16.** Schematic diagram of a Raman spectrometer is shown.

### 3.1.15. Matrix-Assisted Laser Desorption Ionization-Time of Flight (MALDI-TOF)

**Mass Spectrometry:** It is an analytical technique used for measuring the molecular mass of biomolecules (such as proteins, peptides, oligosaccharides and oligonucleotides) on the basis of the mass ( $m$ )-to-charge ( $z$ ) ratio ( $m/z$ ) of charged particles, which tend to be fragile and fragment when ionized by more conventional ionization methods. In MALDI-TOF mass spectrometry (Figure 3.17), the sample molecules are bombarded with a laser light to bring about sample ionization. The sample is pre-mixed with a highly absorbing matrix compound for the most consistent and reliable results and a low concentration of sample to matrix work best. The matrix transforms the laser energy into excitation energy for the sample, which leads to sputtering of analyte and matrix ions from the surface of the

mixture. In this way energy transfer is efficient and also the analyte molecules are spared from excessive direct energy that may otherwise cause decomposition.

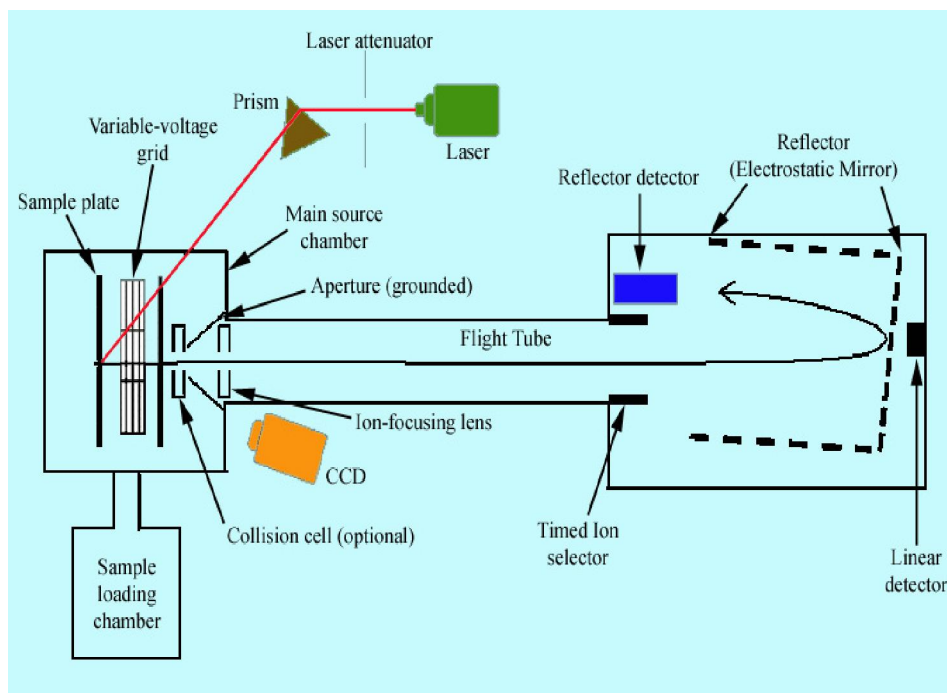


**Figure 3.17.** Schematic diagram of matrix-assisted laser desorption/ionization-time of flight mass spectrometry (MALDI-TOF) spectrometer. MALDI is a soft ionisation method and so results predominantly in the generation of singly charged molecular-related ions regardless of the molecular mass, hence the spectra are relatively easy to interpret. Fragmentation of the sample ions does not usually occur.

The ionized molecules are accelerated in an electric field and enter into a chamber under vacuum that contains no electric fields (analyzer). The time-of-flight analyzer separates ions according to their mass ( $m/z$ ) ratios by measuring the time it takes for ions to travel through a field-free region. A detector is positioned at the end of the analyzer to measure the arrival time of ions. Ions of lesser  $m/z$  arrive first, followed by ions of greater  $m/z$ . A plot of intensity or abundance versus time is made to show the arrival time distribution of the ions detected. The plot of intensity versus time is calibrated and replotted as intensity versus  $m/z$ . The method is used for detection and characterization of

biomolecules with molecular masses between 400 and 350,000 Da. It is a very sensitive method, which allows the detection of low ( $10^{-15}$  to  $10^{-18}$  mole) quantities of sample with an accuracy of 0.1–0.01%. MALDI MS studies were conducted using a Voyager-DE PRO Biospectrometry workstation from Applied Biosystems. A pulsed nitrogen laser of 337 nm was used for the MALDI MS studies. Mass spectra were collected in positive-ion mode and were averaged for 100 shots. Sinapinic acid was used as the matrix for MALDI-TOF MS.

**3.1.16. Electrospray Ionization Mass Spectrometry (ESI-MS):** The Electrospray Ionization is a soft ionization technique extensively used for production of gas phase ions (without fragmentation) of thermally labile large supramolecules. ESI uses electrical energy to assist the transfer of ions from solution into the gaseous phase before they are subjected to mass spectrometric analysis (Figure 3.18). Ionic species in solution can thus be analyzed by ESI-MS with increased sensitivity. Neutral compounds can also be converted to ionic form in solution or in gaseous phase by protonation or cationisation (e.g. metal cationisation), and hence can be studied by ESI-MS. The transfer of ionic species from solution into the gas phase by ESI involves three steps: (1) dispersal of a fine spray of charge droplets, followed by (2) solvent evaporation and (3) ion ejection from the highly charged droplets. Within an ESI source, a continuous stream of sample solution is passed through a stainless steel or quartz silica capillary tube, which is maintained at a high voltage (e.g. 2.5-6.0 kV) relative to the wall of the surrounding chamber. A mist of highly charged droplets with the same polarity as the capillary voltage is generated. The application of a nebulising gas (e.g. nitrogen), which shears around the eluted sample solution, enhances a higher sample flow rate. The charged droplets, generated at the exit of the electrospray tip, pass down a pressure gradient and potential gradient toward the analyzer region of the mass spectrometer. With the aid of an elevated ESI-source temperature and/or another stream of nitrogen drying gas, the charged droplets are continuously reduced in size by evaporation of the solvent, leading to an increase of surface charge density and a decrease of the droplet radius. Finally, the electric field strength within the charged droplet reaches a critical point at which it is kinetically and energetically possible for ions at the surface of the droplets to be ejected into the gaseous phase.

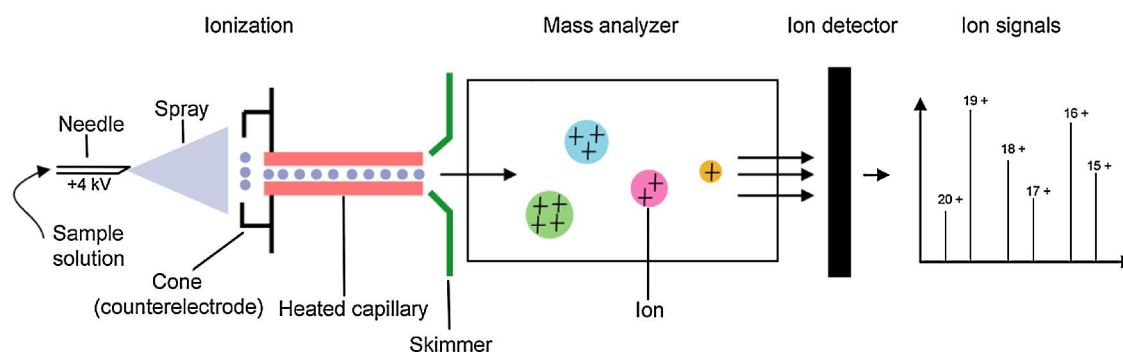


**Figure 3.18.** In ESI-MS, sample molecules are ionized directly in the analyte solution by passing through a heated capillary device, spraying droplets of solution into a vacuum chamber containing a high-strength electric field. The resulting ions pass through a mass analyzer and detector. ESI-MS produces complex spectra with multiply charged ions.

The emitted ions are sampled by a sampling skimmer cone and are then accelerated into the mass analyzer for subsequent analysis of molecular mass and measurement of ion intensity [5].

### 3.2. Sample Preparation:

In this section the different sample preparation methods have been discussed. All the aqueous solutions were prepared using deionized water from Millipore system. Human serum albumin (HSA), tri-sodium citrate, tartaric acid, Hemoglobin (Hb), sodium borohydride, tri-octylphosphine oxide (TOPO), Luminol, Rhodamine, chloroform, Piperidine, malic acid, sodium hydroxide, 4-nitrophenyl anthranilate (NPA), 2-aminopurine (2AP), MTT based cell viability kit, L- arginine hydrochloride, potassium bromide (KBr), synthetic DNA oligomer, as well as all the acetates, nitrates and chlorides of various metal ions of highest commercially available grade were purchased from Sigma-Aldrich (USA). 4', 6-diamidino-2-phenylindole (DAPI), Hoechst (H33258), methylene blue and ethidium bromide (EtBr) were obtained from Molecular Probes. Organic dye COUMARIN 500 (C500) was obtained from exciton. Lake Placid Blue CdSe/ZnS core/shell semiconductor nanocrystals (QDs) in toluene were purchased from Evident Technologies (Troy, NY).

**3.2.1. Synthesis of  $\text{La}_{0.67}\text{Sr}_{0.33}\text{MnO}_3$  Nanoparticles (LSMO NPs):** We have synthesized the bulk LSMO nanoparticles following a reported procedure where a modified sol-gel technique has been designed especially for the preparation of complex oxide nanoparticles and the reaction mechanism was first given by Shankar et. al [6]. We have taken high purity (> 99%) metal acetates (procured from Sigma Aldrich) and then dissolved in the desired stoichiometric proportions in acetic acid and water. To this solution, an appropriate amount of ethylene glycol (molecular weight = 62.07 gm/mol) was added and heated until the sol was formed. The gel was dried overnight at 150°C. Pyrolysis was done at 350°C and 450°C followed by a sintering at higher temperature to obtain the desired chemical phase. For the manganites, phase pure samples can be obtained at temperatures as low as 650°C. Using this chemical solution deposition method precise control of the stoichiometry can be achieved.

**3.2.2. Functionalization and Further Surface Modification of LSMO NPs:** We have functionalized the as prepared LSMO NPs by the following procedure [7]. We have solubilized the as prepared LSMO NPs into water by using the reactivity of hydroxyl (-OH) and carboxylate ( $\text{COO}^-$ ) groups of citrate/tartrate. First, we prepared 6 mL of 0.5 M citrate/tartrate solution (pH~7) and then 200 mg as prepared LSMO NPs was added to the solution followed by 6 hours of extensive mixing by cyclo-mixer. Finally, the non-functionalized bigger sized NPs were filtered out (by a syringe driven filter of 0.22  $\mu\text{m}$  diameter) and UV-vis optical absorption of the resulting greenish-yellow filtrate solution was measured.

Next, we increased the pH of the resulting greenish-yellow Citrate/Tartrate-LSMO solution from pH~7 to pH~12, by drop wise addition of NaOH. The greenish-yellow color of the solution turns to yellowish-brown and the resulting solution was heated at 70°C under vigorous stirring condition for 8 hours. After eight hours the solution became highly fluorescence.

**3.2.3. Incorporation of Tartrate-LSMO NPs into Human Oral Squamous Epithelial Cells:** Tartrate-LSMO NPs were incorporated into squamous epithelial cells by the following procedure [7]. Primary squamous epithelial cells collected from the inner lining of human mouth have been used. Prior to cell imaging, the cells were spread on glass slides in presence of PBS (phosphate buffered saline) and NP solution (at a final

concentration of  $3 \times 10^{-6}$  M) was added followed by 30 min of incubation. After incubation, just before fluorescence imaging, the cells were washed twice with PBS to remove unbound NPs.

**3.2.4. Synthesis of Bulk  $\text{Mn}_3\text{O}_4$  NPs:** We have synthesized the bulk  $\text{Mn}_3\text{O}_4$  nanoparticles following a reported procedure where an ultrasonic-assisted approach has been used to prepare colloidal  $\text{Mn}_3\text{O}_4$  nanoparticles at normal temperature and pressure without any additional surfactant or template [8].

**3.2.5. Functionalization of As-Prepared  $\text{Mn}_3\text{O}_4$  NPs by Different Ligands to Prepare Ligand Functionalized- $\text{Mn}_3\text{O}_4$  NPs:** We have functionalized the as prepared LSMO NPs by the following procedure [9]. In all cases, first we have prepared 0.5 M ligands solution in Milli-Q (from Millipore) water. Then we have adjusted the pH of the solutions at  $\sim 7$  by addition of 1 M sodium hydroxide (NaOH) solution. In the ligand solution of pH $\sim 7$ , we have added as-prepared  $\text{Mn}_3\text{O}_4$  NPs (approximately 100 mg powder  $\text{Mn}_3\text{O}_4$  NPs in 5 mL ligand solution) and followed by extensive mixing for 12 hours in a cyclo-mixer. Finally, the non-functionalized bigger sized NPs were filtered out (by a syringe filter of 0.22  $\mu\text{m}$  diameter) and the resulting filtrated solutions were used for our experiments.

**3.2.6. Further Surface Modification of Tartrate- $\text{Mn}_3\text{O}_4$  (T- $\text{Mn}_3\text{O}_4$ ) NPs to Impart High Photoluminescence:** We have functionalized the as prepared  $\text{Mn}_3\text{O}_4$  NPs by the following procedure [9]. We have increased the pH of the greenish-yellow T- $\text{Mn}_3\text{O}_4$  NPs solution from pH $\sim 7$  to 12 by drop wise addition of 1 (M) sodium hydroxide (NaOH) solution. The greenish-yellow color of the solution turns to yellowish-brown (indicating conversion of surface  $\text{Mn}^{2+}$  to  $\text{Mn}^{3+}$ , as in acidic/neutral pH,  $\text{Mn}^{3+}$  ions are unstable and tend to disproportionate into  $\text{Mn}^{2+}$  and  $\text{Mn}^{4+}$ , whereas it is stabilized by the comproportionation of  $\text{Mn}^{2+}$  and  $\text{Mn}^{4+}$  in alkaline condition [10]) and the resulting solution was heated at  $70^\circ\text{C}$  under vigorous stirring for 10-14 hours. Finally, the solution became highly photoluminescent. It should be noted that we have diluted the as prepared T- $\text{Mn}_3\text{O}_4$  NPs solution about 2-3 times by 0.5 M tartrate solution before high pH and temperature treatment in order to avoid the precipitation of the solubilized NPs.

**3.2.7. Preparation of Water Soluble Arginine Capped QDs:** We have prepared the water-soluble arginine capped QDs by the following procedure [11]. It the TOPO-capped CdSe/ZnS core/shell QDs in toluene were rendered water-soluble by ligand exchange with

L-arginine, following a simple process using the reactivity of the amine group (of L-arginine) with the ZnS shell of the QDs. The addition of 5 ml of the QDs toluene suspension into about 5 ml of the L-arginine aqueous solution (pH~9) under vigorous stirring results in the formation of toluene-in-water microdroplets. The sample was stirred overnight, settled for 3 hours and then the aqueous phase was separated and analyzed by UV-vis, fluorescence spectroscopy and HRTEM.

**3.2.8. Preparation of DNA Samples:** We have prepared the DNA sample by the following procedure [11]. To reassociate the single strand DNA into self-complementary double-strand DNA (CTTTTGCAAAAG)<sub>2</sub>, thermal annealing was performed as per the methodology prescribed by the vendor. The nucleotide concentration was determined by absorption spectroscopy using the average extinction coefficient per nucleotide of the DNA (6600 M<sup>-1</sup> cm<sup>-1</sup> at 260 nm). The EB-DNA complex solution was prepared by adding the requisite amount of probe stock solution to DNA followed by 1 hour of magnetic stirring. To ensure complete complexation of EB with the DNA, the probe concentration was made much less (8 μM) than that of the DNA (30 μM) ([EB-DNA] = 8 μM) for the FRET studies.

**3.2.9. Synthesis of the Protein-Incorporated Fe Quantum Clusters (Fe<sub>QC</sub>s):** In a typical synthesis, first, 60 mg of Hb was dissolved in 5 mL Milli-Q water. 12 mL of piperidine was then added to the protein solution to extract the iron from the protein. The solution was then stirred for 15 min at room temperature. Second, 36 mg of 3 mL ice cold sodium borohydride was slowly added to the solution under vigorous stirring. The reaction mixture was then stirred for 24 hrs, resulting in the formation of a yellowish brown solution that showed a strong yellow luminescence under UV lamp.

**3.2.10. Ligand Exchange and Phase Transfer from Water to Chloroform:** For phase transfer, 0.01M of TOPO was taken in 3 mL of chloroform on the bottom of 3.0 mL (10 mg/ mL) of aqueous Fe<sub>QC</sub>@Hb solution. The mixture was gently stirred for 8-12 hrs at 298 K. Exchange can be observed directly by visible color change of the organic phase from colorless to reddish brown.

**3.2.11. Evidence of “Zero Oxidation State” of Fe<sub>QC</sub> in Hb Matrix, Detection Procedure Using Chemiluminescence:** Luminol solution was prepared (1g/mL) and solution was kept in three test tubes (each contains 1 mL of 1g/mL luminol solution). 0.2

mL of each sample [e.g., Fe<sub>QC</sub>@Hb (2.2 mg/mL), Hb (2.2 mg/mL) and water] was added to that luminol solution. Finally, 1 mL of 3% hydrogen peroxide was added and the photographs were taken immediately.

**3.2.12. Quantum Yield Calculation:** The quantum yield was calculated according to the equation [12]:

$$Q = Q_R \left( \frac{I}{I_R} \right) \left( \frac{OD_R}{OD} \right) \left( \frac{n^2}{n_R^2} \right) \quad (3.9)$$

where Q and Q<sub>R</sub> are the quantum yield of the protein and reference, I and I<sub>R</sub> are the integrated fluorescence intensities of the protein and reference, OD and OD<sub>R</sub> are the optical densities of the protein and reference at the excitation wavelength, and n and n<sub>R</sub> are the refractive indices of the protein and reference solutions.

## References

- [1] R.K. Mitra, S.S. Sinha, S.K. Pal, Temperature-dependent solvation dynamics of water in sodium bis(2-ethylhexyl)sulfosuccinate/isooctane reverse micelles, *Langmuir* 24 (2007) 49.
- [2] R. Sarkar, S.S. Narayanan, L.-O. Palsson, F. Dias, A. Monkman, S.K. Pal, Direct conjugation of semiconductor nanocrystals to a globular protein to study protein-folding intermediates, *J. Phys. Chem. B* 111 (2007) 12294.
- [3] S. Foner, Versatile and sensitive vibrating sample magnetometer, *Rev. Sci. Instrum.* 30 (1959) 548.
- [4] B.D. Josephson, The discovery of tunnelling supercurrents, *Rev. Mod. Phys.* 46 (1974) 251.
- [5] Y. Lin, W. Dynan, J. Lee, Z.-H. Zhu, R. Schade, The current state of proteomics in GI oncology, *Dig. Dis. Sci.* 54 (2009) 431.
- [6] K.S. Shankar, A.K. Raychaudhuri, Low-temperature polymer precursor-based synthesis of nanocrystalline particles of lanthanum calcium manganese oxide ( $\text{La}_{0.67}\text{Ca}_{0.33}\text{MnO}_3$ ) with enhanced ferromagnetic transition temperature, *J Mater. Res.* 21 (2006) 27
- [7] A. Giri, N. Goswami, M.S. Bootharaju, P.L. Xavier, R. John, N.T.K. Thanh, T. Pradeep, B. Ghosh, A.K. Raychaudhuri, S.K. Pal, Emergence of multicolor photoluminescence in  $\text{La}_{0.67}\text{Sr}_{0.33}\text{MnO}_3$  nanoparticles, *J. Phys. Chem. C* 116 (2012) 25623.
- [8] S. Lei, K. Tang, Z. Fang, H. Zheng, Ultrasonic-assisted synthesis of colloidal  $\text{Mn}_3\text{O}_4$  nanoparticles at normal temperature and pressure, *Cryst. Growth Des.* 6 (2006) 1757.
- [9] A. Giri, N. Goswami, M. Pal, M.T. Zar Myint, S. Al-Harhi, A. Singha, B. Ghosh, J. Dutta, S.K. Pal, Rational surface modification of  $\text{Mn}_3\text{O}_4$  nanoparticles to induce multiple photoluminescence and room temperature ferromagnetism, *J. Mater. Chem. C* 1 (2013) 1885.
- [10] T. Takashima, K. Hashimoto, R. Nakamura, Mechanisms of pH-dependent activity for water oxidation to molecular oxygen by  $\text{MnO}_2$  electrocatalysts, *J. Am. Chem. Soc.* 134 (2011) 1519.

- [11] A. Giri, N. Goswami, P. Lemmens, S.K. Pal, Preparation of water soluble L-arginine capped CdSe/ZnS QDs and their interaction with synthetic DNA: Picosecond-resolved FRET study, *Mater. Res. Bull.* 47 (2012) 1912.
- [12] J. Chen, D. Topygin, L. Brand, J. King, Mechanism of the efficient tryptophan fluorescence quenching in human  $\gamma$ D-crystallin studied by time-resolved fluorescence, *Biochemistry* 47 (2008) 10705.

## Chapter 4

# Surface Modification of Nanoparticles for their New Functionality and Better Acceptability in the Biophysical Studies

### 4.1. Introduction

The development of nanomaterials with intrinsic photoluminescence are a key focus in nanotechnology for the rational designing of multifunctional nanoparticles and could have profound impact on many research areas, ranging from fundamental physics to photoluminescence (PL) devices, catalysis, biological detections and therapeutics. Several novel nanomaterials have recently been described, including quantum dots (QDs) [1-4], magnetic nanoparticles (MNPs) [5, 6], magnetofluorescent nanoparticle [7-9] and metallic NPs [10]. Their unique optical, magnetic, electronic and structural properties have addressed a broad spectrum of technological/biological applications [11-14]. Considerable efforts have also been directed towards rational surface modifications in order to modulate their electronic structure and complicated surface chemistry. However, despite recent advancement, much works still need to be done in order to achieve hydrophilic and biocompatible NPs that are luminescent, with surface chemistry adaptable to varied technological/biological applications.

In this chapter, we demonstrate how one can modify the electronic structure of the nanoparticles of functional mixed valance oxides by making a hybrid with an organic molecule and thereby make excitation wavelength addressable multicolor photoluminescent nanoparticles. The investigation has been done on nanoparticles (NPs) of the perovskite manganite  $\text{La}_{0.67}\text{Sr}_{0.33}\text{MnO}_3$  (LSMO) which is known to display a number of exotic properties like colossal magnetoresistance [15]. The functionality of the perovskite manganites arise from mixed valence of Mn ions which in such system as LSMO have two valence states  $\text{Mn}^{3+}$  and  $\text{Mn}^{4+}$ . Presence of  $\text{Mn}^{3+}$  ions lead to Jahn-Teller distortion around Mn ions, while simultaneous presence of  $\text{Mn}^{4+}$  leads to ferromagnetic *double-exchange* interactions and metallic behavior.

In recent times significant efforts have been made to exploit the room temperature ferromagnetism of the perovskite manganite NPs for prospective applications in cancer therapy involving the hyperthermal effect [16] and as dual imaging probes for magnetic resonance imaging and fluorescence microscopy (after tagging an external fluorescent agent) [17]. Several experiments have also been focused to solubilize the manganite NPs in aqueous solution by employing some biocompatible macromolecules, still, resulted only a suspension of the NPs in solution [17-19]. However, in a recent attempt we have functionalized individual manganite NPs with a small biocompatible ligand to solubilize them into water and the functionalized NPs shows extremely high colloidal stability [20].

In this chapter, we report a new class of multifunctional nanoprobe based on  $\text{La}_{0.67}\text{Sr}_{0.33}\text{MnO}_3$  (LSMO) NPs, a mixed-valent manganite where Mn present in two oxidation states, +3 and +4. We have demonstrated the novel optical properties of LSMO NPs upon interaction with sodium tartrate, a dicarboxylate ligand used to solubilized the NPs into water. UV-vis spectroscopic study of the tartrate functionalized LSMO (T-LSMO) NPs reveals different absorption bands originated from various types of electronic transitions involving ligands-NP interaction. One of the important discoveries associated with this work is the observation that the resulting changes on electronic structures (achieved by functionalization with sodium tartrate) can lead to the emergences of multiple color photoluminescence from T-LSMO NPs when it is addressed with different excitation wavelengths, where the respective excitation wavelengths have a direct correlation with the observed UV-vis absorption bands. From X-ray photoelectron spectroscopic (XPS) analysis and time-resolved photoluminescence lifetime measurements we have acquired additional evidence supporting the proposed mechanism regarding the origin of different optical properties of T-LSMO NPs.

## **4.2. Result and Discussion**

### **4.2.1. Emergence of Multicolor Photoluminescence in $\text{La}_{0.67}\text{Sr}_{0.33}\text{MnO}_3$ Nanoparticles [21]:**

Figure 4.2a illustrates the UV-vis absorption spectrum of as-prepared LSMO, tartrate and T-LSMO NPs (at pH ~7). In case of T-LSMO, it shows two peaks at 300 and 440 nm, a shoulder descending into lower energies around 580 nm and a broad band at 758 nm. The

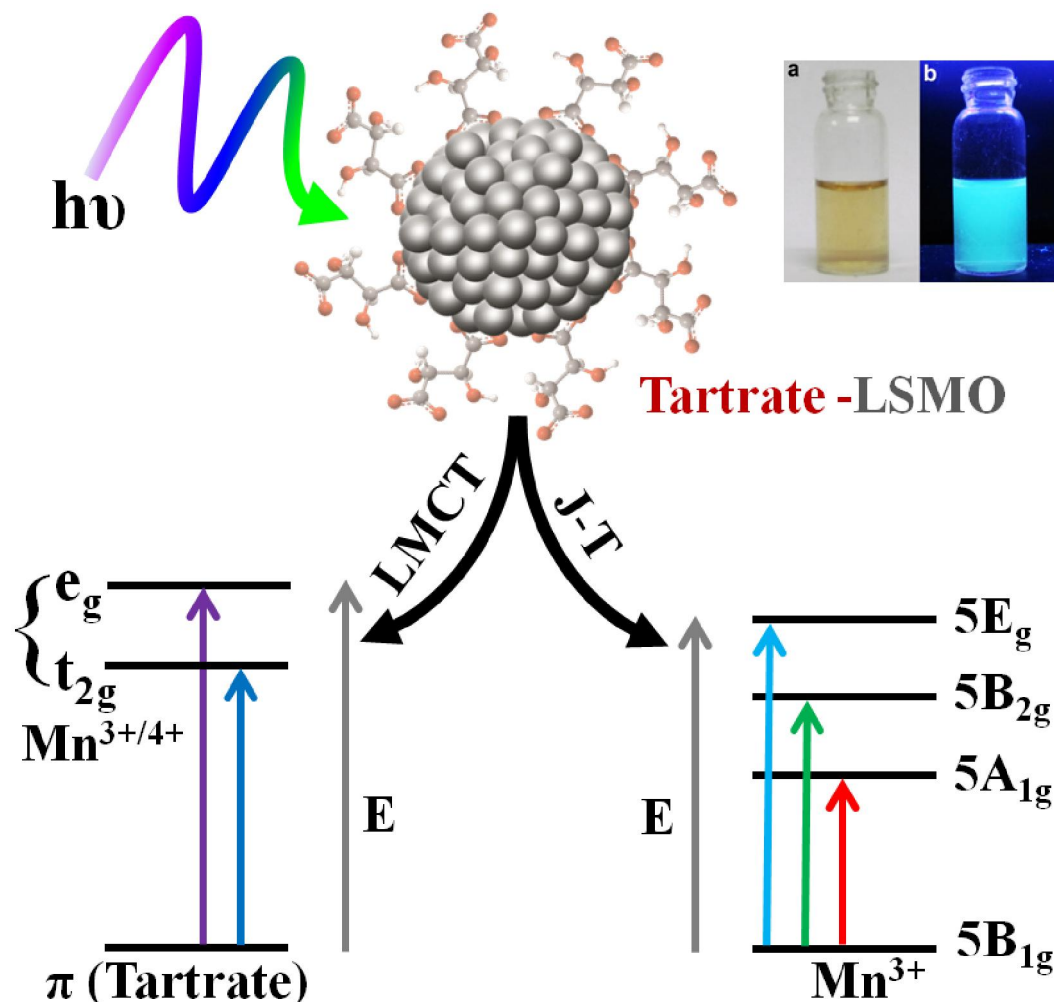


**Figure 4.1.** Schematic presentation of the most likely events occurring when a photon hits a tartrate functionalized LSMO NPs (T-LSMO): ligand-to-metal charge transfer transitions from HOMO (centered in tartrate ligand) to LUMO (centered in  $\text{Mn}^{3+/4+}$  of the NP), and d-d transitions involving Jahn-Teller sensitive  $\text{Mn}^{3+}$  ions in the NP. Arrows show the transition involved upon excitation by photon of different energy. Inset shows the photographs of T-LSMO NPs under visible light (a) and under UV light (b).

peak at 300 nm could be assigned to one of the possible high energy charge-transfer, ligand-to-metal charge transfer (LMCT) processes involving tartrate- $\text{Mn}^{3+/4+}$  interaction [22]. The other expected LMCT band [22] at around 385 nm has not been observed in the absorption spectrum presumably because the band has been masked by the more intense 300 nm absorption, however, is distinctly visible in the excitation spectrum at around 372 nm (Figure 4.2b). Other bands at 440, 580 and 758 nm are reasonably attributed to d-d transitions of  $\text{Mn}^{3+}$  in T-LSMO NPs, as the degeneracy of  $5E_g$  ground state term of  $d^4$

(Mn<sup>3+</sup>) high-spin octahedral environment, has been lifted by the Jahn-Teller effect, that ultimately leads to a tentative assignment of the observed bands to the transitions  $5B_{1g} \rightarrow 5E_g$ ,  $5B_{1g} \rightarrow 5B_{2g}$  and  $5B_{1g} \rightarrow 5A_{1g}$ , respectively [23, 24] (Figure 4.1). Any absorption contribution from other metal ions (La and Sr)-tartrate interaction, tartrate ligand or as-prepared LSMO itself, in the assigned peak positions has been nullified from control experiments. Reflection of the UV-vis absorption patterns into the photoluminescence excitation spectra (shown in Figure 4.2b) of the sample has been expected and indeed observed. Which further supports the assignment of the electronic excited states those give rise to multiple color photoluminescence.

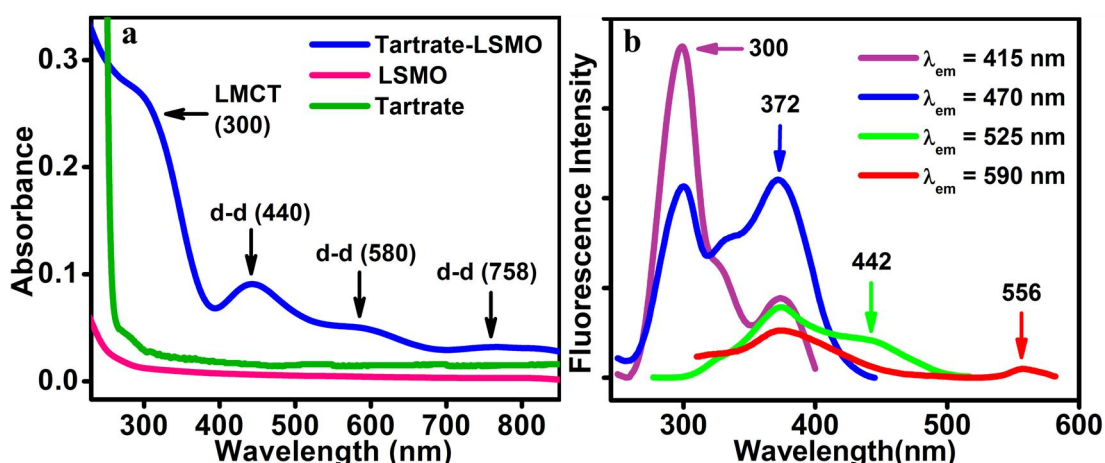


**Figure 4.2.** a) UV-vis absorption spectrum of as-prepared LSMO, tartrate and tartrate-LSMO NPs (in aqueous solution at pH~7). b) Photoluminescence excitation spectra of tartrate-LSMO NPs at different emission maximum (shown in Figure 2a) of 415, 470, 525 and 590 nm.

Figure 4.3a displays the normalized photoluminescence spectra of T-LSMO NPs at room temperature. The four distinct emission bands starting from blue to red region (maximum at 418, 470, 520 and 590 nm) of the spectrum, corresponding with four distinct excitation wavelengths (300, 375, 425 and 570 nm) are clearly observed. The photoluminescence as shown in Figure 4.3a may be assigned to originate predominantly from the LMCT [tartrate  $\rightarrow$  Mn<sup>3+/4+</sup>] excited states and ligand field excited states of the metal (Mn<sup>3+</sup>) d orbitals. Photoluminescence from either an intraligand or metal to ligand charge-transfer (MLCT) excited states are considered unlikely. To represent qualitatively the relationship between emission ‘bands’, we have shown the OD normalized PL spectra

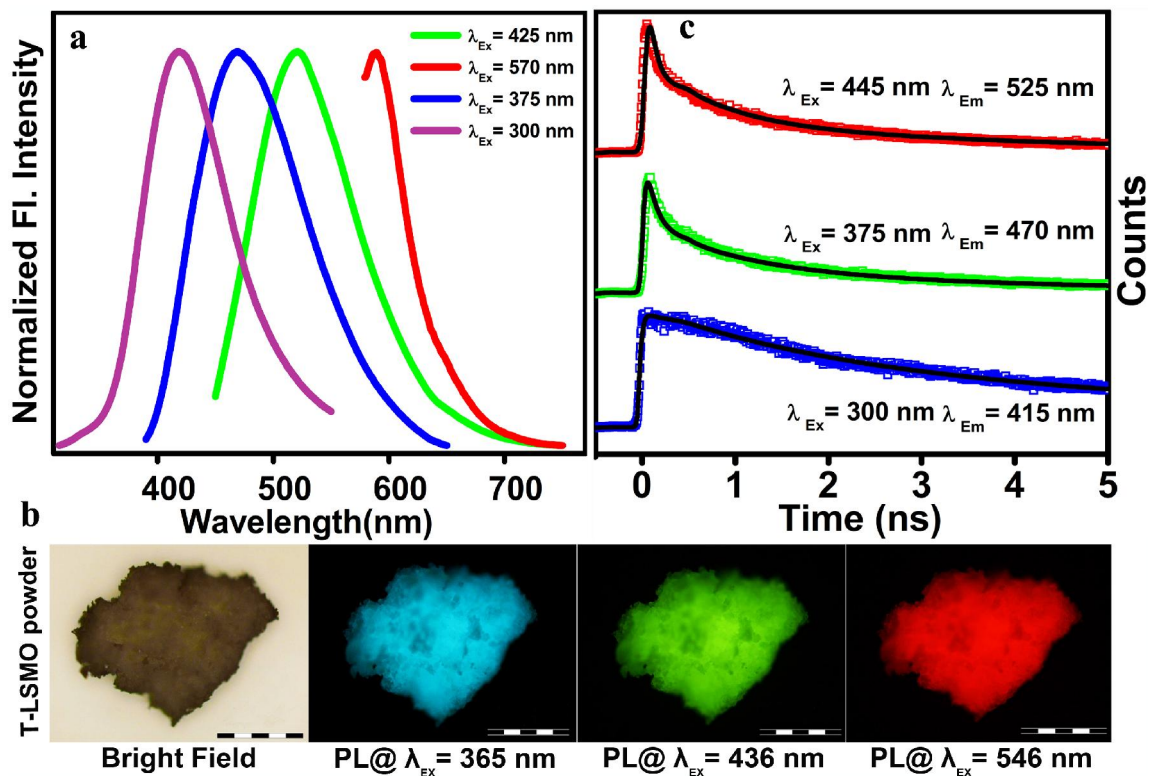


**Figure 4.3.** a) Normalized steady-state photoluminescence spectra collected from tartrate-LSMO NPs with four different excitation wavelengths of 300, 375, 425 and 570 nm at pH~7. b) Fluorescence microscopic images of tartrate-LSMO NP powder under irradiation of white light (bright field) and light of three different wavelengths of 365, 436 and 546 nm. Scale bars in the Figure are of 500  $\mu\text{m}$ . c) Picosecond-resolved photoluminescence decays transients of tartrate-LSMO NPs in water measured at emission wavelengths of 415, 470 and 525 nm upon excitation with laser source of 300, 375 and 445 nm wavelengths respectively.

of T-LSMO NPs in Figure 4.4a. Moreover, in order to confirm that the lower energy emission spectra are not sub-sets of high energy emission tail, we have compared the similar excitation wavelength dependent fluorescence emission of a well known organic dye C500 having one emission maximum centered at 510 nm in water (Figure 4.4c). From the figure, it has been observed that, unlike T-LSMO NPs, despite the change in excitation wavelengths (from 320 to 470 nm), emission maxima of C500 (at around 510 nm) remains same and so its fluorescence decay transients (Figure 4.4d). The observation clearly indicates that the lower energy emission spectra are not sub-sets of high energy emission tail of T-LSMO NPs.

The above speculation regarding the origin of photoluminescence (PL) is also supported by the pH dependent PL measurements of T-LSMO NPs. As revealed from

Figure 4.5 upon changing the pH of the T-LSMO solution from 12 to 3, its PL intensity quenches significantly, however, almost totally recovered again, by changing the pH from 3 to 12. This phenomenon is consistent with the fact that, in acidic/neutral pH,  $Mn^{3+}$  ions are unstable and tend to disproportionate into  $Mn^{2+}$  and  $Mn^{4+}$ , whereas it is stabilized by the comproportionation of  $Mn^{2+}$  and  $Mn^{4+}$  in alkaline conditions [25]. Thus, reduction

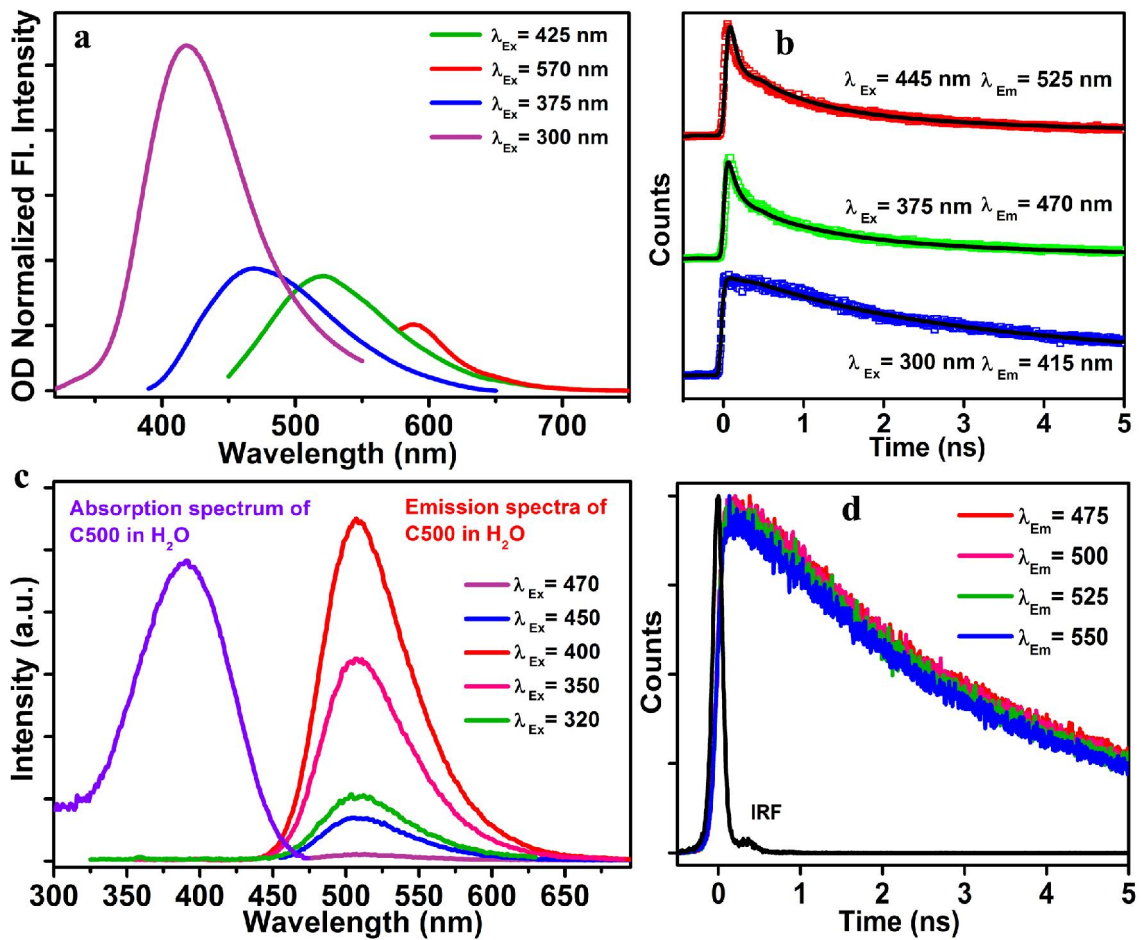


**Figure 4.4.** a) OD normalized PL spectra of Tartrate-LSMO NPs at pH~7. b) Picosecond-resolved photoluminescence decays transients of tartrate-LSMO NPs in water measured at emission wavelengths of 415, 470 and 525 nm upon excitation with laser source of 300, 375 and 445 nm wavelengths respectively. c) Absorption spectrum and excitation wavelength dependent emission spectra of C500 in water. The emission spectra show unique characteristics (position of the emission peak and spectral width) independent of the wavelength of excitation. d) Picosecond-resolved photoluminescence decays transients of C500 in water measured at emission wavelengths of 475, 500, 525 and 550 nm upon excitation with a laser source of 375 nm wavelength. The transients detected at various emission wavelengths show similar decay constants of 2.77 ns (51.61%) and 4.37 ns (48.38%).

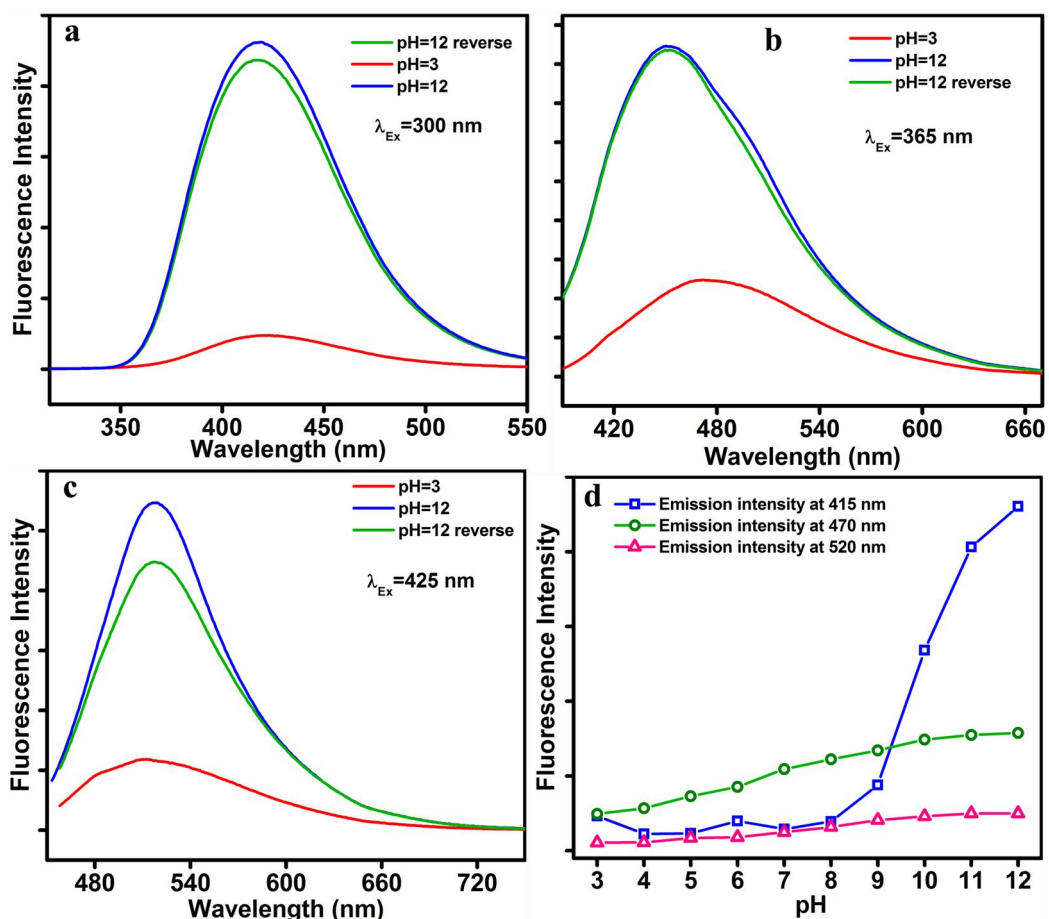


**Figure 4.5.** pH dependent photoluminescence (PL) spectra of T-LSMO NPs. a), b) and c) Represents the photoluminescence quenching and recovery of T-LSMO NPs by changing the pH of the solution from 12 (blue spectrum) to 3 (red spectrum) and again reverse back to 12 (green spectrum). d) Represents the change of PL intensity at different PL maximum with changing the pH of the solution from 12 to 3 by drop wise addition of HCl. Solid lines are guide to the eye.

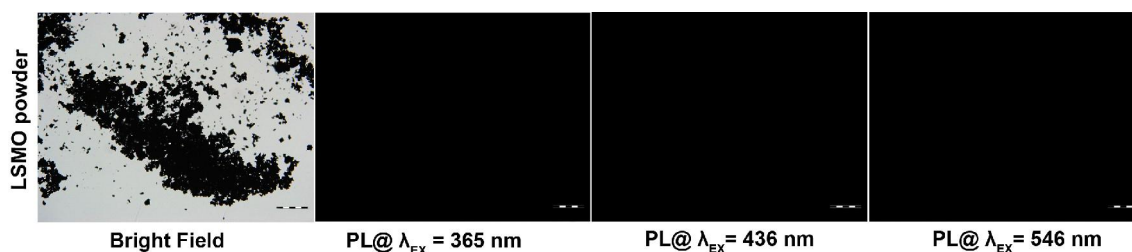


**Figure 4.6.** Fluorescence microscopic images of as-prepared LSMO NPs powder under irradiation of white light (bright field) and light of three different wavelengths of 365, 436 and 546 nm.

potentials of  $\text{Mn}^{3+}/\text{Mn}^{2+}$  system in acidic and basic solutions ( $E^{\circ}_{\text{Mn}^{3+}/\text{Mn}^{2+}} = 1.51\text{V}$  at  $\text{pH}=0$ , while  $E^{\circ}_{\text{Mn}^{3+}/\text{Mn}^{2+}} = -0.25\text{V}$  at  $\text{pH}=14$ ) [26] play a crucial role in understanding the pH dependent PL profile of the studied system. Tartaric acid possesses four protons (two

carboxylic acid protons and two hydroxyl protons) which can be liberated depending on pH. However, due to high  $pK_a$  (11-12) values of the hydroxyl protons in comparison with the carboxylic protons ( $pK_{a1}= 2.95$  and  $pK_{a2}= 4.25$ ), they would not liberate at neutral pH and only available at highly basic pH conditions [27]. Thus at higher pH, strong coordination of tetravalent anionic tartaric acid with  $Mn^{3+}$  facilitates both the LMCT and J-T events, resulting maximization of PL intensity from T-LSMO NPs. However, upon acidification a decrease in pH leads to the protonation of co-ordinated tartrate molecules along with disproportionation of  $Mn^{3+}$  ions, diminishes the overall PL intensity from T-LSMO NPs. Figure 4.3b shows the fluorescence microscopic images of T-LSMO powder under irradiation of white light (bright field) and light of different wavelengths (Figure 4.6 shows the fluorescence microscopic images of as-prepared LSMO powder under identical conditions). Multiple color photoluminescence arising specifically from the functionalized NPs (T-LSMO) upon different excitation are clearly evident from the photographs. Photoluminescence quantum yields (QY) of the T-LSMO NPs at pH~12, were obtained by using the comparative method of Williams *et al.*[28], which involves the use of well characterized standard samples with known QY values. Photoluminescence QY of  $1 \times 10^{-2}$  (for 415 nm PL),  $4 \times 10^{-3}$  (for 470 nm PL),  $8 \times 10^{-4}$  (for 520 nm PL) and  $2.4 \times 10^{-4}$  (for 590 nm PL) were obtained relative to the standards 2-amino-purine (2AP), 4', 6-diamidino-2-phenylindole (DAPI), Hoechst (H33258) and ethidium bromide (EtBr), respectively.

Further insights into the nature of the photoluminescence can be obtained by analyzing the luminescence lifetime decay transients of T-LSMO NPs in water, measured by picosecond-resolved time-correlated single-photon counting (TCSPC) technique. Figure 4.3c shows the luminescence lifetime decay transients of the water soluble NPs at three different emission wavelengths (415, 470 and 525 nm) corresponding with three different laser excitation wavelengths (300, 375 and 445 nm) respectively. Although the origin of 415 and 470 nm emission is from the LMCT excited states, luminescence lifetime of 415 nm emission is much longer ( $\langle \tau \rangle = 4.77$  ns) than the 470 nm ( $\langle \tau \rangle = 0.84$  ns) emission. Substantial shortening in the luminescence lifetime of 470 nm emission and its close resemblance with the 525 nm emission lifetime ( $\langle \tau \rangle = 0.64$  ns, originates from ligand field excited states of the metal d orbital's) presumably due to enhanced radiative deactivation of the excited state by the close proximity with metal d-d states [29].

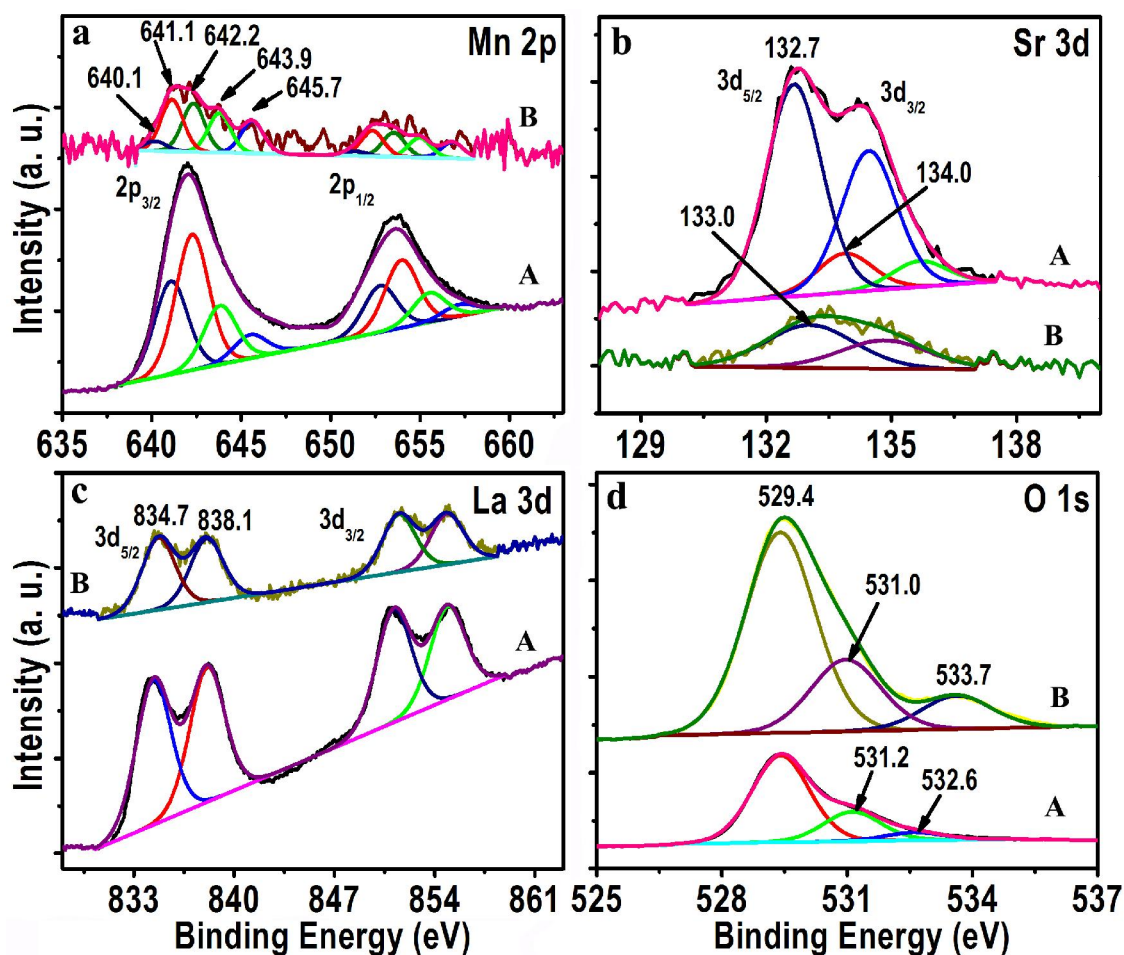


**Figure 4.7.** XPS analysis of LSMO NPs before and after functionalization with tartrate (traces A and B, respectively). (a), (b), (c) and (d) are Mn 2p, Sr 3d, La 3d and O 1s regions respectively, of samples A and B.

In order to get supporting evidence regarding the origin of different optical properties of T-LSMO NPs, XPS analysis has been carried out for LSMO NPs, before (as prepared NPs) and after (T-LSMO) functionalization with sodium tartrate. Figure 4.7 represents the XPS data of as-prepared LSMO (traces A) and T-LSMO NPs (traces B). The Mn 2p region is shown in Figure 4.7a. The peaks of Mn  $2p_{3/2}$  are observed at 641.1, 642.2, 643.9 and 645.7 eV in both the samples. The Mn  $2p_{3/2}$  features at 641.1 and 642.2 eV are attributed to oxides of  $Mn^{3+}$  and  $Mn^{4+}$  respectively [30]. The peak position at 643.9 eV may be due to the manganese in different coordination environment like other metal ions such as  $La^{3+}$  and  $Sr^{2+}$  [30]. The peak position at 645.7 eV may be due to satellite peak [31]. In the T-LSMO a new feature peaking at 640.1 eV is noticed which is attributed to  $Mn^{2+}$

[30]. The formation of  $\text{Mn}^{2+}$  could be due to reduction of some of the  $\text{Mn}^{3+}/\text{Mn}^{4+}$  species with tartrate, as reduction of metal ions by tartrate/citrates is expected [32]. The Sr  $3d_{5/2}$  peaks at 132.7 and 134.0 eV (Figure 4.7b, trace A) are assigned to  $\text{Sr}^{2+}$  in the bulk and surface of the NPs, respectively [33]. In the case of T-LSMO, the Sr  $3d_{5/2}$  is noticed at 133.0 eV which is also due to Sr in the divalent (+2) state [34]. The peaks of La  $3d_{5/2}$  at 834.7 and 838.1 eV are due to  $\text{La}^{3+}$  and satellite, respectively (Figure 4.7c) in both the samples [35]. The O 1s peaks in LSMO NPs (Figure 4.7d) at 529.4 and 531.0 eV are due to lattice oxygen  $\text{O}^{2-}$  associated with Mn and surface oxygen associated hydroxyl ions, respectively [30]. The peak at 532.6 eV is due to the O which is weakly bound to surface [36]. The peak of O 1s at 533.7 eV in T-LSMO sample is due to carboxylate oxygen from the tartrate [37]. So, from XPS study it is evident that, upon functionalization with tartrate a partial reduction of  $\text{Mn}^{3+}$  and  $\text{Mn}^{4+}$  centers in the NPs occur and resulting the formation of  $\text{Mn}^{2+}$  ions, whereas,  $\text{La}^{3+}$  and  $\text{Sr}^{2+}$  centers remains unaffected.

It is argued that the change in the valence states of Mn ions will lead to a perturbation of  $\text{Mn}^{3+}\text{-O-Mn}^{4+}$  bond. We do observe the postulated perturbation through Raman spectroscopic investigation on T-LSMO NPs, as prepared LSMO NPs and tartrate. As shown in Figure 4.8a, between the two characteristic peaks of LSMO NPs at 436 and 636  $\text{cm}^{-1}$  (corresponding with  $A_{1g}$ -like and  $B_{1g}$ -like vibrational modes involving Mn-O stretching vibration modes of  $\text{MnO}_6$  unit, respectively) [38], peak around 436  $\text{cm}^{-1}$  completely disappeared and the 636  $\text{cm}^{-1}$  peak becomes broadened (possibly due to mixing of tartrate features) after their functionalization with tartrate. Hence, the disappearance of  $A_{1g}$ -like stretching vibration mode that represents the extension and compression of Mn-O bond pairs and is directly correlated with Jahn-Teller distortion, provides a strong basis for the changes that occur at the level of  $\text{MnO}_6$  octahedra which provides the physical basis for the change in the optical properties of the NPs upon functionalization.

The direct bonding of tartrate ligands to the surface of the LSMO NP has been confirmed by FTIR spectroscopy. Figure 4.8b represents the FTIR spectra of as-prepared LSMO NPs, tartrate and tartrate functionalized LSMO NPs. In case of tartrate, the appearance of two strong bands at 1412 and 1621  $\text{cm}^{-1}$  represent the symmetric and asymmetric stretching modes of  $\text{-COO}^-$  ions (carboxylate) respectively [39]. Upon

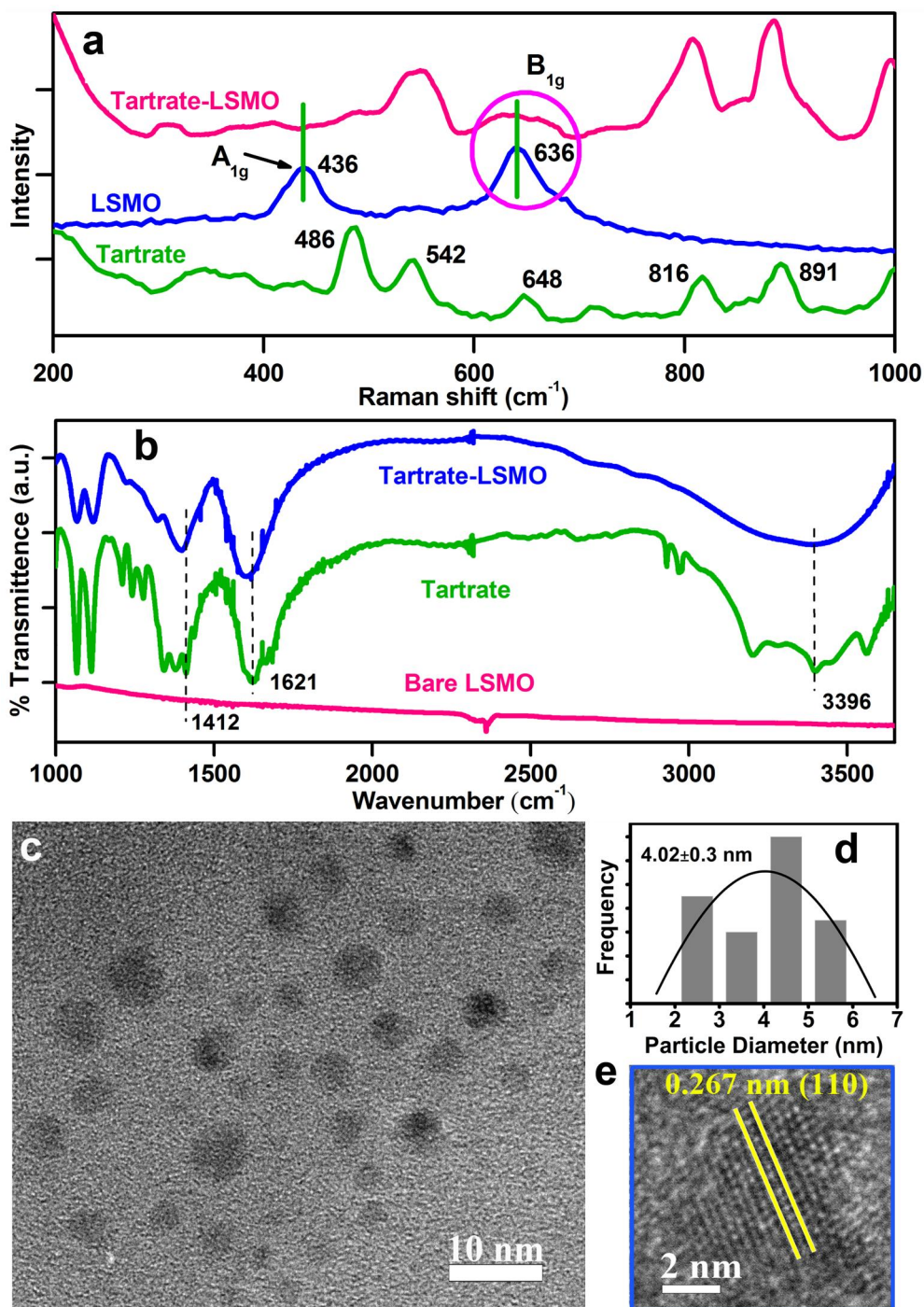


**Figure 4.8.** (a) Raman spectra of as-prepared LSMO NPs, tartrate-LSMO NPs and tartrate. (b) FTIR spectra of as-prepared LSMO NPs, sodium tartrate and tartrate functionalized LSMO (tartrate-LSMO) NPs, recorded with a KBr pellet. (c) TEM image of tartrate-LSMO NPs. (d) Size distribution of the NPs in solution. (e) HRTEM image of the crystalline structure of tartrate-LSMO NPs.

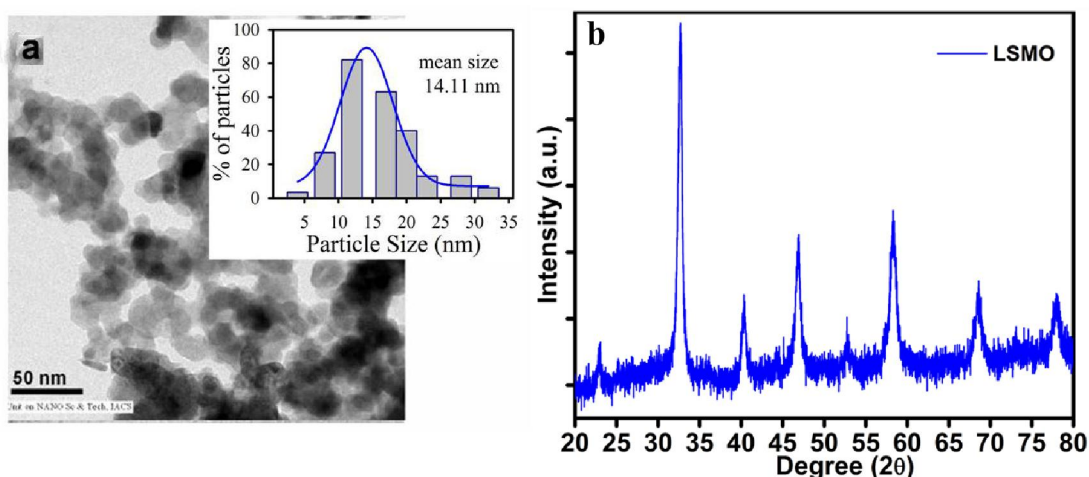


**Figure 4.9.** (a) Represents the TEM image of the as prepared LSMO NPs and the inset showing the particle size distribution. (b) Shows XRD pattern of as-prepared bulk LSMO NPs and the corresponding peak positions matched with the values reported earlier.

attachment with the NP surface these two bands become red-shifted and appear sharply at  $1392$  and  $1596\text{ cm}^{-1}$  respectively, clearly confirm the binding of carboxylate's oxygen with the NPs. Moreover, the significant broadening of the band representing O-H (hydroxyl) stretching vibration mode [40] at  $3396\text{ cm}^{-1}$  for tartrate-LSMO, also substantiate the involvement of hydroxyl groups during the functionalization process.

As shown in Figure 4.8c, transmission electron microscopy (TEM) revealed that T-LSMO NPs are nearly spherical in shape with an average diameter of around 4 nm (Figure 4.8d). Thus, tartrate ligands only solubilized the small sized particles out of a wide range of particle size from  $\sim 2$  to 30 nm in the as-prepared LSMO NPs (see Figure 4.9). The HRTEM image (Figure 4.8e) confirm the crystalline nature of the T-LSMO NPs having interplanar distance of 0.267 nm, which corresponds to the (110) plane of the crystal lattice (as shown in Figure 4.10b, similar interplanar distance have also been observed in case of as-prepared LSMO NPs). Selected area electron diffraction (SAED) and energy dispersive X-ray (EDAX) pattern of LSMO and T-LSMO NPs also provided supporting evidence (Figure 4.10 and Figure 4.11).

Since the tartrate ligand (contains two hydroxyl and two carboxylate groups) is from the class of organic hydroxycarboxylates, we have used two more ligands which are

close mimic of tartrate (trisodium citrate and sodium salt of malic acid) and of the same class, for meaningful comparisons with the data obtained from tartrate.

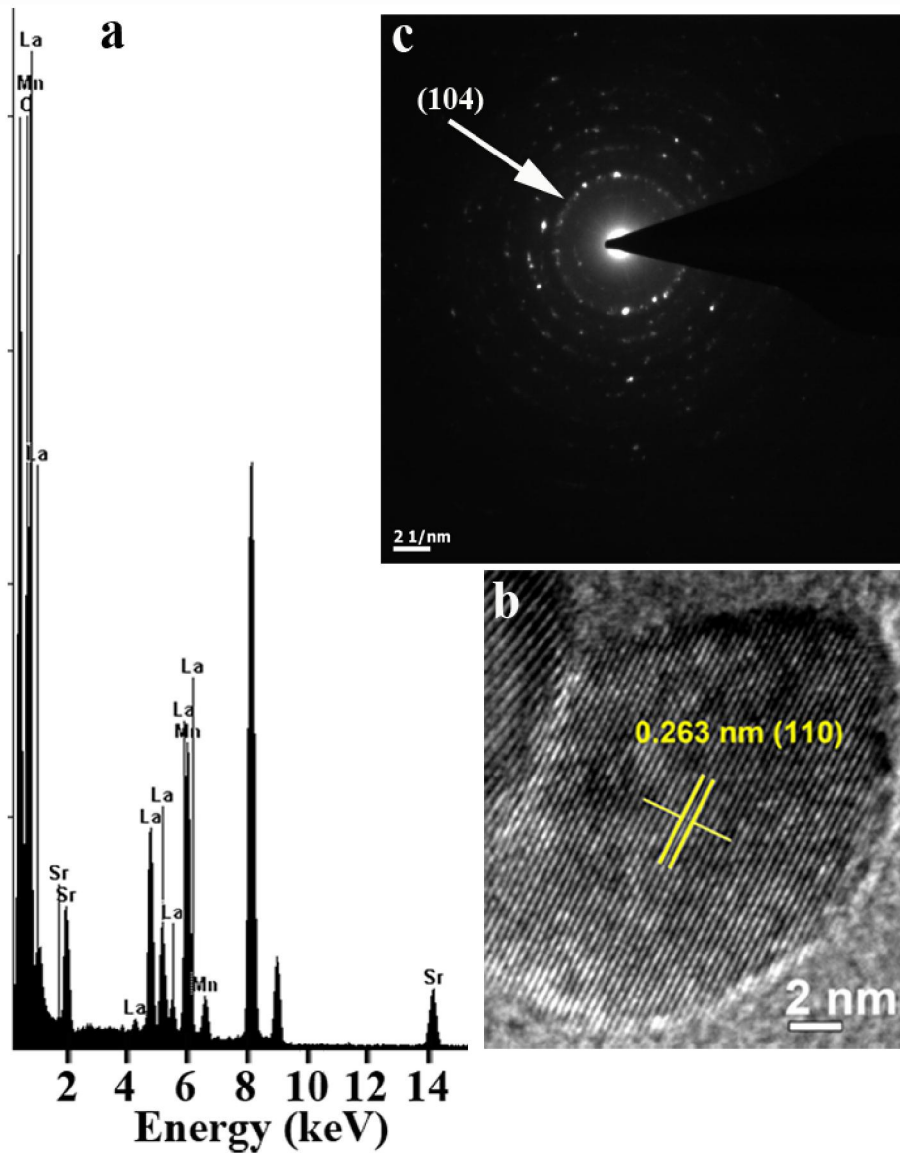


**Figure 4.10.** (a) The EDAX spectrum of as prepared LSMO NPs shows elemental composition of the NPs. (b) HRTEM image of as-prepared LSMO NPs having interplanar distance of 0.263 nm (which is similar with Tartrate-LSMO NPs shown in Figure 4.8e) corresponding to (110) plane of the crystal lattice. (c) SAED pattern of the as prepared LSMO NPs and the arrow head indicates the diffraction ring originated from (104) plane of the crystal lattice.

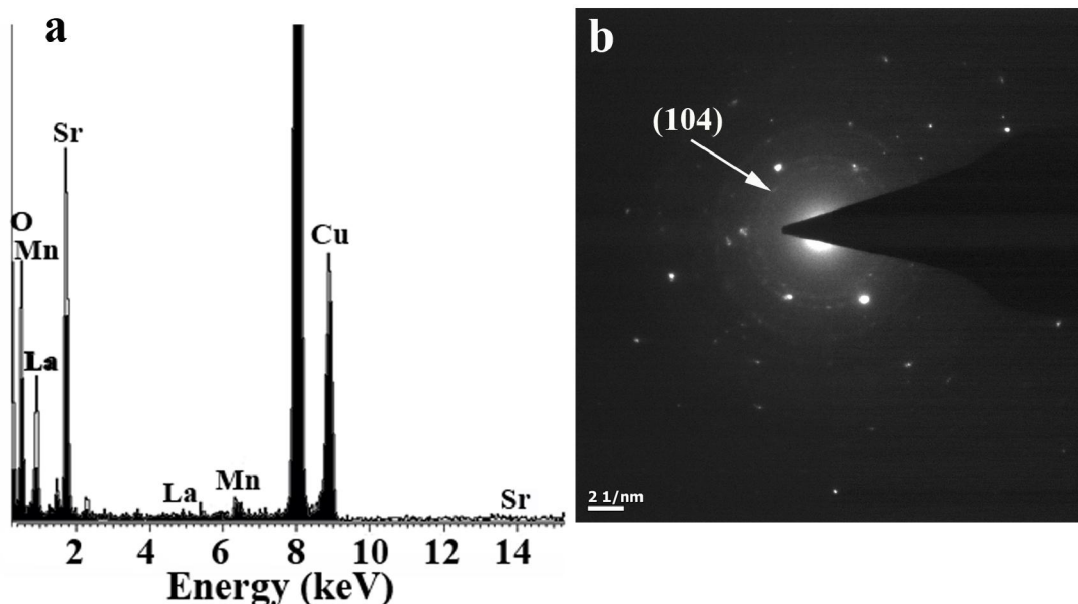


**Figure 4.11.** (a) The EDAX spectrum of Tartrate-LSMO NPs shows elemental composition of the NPs. (b) SAED pattern of the Tartrate-LSMO NPs. Arrow head indicates the appearance of diffraction ring from (104) plane, which have also been observed in case of as prepared LSMO NPs shown in Figure 4.10c.

It has been observed that, both citrate and malate functionalized LSMO NPs exhibit similar UV-vis absorption pattern (Figure 4.13a and 4.12 respectively) and excitation wavelength-dependent multiple photoluminescence (in case of citrate-LSMO, Figure 4.13b and 4.13c), which further substantiate the results obtained using tartrate (spectral position of the observed absorption and photoluminescence peaks from these functionalized NPs has been listed in Table 4.1). Due to the structural similarity of tartrate and citrate, their pH dependent co-ordination behavior with the NP surface has been expected to be alike. It is revealed that the ligand field of tartrate, citrate and malate can activate the Jahn-Teller (J-T) splitting of  $Mn^{3+}$  ions in the NPs and the corresponding d-d transitions along with ligand-to-metal charge transfer transitions (LMCT) plays the crucial role for the emergence of such novel optical properties from LSMO NPs upon functionalization.

In case of as-prepared LSMO NPs, simultaneous electron transfer between  $Mn^{3+}$  and  $Mn^{4+}$  ions via an oxygen ion (i.e. exchange between  $Mn^{3+}$  and  $Mn^{4+}$  ions, well known as *double exchange*) plays the key role for the origin of their room temperature ferromagnetism [41]. So, any perturbation to the parallel alignment of the spins of the two

adjacent cations or if the  $\text{Mn}^{3+}\text{-O-Mn}^{4+}$  bond is bent, the electron transfer becomes more difficult and the magnetic interaction decreases. The magnetization of T-LSMO NPs was measured using superconducting quantum interference device (SQUID) magnetometry and the NPs showed paramagnetic behavior at low temperature (upto 50 K), while they were diamagnetic at around room temperature (shown in Figure 4.14). Thus, upon functionalization with tartrate the magnetic behavior of LSMO NPs has been changed dramatically from room temperature ferromagnetic to diamagnetic. This flipping of magnetism could be due to small average size ( $\sim 4$  nm, see Figure 4.8d) of the T-LSMO NPs (as tartrate only solubilized the small sized particles out of a wide range of particle size from 2 to 30 nm in the as-prepared LSMO NPs) or due to any distortion of the  $\text{Mn}^{3+}\text{-O-Mn}^{4+}$  bond.

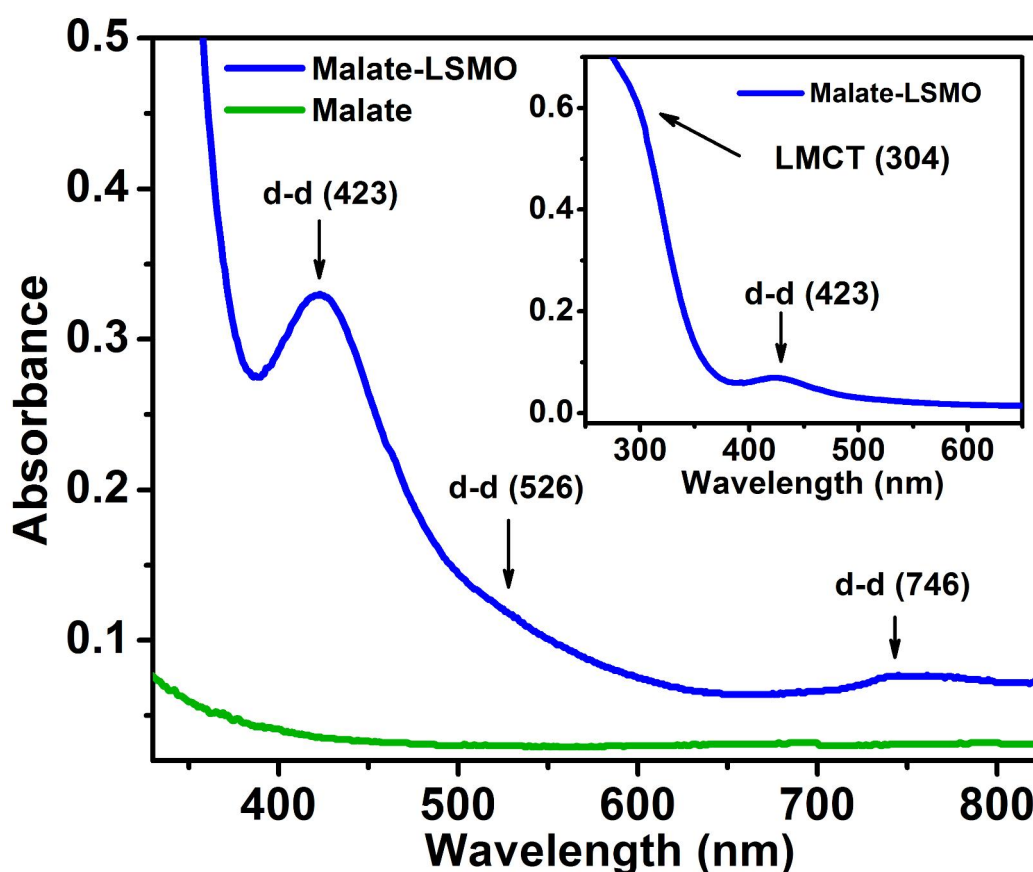


**Figure 4.12.** UV-vis absorption spectrum of malate and malate-LSMO NPs in aqueous solution at pH~7. Inset shows the absorption peak (LMCT) at around 304 nm obtained from diluted solution of malate-LSMO NPs.

**Table 4.1.** Spectral position of UV-vis absorption bands/peaks of tartrate, citrate and malate functionalized LSMO NPs along with their photoluminescence peak positions (except Malate-LSMO).

System	Positions of UV-vis absorption bands/peaks, $\lambda_{\text{abs}}$ (nm)	Position of photoluminescence peaks, $\lambda_{\text{em}}$ (nm)
T-LSMO	300, 440, 580 and 758	418, 470, 520 and 590
Citrate-LSMO	297, 430, 532 and 744	413, 479, 518 and 610
Malate-LSMO	304, 423, 526 and 746	Not been performed

The observed phenomena that there can be multiple photoluminescence from the T-LSMO, has been utilized for investigating possible *in vitro* cells imaging. Importantly, this has been done by employing the intrinsic photoluminescent properties of T-LSMO NPs, without further grafting of any biorecognition molecules (e.g., oligonucleotides, antibodies, or peptides) onto the NP surface. In this study, a primary squamous epithelial cells collected from the inner lining of human mouth have been used. Prior to cell imaging, the cells were spread on glass slides in presence of PBS (phosphate buffered saline) and NP solution (at a final concentration of  $3 \times 10^{-6}$  M) was added followed by 30 min of incubation. After incubation, the cells were washed twice with PBS to remove unbound NPs. Figure 4.15 demonstrates the fluorescence microscopic images of the cell labeled with T-LSMO NPs. Upper left image in the figure represent the bright-field images (black arrows indicate the nucleus of the cell) and other three images represent fluorescence images (employing 365, 436 and 546 nm excitation wavelengths respectively) of the T-LSMO NP labeled cells. Our results show that in case of NP treated cells, all fluorescence of the NPs (365, 436 and 546 nm excitation wavelength) are preferentially derived from the nuclear region of the cells. To verify the sub-cellular localization of the NPs in the cells, double labeling experiments using NPs and other fluorescent organelle marker in a single set of cell was not possible, as the excitation wavelengths of the NPs matched with that of the marker. Therefore, to circumvent this problem, we have done localization experiments with NPs and fluorescent nuclear marker (DAPI) in separate sets of cells (Figure 4.16). The comparative evaluation of the results from these two set of experiments suggest that the particles were indeed in the nucleus.

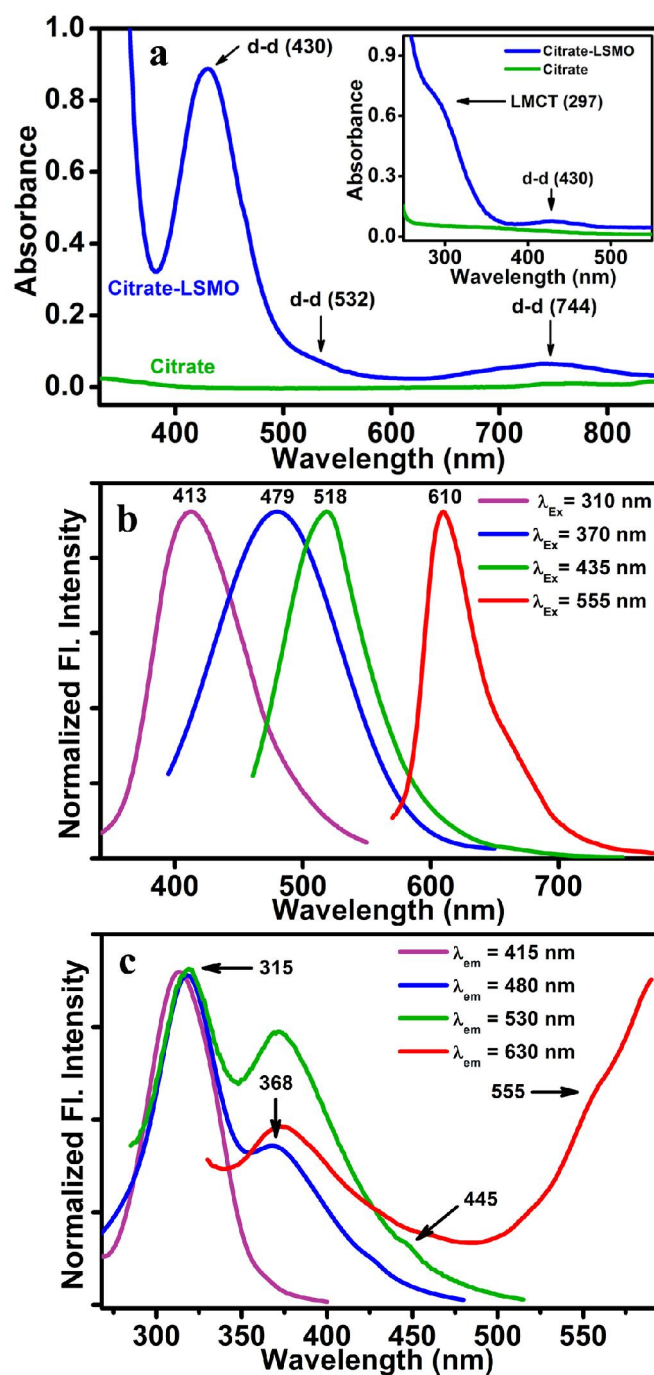


**Figure 4.13.** a) UV-vis absorption spectra of citrate and citrate-LSMO NPs in aqueous solution at pH~7. Inset shows the absorption peak (LMCT) at around 300 nm obtained from diluted solution of citrate-LSMO NPs. Although, the entire characteristic peaks/bands are present in case of citrate-LSMO, the observed shift in their positions with respect to T-LSMO NPs could be due to the structural variations of the two ligands. b) Normalized steady-state photoluminescence spectra collected from citrate-LSMO NPs with four different excitation wavelengths of 310, 370, 435 and 555 nm. c) Photoluminescence excitation spectra of citrate-LSMO NPs at different emission maximum of 415, 480, 530 and 630 nm.

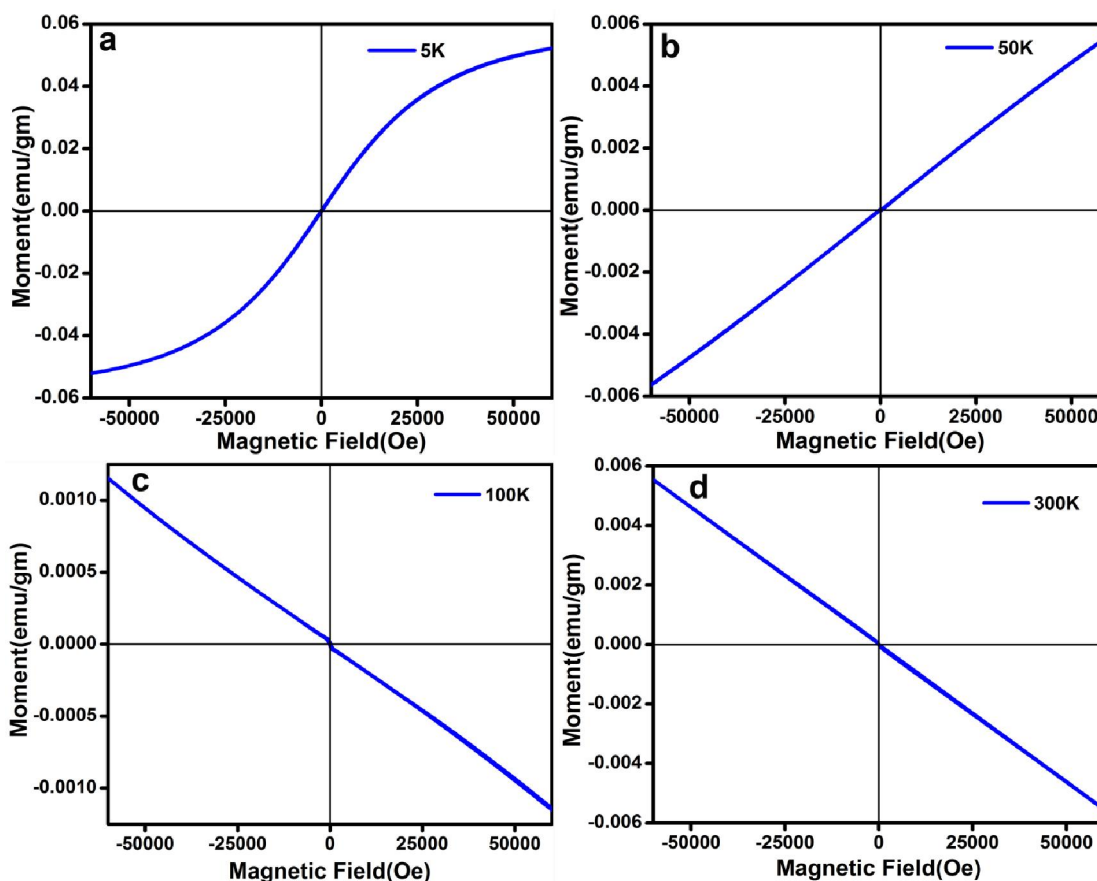


**Figure 4.14.** The M (moment)-H (magnetic field applied) magnetization plots of T-LSMO NPs at different temperature. The M-H plot at different temperatures is shown in (a), (b), (c) and (d).

The control image (Figure 4.17) shows no fluorescence from untreated squamous epithelial cells compared to those with incorporated T-LSMO NPs (Figure 4.15). The efficiency of cellular internalization and subsequent nuclear localization of T-LSMO NPs has also been revealed from time-dependent cellular uptake experiment (Figure 4.18) by monitoring (using fluorescence microscope and excitation wavelength of 365 nm) a single set of cell for 30 min after addition of the NPs. As shown in the figure, within 30 min, the NPs become enriched inside the nucleus of the cells. Although, the cellular internalization of untargeted negatively charged (due to carboxylate groups of tartrate) NPs is believed to occur through nonspecific binding on cationic sites of the plasma membrane followed by their endocytosis [42], the reason behind their efficient nuclear localization is unknown and needs further rigorous investigation. However, taken together these multicolor photoluminescence and efficient nuclear localization results suggest that the T-LSMO NP

has the potential for multifunctional nanoprobe in terms of biological imaging and targeted drug delivery. According to a recent study liquid extract of LSMO nanoparticles are not toxic to the cells [43] and we have also found that T-LSMO NPs are nontoxic by a standard MTT cell viability assay.

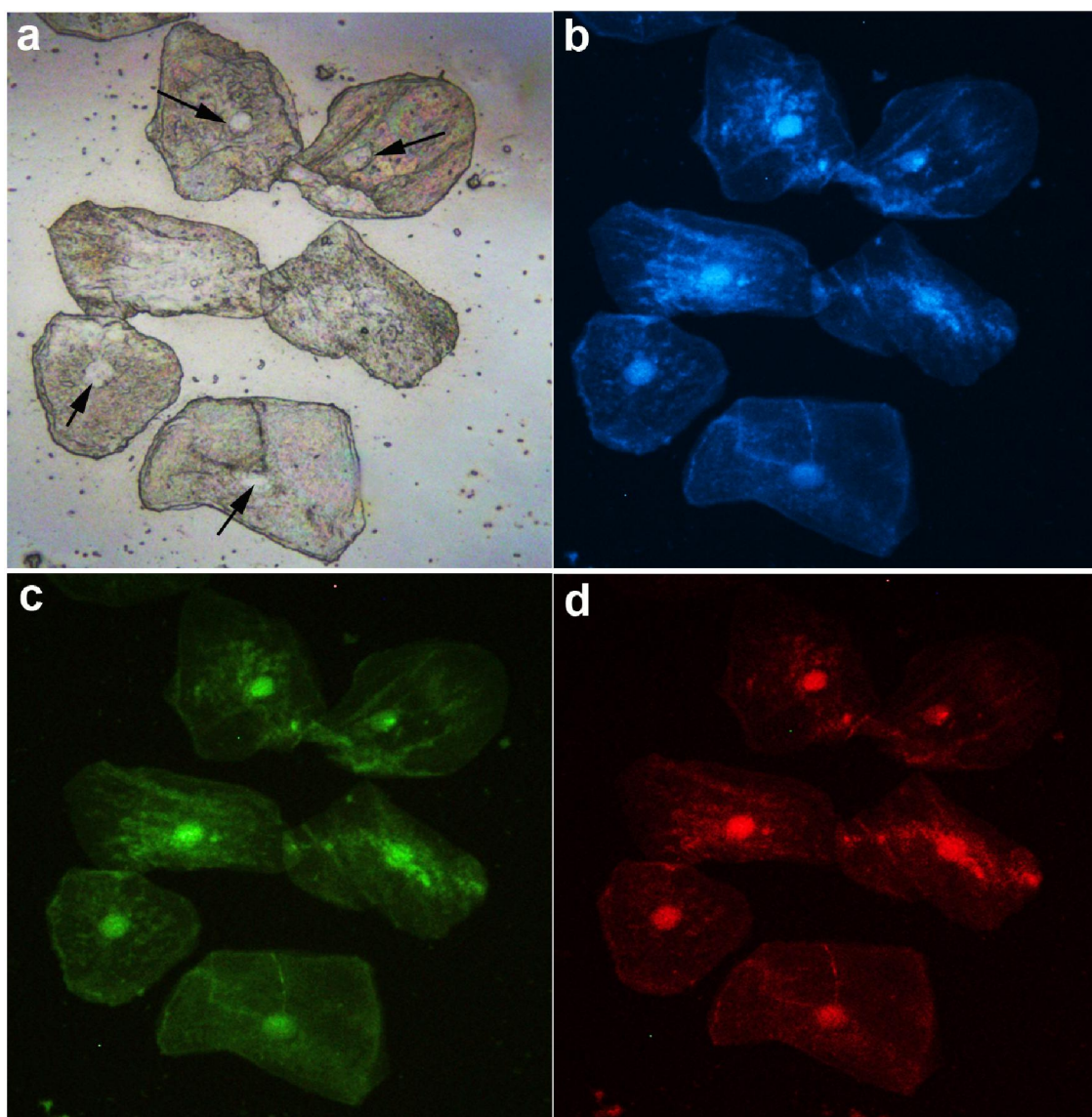


**Figure 4.15.** Representative fluorescence microscopic images of human oral squamous epithelial cells labeled with T-LSMO NPs. Upper left image corresponds to the bright-field image of the cells and the black arrows indicate the nucleus of the cells. The fluorescence images were taken using 365 (b), 436 (c) and 546 nm (d) excitations wavelengths. Selective nuclear localization of the NPs is clearly evident from the multicolor photoluminescence images of the cell.

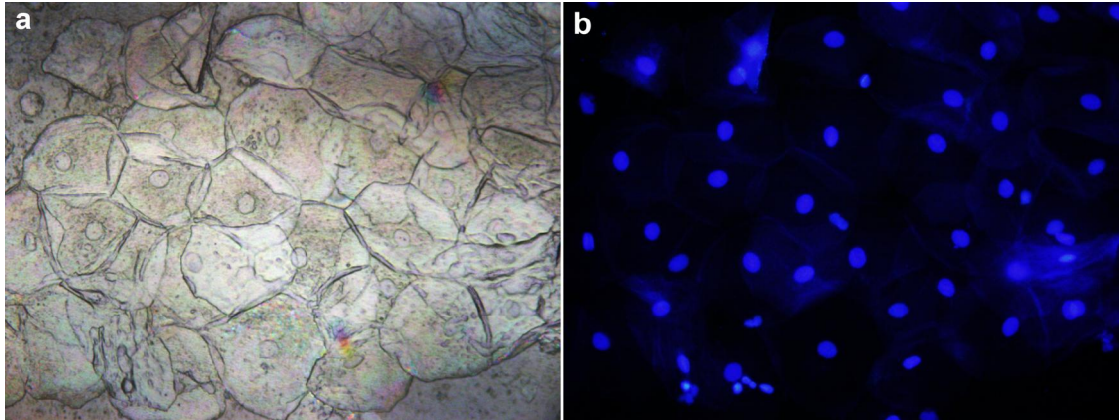


**Figure 4.16.** (a) Bright-field image of human oral squamous epithelial cells and (b) fluorescence micrographs (using an excitation source of 365 nm wavelength) of the same cells stained with DAPI.

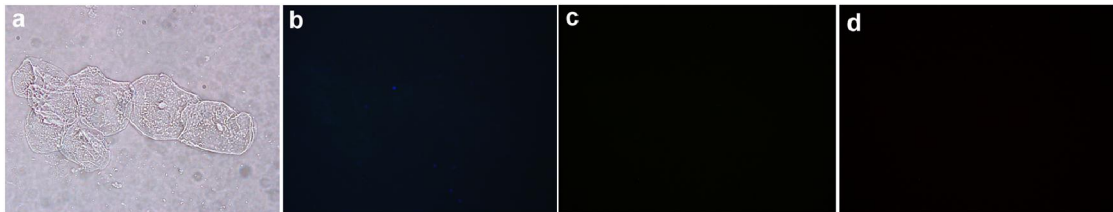


**Figure 4.17.** The fluorescence microscopic images of squamous epithelial cells non-treated with T-LSMO NPs: (a) bright field image; and fluorescence images collected upon excitation at (b) 365 nm, (c) 436 nm and (d) 546 nm wavelengths.

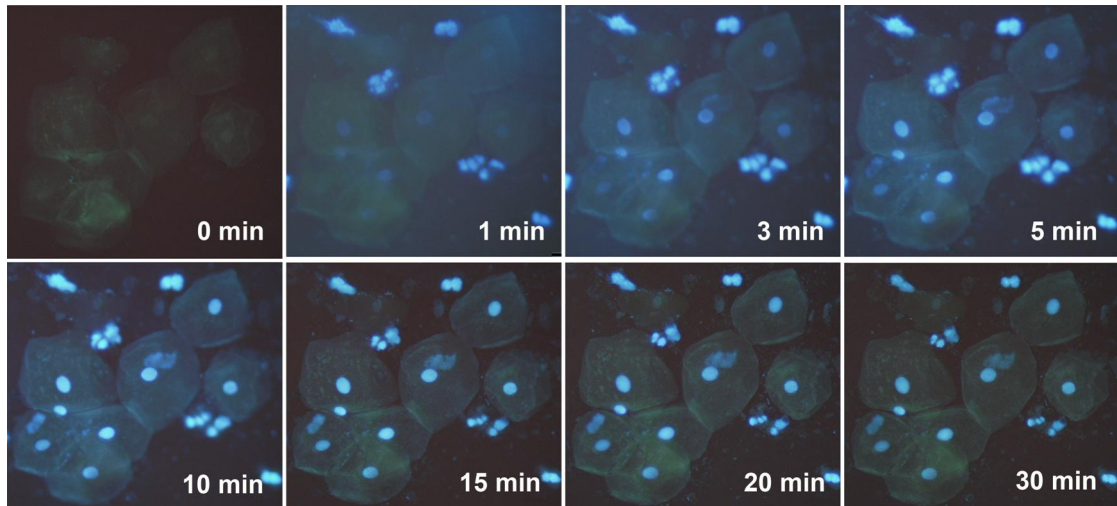


**Figure 4.18.** Time-dependent internalization of T-LSMO NPs into human oral squamous epithelial cells. Fluorescence micrographs (taken using an excitation source of 365 nm wavelength) of a single set of cells clearly indicates that the NPs become localized into to the nucleus of the cells within 30 min of addition.

### 4.3. Conclusion

In the present study, we have demonstrated the possibility of electronic structural modifications of manganites NPs (LSMO, and thus the resulting novel optical properties) by charge transfer through functionalization with small organic ligands. The modified electronic structure notably leads to multicolor photoluminescence from the functionalized NPs when excited with different wavelength. We have also explored the mechanistic insight into the origin of multicolor photoluminescence from the T-LSMO NPs. We envision that, given the potentiality of the interaction of  $Mn^{2+}$  (easy to convert into  $Mn^{3+}$  at high pH),  $Mn^{3+}$  (J-T sensitive) and  $Mn^{4+}$  towards hydroxycarboxylates (tartrate/citrate) and the consequent origin of novel optical properties, a logical extension of this work would be the functionalization of manganese oxides and various manganese doped nanoparticles including manganese ferrites, ZnO, CdS etc. Also, the most challenging extension of this work would be to design the nanoparticle as a multifunctional delivery vehicle for therapeutic agents targeted to specific tissue or cell types and to understand how these NPs are internalized into cells and modulate cell functions.

## Reference

- [1] W.C.W. Chan, S. Nie, Quantum dot bioconjugates for ultrasensitive nonisotopic detection, *Science* 281 (1998) 2016.
- [2] J.R. Taylor, M.M. Fang, S. Nie, Probing specific sequences on single DNA molecules with bioconjugated fluorescent nanoparticles, *Anal. Chem.* 72 (2000) 1979.
- [3] N.H. Bonadeo, J. Erland, D. Gammon, D. Park, D.S. Katzer, D.G. Steel, Coherent optical control of the quantum state of a single quantum dot, *Science* 282 (1998) 1473.
- [4] X.H. Gao, S.M. Nie, Molecular profiling of single cells and tissue specimens with quantum dots, *Trends. Biotechnol.* 21 (2003) 371.
- [5] M. Liong, J. Lu, M. Kovichich, T. Xia, S.G. Ruehm, A.E. Nel, F. Tamanoi, J.I. Zink, Multifunctional inorganic nanoparticles for imaging, targeting, and drug delivery, *ACS Nano* 2 (2008) 889.
- [6] F. Gao, X.Y. Chen, K.B. Yin, S. Dong, Z.F. Ren, F. Yuan, T. Yu, Z.G. Zou, J.M. Liu, Visible-light photocatalytic properties of weak magnetic BiFeO<sub>3</sub> nanoparticles, *Adv. Mater.* 19 (2007) 2889.
- [7] L. Josephson, M.F. Kircher, U. Mahmood, Y. Tang, R. Weissleder, Near-infrared fluorescent nanoparticles as combined MR/optical imaging probes, *Bioconjugate Chem.* 13 (2002) 554.
- [8] M.F. Kircher, R. Weissleder, L. Josephson, A dual fluorochrome probe for imaging proteases, *Bioconjugate Chem.* 15 (2004) 242.
- [9] N.-H. Cho, T.-C. Cheong, J.H. Min, J.H. Wu, S.J. Lee, D. Kim, J.-S. Yang, S. Kim, Y.K. Kim, S.-Y. Seong, A multifunctional core-shell nanoparticle for dendritic cell-based cancer immunotherapy, *Nat. Nanotechnol.* 6 (2011) 675.
- [10] P.K. Verma, A. Giri, N.T.K. Thanh, L.D. Tung, O. Mondal, M. Pal, S.K. Pal, Superparamagnetic fluorescent nickel-enzyme nanobioconjugates: synthesis and characterization of a novel multifunctional biological probe, *J. Mater. Chem.* 20 (2010) 3722.
- [11] R.A. Petros, J.M. DeSimone, Strategies in the design of nanoparticles for therapeutic applications, *Nat. Rev. Drug Discov.* 9 (2010) 615.
- [12] X. Luo, A. Morrin, A.J. Killard, M.R. Smyth, Application of nanoparticles in electrochemical sensors and biosensors, *Electroanalysis* 18 (2006) 319.

- [13] W. Chen, Nanoparticle fluorescence based technology for biological applications, *J. Nanosci. Nanotechnol.* 8 (2008) 1019.
- [14] Q.A. Pankhurst, N.T.K. Thanh, S.K. Jones, J. Dobson, Progress in applications of magnetic nanoparticles in biomedicine, *J. Phys. D: Appl. Phys.* 42 (2009) 224001.
- [15] C.N.R. Rao, B. Raveau, Colossal magnetoresistance, charge ordering and related properties of manganese oxides, World Scientific, Singapore, 1998.
- [16] D.K. Kim, M.S. Amin, S. Elborai, S.H. Lee, Y. Koseoglu, M. Zahn, M. Muhammed, Energy absorption of superparamagnetic iron oxide nanoparticles by microwave irradiation, *J. Appl. Phys.* 97 (2005) 105101.
- [17] M. Kacenska, O. Kaman, J. Kotek, L. Falteisek, J. Cerny, D. Jirak, V. Herynek, K. Zacharovova, Z. Berkova, P. Jendelova, J. Kupcik, E. Pollert, P. Veverka, I. Lukes, Dual imaging probes for magnetic resonance imaging and fluorescence microscopy based on perovskite manganite nanoparticles, *J. Mater. Chem.* 21 (2011) 157.
- [18] K.R. Bhayani, S.N. Kale, S. Arora, R. Rajagopal, H. Mangain, R. Kaul-Ghanekar, D.C. Kundaliya, S.D. Kulkarni, R. Pasricha, S.D. Dhole, S.B. Ogale, K.M. Paknikar, Protein and polymer immobilized  $\text{La}_{0.7}\text{Sr}_{0.3}\text{MnO}_3$  nanoparticles for possible biomedical applications, *Nanotechnology* 18 (2007) 345101.
- [19] R. Rajagopal, J. Mona, S.N. Kale, T. Bala, R. Pasricha, P. Poddar, M. Sastry, B.L.V. Prasad, D.C. Kundaliya, S.B. S. B. Ogale,  $\text{La}_{0.7}\text{Sr}_{0.3}\text{MnO}_3$  nanoparticles coated with fatty amine, *Appl. Phys. Lett.* 89 (2006) 023107.
- [20] A. Giri, A. Makhil, B. Ghosh, A.K. Raychaudhuri, S.K. Pal, Functionalization of manganite nanoparticles and their interaction with biologically relevant small ligands: Picosecond time-resolved FRET studies, *Nanoscale* 2 (2010) 2704.
- [21] A. Giri, N. Goswami, M.S. Bootharaju, P.L. Xavier, R. John, N.T.K. Thanh, T. Pradeep, B. Ghosh, A.K. Raychaudhuri, S.K. Pal, Emergence of multicolor photoluminescence in  $\text{La}_{0.67}\text{Sr}_{0.33}\text{MnO}_3$  nanoparticles, *J. Phys. Chem. C* 116 (2012) 25623.
- [22] M.E. Bordini, L.A. Willis, T.L. Riechel, D.T. Sawyer, Electrochemical and spectroscopic studies of manganese(II), -(III), and -(IV) gluconate complexes. 1. Formulas and oxidation-reduction stoichiometry, *Inorg. Chem.* 15 (1976) 1538.
- [23] M. Matzapetakis, N. Karligiano, A. Bino, M. Dakanali, C.P. Raptopoulou, V. Tangoulis, A. Terzis, J. Giapintzakis, A. Salifoglou, Manganese citrate chemistry:

Syntheses, spectroscopic studies, and structural characterizations of novel mononuclear, water-soluble manganese citrate complexes, *Inorg. Chem.* 39 (2000) 4044.

[24] F. Aguado, F. Rodriguez, P. Núñez, Pressure-induced Jahn-Teller suppression and simultaneous high-spin to low-spin transition in the layered perovskite CsMnF<sub>4</sub>, *Phys. Rev. B: Condens. Matter* 76 (2007) 094417.

[25] T. Takashima, K. Hashimoto, R. Nakamura, Mechanisms of pH-dependent activity for water oxidation to molecular oxygen by MnO<sub>2</sub> electrocatalysts, *J. Am. Chem. Soc.* 134 (2011) 1519.

[26] G.L. Miessler, D.A. Tarr, Inorganic chemistry, 3rd ed., Prentice-Hall, Englewood Cliffs, NJ 2004.

[27] A. Topolski, Insight into the degradation of a manganese(III)-citrate complex in aqueous solutions, *Chem. Pap.* 65 (2011) 389.

[28] A.T.R. Williams, S.A. Winfield, J.N. Miller, Relative fluorescence quantum yields using a computer-controlled luminescence spectrometer, *Analyst* 108 (1983) 1067.

[29] Y.F. Lee, J.R. Kirchhoff, Absorption and luminescence spectroelectrochemical characterization of a highly luminescent rhenium(II) complex, *J. Am. Chem. Soc.* 116 (1994) 3599.

[30] F. Li, L.H. Zhang, D.G. Evans, X. Duan, Structure and surface chemistry of manganese-doped copper-based mixed metal oxides derived from layered double hydroxides, *Colloids Surf. A* 244 (2004) 169.

[31] A. Sandell, A.J. Jaworowski, The Mn 2p core-level photoelectron spectrum of Pd-Mn bimetallic systems on Pd(100), *J. Electron Spectrosc. Relat. Phenom.* 135 (2004) 7.

[32] N.M. Guindy, E.K. Basily, N.E. Milad, A kinetic study on the reduction of manganese III in presence of citric acid, *J. Appl. Chem. Biotech.* 24 (1974) 407.

[33] M. Cantoni, D. Petti, R. Bertacco, I. Pallecchi, D. Marre, G. Colizzi, A. Filippetti, V. Fiorentini, Band alignment at Cu<sub>2</sub>O/La<sub>0.7</sub>Sr<sub>0.3</sub>MnO<sub>3</sub> interface: A combined experimental-theoretical determination, *Appl. Phys. Lett.* 97 (2010) 032115.

[34] T.Z. Ding, J. Li, Q.G. Qi, B.H. Ji, J. Liu, C.Z. Zhang, XPS studies on rare earth oxide LSCO/YSZ electrodes, *J. Rare Earth.* 21 (2003) 453.

[35] A.K. Samal, T. Pradeep, Lanthanum telluride nanowires: Formation, doping, and raman studies, *J. Phys. Chem. C* 114 (2010) 5871.

- [36] G. Zou, X. You, P. He, Patterning of nanocrystalline  $\text{La}_{0.7}\text{Sr}_{0.3}\text{MnO}_3$  thin films prepared by sol-gel process combined with soft lithography, *Mat. Lett.* 62 (2008) 1785.
- [37] M.S. Bootharaju, T. Pradeep, Uptake of toxic metal ions from water by naked and monolayer protected silver nanoparticles: An X-ray photoelectron spectroscopic investigation, *J. Phys. Chem. C* 114 (2010) 8328.
- [38] S. Liang, F. Teng, G. Bulgan, Y. Zhu, Effect of Jahn-Teller distortion in  $\text{La}_{0.5}\text{Sr}_{0.5}\text{MnO}_3$  cubes and nanoparticles on the catalytic oxidation of CO and  $\text{CH}_4$ , *J. Phys. Chem. C* 111 (2007) 16742.
- [39] V. Ramakrishnan, J.M.T. Maroor, IR and Raman studies of gel grown manganese tartrate, *Infra. Phys.* 28 (1988) 201.
- [40] N. Kaneko, M. Kaneko, H. Takahashi, Infrared and Raman spectra and vibrational assignment of some metal tartrates, *Spectrochim. Acta Mol.* 40 (1984) 33.
- [41] J.M.D. Coey, M. Viret, S. von Molnár, Mixed-valence manganites, *Adv. Phys.* 48 (1999) 167.
- [42] A. Verma, F. Stellacci, Effect of surface properties on nanoparticle-cell interactions, *Small* 6 (2010) 12.
- [43] S. Daengsakul, C. Thomas, I. Thomas, C. Mongkolkachit, S. Siri, V. Amornkitbamrung, S. Maensiri, Magnetic and cytotoxicity properties of  $\text{La}_{(1-x)}\text{Sr}_{(x)}\text{MnO}_3$  ( $0 \leq x \leq 0.5$ ) nanoparticles prepared by a simple thermal hydro-decomposition, *Nanoscale Res. Lett.* 4 (2009) 839.

## Chapter 5

# Synthesis of Biocompatible Nanoparticles with Novel Optical & Magnetic Properties and their Characterization

### 5.1. Introduction

Over the past decade, magnetic nanoparticles (NPs) of the 3d transition metal oxides have witnessed enormous interest due to their potential applications in various fields ranging from catalysis [1, 2], energy storage [3] and magnetic data storage [4] to drug delivery and biomedical imaging [5-7]. In particular, colloidal metal-oxide materials fabricated on nanoscale can exhibit better optical, magnetic, thermal and electrical properties than bulk materials [8-11]. Therefore, long-term endeavors have been focused on the morphology controllable synthesis and functionalization of nanocrystals for their advanced physicochemical properties and technological applications [12, 13].

As an important functional metal oxide, manganese oxides have attracted considerable attention because of their potential applications in diverse areas, including catalysis [14], rechargeable lithium ion batteries [15, 16], molecular adsorption, gas sensing and in magnetics [17, 18]. Among them,  $Mn_3O_4$  has been demonstrated to be one of the most inexpensive and earth-abundant catalyst exhibited excellent bifunctional oxygen electrode activity [19] (similar to those of best known precious metal catalysts: Platinum, Ruthenium, and Iridium), also an active catalyst for the oxidation of methane and carbon monoxide [20, 21]. Most recently, hollow  $Mn_3O_4$  NPs have been utilized as positive MRI contrast agent (exploiting their room temperature paramagnetism) with enhanced relaxivity attributed to an increased water-accessible surface area and the flexibility of further functional surface modifications [22, 23]. However, despite recent advancement, to date, study of any synthesis/surface modification technique for achieving  $Mn_3O_4$  NPs having intrinsic photoluminescence and/or room temperature ferromagnetism is sparse in the existing literature. In particular, the effects of capping ligands, especially how they regulate the surface properties of  $Mn_3O_4$  NPs and subsequent appearance of novel optical/magnetic properties, have not been studied thoroughly. Besides being of

fundamental scientific interest, such an understanding is important for optimizing nanoparticles properties. So, it would be of great interest to develop approaches to control surface chemistry for better understanding the origin of surface-induced optical and magnetic properties, as subtle differences in ligand functional groups or the structural position of the functional groups can dramatically change the optical/magnetic responses.

In this chapter, we have used a procedure published by Lei et al [24] to synthesize  $\text{Mn}_3\text{O}_4$  NPs and carried out a series of surface modification studies by systematic variation of the nature of surface-protecting ligands. We define how these NP-ligand interactions modify the electronic properties of the NPs that ultimately govern multiple PL starting from blue, cyan and green to near IR under mild conditions. Most importantly, in a logical variation of the functional groups and their structural position, we have identified the necessary and sufficient structural requirement of the ligands, to induce such novel optical/magnetic responses from the NPs upon functionalization. Although, all the ligands used in our study offer ligand-to-metal charge transfer transitions (LMCT), the presence of  $\alpha$ -hydroxy carboxylate moiety in the capping ligand appears to be necessary to activate the Jahn-Teller (J-T) splitting of  $\text{Mn}^{3+}$  ions in the NPs which corresponds to the d-d transitions and plays the deciding role to induce the optical outcomes. Among all the ligands, we have studied tartrate (having two  $\alpha$ -hydroxy carboxylate moiety) functionalized  $\text{Mn}_3\text{O}_4$  NPs (will be referred as T- $\text{Mn}_3\text{O}_4$  NPs henceforth) in details as the optical responses induced by tartrate have been optimal. Magnetic properties of the  $\text{Mn}_3\text{O}_4$  NPs have also been found to be strongly ligand-dependent. We have shown that the presence of a carboxylate group in the surface coordinated ligands is sufficient to activate room temperature ferromagnetism. Moreover, a relationship between the nature of the surface bound ligands and magnetic responses of the NPs upon functionalization has been demonstrated employing crystal field splitting energy (CFSE) of the surface  $\text{Mn}^{3+}$  ions. Uses of  $\text{Mn}_3\text{O}_4$  nanocrystals having different morphologies as a catalyst for the degradation of cationic organic dye have been reported recently; however, in all cases the degradation rate is very slow [25, 26]. We have observed that our surface modified T- $\text{Mn}_3\text{O}_4$  NPs have better photocatalytic activity towards a model cationic organic dye (methylene blue) compared to other existing reports, thus, we infer that the increased surface reactivity and PL of T- $\text{Mn}_3\text{O}_4$  NPs plays an important role in enhancing the catalytic activity.

## 5.2. Result and Discussion

### 5.2.1. Rational Surface Modification of $\text{Mn}_3\text{O}_4$ Nanoparticles to Induce Multiple Photoluminescence and Room Temperature Ferromagnetism [27]:

Functionalization of  $\text{Mn}_3\text{O}_4$  NPs with small organic ligands causes significant changes to their surface electronic structures. Before intentional variation of the ligands, we have examined the UV-vis electronic absorption pattern of the as-prepared  $\text{Mn}_3\text{O}_4$  NPs alone. However, as revealed from Figure 5.1, it has no such characteristic absorption signature in the UV-vis region. The absorption spectra recorded in Figure 5.2 for ligand functionalized  $\text{Mn}_3\text{O}_4$  NPs exhibit distinct features depending upon the types of ligand functional groups used. Figure 5.2a-f represent the absorption spectra of functionalized  $\text{Mn}_3\text{O}_4$  NPs where -OH (hydroxyl group of glycerol), -OH & - $\text{NH}_2$  (hydroxyl & amine groups of ethanol amine), - $\text{NH}_2$  (amine group of guanidine), - $\text{COO}^-$  (carboxylate group of succinate), - $\text{COO}^-$  & - $\text{NH}_2$  (carboxylate & amine groups of glycine), and - $\text{COO}^-$  & -SH (carboxylate & thiol groups of thioglycolate) functional groups of the ligands have been chosen to functionalize the NPs. In all cases, a characteristic absorption band (marked by arrows) between 300 and 360 nm has been observed. We assume that this high energy absorption band is the result of the interaction between the ligand functional group and the  $\text{Mn}^{2+}/\text{Mn}^{3+}$  onto the NPs surface, therefore assigned as LMCT band. However, inclusion of a -OH group at the  $\alpha$  position with respect to - $\text{COO}^-$  i.e. in case of lactate- $\text{Mn}_3\text{O}_4$  (Figure 5.2g and 5.3), the UV-vis absorption spectrum results distinctly different features at the low energy region.

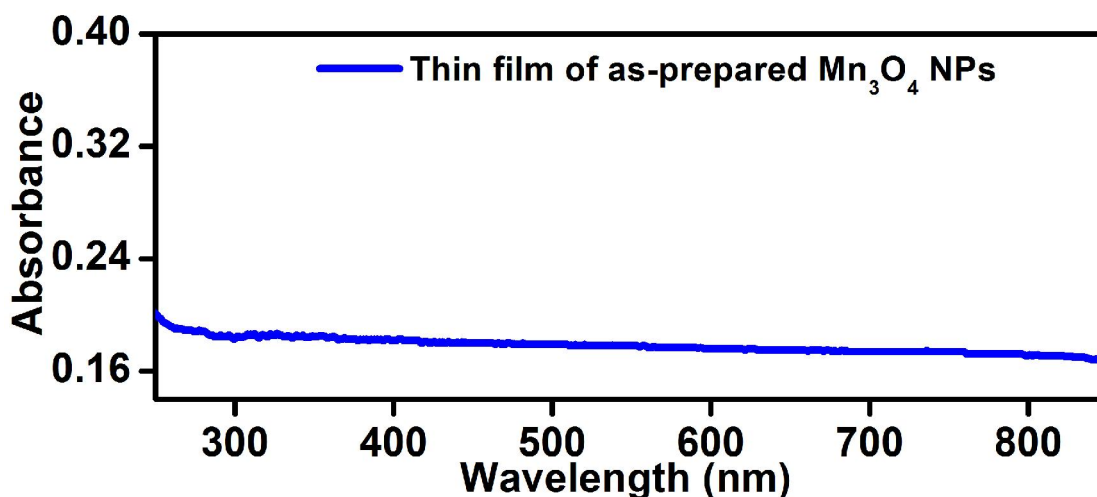
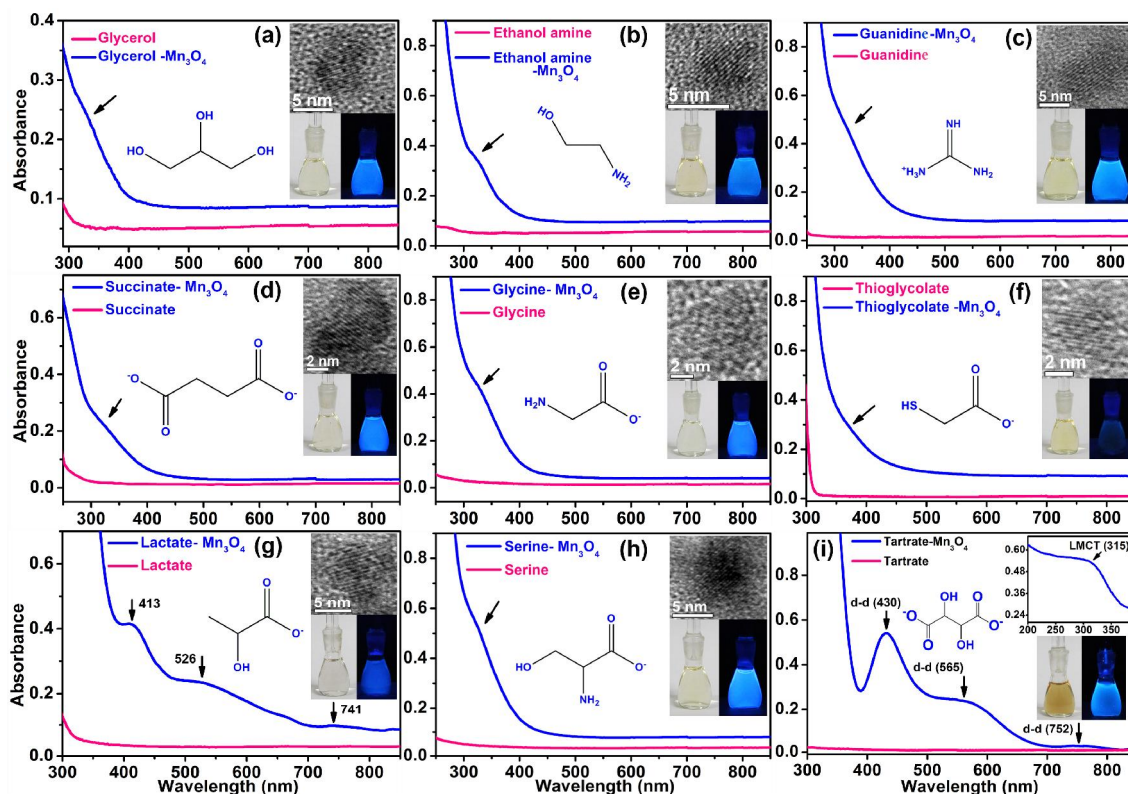


Figure 5.1. UV-vis absorption spectrum of as- prepared  $\text{Mn}_3\text{O}_4$  NPs thin film on quartz plate.



**Figure 5.2.** (a)-(i) Represents the UV-vis absorption spectra of ligand functionalized-Mn<sub>3</sub>O<sub>4</sub> NPs in aqueous solution at pH~7. Different combinations of ligand functional groups have been employed in order to activate the Jahn-Teller (J-T) splitting of Mn<sup>3+</sup> ions in the NPs surface and to bring out optimal optical responses from the functionalized NPs. (a) -OH (hydroxyl) group of glycerol (b) -OH & -NH<sub>2</sub> (hydroxyl & amine) groups of ethanol amine, (c) -NH<sub>2</sub> group of guanidine, (d) -COO<sup>-</sup> (carboxylate) group of succinate, (e) -COO<sup>-</sup> & -NH<sub>2</sub> groups of glycine, (f) -COO<sup>-</sup> & -SH (carboxylate & thiol) groups of thioglycolate, (g) -COO<sup>-</sup> & -OH (at  $\alpha$  position) groups of lactate, (h) -COO<sup>-</sup> & -OH (at  $\alpha$  position) groups of serine and (i) -COO<sup>-</sup> & -OH (two  $\alpha$  hydroxyl groups) groups of tartrate have been used respectively, to functionalize the as-prepared Mn<sub>3</sub>O<sub>4</sub> NPs. Upper inset of Figure (a)-(h) show the corresponding HRTEM image of various ligand functionalized Mn<sub>3</sub>O<sub>4</sub> NPs. Photographs under visible (left) and UV light (right) of various ligand functionalized Mn<sub>3</sub>O<sub>4</sub> NPs have been shown in the lower inset.

Even more interestingly, on shifting the structural position of the -OH group from  $\alpha$  to  $\beta$  with respect to -COO<sup>-</sup> i.e. in case of serine-Mn<sub>3</sub>O<sub>4</sub> (although serine contains a  $\alpha$  NH<sub>2</sub> group, however, results of glycine-Mn<sub>3</sub>O<sub>4</sub> could be considered as control study), those low energy UV-vis bands vanishes. The observation clearly indicates that the origin of distinct absorption features is a special case only for  $\alpha$ -hydroxy carboxylate (like lactate) moiety containing ligand functionalized Mn<sub>3</sub>O<sub>4</sub> NPs. To further corroborate this phenomenon, we have employed tartrate ligands, having two  $\alpha$ -hydroxy carboxylate groups, as a capping

ligand. Akin to lactate-Mn<sub>3</sub>O<sub>4</sub>, T-Mn<sub>3</sub>O<sub>4</sub> possesses LMCT band as well as distinct even more pronounced absorption features at the low energy region. Thus, from the above investigation we can infer that the presence of  $\alpha$ -hydroxy carboxylate moiety in the surface coordinating ligand is necessary to activate the observed distinct absorption features (detail identification of the absorption bands is discussed later in the text). Upper insets of Figure 5.2a-h represent high resolution transmission electron microscopic (HRTEM) images of the corresponding ligand functionalized Mn<sub>3</sub>O<sub>4</sub> NPs showing their tentative diameters within 3-5 nm. Lower insets of Figure 5.2a-i represent the photographs of various ligands functionalized Mn<sub>3</sub>O<sub>4</sub> NPs under visible (left) and under UV light (right), respectively. As evident from the photographs, except thioglycolate-Mn<sub>3</sub>O<sub>4</sub> and lactate-Mn<sub>3</sub>O<sub>4</sub> NPs, other ligand functionalized NPs exhibit very bright photoluminescence under UV light. Considering the optical responses obtained from T-Mn<sub>3</sub>O<sub>4</sub> NPs as optimal, we have investigated only T-Mn<sub>3</sub>O<sub>4</sub> NPs in detail in order to gain insights of the origin of these distinct absorption characteristics, bright PL under UV light and also the effect of further surface modification.

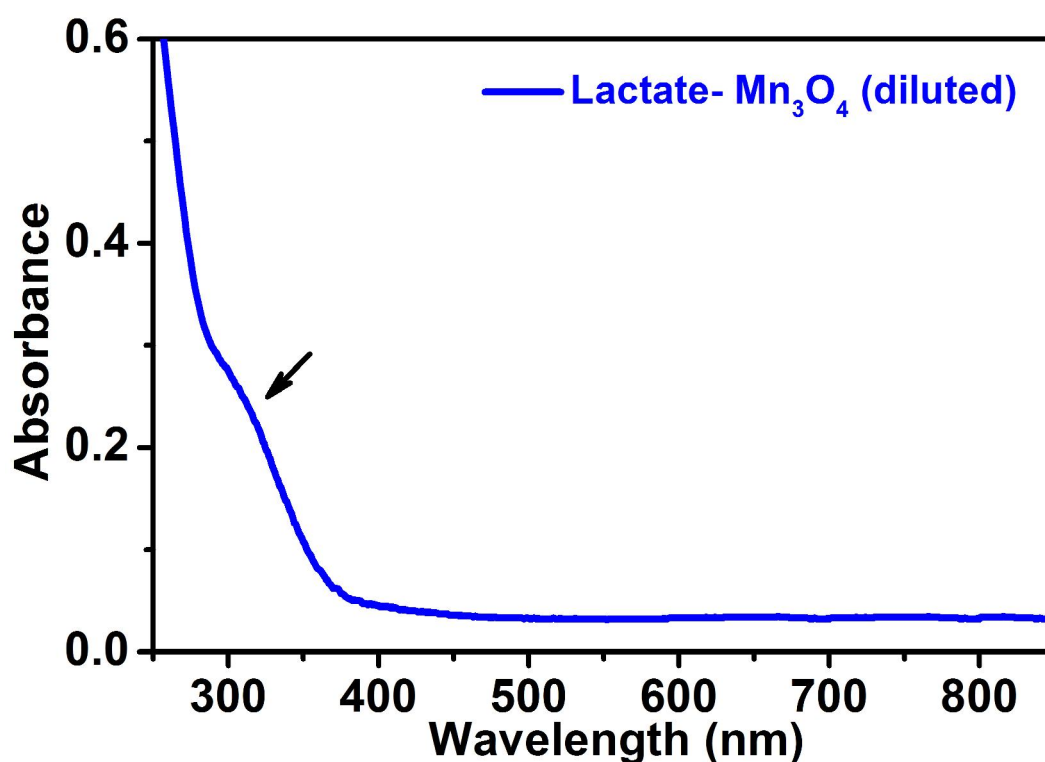


**Figure 5.3.** UV-vis absorption spectrum of diluted solution of Lactate-Mn<sub>3</sub>O<sub>4</sub> NPs.

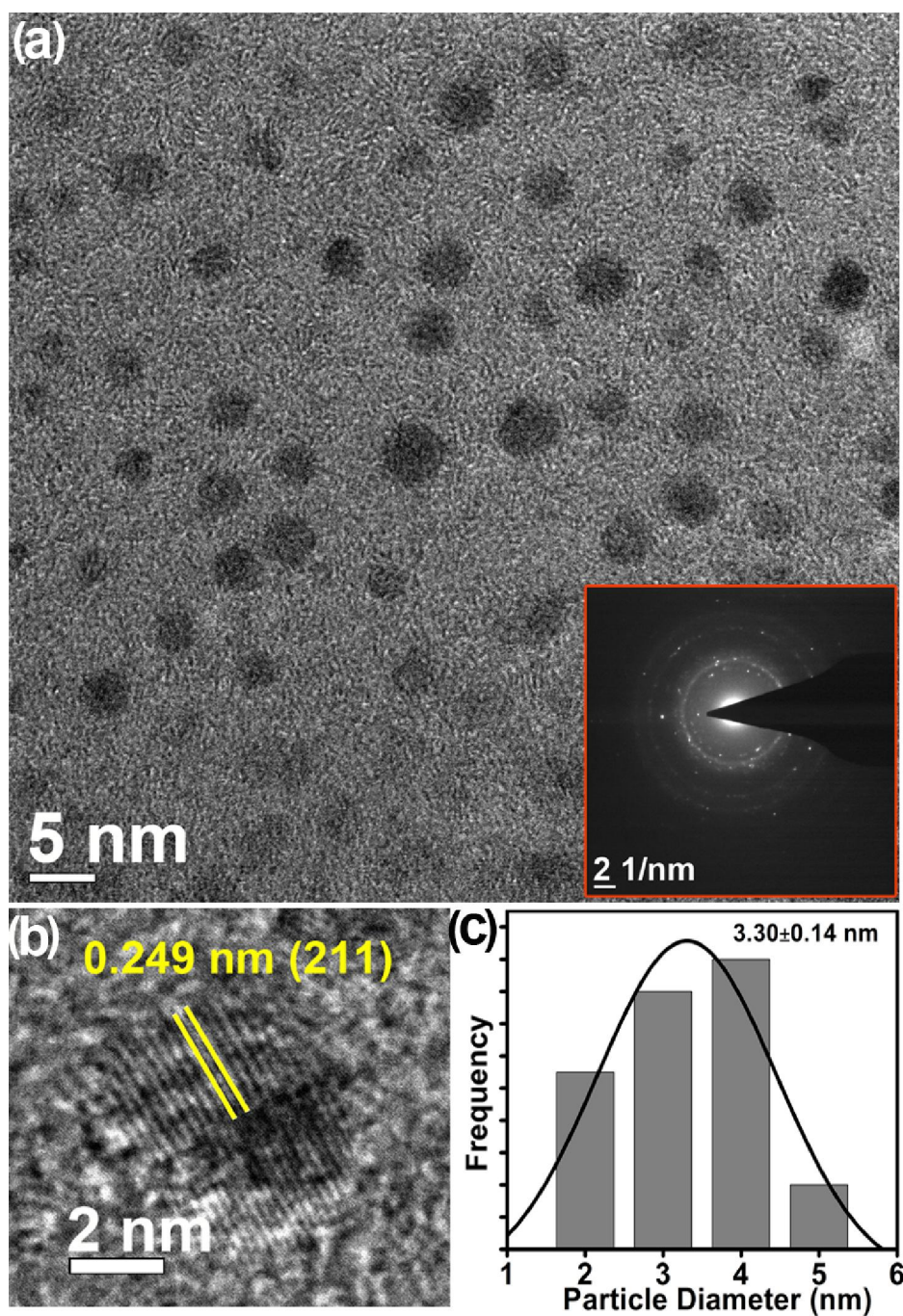


**Figure 5.4.** (a) TEM image of T-Mn<sub>3</sub>O<sub>4</sub> NPs. Inset shows the selective area electron diffraction (SAED) pattern of the T-Mn<sub>3</sub>O<sub>4</sub> NPs. (b) HRTEM image of the crystalline structure of T-Mn<sub>3</sub>O<sub>4</sub> NPs. (c) Size distribution of the T-Mn<sub>3</sub>O<sub>4</sub> NPs.

TEM study has been carried out in order to characterize the water soluble T-Mn<sub>3</sub>O<sub>4</sub> NPs in details and also to substantiate the functionalization process. As shown in Figure

5.4a, T-Mn<sub>3</sub>O<sub>4</sub> NPs have a broad size distribution (1.5-5.5 nm) with an average diameter of 3.30±0.14 nm (Figure 5.4c) and nearly spherical in shape. The corresponding HRTEM image (Figure 5.4b) confirms the crystallinity of the NPs. The interplanar distance between the fringes is about 0.249 nm which corresponds to the distance between (211) planes of Mn<sub>3</sub>O<sub>4</sub> tetragonal crystal lattice. Selective area electron diffraction (SAED) pattern (inset of Figure 5.4a) also indicates the crystalline structure of the NPs. Energy dispersive X-ray (EDX) spectroscopic analysis of T-Mn<sub>3</sub>O<sub>4</sub> NPs (Figure 5.5) has confirmed that the crystallites consist of solely manganese and oxygen.

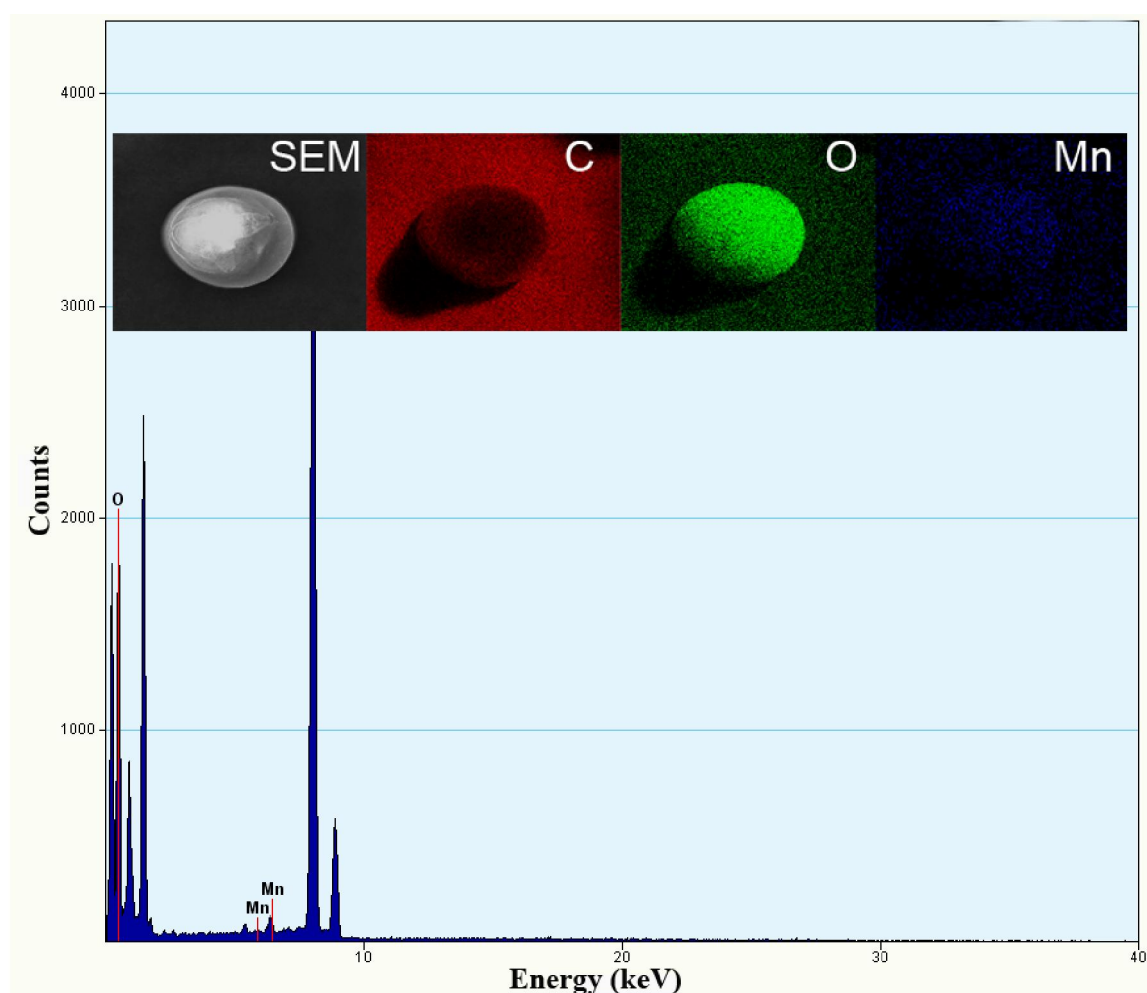


**Figure 5.5.** The EDX spectrum of T-Mn<sub>3</sub>O<sub>4</sub> NPs shows the elemental composition of the NPs. Inset shows the SEM image of the T-Mn<sub>3</sub>O<sub>4</sub> NPs sample. EDX maps of C K, O K, and Mn L lines are also shown in the inset.



**Figure 5.6.** Shows the fluorescence microscopic images of powder as-prepared  $\text{Mn}_3\text{O}_4$  NPs under irradiation of white light (I, bright field) and light of two different wavelengths of 365 (II) and 436 nm (III), respectively.

In Figure 5.2i, the UV-vis absorption spectra of T- $\text{Mn}_3\text{O}_4$  NPs (at pH  $\sim$ 7) exhibits two absorption peaks at 315 (shown in the inset) and 430 nm, a shoulder descending into lower energies around 565 nm and a broad band at 752 nm. The observed peak at 315 nm could be assigned to the possible high energy LMCT processes involving tartrate- $\text{Mn}^{2+}/\text{Mn}^{3+}$  interactions [28]. Other bands at 430, 565 and 752 nm are attributed to d-d transitions of  $\text{Mn}^{3+}$  in T- $\text{Mn}_3\text{O}_4$  NPs, as the degeneracy of  $5E_g$  ground state term of  $d^4$  ( $\text{Mn}^{3+}$ ) in high-spin octahedral environment has been lifted by the J-T effect, that leads to the observed bands for the transitions of  $5B_{1g} \rightarrow 5E_g$ ,  $5B_{1g} \rightarrow 5B_{2g}$  and  $5B_{1g} \rightarrow 5A_{1g}$ , respectively [29, 30]. In case of as-prepared T- $\text{Mn}_3\text{O}_4$  NPs (at pH  $\sim$ 7), LMCT excited state has been observed to be strongly photoluminescent, whereas, PL from d-d excited states have been found considerably weak. Thus, in order to make d-d excited states highly photoluminescent, we have heat-treated as prepared T- $\text{Mn}_3\text{O}_4$  NPs at pH  $\sim$ 12 and 70  $^\circ\text{C}$  for 12 hrs (details in experimental section). As evident from Figure 5.7a, the UV-vis absorption spectrum of heat treated T- $\text{Mn}_3\text{O}_4$  NPs changes from the initial spectrum of T- $\text{Mn}_3\text{O}_4$  NPs (Figure 5.2i). Specifically, the peak at 430 nm and lower energy shoulder at 565 nm (both originate due to d-d transitions involving  $\text{Mn}^{3+}$ ) are significantly perturbed and blue shifted to 385 and 440 nm, respectively (justification later in the text). However, the LMCT band at 315 nm and another d-d band at 758 nm remain almost unaffected. Inset of Figure 3a shows the fluorescence microscopic images of powder containing T- $\text{Mn}_3\text{O}_4$  NPs (after treatment) under irradiation of white light (bright field, I) and light of two different wavelengths (II-365 nm and III-436 nm), respectively. Multi-color PL arising from different excitation of the NPs are clearly evident from the photographs. Figure 5.6 shows the fluorescence microscopic images of powder consisting of as-prepared  $\text{Mn}_3\text{O}_4$

NPs under identical conditions, showing no such PL. Figure 5.7b shows the normalized PL spectra of T-Mn<sub>3</sub>O<sub>4</sub> NPs at room temperature and pH ~12. Multiple PL of T-Mn<sub>3</sub>O<sub>4</sub> NPs starting from blue, cyan, green to near-infrared region (PL maximum at 417, 473, 515 and 834 nm) of the spectra against excitation at four different wavelengths (315, 370, 440 and 760 nm, respectively) are clearly evident from the figure. In the excitation spectra (Figure 5.7c) of T-Mn<sub>3</sub>O<sub>4</sub> NPs at their respective PL maxima, the observed peaks/bands have a direct correlation with the absorption peaks/bands involving LMCT and d-d transitions (Figure 5.7a).

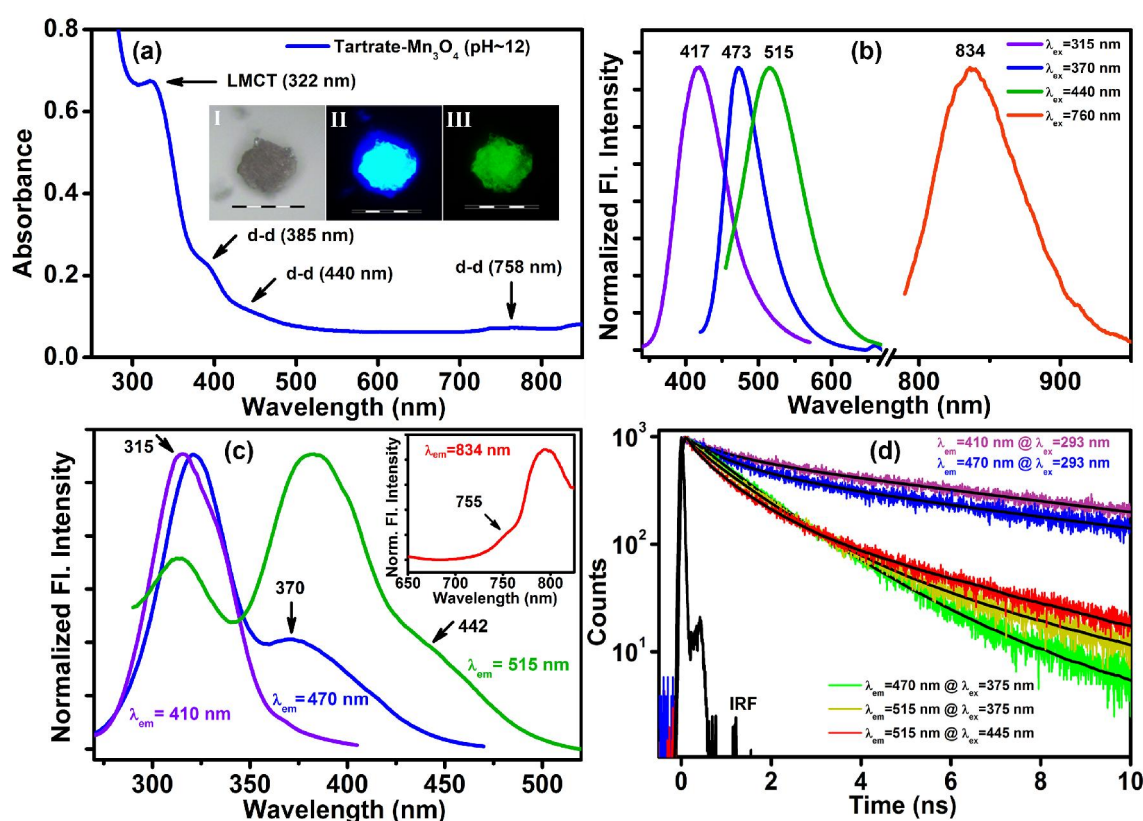


**Figure 5.7.** (a) UV-vis absorption spectrum of T-Mn<sub>3</sub>O<sub>4</sub> NPs after treatment (at pH ~12 and 70 °C for 12 hrs). Inset shows the fluorescence microscopic images of the same under irradiation of white light (bright field, I) and light of two different wavelengths 365 (II) and 436 (III) nm. Scale bars in the images are of 500  $\mu$ m. (b) Normalized steady-state PL spectra collected from T-Mn<sub>3</sub>O<sub>4</sub> NPs with four different excitation wavelengths of 315, 370, 440 and 760 nm at pH~12. (c) Excitation spectra of T-Mn<sub>3</sub>O<sub>4</sub> NPs at different PL maxima of 410, 470, 515 and 834 nm. (d) Picosecond-resolved PL transients of T-Mn<sub>3</sub>O<sub>4</sub> NPs in water measured at emission wavelengths of 410, 470 and 515 nm upon excitation with excitation source of 293, 375 and 445 nm wavelengths.

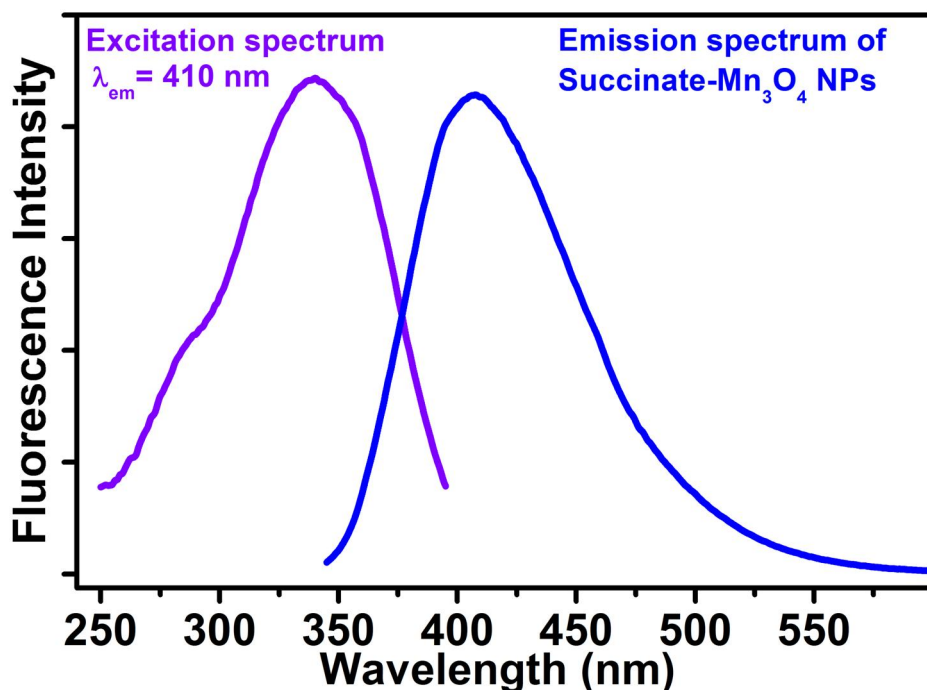


**Figure 5.8.** Steady-state excitation and PL spectra ( $\lambda_{\text{ex}}=330$  nm) collected from Succinate- $\text{Mn}_3\text{O}_4$  NPs.

Thus, the PL as shown in Figure 5.7b may be assigned to originate predominantly from the LMCT [tartrate  $\rightarrow$   $\text{Mn}^{3+}$ ] excited states and ligand field excited states of the metal ( $\text{Mn}^{3+}$ ) d orbitals. PL from either an intraligand or metal to ligand charge-transfer (MLCT) excited states are considered unlikely. In case of other ligand functionalized  $\text{Mn}_3\text{O}_4$  NPs having solely LMCT absorption band e.g. succinate- $\text{Mn}_3\text{O}_4$ , single PL with a maximum ( $\lambda_{\text{max}}$ ) around 410 nm has been observed (Figure 5.8). PL quantum yields (QY) of the T- $\text{Mn}_3\text{O}_4$  NPs at pH~12, have calculated by using the comparative method of Williams *et al.*[31], which involves the use of well characterized standard samples with known QY values. PL QY of 4.20% (for 417 nm PL), 2.88% (for 473 nm PL), 0.54% (for 515 nm PL) and 0.0018% (for 834 nm PL) were obtained relative to the standards 2-amino-purine (2AP), 4', 6-diamidino-2-phenylindole (DAPI), Hoechst (H33258) and 2-[7-[1,3-dihydro-1,1-dimethyl-3-(4-sulfobutyl)-2H-benz[e]indol-2-ylidene]-1,3,5-heptatrienyl] 1,1-dimethyl-3-(4-sulfobutyl)-1H benz[e]indolium hydroxide, inner salt, sodium salt (IR-125), respectively. Except thioglycolate- $\text{Mn}_3\text{O}_4$  and lactate- $\text{Mn}_3\text{O}_4$  NPs, the PL of other ligand functionalized  $\text{Mn}_3\text{O}_4$  NPs arises from LMCT excited state, exhibiting QY values between 4 to 7%.

Picosecond-resolved PL decay transients of T-Mn<sub>3</sub>O<sub>4</sub> NPs have been collected to further understand the origin of PL due to the functionalization of the NPs. Figure 5.7d represents the PL decay transients of T-Mn<sub>3</sub>O<sub>4</sub> NPs at three different PL maxima of 410, 470 and 515 nm using three different excitation sources of 293, 375 and 445 nm wavelengths, respectively. The observed differences in the excited-state lifetime of T-Mn<sub>3</sub>O<sub>4</sub> NPs at 410 nm PL compared to the lifetimes at 470 and 515 nm PL, suggest a difference in the origin of the PL. The average lifetime ( $\tau$ ) for 470 and 515 nm PL (upon excitation by 375 and 445 nm sources, respectively) have been observed to be 1.13 and 0.78 ns respectively, whereas, relatively longer  $\tau$  of 5.32 ns has been observed for 410 nm PL (Table 5.1). Moreover, distinctly different lifetime values of 470 nm PL upon excitation using 293 (4.04 ns) and 375 (1.13 ns) nm source clearly differentiate the origin of two excitation. Thus, the lifetime data and steady-state measurements clearly suggest that LMCT excited states are responsible for PL at 417 nm, whereas the J-T excited states lead to the PL maxima at 470, 515 and 834 nm.

**Table 5.1.** Lifetime values of picosecond time-resolved PL transients of T-Mn<sub>3</sub>O<sub>4</sub> NPs, detected at various PL maxima upon excitation at different wavelengths. The Values in parentheses represent the relative weight percentage of the time components.

System	$\lambda_{\text{ex}}$ (nm)	PL peak, $\lambda_{\text{em}}$ (nm)	$\tau_1$ (ns)	$\tau_2$ (ns)	$\tau_3$ (ns)	$\tau_{\text{av}}$ (ns)
T-Mn <sub>3</sub> O <sub>4</sub> NPs	293	410	0.26 (11)	1.05 (29)	8.37 (60)	5.32
	293	470	0.54 (29)	1.43 (29)	8.20 (42)	4.04
	375	470	0.43 (20)	1.16 (74)	3.09 (6)	1.13
	375	515	0.18 (30)	1.06 (62)	3.93 (8)	1.03
	445	515	0.18 (47)	0.87 (44)	3.58 (9)	0.78

In order to get supporting evidence regarding the origin of optical properties in T-Mn<sub>3</sub>O<sub>4</sub> NPs, XPS analysis has been carried out on Mn<sub>3</sub>O<sub>4</sub> NPs, before and after functionalization (Figure 5.9) with sodium tartrate (Figure 5.10a traces A and B respectively). In the high-resolution spectrum of Mn 2p of Mn<sub>3</sub>O<sub>4</sub> (trace A), 2p<sub>3/2</sub>-2p<sub>1/2</sub> doublet has been observed to be at 637.61 and 649.31 eV respectively, with a spin-orbit splitting (difference between the BE values of Mn 2p<sub>3/2</sub> and Mn 2p<sub>1/2</sub> levels) value of 11.70 eV, which is in good agreement with previous reports [32, 33]. The Mn 2p<sub>3/2</sub> features at 637.61 and 641.383 eV are attributed to oxides of Mn<sup>2+</sup> and Mn<sup>3+</sup> respectively [34]. In case of T-Mn<sub>3</sub>O<sub>4</sub> NPs (trace B), similar spin-orbit splitting (11.69 eV) have been observed and

in the deconvoluted Mn 2p<sub>3/2</sub> spectrum the peak at binding energy of 640.00 eV, is attributed to the +3 oxidation state of Mn, assuming the peak at 643.54 eV to be a shake up satellite. The greater intensity of the shake-up satellite peak could be due to the convolution of shake-up satellite plus the shoulder just in front of the 2p<sub>1/2</sub> peak. So, the presence of Mn<sup>3+</sup> in the T-Mn<sub>3</sub>O<sub>4</sub> NPs further supports our arguments regarding the origin of optical properties.

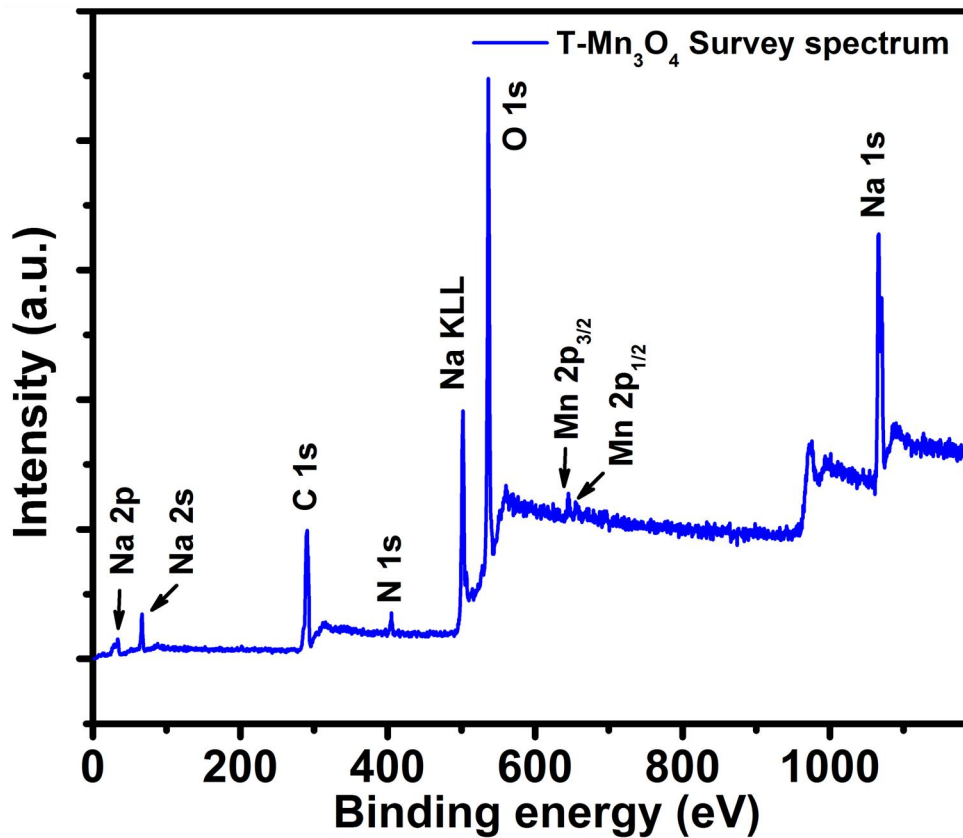


**Figure 5.9.** XPS survey spectrum of T-Mn<sub>3</sub>O<sub>4</sub> NPs.

Raman spectroscopy, which is a sensitive probe to the local atomic arrangements and vibrations, has been used to investigate any structural perturbation of Mn<sub>3</sub>O<sub>4</sub> NPs upon their functionalization with tartrate. As evident from Figure 5.10b, we have observed a substantial perturbation of the main characteristic Raman peak (at 650 cm<sup>-1</sup>, represents the Mn-O breathing vibration of divalent manganese ions in tetrahedral coordination [35]) of

Mn<sub>3</sub>O<sub>4</sub> NPs [36] as a result of tartrate functionalization. Thus, the drastic perturbation of symmetric stretching of tetragonal Mn<sub>3</sub>O<sub>4</sub> structure (corresponding to 650 cm<sup>-1</sup> peak [37]) provides a strong physical basis for the origin of novel optical properties of the NPs upon functionalization. Similar perturbation of 650 cm<sup>-1</sup> peak in case of glycerol-Mn<sub>3</sub>O<sub>4</sub> NPs further indicates that the decrease of the Raman peak has not been originated from J-T splitting rather is the outcome of ligand functionalization.

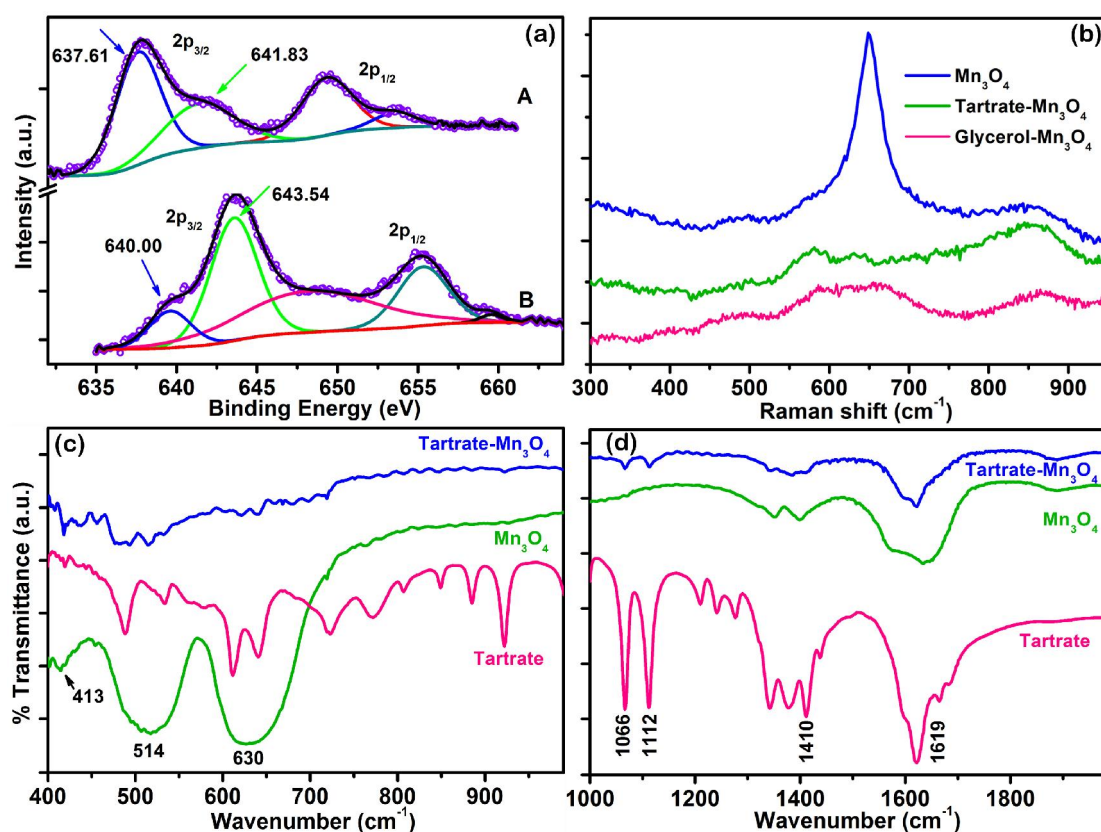


**Figure 5.10.** (a) XPS spectra of Mn 2p region for Mn<sub>3</sub>O<sub>4</sub> NPs (trace A) and T-Mn<sub>3</sub>O<sub>4</sub> NPs (trace B). (b) Raman spectra of as prepared Mn<sub>3</sub>O<sub>4</sub>, glycerol-Mn<sub>3</sub>O<sub>4</sub> and T-Mn<sub>3</sub>O<sub>4</sub> NPs. (c,d) FTIR spectra of sodium tartrate, T-Mn<sub>3</sub>O<sub>4</sub> and as prepared Mn<sub>3</sub>O<sub>4</sub> NPs recorded with a KBr pellet.

To obtain direct evidence of the covalent functionalization of Mn<sub>3</sub>O<sub>4</sub> NPs with tartrate ligands, FTIR measurements have been performed on both as-prepared and tartrate functionalized Mn<sub>3</sub>O<sub>4</sub> NPs along with the tartrate itself. As shown in Figure 5.10c, bare as-prepared Mn<sub>3</sub>O<sub>4</sub> NPs exhibit three characteristic bands (in the range of 400–1000 cm<sup>-1</sup>) at 630, 514 and 413 cm<sup>-1</sup>, which are associated with the stretching vibration of Mn-O and Mn-O-Mn bonds [38, 39]. However, these bands are not distinctly visible after

functionalization (i.e. in case T-Mn<sub>3</sub>O<sub>4</sub> NPs), suggesting a potent surface modification of the NPs has taken place upon interaction with tartrate ligands. On the other hand, in case of tartrate, the appearance of two sharp bands at 1066 and 1112 cm<sup>-1</sup> (Figure 5.10d) could be reasonably assigned to C-OH stretching modes of tartrate [40, 41]. However, substantial broadening of these two bands upon attachment with the NPs surface strongly indicates their significant interaction with the surface of the NPs. Moreover, considerable perturbation of the symmetric (1410 cm<sup>-1</sup>) and asymmetric (1619 cm<sup>-1</sup>) stretching modes of carboxylate groups (COO<sup>-</sup>) of tartrate [42] in T-Mn<sub>3</sub>O<sub>4</sub> NPs clearly confirms the covalent binding of carboxylate's oxygen with the NPs surface.

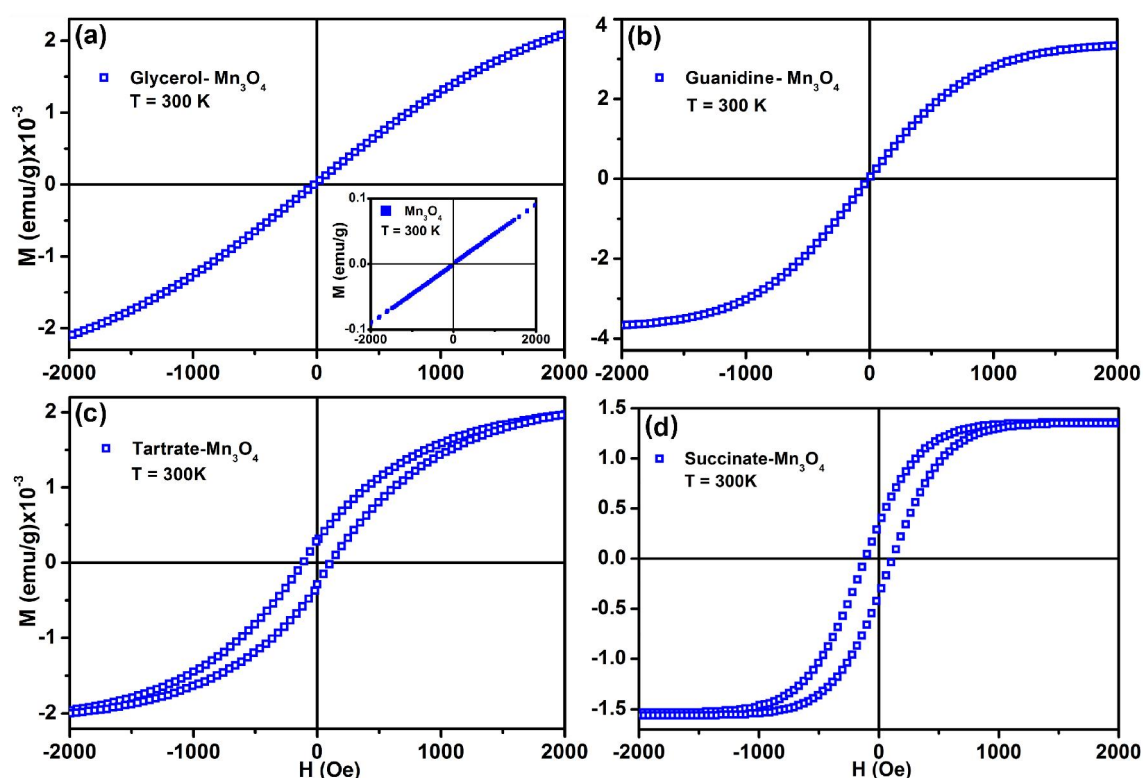


**Figure 5.11.** Field dependent magnetization (M vs H) at room temperature (300 K) (a) glycerol-Mn<sub>3</sub>O<sub>4</sub>, (b) guanidine-Mn<sub>3</sub>O<sub>4</sub>, (c) tartrate-Mn<sub>3</sub>O<sub>4</sub> and (d) succinate-Mn<sub>3</sub>O<sub>4</sub> NPs. Inset shows the same for as-prepared Mn<sub>3</sub>O<sub>4</sub> NPs. The distinct hysteresis loop observed in case of c and d confirm ferromagnetic activation of the NPs upon functionalization with carboxylate ligand.

To study the effect of surface bound ligands on the magnetic behaviour of Mn<sub>3</sub>O<sub>4</sub> NPs, we have characterized both as-prepared and ligand functionalized NPs, where the nature of the surface ligands was varied depending on their functional groups. Figure 5.11

shows the applied field dependent magnetization measurements (M-H curves) at room temperature (300 K). M-H curve (inset of Figure 5.11a) of as-prepared  $\text{Mn}_3\text{O}_4$  NPs is linear with the applied field and has no hysteresis loop at 300 K, indicating the paramagnetic behaviour of the nanocrystals, which is as expected. However, at 300 K, the M-H curve of each ligand functionalized- $\text{Mn}_3\text{O}_4$  NPs represents a distinctly different response of magnetization compared to the as-prepared NPs. Clearly, each ligand evokes different magnitude of ferromagnetism to the as-prepared  $\text{Mn}_3\text{O}_4$  NPs upon functionalization. While the room temperature ferromagnetism can be activated by functionalization with glycerol and guanidine, it can be further enhanced by succinate and tartrate (Figure 5.11 a-d). Both succinate and tartrate functionalized  $\text{Mn}_3\text{O}_4$  NPs show well-defined hysteresis loop with saturation magnetization and coercive field ( $H_C$ ) of around  $2 \times 10^{-3}$  emu/g and 105 Oe, respectively. Several investigations showed that this kind of room temperature ferromagnetism could be controlled by surface treatments of the nanocrystals, although, most of these studies have been focused mainly on transition metal doped ZnO and  $\text{TiO}_2$  nanomaterial systems [43-45]. Unfortunately, the exact origin of such room temperature ferromagnetic activation of  $\text{Mn}_3\text{O}_4$  nanocrystals is not known at the present time. However, based on the correlation between crystal field splitting energy (CFSE) of  $\text{Mn}^{3+}$  ions upon interaction with the ligand fields and the increase in coercive force from glycerol- $\text{Mn}_3\text{O}_4$  to succinate- $\text{Mn}_3\text{O}_4$  NPs, one might expect that the field strength of the functional ligands is at play. According to ligand field theory, transition metal ions having a larger d orbital splitting energy due to ligand coordination should have a smaller spin-orbit coupling [46]. Any decrease in the spin-orbit coupling of surface magnetic cations results a smaller surface magnetic anisotropy and subsequently the coercivity of the NPs will be reduced [47]. It is also well known that  $\sigma$  donor ligands result in larger CFSE than  $\pi$  donors [46]. Among the four ligands used for magnetic measurements, glycerol (having -OH group) and guanidine (- $\text{NH}_2$ ) are in the class of  $\sigma$  donor, tartrate having both  $\sigma$  donor (-OH) and  $\pi$  donor (- $\text{COO}^-$ ) properties, whereas, succinate (having only - $\text{COO}^-$ ) is a  $\pi$  donor ligand [46]. Thus, because of the higher CFSE, glycerol and guanidine functionalized  $\text{Mn}_3\text{O}_4$  NPs show no coercivity, however, tartrate and succinate functionalized NPs show coercivity of 97.5 and 109 Oe, respectively. Very recently, Zhang et al. has also described similar regulation of magnetic behavior in the case

of surface modified (using sodium bis [2-ethylhexyl] sulfosuccinate, AOT) Mn-doped ZnO nanorods, on the basis of ligand field multiplet theory and the ligand-to-metal charge transfer effects [48]. Their theoretical simulation results indicate that different surface modifications induce alteration of the  $\text{Mn}^{3+}$  ( $3d^4$ )-ligand anions p orbital hybridization strength and the density of a midgap state with strong O-2p character have been correlated to the observed ferromagnetism. Since the XPS study confirms the presence of  $\text{Mn}^{3+}$  ions at the surface of the functionalized NPs and FTIR study substantiates the strong interaction of carboxylate and hydroxyl groups with the nanoparticle surface (in case of T- $\text{Mn}_3\text{O}_4$  NPs), we anticipate that, surface modifications induce alteration of the  $\text{Mn}^{3+}$  ( $3d^4$ )-ligand anions p orbital hybridization strength can also play a crucial role in the observed ferromagnetic activation of succinate and tartrate functionalized  $\text{Mn}_3\text{O}_4$  NPs. This observation of room temperature ferromagnetism is an important enabling result and encouraging from fundamental perspective.

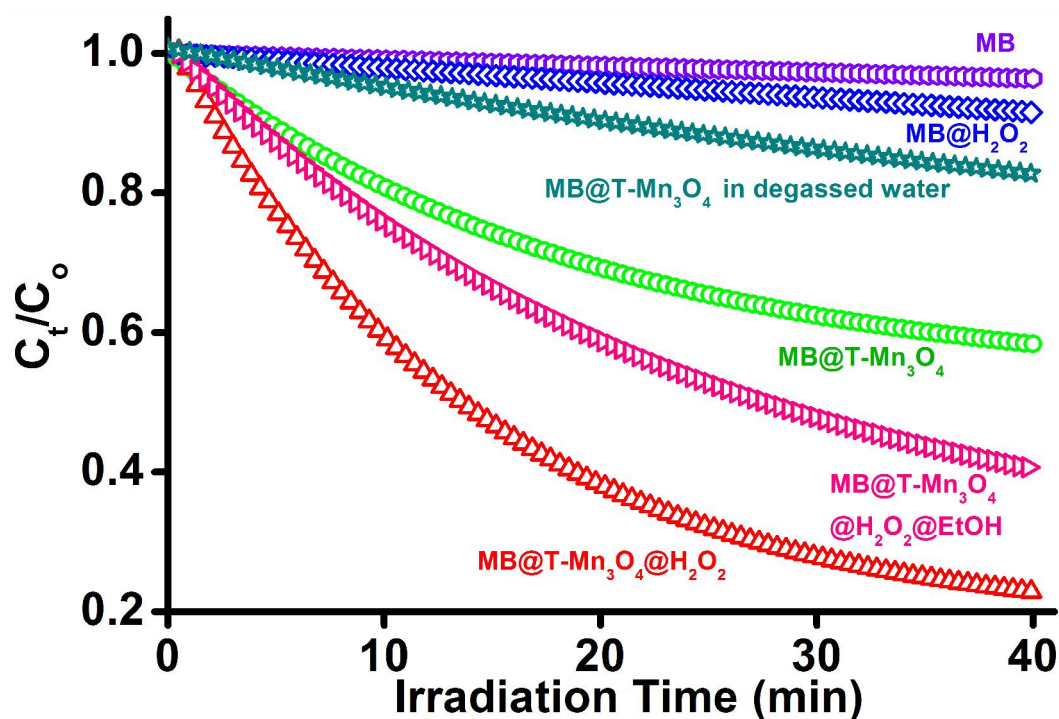


**Figure 5.12.** Plots of relative concentration ( $C_t/C_0$ ) versus time for the photodegradation of MB (monitored at 660 nm) alone and in presence of T- $\text{Mn}_3\text{O}_4$  NPs,  $\text{H}_2\text{O}_2$ , T- $\text{Mn}_3\text{O}_4$ @ $\text{H}_2\text{O}_2$  and T- $\text{Mn}_3\text{O}_4$ @ $\text{H}_2\text{O}_2$ @EtOH, are shown.

Finally, considering the growing interest of manganese oxide based nanostructures as catalyst [25]; photocatalytic activity of magneto-luminescent T-Mn<sub>3</sub>O<sub>4</sub> NPs has been evaluated by measuring the decomposition rates of methylene blue (MB) under irradiation of UV light. MB is a common cationic dye in textile industry and also known to be an excellent probe for the study of interfacial electron transfer in colloidal semiconductor systems [49]. To measure the UV light-induced chemical processes with spectroscopic precision, we have used a versatile fiber-optics based system for sensitive optical measurements in strong ambient light [50]. The characteristic absorption of MB at 660 nm has been chosen for monitoring the photocatalytic process with T-Mn<sub>3</sub>O<sub>4</sub> NPs under UV light at room temperature. We have recorded the absorption spectra of MB at 30 second intervals, using SPECTRA SUITE software supplied by Ocean Optics, and finally plotted MB absorption at 660 nm with the time of photo-irradiation. Figure 5.12 shows the relative concentration ( $C_t/C_0$ ) of MB (in absence and in presence of T-Mn<sub>3</sub>O<sub>4</sub> NPs) in solution plotted with UV irradiation time. The photodegradation curve of MB in the presence of T-Mn<sub>3</sub>O<sub>4</sub> NPs has been found to follow a first-order exponential equation with kinetic rate constant ( $k$ ) of  $5.23 \times 10^{-2} \text{ s}^{-1}$  and a total photodegradation of 48% within 40 minutes of irradiation. In photocatalytic reaction, major energy wasting step is the recombination of photo-generated electrons and holes, leading to the low quantum yield of the process. However, this recombination process is reduced as the particle size goes down and consequently better transfer of the photogenerated electrons and holes to the surface bound molecules increases the efficiency of photocatalysis [51]. Moreover, this electron-hole recombination could be prevented by adding a proper electron acceptor such as H<sub>2</sub>O<sub>2</sub> in to the system. Acting as an electron acceptor and also a source of •OH radical, H<sub>2</sub>O<sub>2</sub> increases the photocatalytic activity in both ways. We do observe this postulated fact by the addition of a small amount of H<sub>2</sub>O<sub>2</sub> (final concentration of 415  $\mu\text{M}$ ) in to the MB@T-Mn<sub>3</sub>O<sub>4</sub> reaction mixture. As observed from the figure, upon addition of H<sub>2</sub>O<sub>2</sub> the photodegradation of MB enhanced significantly (with kinetic rate constant ( $k$ ) of  $7.25 \times 10^{-2} \text{ min}^{-1}$  and total photodegradation of 85% for the same 40 minutes of irradiation). In order to confirm the involvement of •OH radicals in the photocatalytic process, we have examined the effect of •OH scavenging agent (ethanol) and oxygen free environment (achieved by 2 hours of Argon flow into the reaction mixture before UV irradiation) on the degradation process. As

shown in the figure, in both cases, reduction of photocatalytic rate have been observed, which validates the role of  $\bullet\text{OH}$  radicals in the photocatalytic process. Zhan and co-workers have recently demonstrated the degradation of methylene blue using  $\text{Mn}_3\text{O}_4$  nanocrystals at 80 °C and in presence of  $\text{H}_2\text{O}_2$ , however, in absence of  $\text{H}_2\text{O}_2$  no obvious MB degradation has been observed for up to 3 hrs [26]. Thus, we infer that the small average diameter, favorable surface functionalization (by tartrate) for cationic MB attachment and most importantly the photoluminescence of T- $\text{Mn}_3\text{O}_4$  NPs, plays the beneficial role to accelerate the photocatalytic activity of  $\text{Mn}_3\text{O}_4$  NPs.

### 5.3. Conclusion

Surface modifications of  $\text{Mn}_3\text{O}_4$  NPs with a series of small organic ligands provide a good platform for studying the effects of surface chemistry on the optical/magnetic responses of the NPs. In all cases, LMCT optical bands in the electronic spectra are present and found to be almost independent of the nature of the ligands. However, among the wide variety of ligands, only  $\alpha$ -hydroxy carboxylate moiety containing ligands can activate the Jahn-Teller (J-T) splitting of  $\text{Mn}^{3+}$  ions. Apparently, the optical response of NPs to the surface modification elucidates the quantum origins of multiple PL properties and which further corroborated by time resolved lifetime studies. Convergent evidence from XPS, FTIR and Raman analyses shows that the coordinating-capping ligand can greatly affect the surface of  $\text{Mn}_3\text{O}_4$  NPs. Moreover, the presence of a carboxylate group in the surface coordinating ligands is found to be sufficient to activate the room temperature ferromagnetism of the NPs. A correlation between the nature of the surface bound ligands and the magnetic responses of the functionalized NPs has been demonstrated employing crystal field splitting energy (CFSE) of the  $\text{Mn}^{3+}$  ions. Finally, we have evaluated the photocatalytic activity of T- $\text{Mn}_3\text{O}_4$  NPs by monitoring the degradation of an organic pollutant under UV irradiation and an enhanced photocatalytic activity of the NPs has been observed. We believe that this work represents a step forward in the rational design of multifunctional NPs and the approach developed to systematically alter surface chemistry could also be applied more generally to the investigation of other manganese oxides and various manganese doped NPs.

## References

- [1] T. Zeng, W.-W. Chen, C.M. Cirtiu, A. Moores, G. Song, C.-J. Li, Fe<sub>3</sub>O<sub>4</sub> nanoparticles: A robust and magnetically recoverable catalyst for three-component coupling of aldehyde, alkyne and amine, *Green Chem.* 12 (2010) 570.
- [2] R. Hudson, A. Riviere, C.M. Cirtiu, K.L. Luska, A. Moores, Iron-iron oxide core-shell nanoparticles are active and magnetically recyclable olefin and alkyne hydrogenation catalysts in protic and aqueous media, *Chem. Commun.* 48 (2012) 3360.
- [3] P. Simon, Y. Gogotsi, Materials for electrochemical capacitors, *Nat. Mater.* 7 (2008) 845.
- [4] T. Hyeon, Chemical synthesis of magnetic nanoparticles, *Chem. Commun.* (2003) 927.
- [5] N. Lee, T. Hyeon, Designed synthesis of uniformly sized iron oxide nanoparticles for efficient magnetic resonance imaging contrast agents, *Chem. Soc. Rev.* 41 (2012) 2575.
- [6] Q.A. Pankhurst, N.T.K. Thanh, S.K. Jones, J. Dobson, Progress in applications of magnetic nanoparticles in biomedicine, *J. Phys. D: Appl. Phys.* 42 (2009) 224001.
- [7] R. Mout, D.F. Moyano, S. Rana, V.M. Rotello, Surface functionalization of nanoparticles for nanomedicine, *Chem. Soc. Rev.* 41 (2012) 2539.
- [8] M.A. El-Sayed, Some interesting properties of metals confined in time and nanometer space of different shapes, *Acc. Chem. Res.* 34 (2001) 257.
- [9] R. Narayanan, M.A. El-Sayed, Catalysis with transition metal nanoparticles in colloidal solution: Nanoparticle shape dependence and stability, *J. Phys. Chem. B* 109 (2005) 12663.
- [10] S. Laurent, D. Forge, M. Port, A. Roch, C. Robic, L. Vander Elst, R.N. Muller, Magnetic iron oxide nanoparticles: Synthesis, stabilization, vectorization, physicochemical characterizations, and biological applications, *Chem. Rev.* 108 (2008) 2064.
- [11] M.B. Cortie, A.M. McDonagh, Synthesis and optical properties of hybrid and alloy plasmonic nanoparticles, *Chem. Rev.* 111 (2011) 3713.
- [12] E. Oh, K. Susumu, R. Goswami, H. Mattoussi, One-phase synthesis of water-soluble gold nanoparticles with control over size and surface functionalities, *Langmuir* 26 (2010) 7604.

- [13] Y. Peng, A.-W. Xu, B. Deng, M. Antonietti, H. Cölfen, Polymer-controlled crystallization of Zinc Oxide hexagonal nanorings and disks, *J. Phys. Chem. B* 110 (2006) 2988.
- [14] T. Yamashita, A. Vannice, Temperature-programmed desorption of NO adsorbed on Mn<sub>2</sub>O<sub>3</sub> and Mn<sub>3</sub>O<sub>4</sub>, *Appl. Catal., B* 13 (1997) 141.
- [15] D.K. Kim, P. Muralidharan, H.-W. Lee, R. Ruffo, Y. Yang, C.K. Chan, H. Peng, R.A. Huggins, Y. Cui, Spinel LiMn<sub>2</sub>O<sub>4</sub> nanorods as lithium ion battery cathodes, *Nano Lett.* 8 (2008) 3948.
- [16] M.M. Thackeray, Manganese oxides for lithium batteries, *Prog. Solid State Ch.* 25 (1997) 1.
- [17] W.S. Seo, H.H. Jo, K. Lee, B. Kim, S.J. Oh, J.T. Park, Size-dependent magnetic properties of colloidal Mn<sub>3</sub>O<sub>4</sub> and MnO nanoparticles, *Angew. Chem. Int. Ed.* 43 (2004) 1115.
- [18] Y.F. Shen, R.P. Zerger, R.N. DeGuzman, S.L. Suib, L. McCurdy, D.I. Potter, C.L. O'Young, Manganese oxide octahedral molecular sieves: Preparation, characterization, and applications, *Science* 260 (1993) 511.
- [19] Y. Gorlin, T.F. Jaramillo, A bifunctional nonprecious metal catalyst for oxygen reduction and water oxidation, *J. Am. Chem. Soc.* 132 (2010) 13612.
- [20] E.R. Stobbe, B.A. de Boer, J.W. Geus, The reduction and oxidation behaviour of manganese oxides, *Catal. Today* 47 (1999) 161.
- [21] R. Alizadeh, E. Jamshidi, G. Zhang, Transformation of methane to synthesis gas over metal oxides without using catalyst, *J. Nat. Gas Chem.* 18 (2009) 124.
- [22] J. Shin, R.M. Anisur, M.K. Ko, G.H. Im, J.H. Lee, I.S. Lee, Hollow manganese oxide nanoparticles as multifunctional agents for magnetic resonance imaging and drug delivery, *Angew. Chem. Int. Ed.* 48 (2009) 321.
- [23] T.-L. Ha, H.J. Kim, J. Shin, G.H. Im, J.W. Lee, H. Heo, J. Yang, C.M. Kang, Y.S. Choe, J.H. Lee, I.S. Lee, Development of target-specific multimodality imaging agent by using hollow manganese oxide nanoparticles as a platform, *Chem. Commun.* 47 (2011) 9176.

- [24] S. Lei, K. Tang, Z. Fang, H. Zheng, Ultrasonic-assisted synthesis of colloidal  $\text{Mn}_3\text{O}_4$  nanoparticles at normal temperature and pressure, *Cryst. Growth Des.* 6 (2006) 1757.
- [25] Y. Li, H. Tan, X.-Y. Yang, B. Goris, J. Verbeeck, S. Bals, P. Colson, R. Cloots, G. Van Tendeloo, B.-L. Su, Well shaped  $\text{Mn}_3\text{O}_4$  nano-octahedra with anomalous magnetic behavior and enhanced photodecomposition properties, *Small* 7 (2011) 475.
- [26] P.Q. Zhang, Y.G. Zhan, B.X. Cai, C.C. Hao, J. Wang, C.X. Liu, Z.J. Meng, Z.L. Yin, Q.Y. Chen, Shape-controlled synthesis of  $\text{Mn}_3\text{O}_4$  nanocrystals and their catalysis of the degradation of methylene blue, *Nano Res.* 3 (2010) 235.
- [27] A. Giri, N. Goswami, M. Pal, M.T. Zar Myint, S. Al-Harhi, A. Singha, B. Ghosh, J. Dutta, S.K. Pal, Rational surface modification of  $\text{Mn}_3\text{O}_4$  nanoparticles to induce multiple photoluminescence and room temperature ferromagnetism, *J. Mater. Chem. C* 1 (2013) 1885.
- [28] M.E. Bodini, L.A. Willis, T.L. Riechel, D.T. Sawyer, Electrochemical and spectroscopic studies of manganese(II), -(III), and -(IV) gluconate complexes. 1. Formulas and oxidation-reduction stoichiometry, *Inorg. Chem.* 15 (1976) 1538.
- [29] F. Aguado, F. Rodriguez, P. Núñez, Pressure-induced jahn-teller suppression and simultaneous high-spin to low-spin transition in the layered perovskite  $\text{CsMnF}_4$ , *Phys. Rev. B* 76 (2007) 094417.
- [30] M. Matzapetakis, N. Karligiano, A. Bino, M. Dakanali, C.P. Raptopoulou, V. Tangoulis, A. Terzis, J. Giapintzakis, A. Salifoglou, Manganese citrate chemistry: Syntheses, spectroscopic studies, and structural characterizations of novel mononuclear, water-soluble manganese citrate complexes, *Inorg. Chem.* 39 (2000) 4044.
- [31] A.T.R. Williams, S.A. Winfield, J.N. Miller, Relative fluorescence quantum yields using a computer-controlled luminescence spectrometer, *Analyst* 108 (1983) 1067.
- [32] J.W. Lee, A.S. Hall, J.-D. Kim, T.E. Mallouk, A facile and template-free hydrothermal synthesis of  $\text{Mn}_3\text{O}_4$  nanorods on graphene sheets for supercapacitor electrodes with long cycle stability, *Chem. Mat.* 24 (2012) 1158.
- [33] M. Salavati-Niasari, F. Davar, M. Mazaheri, Synthesis of  $\text{Mn}_3\text{O}_4$  nanoparticles by thermal decomposition of a [bis(salicylidiminato)manganese(II)] complex, *Polyhedron* 27 (2008) 3467.

- [34] F. Li, L.H. Zhang, D.G. Evans, X. Duan, Structure and surface chemistry of manganese-doped copper-based mixed metal oxides derived from layered double hydroxides, *Colloids Surf. A* 244 (2004) 169.
- [35] G.C. Silva, F.S. Almeida, A.M. Ferreira, V.S.T. Ciminelli, Preparation and application of a magnetic composite ( $\text{Mn}_3\text{O}_4/\text{Fe}_3\text{O}_4$ ) for removal of As(III) from aqueous solutions, *Mat. Res.* 15 (2012) 403.
- [36] F. Buciuman, F. Patcas, R. Craciun, D. R. T. Zahn, Vibrational spectroscopy of bulk and supported manganese oxides, *Phys. Chem. Chem. Phys.* 1 (1999) 185.
- [37] Y.-F. Han, F. Chen, Z. Zhong, K. Ramesh, L. Chen, E. Widjaja, Controlled synthesis, characterization, and catalytic properties of  $\text{Mn}_2\text{O}_3$  and  $\text{Mn}_3\text{O}_4$  nanoparticles supported on mesoporous silica SBA-15, *J. Phys. Chem. B* 110 (2006) 24450.
- [38] C.-C. Huang, N.-H. Khu, C.-S. Yeh, The characteristics of sub 10 nm manganese oxide  $\text{T}_1$  contrast agents of different nanostructured morphologies, *Biomaterials* 31 (2010) 4073.
- [39] H. Chen, J. He, Facile synthesis of monodisperse manganese oxide nanostructures and their application in water treatment, *J. Phys. Chem. C* 112 (2008) 17540.
- [40] N. Kaneko, M. Kaneko, H. Takahashi, Infrared and Raman spectra and vibrational assignment of some metal tartrates, *Spectrochim. Acta, Part A* 40 (1984) 33.
- [41] V. Krishnakumar, S. Dheivamalar, Growth and vibrational spectroscopic studies of strontium tartrate ( $\text{C}_4\text{H}_4\text{O}_6\text{Sr}$ ): A nonlinear optical single crystal, *J. Raman Spectrosc.* 40 (2009) 627.
- [42] V. Ramakrishnan, J.M.T. Maroor, IR and Raman studies of gel grown manganese tartrate, *Infra. Phys.* 28 (1988) 201.
- [43] S. Kolesnik, B. Dabrowski, J. Mais, Structural and magnetic properties of transition metal substituted ZnO, *J. Appl. Phys.* 95 (2004) 2582.
- [44] K.R. Kittilstved, D.R. Gamelin, Activation of high- $T_C$  ferromagnetism in  $\text{Mn}^{2+}$ -doped ZnO using amines, *J. Am. Chem. Soc.* 127 (2005) 5292.
- [45] K.R. Kittilstved, D.A. Schwartz, A.C. Tuan, S.M. Heald, S.A. Chambers, D.R. Gamelin, Direct kinetic correlation of carriers and ferromagnetism in  $\text{Co}^{2+}$ : ZnO, *Phys. Rev. Lett.* 97 (2006) 037203.

- [46] B.N. Figgis, M.A. Hitchman, Ligand field theory and its applications, 1st ed., Wiley-VCH, New York, 2000.
- [47] C.R. Vestal, Z.J. Zhang, Effects of surface coordination chemistry on the magnetic properties of  $\text{MnFe}_2\text{O}_4$  spinel ferrite nanoparticles, *J. Am. Chem. Soc.* 125 (2003) 9828.
- [48] L. Zhang, J.-Q. Wang, J. Li, S. Zhang, Z. Jiang, J. Zhou, J. Cheng, T. Hu, W. Yan, X. Wei, Z. Wu, Regulation of magnetic behavior and electronic configuration in Mn-doped ZnO nanorods through surface modifications, *Chem. Mater.* 24 (2012) 1676.
- [49] S. Baruah, S.S. Sinha, B. Ghosh, S.K. Pal, A.K. Raychaudhuri, J. Dutta, Photoreactivity of ZnO nanoparticles in visible light: Effect of surface states on electron transfer reaction, *J. Appl. Phys.* 105 (2009) 074308.
- [50] S.S. Sinha, P.K. Verma, A. Makhil, S.K. Pal, A versatile fiber-optic coupled system for sensitive optical spectroscopy in strong ambient light *Rev. Sci. Instrum.* 80 (2009) 053109.
- [51] A. Kudo, K. Omori, H. Kato, A novel aqueous process for preparation of crystal form-controlled and highly crystalline  $\text{BiVO}_4$  powder from layered vanadates at room temperature and its photocatalytic and photophysical properties, *J. Am. Chem. Soc.* 121 (1999) 11459.

## Chapter 6

# Surface Functionalization of Nanoparticles and their Interaction with Small Organic Molecules

### 6.1. Introduction

Functionalization of magnetic nanoparticles is very crucial for their practical use in nanobiotechnology [1-3]. Particularly, the use of properly functionalized magnetic nanoparticles in clinical medicine has also intensified [4, 5]. With proper surface coating, these magnetic nanoparticles can be dispersed into water, forming monodisperse water-based suspensions [6-8]. Formation of nanoparticles involving biological macromolecules is one of the very effective routes for the biocompatible magnetic materials [9-12]. Mixed-valent manganites have been recognized to be very useful magnetic materials for their potentiality in colossal magnetoresistance [13, 14] and spintronics [15]. In recent times significant efforts have been made to use the manganite nanoparticles for the prospective application in cancer therapy involving the effect of hyperthermia [16]. In this regard several attempts have been made to solubilize the manganite nanoparticles in aqueous solution by biocompatible macromolecules including dextran, bovine serum albumin, fatty amines, resulting a suspension of the manganite nanoparticles in the solution [17, 18]. However, till date no attempt has been made to functionalize individual manganite nanoparticles with small biocompatible ligands. The individual functionalized nanoparticles are important in order to study their interaction with other biologically relevant ligand/drug molecules [19, 20].

In this chapter, we report the functionalization of one of the most promising manganite nanoparticles (NPs),  $\text{La}_{0.67}\text{Sr}_{0.33}\text{MnO}_3$  (called LSMO hereafter) with biocompatible citrate ligand. The size selective solubilization of the functionalized NPs in aqueous solution has also been demonstrated from HRTEM. The UV-vis spectroscopic study on the functionalized NPs shows an intense peak at visible region as a consequence of electronic interaction of the citrate ligand with the surface atoms of the NPs. In our studies we have exploited the visible band of the functionalized NPs in order to study the interaction of the NPs with small biologically relevant ligands namely 2-aminopurine

(2AP) and 4-nitrophenyl anthranilate (NPA). Picosecond time-resolved Förster resonance energy transfer (FRET) studies on the ligands with the functionalized NPs, confirm the dipolar interactions of the ligands with the NPs and reveals the ligand binding sites of the NPs in the aqueous solutions. The FRET distances from the attached ligand to the host LSMO NPs also confirm the existence of the isolated functionalized NPs in the aqueous solution.

## **6.2. Result and discussion**

### **6.2.1. Functionalization of Manganite Nanoparticles and their Interaction with Biologically Relevant Small Ligands: Picosecond Time-Resolved FRET Studies [21]:**

To obtain direct evidence for the functionalization of LSMO NPs, FTIR measurements were performed on both the as-prepared and functionalized samples. The FTIR spectra of LSMO NPs, Citrate-LSMO conjugates and tri-sodium citrate were shown in Figure 6.1a. For tri-sodium citrate the characteristic bands (centre of gravity at  $1417\text{ cm}^{-1}$ ) corresponds the symmetric stretching of  $\text{-COO}^-$ , at  $1592\text{ cm}^{-1}$  for the anti-symmetric stretching of  $\text{-COO}^-$  [22-25], and at  $3455\text{ cm}^{-1}$  due to stretching vibration of  $\text{-OH}$  [26] are clearly shown in Figure 6.1a(I). When the citrate ligand bound to NPs surface (Figure 6.1a(II)) the anti-symmetric stretching of  $\text{COO}^-$  at  $1595\text{ cm}^{-1}$  almost remain same but the symmetric  $\text{COO}^-$  stretching mode of citrate become red-shifted and appears sharply at  $1398\text{ cm}^{-1}$ . It has been shown that Mn remains in the form of  $\text{Mn}^{+3}$  at the surface of LSMO NPs [17]. The red-shifted symmetric  $\text{COO}^-$  stretching mode clearly confirms the bi-dentate binding of two carboxylate oxygens with the surface  $\text{Mn}^{3+}$  ions of LSMO NPs. In order to confirm that Mn is the main interacting species, we have studied the interactions of the citrate ligands with  $\text{La}_2\text{O}_3$  and  $\text{LaMnO}_3$ , which reveals a visible band only for  $\text{LaMnO}_3$ . Our observation is consistent with the fact that Mn is the main interacting species which can interact with the ligand. It is also evident that the position of  $\text{-OH}$  stretching vibration of citrate remains same but become more broaden after interacting with the NPs surface. So, from FTIR study it is evident that the  $\text{COO}^-$  functional group/groups present in citrate, covalently bonded to the NPs surface and the remaining polar functional groups make the NPs water soluble. Since LSMO is a stable oxide [27] in water and due to the presence of citrate as

capping agent, there will be no change to the surface property of LSMO upon solubilization into water.

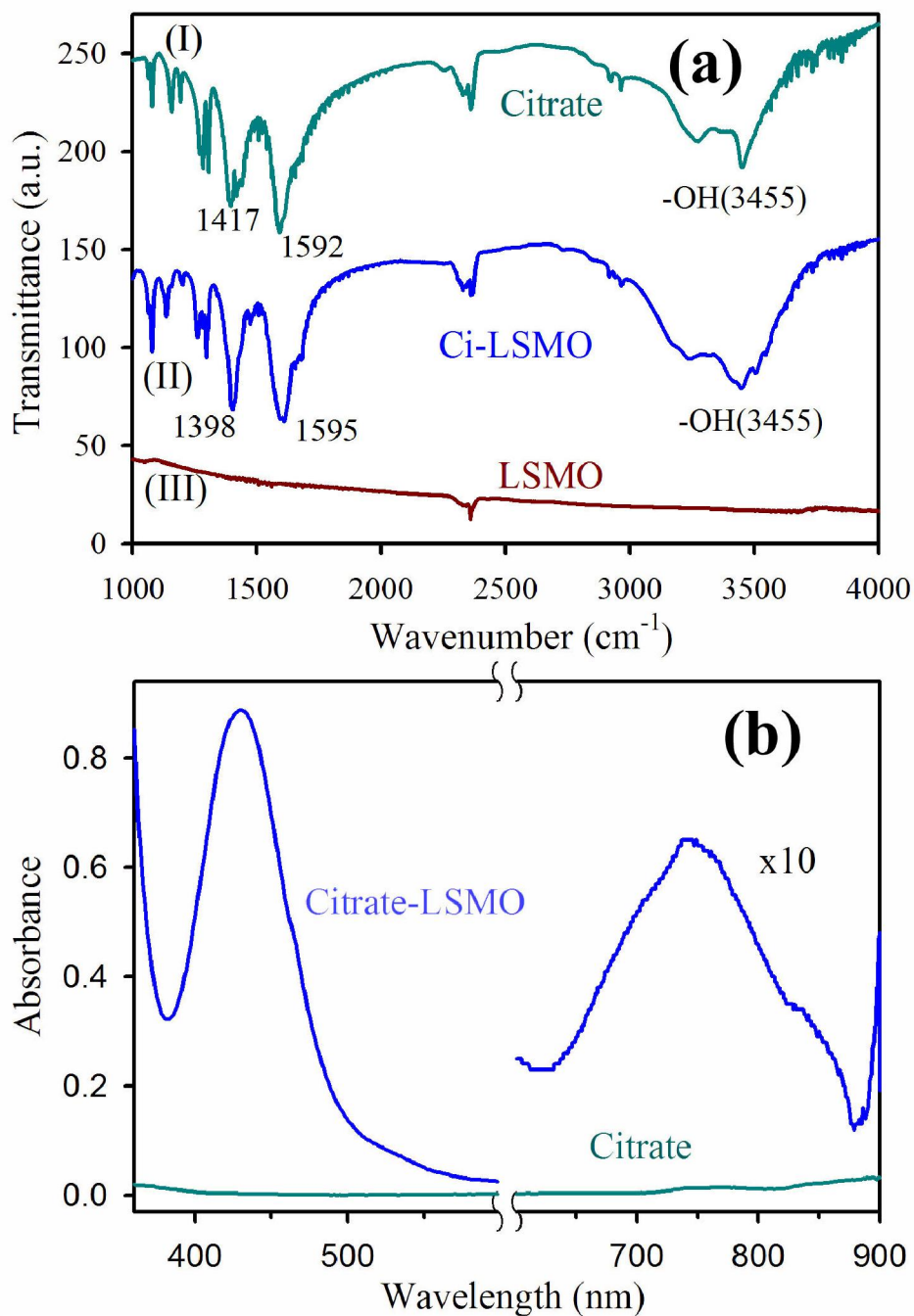


**Figure 6.1.** (a) Shows FTIR spectra of (I) pure tri-sodium citrate crystals, (II) functionalized citrate-LSMO and (III) as-prepared bulk LSMO, recorded with a KBr pellet. (b) Shows UV-vis absorption spectra of citrate and citrate functionalized LSMO NPs in solution.

Figure 6.1b illustrates the UV-vis spectrum of the citrate capped LSMO. A high intensity broad band centered at 430 nm is clearly shown, along with a smaller band centered at 742 nm. The near visible absorption of  $\text{La}_{0.9}\text{Sr}_{0.1}\text{MnO}_3$  single crystal has been reported in literature [28], to be at 1.75 eV (710 nm). The near visible band with a peak at 1.75 eV is attributed to an  $e^1_g(\text{Mn}^{3+})-e^2_g(\text{Mn}^{3+})$  transition between states split by Jahn-Teller interaction. The smaller band at 742 nm for Citrate-LSMO arises because of the above (d-d) transition and is shifted towards lower energy (compared to  $\text{La}_{0.9}\text{Sr}_{0.1}\text{MnO}_3$  single crystal at 710 nm) due to the presence of  $\text{COO}^-$  (of citrate), which is a low field ligand compared to [29]  $\text{O}^{2-}$  (of LSMO). The origin of the high intensity band at 430 nm is attributed to, ligand (citrate) to metal ( $\text{Mn}^{3+}$ ) charge transfer (LMCT), and the transition occurs from filled ligand  $p_\pi$  orbitals to empty metal ( $\text{Mn}^{3+}$ ) 3d orbitals [29, 30].

Magnetic property of Citrate-LSMO was studied by using the standard field dependent magnetization measurements. The starting as-prepared NP is a room temperature ferromagnetic material [28]. The details magnetic measurements of the as-prepared bulk NPs are described in the supporting information. The M (H) curve at room temperature and at 80 K of the functionalized NPs in water shows a linear behaviour with low magnetization values, indicative of paramagnetic behavior. So the ferromagnetic NPs (as-prepared) become paramagnetic upon size selective (av. 2.6 nm) functionalization (see below) and consequent solubilization by citrate ligand [27-31].

Figure 6.2a represents the TEM image of the solubilized Citrate-LSMO NPs. The image reveals that the solubilized NPs are almost spherical in shape and follow a uniform size distribution. The average sizes of the solubilized NPs as estimated from the TEM image, has been found to be 2.6 nm. The corresponding HRTEM image (upper inset of Figure 6.2a) confirms the crystallinity of the NPs in their structure. The interplanar distance of the fringes is measured to be about 0.29 nm, corresponding to the distance between (104) planes of the LSMO crystal lattice. The selective area electron diffraction (SAED) pattern simultaneously obtained from the TEM measurements (lower inset of Figure 6.2a) suggests single crystalline structure of Citrate-LSMO.

The elemental composition of the Citrate-LSMO conjugates was examined using an EDAX spectrometer attached to TEM operated at 200 kV. EDAX spectrum (Figure 6.2b) of the solubilized NPs confirms the presence of La, Sr and Mn as elemental

composition. The image in the inset of Figure 6.2b represents the corresponding fast fourier transform (FFT) pattern.

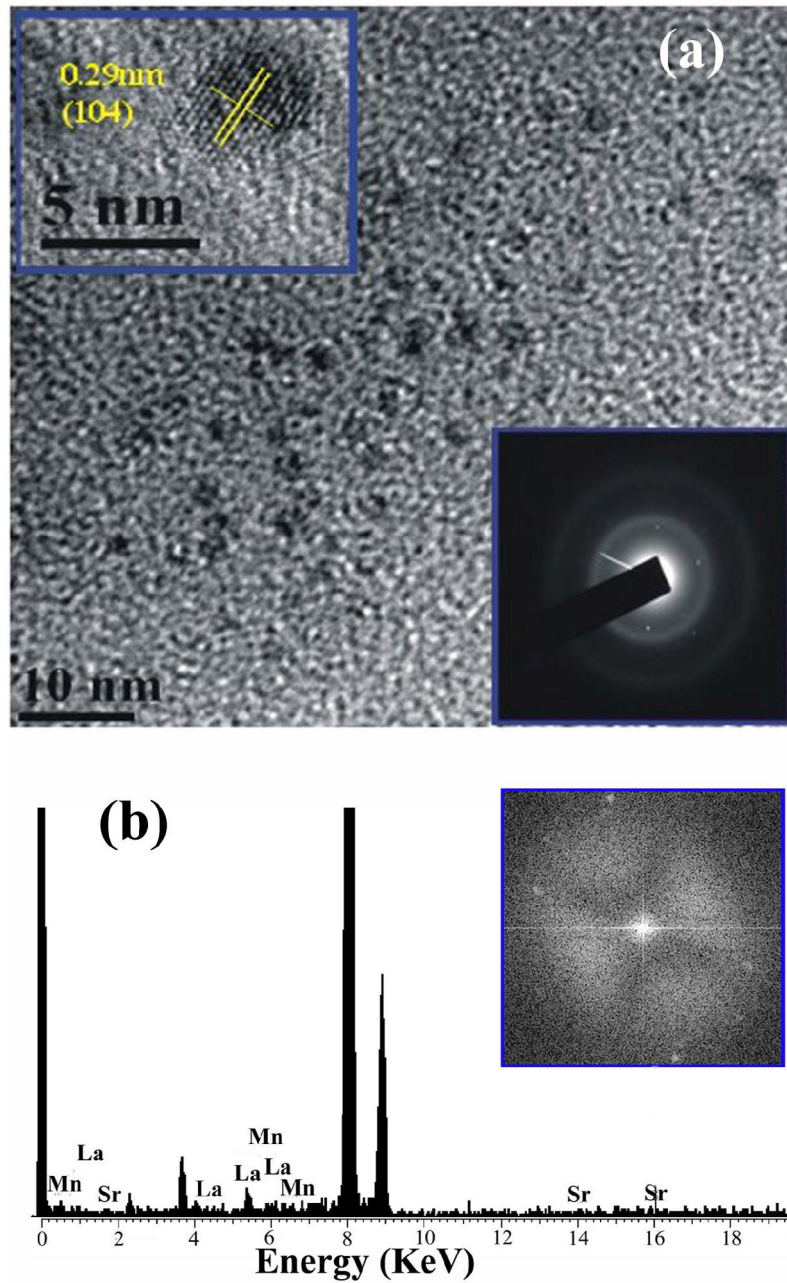


**Figure 6.2.** (a) TEM image of Citrate-LSMO NPs, upper inset shows a HRTEM image of the crystalline structure of Citrate-LSMO NPs, lower inset shows the selective area electron diffraction (SAED) pattern of the Citrate-LSMO NPs. (b) shows EDAX spectrum of the Citrate-LSMO NPs, an FFT image of the functionalized NPs is shown in the inset.

The direct bonding of citrate ligands to the LSMO NPs surfaces ensured that the overall size of the NPs remain small with a thin solubilizing shell. The –OH functional groups of Citrate-LSMO were labelled covalently with 4-nitrophenyl anthranilate (NPA) chromophore [32] and an efficient FRET occurs. The chromophore, NPA, has an active p-nitrophenyl ester group that can react with nucleophiles [33]. NPA was reacted with the hydroxyl groups of the citrate ligands anchored on the LSMO NPs surface, where the hydroxyl groups have been used as the nucleophile.

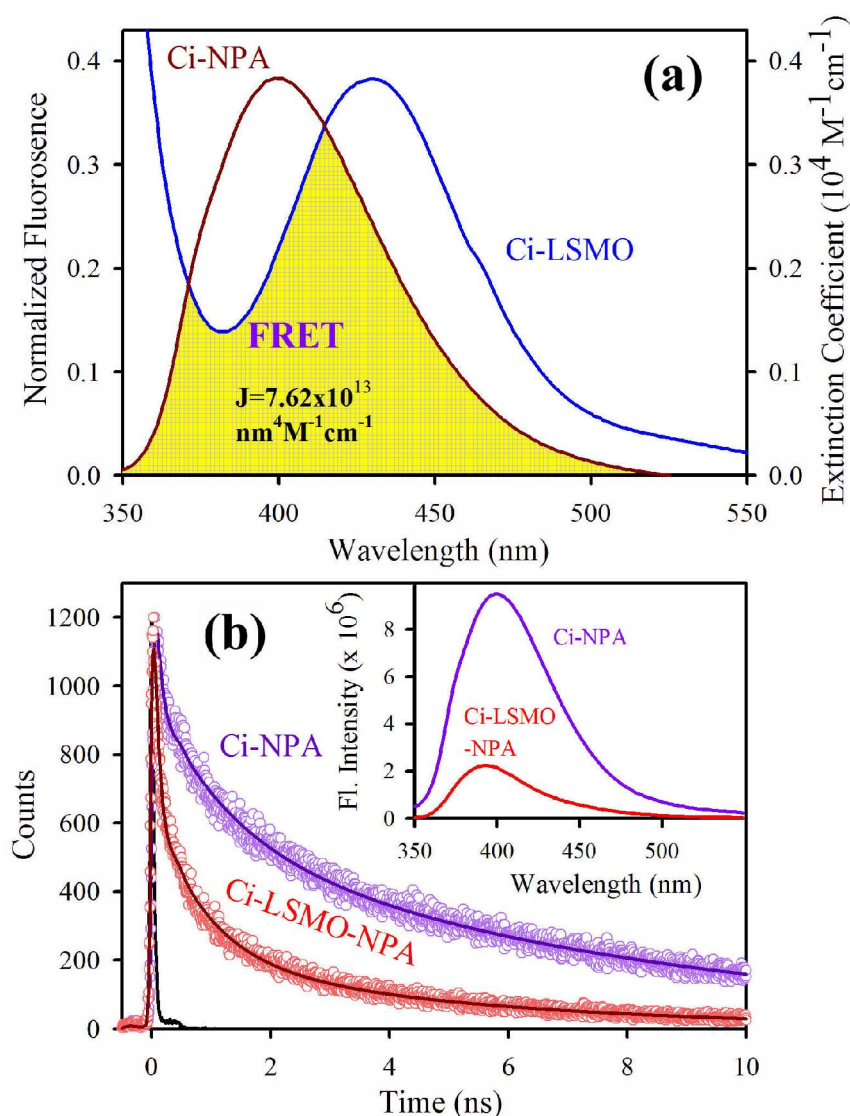


**Figure 6.3.** (a) Shows the spectral overlap between donor (Citrate-NPA) emission and acceptor (Citrate-LSMO) absorption, (b) Shows quenching of the donors excitation lifetime in the presence of the acceptor, inset shows steady-state quenching of the donor emission. Excitation wavelength of 320 nm and 375 nm is used for steady state and time resolved experiments respectfully.

**Table 6.1.** Fluorescence lifetimes ( $\tau_i$ ), FRET efficiency from time resolved experiment ( $E_{TR}$ ), FRET efficiency from steady state experiment ( $E_{SS}$ ), donor–acceptor distance from time resolved experiment ( $r_{TR}$ ) and steady state experiment ( $r_{SS}$ ). Numbers in parentheses in the lifetime column signify the relative percentage of the components in the total lifetime,  $\tau_{av}$  is the average lifetime.

Systems	Lifetimes (ns)	$E_{TR}$ (%)	$r_{TR}$ (nm)	$E_{SS}$ (%)	$r_{SS}$ (nm)
Citrate-NPA	$\tau_1 = 0.99$ (21%), $\tau_2 = 7.16$ (32%), $\tau_3 = 0.07$ (46%). $\tau_{av} = 2.53$	-	-	-	-
Citrate-LSMO-NPA	$\tau_1 = 0.94$ (20%), $\tau_2 = 5.14$ (10%), $\tau_3 = 0.08$ (69%), $\tau_{av} = 0.75$	70.00	2.51	80.00	2.31
Citrate-2AP	$\tau_1 = 8.03$ (100%)	-	-	-	-
Citrate-LSMO-2AP	$\tau_1 = 10.50$ (14%), $\tau_2 = 0.11$ (86%), $\tau_{av} = 1.55$	80.60	2.24	96.00	1.66

Figure 6.3a reveals a huge spectral overlap between the emission spectrum of Citrate-NPA (donor) and the absorption spectrum of Citrate-LSMO (acceptor) suggesting an efficient FRET between the donor and acceptor. Inset of Figure 6.3b, represents the steady state photoluminescence (PL) spectra of both Citrate-LSMO-NPA, and Citrate-NPA and it is found that the NPA emission undergoes drastic quenching in presence of the LSMO NPs, that clearly indicates the energy transfer occurs between the chromophore (NPA) and the nanoparticles. We further confirm the FRET, measuring the excited state lifetime of NPA from picosecond time-resolved study. Figure 6.3b shows the picosecond time-resolved PL transients of Citrate-NPA and Citrate-LSMO-NPA at 450 nm. The picosecond time-resolved fluorescence decay of Citrate-NPA (donor) revealed multi exponential time constants of 0.99 ns (21%), 7.16 ns (32%), 0.07 ns (46%) giving an average time constant ( $\tau_{av}$ ) of 2.53 ns as shown in Table 6.1. For the donor-acceptor system (Citrate-LSMO-NPA) the time constants obtained as 0.94 ns (20%), 5.14 ns (10%) and 0.08 ns (69%) giving an average time constant ( $\tau_{av}$ ) of 0.75 ns (Table 6.1). The substantial shortening in the NPA fluorescence lifetime upon conjugation with NPs indicates conclusively that efficient FRET occurs from the NPA donor to the Citrate-LSMO acceptor. We have estimated the extinction coefficient ( $3827.58 \text{ mole}^{-1} \text{ cm}^{-1}$ ) of the acceptor Ci-LSMO using the UV-vis absorption (at 430 nm) of the functionalized NPs in water. Taking quantum yield of NPA [34] in absence of acceptor as 0.51 and based on the

spectral overlap, we have estimated a FRET efficiency of 70% in our FRET system. The calculated Förster distance  $R_0$ , for the NPA-(Citrate-LSMO) complex is 2.90 nm. The calculated donor-acceptor distance ( $r$ ) is 2.51 nm (Table 6.1). The distance is consistent with the covalent attachment of NPA ligand with –OH group of the citrate at the surface of LSMO NPs.

Figure 6.4a shows the spectral overlap between the emission spectrum of Citrate-2AP (donor) and the absorption spectrum of Citrate-LSMO (acceptor) suggesting the possibility of efficient FRET between the donor and the acceptor, when 2AP becomes adsorbed at the surface of the Citrate-LSMO NPs. Inset of Figure 6.4b represents the steady state photoluminescence (PL) quenching of donor (Citrate-2AP) in presence of LSMO NPs. Picosecond time-resolved PL transients (Figure 6.4b) of both donor and donor-acceptor systems monitored at 400 nm, shows significant shortening in the 2AP fluorescence lifetime upon adsorption at the NPs surface. The picosecond time-resolved fluorescence decay of Citrate-2AP (donor) revealed single exponential time constant of 8.03 ns. For the donor-acceptor system (Citrate-LSMO-2AP) the time constants are obtained as 10.5 ns (14%), 0.11 ns (86%) giving an average time constant ( $\tau_{av}$ ) of 1.55 ns (Table 6.1). The extensive quenching in the 2AP fluorescence lifetime upon surface adsorption conclusively indicates that efficient FRET occurs from the 2AP donor to the citrate-LSMO acceptor. Taking quantum yield of 2AP [35] in absence of acceptor as 0.66 and based on the spectral overlap, here also, we have estimated a FRET efficiency of 80.6 %. The measured Förster distance,  $R_0$ , for the (Citrate-LSMO-2AP) complex is 2.84 nm. The donor-acceptor distance ( $r$ ) calculated is 2.24 nm (Table 6.1), which indicates a very high efficiency of energy transfer and evidently supports that 2AP was at a close proximity of the solubilized LSMO NP surface. Despite the fact that the area integral of donor-acceptor overlap ( $J$  value) is much larger for NPA, 2AP is showing more efficient energy transfer. As the rate of energy transfer strongly depends upon the donor-acceptor distance ( $k_{FRET} \propto 1/r^6$ ), 2AP ( $r = 2.24$  nm) shows more efficient energy transfer with the functionalized NPs than NPA ( $r = 2.51$  nm). It has to be noted that the fluorescence quenching mechanism of 2AP and NPA could be due to electron transfer in the system, which normally demands surface to surface contact of the donor and acceptor [36-38]. However, in our system the donors are apart ( $\sim 1$  nm) from the surface of the acceptor NPs.

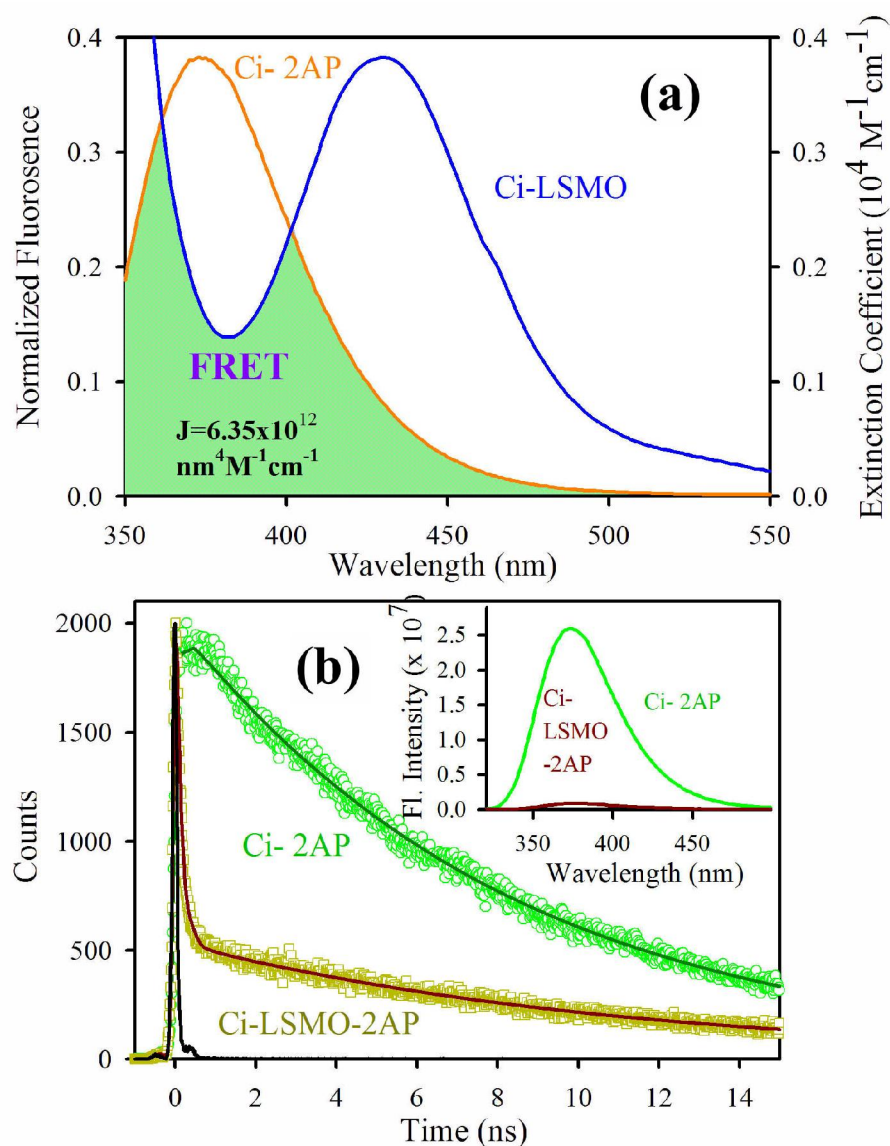
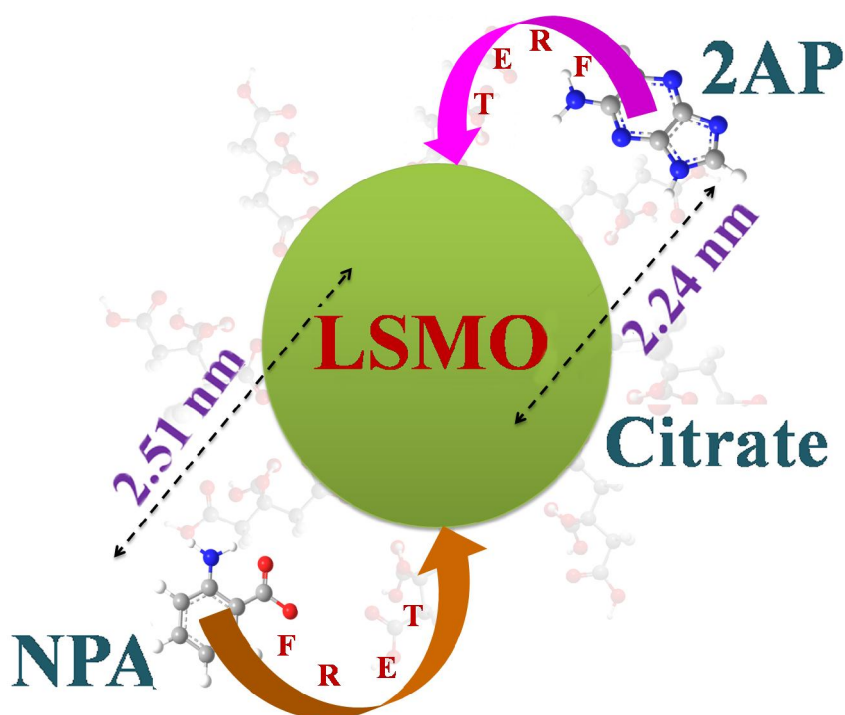


**Figure 6.4.** (a) Shows the spectral overlap between donor (Citrate-2AP) emission and acceptor (Citrate-LSMO) absorption, (b) shows quenching of the donors excitation lifetime in the presence of the acceptor, inset shows steady-state quenching of the donor emission. Excitation wavelength of 300 nm is used for both the experiments.

Moreover, there are several reports regarding the fluorescence quenching of 2AP caused by charge transfer with other DNA bases, however, the associated fluorescence life times are much shorter (21-35 ps) [35, 39, 40] compared to an observed value of 110 ps (Table 6.1). Again NPA is a well known resonance energy transferring probe [11, 34, 41] and there is no report of electron transfer or charge transfer involving NPA. The overall picture

that is revealed from our studies is schematically shown in Scheme 6.1. It has to be noted that application of FRET model in the dye-nanoparticle systems is evidenced in number of recent literatures [42-44]. In order to rationalize the non radiative energy transfer from fluorescent ligands to the nanoparticles is also tricky as the measured distances are comparable to the diameter of the nanoparticles, and more appropriate model is nano surface energy transfer (NSET) [45]. However, the physical parameters [Fermi frequency ( $\omega_f$ ) and Fermi wave vector ( $k_f$ ) of acceptor metal NPs] regarding this calculation is not available in the published literature.



**Scheme 6.1.** Functionalization of the manganite nanoparticles (NPs) with citrate ligands is shown. Covalent attachment of the fluorescent probe NPA and non-covalent adduction of one of DNA base mimics 2AP are also shown. The efficient energy transfer (FRET) from the fluorescent ligands to the NPs and corresponding donor-acceptor distances are also indicated.

### 6.3. Conclusion

In summary, we have functionalized individual LSMO nanoparticles (NPs) by using citrate ligand as capping agents. While FTIR spectroscopy confirms the covalent attachment of the citrate ligand with the surface of the NPs, the UV-vis spectroscopy reveals strong

electronic interaction of the ligands with the electronic states of the NPs, resulting a strong absorption band in the visible region. The uniform size selection (average diameter = 2.6 nm) upon functionalization of the LSMO NPs in the aqueous solutions has been confirmed from HRTEM. The magnetic property of the NPs in aqueous solutions shows significant change compared to that of the as-prepared material. The FRET from a covalently attached ligand NPA to the core of the NPs reveals a distance of 2.51 nm indicating the covalent attachment of the fluorescent ligand with the -OH functional group of the capped Citrate-LSMO. Fluorescent analogue of adenine, 2AP also shows drastic quenching of its excited state lifetime in presence of the solubilized NPs and the calculated FRET distance (2.24 nm) indicates its surface adsorption at the NPs. The functionalized manganite NPs may find applications in the field of nano-biotechnology, as the solubilizing layer (citrate) provides multiple functional groups (hydroxyl and carboxylic acids) for covalent conjugation with other biological macromolecules such as small peptides, DNA, RNA and biocompatible polymers etc.

## References

- [1] G.M. Whitesides, The 'right' size in nanobiotechnology, *Nat. Biotechnol.* 21 (2003) 1161.
- [2] C.M. Niemeyer, Nanoparticles, proteins, and nucleic acids: Biotechnology meets materials science *Angew. Chem. Int. Ed.* 40 (2001) 4128.
- [3] J.C. Love, L.A. Estroff, J.K. Kriebel, R.G. Nuzzo, G.M. Whitesides, Self-assembled monolayers of thiolates on metals as a form of nanotechnology, *Chem. Rev.* 105 (2005) 1103.
- [4] C. Xu, K. Xu, H. Gu, R. Zheng, H. Liu, X. Zhang, Z. Guo, B. Xu, Dopamine as a robust anchor to immobilize functional molecules on the iron oxide shell of magnetic nanoparticles, *J. Am. Chem. Soc.* 126 (2004) 9938.
- [5] C. Xu, K. Xu, H. Gu, X. Zhong, Z. Guo, R. Zheng, X. Zhang, B. Xu, Nitrilotriacetic acid-modified magnetic nanoparticles as a general agent to bind histidine-tagged proteins, *J. Am. Chem. Soc.* 126 (2004) 3392.
- [6] S.H. Sun, Recent advances in chemical synthesis, self-assembly, and applications of FePt nanoparticles, *Adv. Mater.* 18 (2006) 393.
- [7] J. Park, J. Joo, S.G. Kwon, Y. Jang, T. Hyeon, Synthesis of monodisperse spherical nanocrystals, *Angew. Chem. Int. Ed.* 46 (2007) 4630.
- [8] L. Fu, V.P. Dravid, D.L. Johnson, Self-assembled (SA) bilayer molecular coating on magnetic nanoparticles, *Appl. Surf. Sci.* 181 (2001) 173.
- [9] C.M. Niemeyer, Functional hybrid devices of proteins and inorganic nanoparticles, *Angew. Chem. Int. Ed.* 42 (2003) 5796.
- [10] C.M. Niemeyer, Nanoparticles, proteins, and nucleic acids: Biotechnology meets materials science *Angew. Chem. Int. Ed.* 40 (2001) 4128.
- [11] P.K. Verma, A. Giri, N.T. Thanh, L.D. Tung, O. Mondal, M. Pal, S.K. Pal, Superparamagnetic fluorescent nickel-enzyme nanobioconjugates: Synthesis and characterization of a novel multifunctional biological probe, *J. Mater. Chem.* 20 (2010) 3722.
- [12] R.K. Mitra, P.K. Verma, D. Wulferding, D. Menzel, T. Mitra, A.M. Todea, P. Lemmens, A. Mueller, S.K. Pal, A molecular magnet confined in the nanocage of a globular protein, *Chem. Phys. Chem.* 11 (2010) 389.

- [13] C.N.R. Rao, B. Raveau, Colossal magnetoresistance, charge ordering and related properties of manganese oxides, 1st ed., World Scientific, Singapore, 1998.
- [14] Y. Tokura, Colossal magnetoresistive oxide, Gordon & Breach, London, 2000.
- [15] I. Bergenti, V. Dediu, M. Cavallini, E. Arisi, A. A. Riminucci, C. Taliani, Properties of thin manganite films grown on semiconducting substrates for spintronics applications, *Curr. Appl. Phys.* 7 (2007) 47.
- [16] D.K. Kim, M.S. Amin, S. Elborai, S.H. Lee, Y. Koseoglu, M. Zahn, M. Muhammed, Energy absorption of superparamagnetic iron oxide nanoparticles by microwave irradiation, *J. Appl. Phys.* 97 (2005) 105101.
- [17] R. Rajagopal, J. Mona, S.N. Kale, T. Bala, R. Pasricha, P. Poddar, M. Sastry, B.L.V. Prasad, D.C. Kundaliya, S.B. Ogale,  $\text{La}_{0.7}\text{Sr}_{0.3}\text{MnO}_3$  nanoparticles coated with fatty amine, *Appl. Phys. Lett.* 89 (2006) 023107.
- [18] K.R. Bhayani, S.N. Kale, S. Arora, R. Rajagopal, H. Mamgain, R. Kaul-Ghanekar, D.C. Kundaliya, S.D. Kulkarni, R. Pasricha, S.D. Dhole, S.B. Ogale, K.M. Paknikar, Protein and polymer immobilized  $\text{La}_{0.7}\text{Sr}_{0.3}\text{MnO}_3$  nanoparticles for possible biomedical applications, *Nanotechnology* 18 (2007) 345101.
- [19] A.K. Gupta, M. Gupta, Synthesis and surface engineering of iron oxide nanoparticles for biomedical applications, *Biomaterials* 26 (2005) 3995.
- [20] S.J. Rosenthal, I. Tomlinson, E.M. Adkins, S. Schroeter, S. Adams, L. Swafford, J. McBride, Y. Wang, L.J. DeFelice, R.D. Blakely, Targeting cell surface receptors with ligand-conjugated nanocrystals, *J. Am. Chem. Soc.* 124 (2002) 4586.
- [21] A. Giri, A. Makhil, B. Ghosh, A.K. Raychaudhuri, S.K. Pal, Functionalization of manganite nanoparticles and their interaction with biologically relevant small ligands: Picosecond time-resolved FRET studies, *Nanoscale* 2 (2010) 2704.
- [22] X. Zou, E. Ying, S. Dong, Seed-mediated synthesis of branched gold nanoparticles with the assistance of citrate and the surface-enhanced Raman scattering properties, *Nanotechnology* 17 (2006) 4758.
- [23] T. Zhu, K. Vasilev, M. Kreiter, S. Mittler, W. Knoll, Surface modification of citrate-reduced colloidal gold nanoparticles with 2-mercaptosuccinic acid, *Langmuir* 19 (2003) 9518.

- [24] M. Dakanali, E.T. Kefalas, C.P. Raptopoulou, A. Terzis, T. Mavromoustakos, A. Salifoglou, Synthesis and spectroscopic and structural studies of a new cadmium(II)-citrate aqueous complex.potential relevance to cadmium(II)-citrate speciation and links to cadmium toxicity, *Inorg.Chem.* 42 ( 2003) 2531.
- [25] P. Uznanski, E. Bryszewska, Synthesis of silver nanoparticles from carboxylate precursors under hydrogen pressure, *J. Mater. Sci.* 45 (2010) 1547.
- [26] R.M. Silverstein, F.X. Webster, Spectroscopic identification of organic compounds, 6<sup>th</sup> ed., John Wiley & Sons, Inc., New York, 1998.
- [27] Y. Tian, D. Chen, X. Jiao, La<sub>1-x</sub>Sr<sub>x</sub>MnO<sub>3</sub> (x = 0, 0.3, 0.5, 0.7) nanoparticles nearly freestanding in water: Preparation and magnetic properties, *Chem. Mater.* 18 (2006) 6088.
- [28] N.N. Loshkareva, Y.P. Sukhorukov, E.A. Neifel'd, V.E. Arkhipov, A.V. Korolev, V.S. Gaviko, E.V. Panfilova, V.P. Dyakina, Y.M. Mukovskiĭ, D.A. Shulyatev, Centers of charge nonuniformity in absorption spectra of lanthanum manganites, *J. Exp. Theor. Phys.* 90 (2000) 389.
- [29] J.E. Huheey, E.A. Keiter, R.L. Keiter, Inorganic chemistry-principles of structure and reactivity, 4<sup>th</sup> ed., Pearson Education, Singapore.
- [30] J.B. Vincent, K. Folting, J.C. Huffman, G. Christou, Use of tetra-n-butylammonium permanganate for inorganic syntheses in nonaqueous solvents. Preparation and structure of a manganese(III) dimer containing bridging phenoxo oxygen atoms, *Inorg. Chem.* 25 (1986) 996.
- [31] Y. Labaye, O. Crisan, L. Berger, J.M. Greneche, J.M.D. Coey, Surface anisotropy in ferromagnetic nanoparticles, *J. Appl. Phys.* 91 (2002) 8715.
- [32] J. Broos, A.J.W.G. Visser, J.F.J. Engbersen, W. Verboom, A.V. Hoek, D.N. Reinhoudt, Flexibility of enzymes suspended in organic solvents probed by time-resolved fluorescence anisotropy. Evidence that enzyme activity and enantioselectivity are directly related to enzyme flexibility, *J. Am. Chem. Soc.* 117 (1995) 12657.
- [33] A. Luyai, Y. Lasanajak, D. Smith, R. Cummings, X. Song, Facile preparation of fluorescent neoglycoproteins using p-nitrophenyl anthranilate as a heterobifunctional linker, *Bioconjugate Chem.* 20 (2009) 1618.
- [34] S.S. Narayanan, S.K. Pal, Structural and functional characterization of luminescent silver-protein nanobioconjugates, *J. Phys. Chem. C* 112 (2008) 4874.

- [35] O.J.G. Somsen, V.A. Hoek, V.H. Amerongen, Fluorescence quenching of 2-aminopurine in dinucleotides, *Chem. Phys. Lett.* 402 (2005) 61.
- [36] M. Gratzel, Photoelectrochemical cells, *Nature* 414 (2001) 338.
- [37] V.K. Thorsmølle, B. Wenger, J. Teuscher, C. Bauer, J.-E. Moser, Dynamics of photoinduced interfacial electron transfer and charge transport in dye-sensitized mesoscopic semiconductors, *Chimia* 61 (2007) 631.
- [38] A. Furube, L. Du, K. Hara, R. Katoh, M. Tachiya, Ultrafast plasmon-induced electron transfer from gold nanodots into TiO<sub>2</sub> nanoparticles, *J. Am. Chem. Soc.* 129 (2007) 14852.
- [39] E.L. Rachofsky, R. Osman, J.B.A. Ross, Probing structure and dynamics of DNA with 2-aminopurine: Effects of local environment on fluorescence, *Biochemistry* 40 (2001) 946.
- [40] O.F.A. Larsen, I.H.M. van Stokkum, F.L. de Weerd, M. Vengris, C.T. Aravindakumar, R. van Grondelle, N.E. Geacintov, H. van Amerongen, Ultrafast transient-absorption and steady-state fluorescence measurements on 2-aminopurine substituted dinucleotides and 2-aminopurine substituted DNA duplexes, *Phys. Chem. Chem. Phys.* 6 (2004) 154.
- [41] N. Hagag, E.R. Birnbaum, D.W. Darnall, Resonance energy transfer between Cys-34, Trp-214, and Tyr-411 of human serum albumin, *Biochemistry* 22 (1983) 2420.
- [42] T.C. Lim, V.J. Bailey, Y.-P. Ho, T.-H. Wang, Intercalating dye as an acceptor in quantum-dot-mediated FRET, *Nanotechnology* 19 (2008) 075701.
- [43] J. Bujda'k, D. Chorva't, N. Iyi, Resonance energy transfer between rhodamine molecules adsorbed on layered silicate particles, *J. Phys. Chem. C* 114 (2010) 1246.
- [44] I.L. Medintz, H.T. Uyeda, E.R. Goldman, H. Mattoussi, Quantum dot bioconjugates for imaging, labelling and sensing, *Nat. Mater.* 4 (2005) 435.
- [45] C.S. Yun, A. Javier, T. Jennings, M. Fisher, S. Hira, S. Peterson, B. Hopkins, N.O. Reich, G.F. Strouse, Nanometal surface energy transfer in optical rulers, breaking the FRET barrier, *J. Am. Chem. Soc.* 127 (2005) 3115.

## Chapter 7

# Synthesis of Amino-Acid Modified Fluorescent Quantum Dots in Aqueous Solution and their Interaction with Biological Macromolecules

### 7.1. Introduction

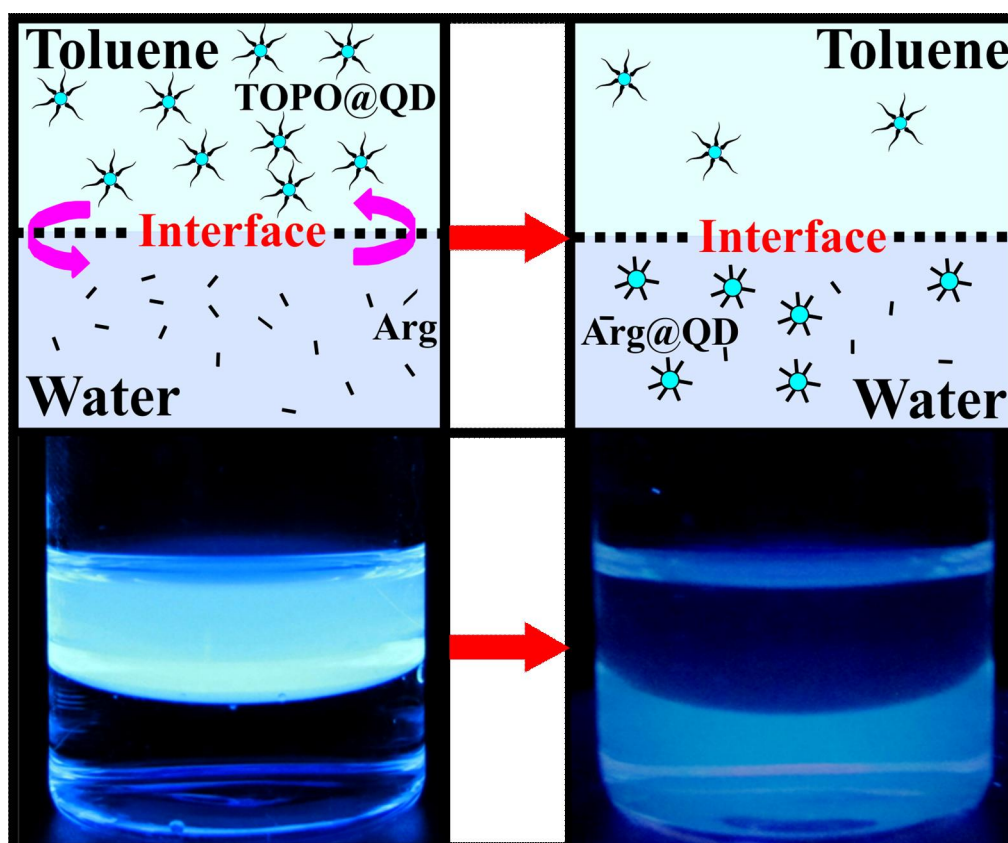
Semiconductor quantum dots (QDs) have attracted great interest over the past decade due to their unique optical properties, such as a bright, narrow and tunable fluorescence signatures, broad excitation but specific emission spectra and good photochemical stability [1-3]. Because of these distinct optical properties, QDs are being extensively explored with respect to biomedical use as imaging contrast agents, traceable therapeutic vectors and for energy applications including photovoltaic solar cells [4-7]. However, their advantageous properties are undermined by the inherent insolubility of QDs in aqueous solution. While, water solubilization of QDs is essential for many biological applications, it presents a significant challenge. Use of mercaptoacetic acid ligands was one of the first strategies applied to produce water soluble QDs [8]. Since then, a number of other thioalkyl acid ligands have been used, including 3-mercapto-propionic acid [9, 10] and dihydrolipoic acid [11]. These ligands form a self-assembly on the surface of the QDs that proceeds via a metal-thiol affinity interaction and other polar groups of the ligands are exposed to the surrounding aqueous solution [12]. Other approaches using non-thiol based organic ligands have also been employed including 4-substituted pyridine, oligomeric phosphine, poly (dimethylaminoethyl) methacrylate [13], polymers [14], amphiphilic polymers [15, 16] and phospholipids [17]. There has been a growing emphasis on assembling biological molecules to the water-soluble QDs through different types of interactions. In most cases these interactions involve covalent conjugation or simple adsorption of the biological molecules to the solubilizing layer around the QDs [8, 10, 14, 18]. In addition to these, the formations of nanobioconjugates through various nonspecific interactions (electrostatic, hydrogen-bonding interactions etc) between biological molecules and nanoparticles have also been explored [1, 19-21].

To date, CdSe/ZnS core/shell QDs remain among the best available for many biological applications [6, 22, 23]. However, QDs synthesized in organic solvents contain hydrophobic surface ligands such as trioctylphosphine oxide (TOPO), trioctylphosphine (TOP) [24], tetradecylphosphonic acid (TDPA) or oleic acid [25]. As a result they are insoluble in water and in other protic solvents namely methanol or ethanol [26]. So, their biological applications are restricted, where water solubility is highly desirable. Hence, the main challenge, to make quantum dots soluble in water for their further prospective bioconjugate reactions, remains.

Amino acids are inherently biocompatible and among common amino acids L-arginine along with lysine are positively charged. Upon functionalization of nanoparticle with these amino acids, the nanoparticles become positively charged and their interaction with the negatively charged biomolecules is much more efficient. However, in comparison with lysine, due to the presence of a guanidyl group, arginine molecules can highly facilitate the interaction of nanoparticle with biological macromolecules [27].

In the present chapter, we have exploited the toluene/water interface to replace the original TOPO capping of CdSe/ZnS core/shell QDs dispersed in toluene, with a natural amino acid L-arginine (Arg) using the reactivity of the amine groups. This allows a dispersal of the QDs in aqueous solutions with a quantum yield of 14%. We have confirmed the conjugation of arginine molecules with the QDs by using FTIR spectroscopy. The structural integrity of the QDs upon water solubilization has been confirmed with HRTEM. Using picosecond-resolved photoluminescence measurements, we have explored an efficient ultrafast energy transfer from arg-capped CdSe/ZnS QDs (donor) to ethidium bromide-labeled DNA (EB-DNA, acceptor) applying the sensitivity of FRET. Employing the kinetic model developed by Tachiya (for the quenching of luminescent probes), we have also analyzed the picosecond-resolved photoluminescence measurement results to understand the kinetics of energy transfer with the dye labeled DNA and the distribution of acceptor molecules around the donor QDs, as it is a driving factor for efficient energy transfer and for the accurate donor-acceptor measurements. In order to confirm any structural perturbation of dodecamer DNA in the nanobioconjugate, circular dichroism (CD) studies have also been performed on both the DNA and DNA-QD conjugate. To investigate in more details the type of interaction taking place between the

QDs and DNA, using CD we have monitored the melting and rehybridization pathways of the dodecamer DNA conjugated to the QDs. This reveals that hydrogen bonding is the accompanied mechanism involved during the formation of this QD-DNA nanobioconjugate.



**Scheme 7.1.** Trioctylphosphine oxide (TOPO) stabilized CdSe/ZnS quantum dots (QD) were modified with L-arginine via ligand exchange. Phase transfer of arginine-modified QDs from toluene phase into water was achieved by using the reactivity of amine group of arginine. Upon replacement of the initial TOPO ligand with arginine the emission of the QDs is decreased.

## 7.2. Result and Discussion

### 7.2.1. Preparation of Water Soluble L-Arginine Capped CdSe/Zns QDs and their Interaction with Synthetic DNA: Picosecond-Resolved FRET Study [28]:

As Scheme 7.1 illustrates, the addition of QDs toluene suspension into the aqueous solution of L-arginine (pH~9) under vigorous stirring condition results in the formation of toluene microdroplets, and the QDs in toluene get the chance to interact strongly with the arginine molecules through the liquid-liquid interface [29, 30]. Photo images of the QDs

under UV excitation before and after ligand exchange clearly indicate the successful phase transfer of the QDs from toluene into the aqueous medium. Efficient ligand exchange through this process is driven by an interaction between the amine group of the stabilizing amino acid in the aqueous phase and the ZnS shell of the QDs in the toluene phase at the interface [31, 32]. Computational studies have shown that primary amines have greater surface binding energy than carboxylic acids, though lower binding energy compared to TOPO and phosphonic acids [33-35]. However, primary amines have the advantage of more complete surface coverage which can theoretically reach 100% - over TOPO (30% coverage) due to reduced steric effects [36].

To obtain direct evidence for the arginine functionalization of QDs, FTIR measurements were performed on both the free arginine molecules and arginine molecules attached to the QDs. The FTIR spectra of arginine capped QDs and free arginine molecules are shown in Figure 7.1. For arginine, the characteristic band at  $3161\text{ cm}^{-1}$  (Figure 7.1b) corresponding to the N-H stretching mode [37], is broadened and red-shifted to  $3152\text{ cm}^{-1}$ , suggesting its interaction with the QD surface. Moreover, as shown in Figure 7.1a, the significant perturbation of other characteristic bands of arginine at  $790\text{ cm}^{-1}$  (C-N-H stretching),  $847\text{ cm}^{-1}$  (C-C stretching),  $1095\text{ cm}^{-1}$  (C-N stretching),  $1174\text{ cm}^{-1}$  (C-C-C symmetric stretching) and  $1406\text{ cm}^{-1}$  ( $\text{COO}^-$  symmetric stretching) [37, 38] also confirm the binding of arginine molecules to the QD surface. The direct interaction of arginine molecules with the QDs surfaces ensured that the overall size of the QDs remains unchanged, with a thin solubilizing shell. Inset of Figure 7.2a shows the HRTEM images of arg-capped QDs in water, which reveal the diameters of the QDs to be 3.2 nm. The existence of lattice fringes illustrates the highly crystalline nature of the QDs. We have employed FRET to study the interaction of the synthetic dodecamer DNA (EB labelled) with the water soluble QDs (pH~7). Figure 7.2a shows the spectral overlap between the emission spectrum of arginine capped QDs (donor) and the absorption spectrum of EB-labeled DNA (acceptor) suggesting the possibility of efficient Förster resonance energy transfer (FRET) between the donor and the acceptor, when EB-labeled DNA becomes adsorbed at the surface of the arginine capped QDs. Figure 7.2b represents the steady state photoluminescence (PL) quenching of the donor (arginine capped QDs) in presence of EB-

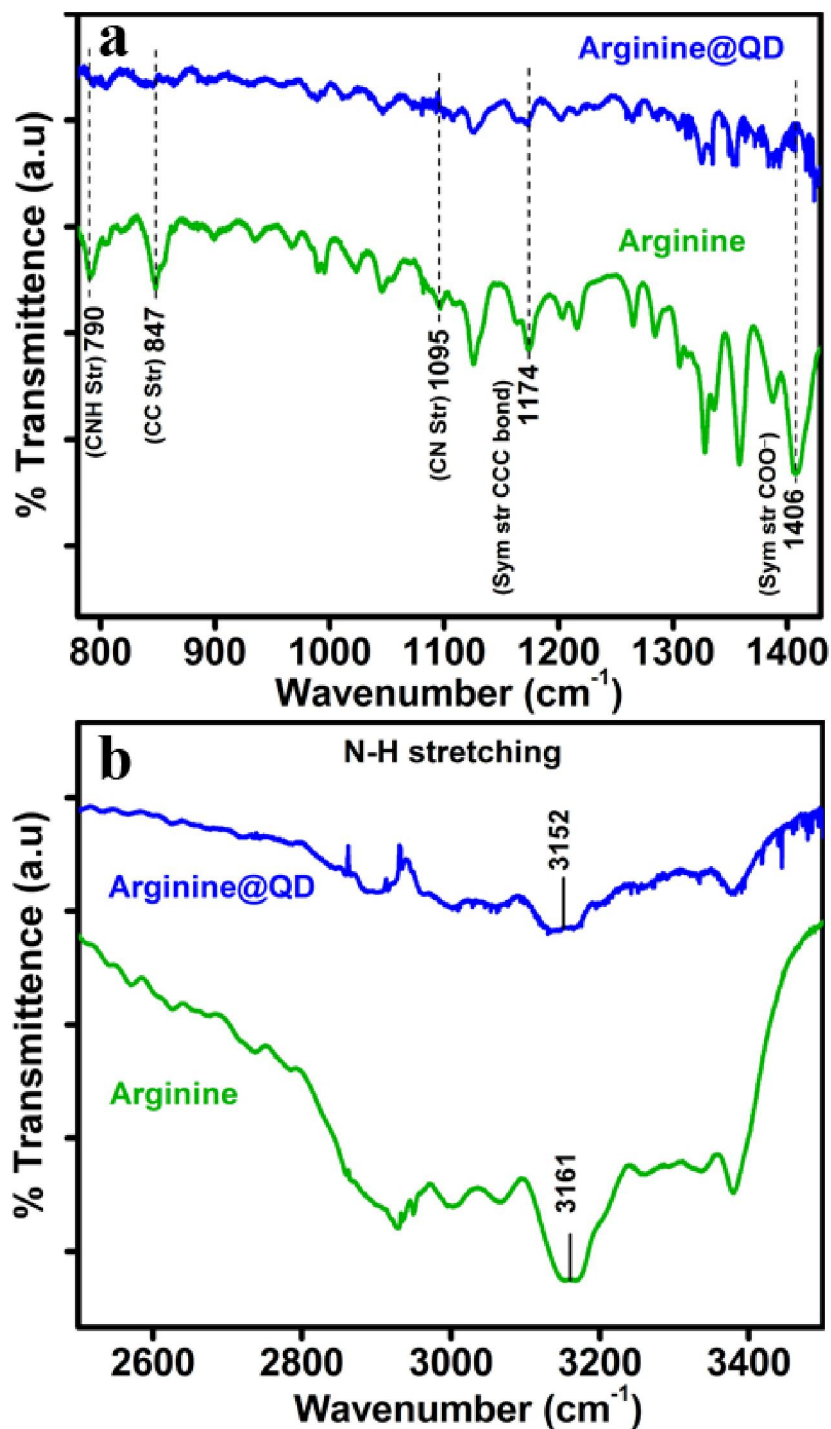


**Figure 7.1.** FTIR spectra of free arginine molecules and arginine molecules attached to the QDs. (a) Spectral broadening of C-N-H, C-C and C-C-C stretching frequencies of arginine upon interaction with the QDs. Perturbation of C-N and COO<sup>-</sup> stretching frequencies of arginine is also observed after interaction with the QDs. (b) Spectral broadening and red shift of N-H stretching frequency of arginine upon interaction with the QDs.

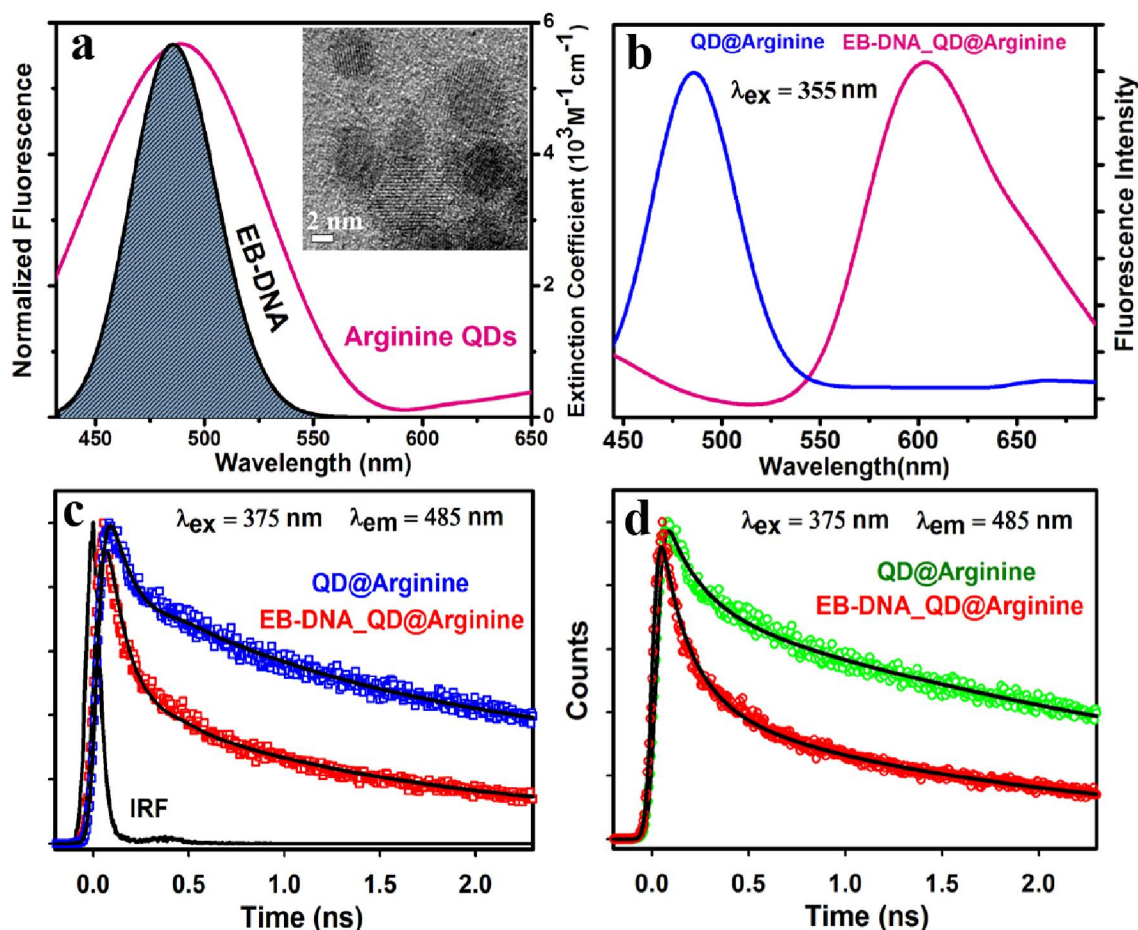


**Figure 7.2.** (a) Spectral overlap between emission spectrum of arginine-capped CdSe/ZnS core/shell QDs and the absorption spectrum of EB-labeled DNA (the extinction coefficient value is for the acceptor, EB-labelled DNA). Inset shows the HRTEM image of QD in toluene. (b) Steady-state fluorescence quenching of arginine-capped QDs in presence of the acceptor EB-DNA (c) Picosecond-resolved PL transients of arginine-capped CdSe/ZnS QDs and (EB-DNA)-QD complex monitored at  $\lambda_{em} = 485$  nm. (d) Picosecond-resolved PL transients of arginine-capped CdSe/ZnS QDs and (EB-DNA)-QD complex, fitted with Tachiya kinetic model. The fitted curves are shown in black.

labeled DNA. Picosecond resolved PL transients (Figure 7.2c) of both donor and donor-acceptor systems monitored at 485 nm, shows significant shortening in the QDs fluorescence lifetime upon adsorption of EB-labeled DNA at the QDs surface. The picosecond resolved fluorescence decay of arginine capped QDs (donor) in buffer revealed multiexponential time constants of 0.08 ns (45%), 1.15 ns (25%) and 8.50 ns (29%) giving an average time constant ( $\langle\tau\rangle$ ) of 2.80 ns. For the donor-acceptor system (arginine capped QDs- EB labeled DNA) time constants are obtained as 0.09 ns (72%), 1.23 ns (18%) and 5.40 ns (8%) giving an average time constant ( $\langle\tau\rangle$ ) of 0.72 ns (Table 7.1). The substantial

shortening in the QDs excited state lifetime upon conjugate formation indicates conclusively that efficient FRET occurs from the QD donor to the EB-DNA acceptor. Taking the calculated quantum yield of Arg-capped QDs in absence of acceptor as 0.14 and based on the spectral overlap, we have estimated a FRET efficiency of 74% using Eq. 2.7b. The measured Förster distance,  $R_0$ , for the QD-DNA nanobioconjugate is 2.88 nm. The donor–acceptor distance (R) calculated using Eq. 2.6 is 2.42 nm (Table 7.1).

**Table 7.1.** Fitted decay time constants of QD and QD-(EB-DNA) complex from picosecond experiments. Values in parentheses represent the relative weight percentage of the time components.

System	$\tau_1$ [ps]	$\tau_2$ [ps]	$\tau_3$ [ps]	$\langle\tau\rangle$ [ps]
QD	85 (45)	1153 (26)	8527 (29)	2799
QD-EB-DNA	98 (73)	1239 (19)	5403 (8)	726

For better understanding of the energy transfer between the excited state of QDs with EB-DNA, it is essential to know the distribution of acceptor molecules around the QDs because this is a governing factor that can influence the efficient energy transfer as observed from the time resolved fluorescence studies. In this regard, we have applied a kinetic model developed by Tachiya for the quenching of luminescent probes [39, 40]. We have determined the values of the parameters  $m_t$ ,  $k_{qt}$ ,  $k_0$ ,  $m$ , and  $k_q$  by fitting Eq. 2.14 and 2.15 to the decay curves in the absence and presence of acceptor EB-DNA molecules.

Figure 7.2d shows the time resolved fluorescence transients of CdSe/ZnS QDs in absence and presence of EB-DNA molecules and black curves represents the result of fitting the curves with Eq. 7.7 and 7.8. The observed fluorescence transients were fitted using a nonlinear least squares fitting procedure (software SCIENTIST<sup>TM</sup>) to a function  $(X(t) = \int_0^t E(t')P(t-t')dt')$  comprising of the convolution of the instrument response function (IRF)  $(E(t))$  with exponential  $(P(t, m) = P(0)\exp\{-k_0t - m_t[1 - \exp(-k_{qt}t)] - m[1 - \exp(-k_qt)]\})$ . The purpose of this fitting is to obtain the decays in an analytic form suitable for further data analysis. As evident from the Figure 7.2d, the fitting of the decay curves according to the model is

reasonably well. The quenching parameters are summarized in Table 7.2. The quenching rate constant ( $k_{qt}$ ) due to unidentified traps on the surface of the nanocrystals are the same even after addition of acceptor (EB-DNA) molecules, and this indicates the average number of unidentified trap states to be the same. However, it is observed from Table 7.2 that the average number of unidentified traps state increases with addition of acceptor molecules. Since, there are still many unknown parameters in the QDs excitation dynamics, for an accurate interpretation of this observation a more complex model and a larger data set is required. As summarized in Table 7.2, the mean number of acceptor (EB-DNA) molecules associated with the QDs is 1.15 and the estimated rate constant for energy transfer ( $k_q$ ) per acceptor molecules is  $0.20 \text{ ns}^{-1}$ . The energy transfer rate calculated from conventional FRET model is found to be somewhat different ( $1.01 \text{ ns}^{-1}$ ) from the value obtained using Tachiya's model ( $0.20 \text{ ns}^{-1}$ ). However, as shown in Table 7.1, the contribution of the longer lifetime (8.52 ns) in the overall average lifetime of the donor is significant. Other lifetime values of 1.15 ns and 0.08 ns could be associated with the unidentified trap states on the QDs surface [41]. Thus, considering 8.52 ns to be excited state lifetime of the donor QDs, the estimated energy transfer rate is found to be  $0.33 \text{ ns}^{-1}$ , which is consistent with that from Tachiya model.

**Table 7.2.** Overview of the value of quenching parameters using a kinetic model.

System	$k_o[\text{ns}^{-1}]$	$m_t$	$k_{qt}[\text{ns}^{-1}]$	$m$	$k_q[\text{ns}^{-1}]$
QD	0.28	0.40	4.60	-	-
QD-EB-DNA	0.28	1.06	4.67	1.15	0.20

In order to confirm any structural perturbation in the native structure of the dodecamer DNA adsorbed onto the QDs surface, we have performed circular dichroism (CD) studies. As revealed from Figure 7.3a CD spectrum, the hybridized DNA used in our studies were in a B-form, evidenced by a negative band at 248 nm and a positive band at 280 nm [19, 42], also the structural integrity of DNA B-form is almost retained in the QD-DNA nanobioconjugates. Figure 7.3b shows the overall secondary structure of the QD conjugated dodecamer DNA at 20°C and 70°C temperatures. It is clear that both the peaks

at 252 nm and 280 nm are affected by the temperature-induced melting of the QD conjugated dodecamer DNA. The change in the molar ellipticity associated with the 252 nm peak has been monitored to construct the temperature-induced melting and rehybridization profiles of the QD conjugated dodecamer DNA, as shown in Figure 7.3c (melting) and 7.3d (rehybridization). The melting of DNA is accompanied by structural changes involving unwinding of the helix, destruction of major and minor grooves, and finally the separation of the two strands resulting in the formation of two single strands of complementary sequence. The melting and rehybridization temperatures have been estimated to be 42.6°C and 41.0°C, respectively, for the QD conjugated dodecamer DNA and this is in good agreement with the dodecamer DNA alone reported previously [43].

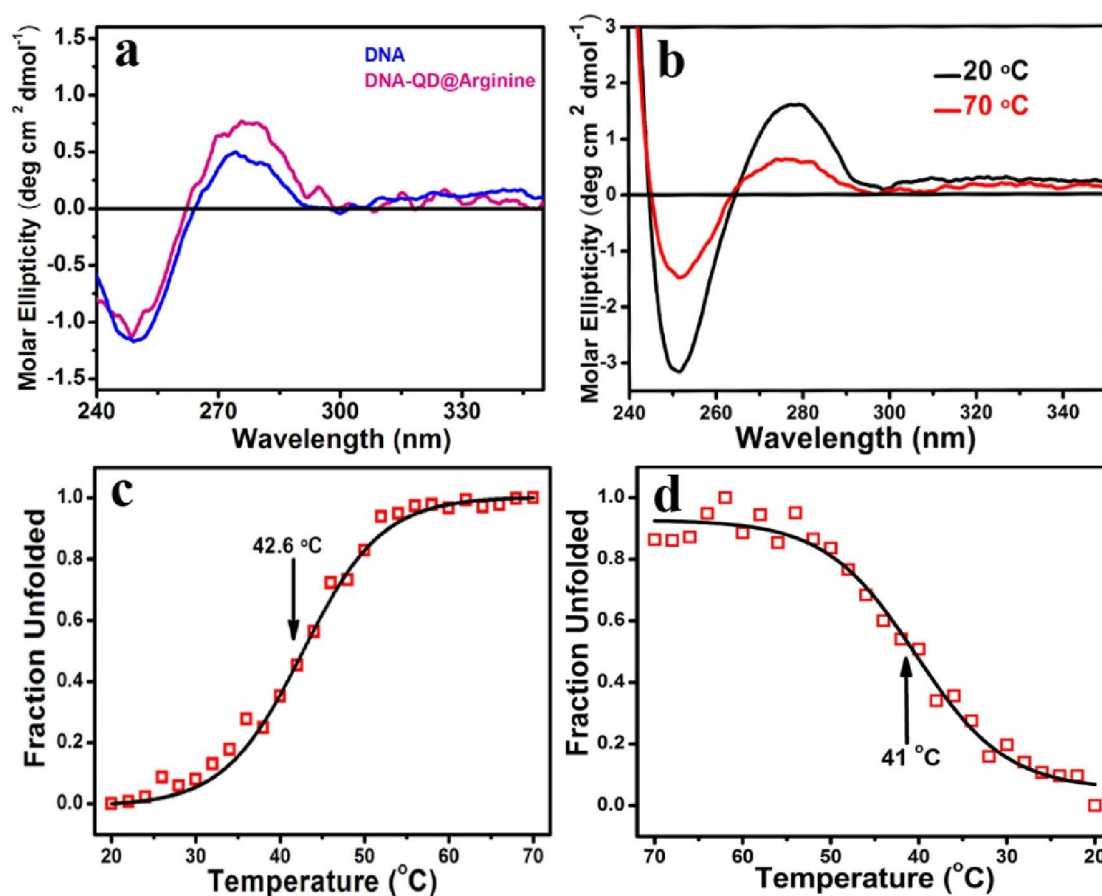


**Figure 7.3.** (a) Circular dichroism (CD) spectra of dodecamer DNA and dodecamer DNA conjugated to QDs. Structural integrity of the DNA in the QD-DNA conjugate is clearly evident. (b) CD spectra of dodecamer DNA-QD conjugates at two different temperatures. (c) and (d) the melting and rehybridization of dodecamer DNA conjugated to QDs. Solid lines are the fitted sigmoidal curve.

Figure (7.3c and 7.3d) show that the dodecamer is rehybridized into its original form maintaining the same hysteresis as it follows during its melting, which indicates that the  $\pi$  stacking interaction between the complementary base pair of the two strands is greater than the electrostatic interaction of each strand with the QDs. Moreover, an electrostatic interaction between the positively charged groups of the arg-capped QDs and the negatively charged DNA dodecamer, could have changed its conformation as well as its melting temperature and rehybridization pathway [44]. However, as revealed from the CD study, all of its characteristic conformational features remain the same, before and after conjugation with the QDs. So, it appears that hydrogen-bonding interactions (instead of electrostatic interactions) are playing the dominant role in the adsorption of DNA onto the surface of arg-capped QDs involving the protonated carboxyl surface groups of the thin solubilizing layer of amino acids around the QDs [45].

### **7.3. Conclusion**

In conclusion, we report on a convenient approach for preparing water-soluble, biocompatible QDs following a liquid-liquid interfacial ligand exchange method, where L-arginine acts as a capping ligand. The successful conjugation of arginine with the QDs has been confirmed by FTIR spectroscopy. We have employed picosecond-resolved spectroscopic measurements, to demonstrate a highly efficient FRET from arginine-capped CdSe/ZnS QDs (donor) to EB-DNA (acceptor). The corresponding donor-acceptor distance has been calculated to be 2.42 nm, which suggest an adsorptive interaction between the dodecamer DNA molecules and arginine-capped QDs. From CD spectroscopic studies it is found that the dodecamer DNA retained their structural integrity upon conjugation with the QDs. Moreover, temperature induced melting and rehybridization of the QD conjugated dodecamer DNA suggest that hydrogen-bonding interaction could be the associated mechanism operating during the formation of QD-DNA nanobioconjugates. Considering the spread in use of QDs and the number of applications employing QD bioconjugates, understanding the interactions between QDs and biomolecules is of considerable importance and multidisciplinary interest. So, it is expected that this study may prove to be useful in making sensitive FRET-based sensors.

## References

- [1] H. Mattoussi, J.M. Mauro, E.R. Goldman, G.P. Anderson, V.C. Sundar, F.V. Mikulec, M.G. Bawendi, Self-assembly of CdSe–ZnS quantum dot bioconjugates using an engineered recombinant protein, *J. Am. Chem. Soc.* 122 (2000) 12142.
- [2] D.V. Talapin, A.L. Rogach, A. Kornowski, M. Haase, H. Weller, Highly luminescent monodisperse CdSe and CdSe/ZnS nanocrystals synthesized in a hexadecylamine– trioctylphosphine oxide–trioctylphosphine mixture, *Nano Lett.* 1 (2001) 207.
- [3] T. Jamieson, R. Bakhshi, D. Petrova, R. Pocock, M. Imani, A.M. Seifalian, Biological applications of quantum dots, *Biomaterials* 28 (2007) 4717.
- [4] H. Li, Y. Yao, C. Han, J. Zhan, Triazole-ester modified silver nanoparticles: Click synthesis and Cd<sup>2+</sup> colorimetric sensing, *Chem. Commun.* (2009) 4812.
- [5] P. Brown, P.V. Kamat, Quantum dot solar cells. Electrophoretic deposition of CdSe-C-60 composite films and capture of photogenerated electrons with nC(60) cluster shell, *J. Am. Chem. Soc.* 130 (2008) 8890.
- [6] X. Michalet, F.F. Pinaud, L.A. Bentolila, J.M. Tsay, S. Doose, J.J. Li, G. Sundaresan, A.M. Wu, S.S. Gambhir, S. Weiss, Quantum dots for live cells, in vivo imaging, and diagnostics, *Science* 307 (2005) 538.
- [7] Q. Shen, J. Kobayashi, L.J. Diguna, T. Toyoda, Effect of ZnS coating on the photovoltaic properties of CdSe quantum dot-sensitized solar cells, *J. Appl. Phys.* 103 (2008) 084304.
- [8] W.C.W. Chan, S.M. Nie, Quantum dot bioconjugates for ultrasensitive nonisotopic detection, *Science* 281 (1998) 2016.
- [9] D. Zhou, J.D. Piper, C. Abell, D. Klenerman, D.-J. Kang, L. Ying, Fluorescence resonance energy transfer between a quantum dot donor and a dye acceptor attached to DNA, *Chem. Commun.* (2005) 4807.
- [10] G.P. Mitchell, C.A. Mirkin, R.L. Letsinger, Programmed assembly of DNA functionalized quantum dots, *J. Am. Chem. Soc.* 121 (1999) 8122.
- [11] I.L. Medintz, A.R. Clapp, H. Mattoussi, E.R. Goldman, B. Fisher, J.M. Mauro, Self-assembled nanoscale biosensors based on quantum dot FRET donors, *Nat. Mater.* 2 (2003) 630.

- [12] W.R. Algar, U.J. Krull, Luminescence and stability of aqueous thioalkyl acid capped CdSe/ZnS quantum dots correlated to ligand ionization, *Chem. Phys. Chem.* 8 (2007) 561.
- [13] H. Li, X. Wang, Z. Gao, Z. He, Gemini surfactant for fluorescent and stable quantum dots in aqueous solution, *Nanotechnology* 18 (2007) 205603.
- [14] X.Y. Wu, H.J. Liu, J.Q. Liu, K.N. Haley, J.A. Treadway, J.P. Larson, N.F. Ge, F. Peale, M.P. Bruchez, Immunofluorescent labeling of cancer marker Her<sub>2</sub> and other cellular targets with semiconductor quantum dots, *Nat. Biotech.* 21 (2003) 41.
- [15] W.W. Yu, E. Chang, J.C. Falkner, J. Zhang, A.M. Al-Somali, C.M. Sayes, J. Johns, R. Drezek, V.L. Colvin, Forming biocompatible and nonaggregated nanocrystals in water using amphiphilic polymers, *J. Am. Chem. Soc.* 129 (2007) 2871.
- [16] X. Gao, Y. Cui, R.M. Levenson, L.W.K. Chung, S. Nie, In vivo cancer targeting and imaging with semiconductor quantum dots, *Nat. Biotech.* 22 (2004) 969.
- [17] B. Dubertret, P. Skourides, D.J. Norris, V. Noireaux, A.H. Brivanlou, A. Libchaber, In vivo imaging of quantum dots encapsulated in phospholipid micelles, *Science* 298 (2002) 1759.
- [18] R. Mahtab, H.H. Harden, C.J. Murphy, Temperature- and salt-dependent binding of long DNA to protein-sized quantum dots: Thermodynamics of “inorganic protein”–DNA interactions, *J. Am. Chem. Soc.* 122 (1999) 14.
- [19] S.S. Narayanan, S.S. Sinha, P.K. Verma, S.K. Pal, Ultrafast energy transfer from 3-mercaptopropionic acid-capped CdSe/ZnS QDs to dye-labelled DNA, *Chem. Phys. Lett.* 463 (2008) 160.
- [20] H. Mattoussi, J.M. Mauro, E.R. Goldman, T.M. Green, G.P. Anderson, V.C. Sundar, M.G. Bawendi, Bioconjugation of highly luminescent colloidal CdSe–ZnS quantum dots with an engineered two-domain recombinant protein, *Phys. Status Solidi B.* 224 (2001) 277.
- [21] J.a. Liu, H. Li, W. Wang, H. Xu, X. Yang, J. Liang, Z. He, Use of ester-terminated polyamidoamine dendrimers for stabilizing quantum dots in aqueous solutions, *Small* 2 (2006) 999.
- [22] B.O. Dabbousi, J. RodriguezViejo, F.V. Mikulec, J.R. Heine, H. Mattoussi, R. Ober, K.F. Jensen, M.G. Bawendi, (CdSe)ZnS core-shell quantum dots: Synthesis and

characterization of a size series of highly luminescent nanocrystallites, *J. Phys. Chem. B* 101 (1997) 9463.

[23] C.J. Murphy, Peer reviewed: Optical sensing with quantum dots, *Anal. Chem.* 74 (2002) 520 A.

[24] C.B. Murray, D.J. Norris, M.G. Bawendi, Synthesis and characterization of nearly monodisperse CdE (E = sulfur, selenium, tellurium) semiconductor nanocrystallites, *J. Am. Chem. Soc.* 115 (1993) 8706.

[25] W.W. Yu, Y.A. Wang, X. Peng, Formation and stability of size-, shape-, and structure-controlled CdTe nanocrystals: Ligand effects on monomers and nanocrystals, *Chem. Mat.* 15 (2003) 4300.

[26] W.W. Yu, E. Chang, R. Drezek, V.L. Colvin, Water-soluble quantum dots for biomedical applications, *Biochem. Biophys. Commun.* 348 (2006) 781.

[27] H. Brooks, B. Lebleu, E. Vivès, Tat peptide-mediated cellular delivery: Back to basics, *Adv. Drug. Delivery Rev.* 57 (2005) 559.

[28] A. Giri, N. Goswami, P. Lemmens, S.K. Pal, Preparation of water soluble l-arginine capped CdSe/ZnS QDs and their interaction with synthetic DNA: Picosecond-resolved FRET study, *Mater. Res. Bull.* 47 (2012) 1912.

[29] C.N.R. Rao, K.P. Kalyanikutty, The liquid–liquid interface as a medium to generate nanocrystalline films of inorganic materials, *Acc. Chem. Res.* 41 (2008) 489.

[30] N. Varghese, C.N.R. Rao, Magnetic nanofilms of nickel prepared at the liquid–liquid interface, *Mater. Res. Bull.* 46 (2011) 1500.

[31] B. Trzaskowski, L. Adamowicz, P.A. Deymier, A theoretical study of zinc (II) interactions with amino acid models and peptide fragments, *J. Biol. Inorg. Chem.* 13 (2008) 133.

[32] X. Ai, Q. Xu, M. Jones, Q. Song, S.-y. Ding, R.J. Ellingson, M. Himmel, G. Rumbles, Photophysics of (CdSe)ZnS colloidal quantum dots in an aqueous environment stabilized with amino acids and genetically-modified proteins, *Photochem. Photobiol. Sci.* 6 (2007) 1027.

[33] P. Schapotschnikow, B. Hommersom, T.J.H. Vlugt, Adsorption and binding of ligands to CdSe nanocrystals, *J. Phys. Chem. C* 113 (2009) 12690.

- [34] J.Y. Rempel, B.L. Trout, M.G. Bawendi, K.F. Jensen, Density functional theory study of ligand binding on CdSe (0001), (0001), and (1120) single crystal relaxed and reconstructed surfaces: Implications for nanocrystalline growth, *J. Phys. Chem. B* 110 (2006) 18007.
- [35] J.K. Cooper, A.M. Franco, S. Gul, C. Corrado, J.Z. Zhang, Characterization of primary amine capped CdSe, ZnSe, and ZnS quantum dots by FT-IR: Determination of surface bonding interaction and identification of selective desorption, *Langmuir* 27 (2011) 8486.
- [36] C. Bullen, P. Mulvaney, The effects of chemisorption on the luminescence of CdSe quantum dots, *Langmuir* 22 (2006) 3007.
- [37] S. Kumar, S.B. Rai, Spectroscopic studies of L-arginine molecule, *Indian J. Pure Appl. Phys.* 48 (2010) 251.
- [38] D. Kalaiselvi, R.M. Kumar, R. Jayavel, Single crystal growth and properties of semiorganic nonlinear optical L-arginine hydrochloride monohydrate crystals, *Cryst. Res. Technol.* 43 (2008) 851.
- [39] T. Masanori, Application of a generating function to reaction kinetics in micelles. Kinetics of quenching of luminescent probes in micelles, *Chem. Phys. Lett.* 33 (1975) 289.
- [40] M. Tachiya, Kinetics of quenching of luminescent probes in micellar systems. II, *J. Chem. Phys.* 76 (1982) 340.
- [41] S. Sadhu, K.K. Haldar, A. Patra, Size dependent resonance energy transfer between semiconductor quantum dots and dye using FRET and kinetic model, *J. Phys. Chem. C* 114 (2010) 3891.
- [42] R. Sarkar, S.K. Pal, Ligand-DNA interaction in a nanocage of reverse micelle, *Biopolymers* 83 (2006) 675.
- [43] D. Banerjee, S.K. Pal, Direct observation of essential DNA dynamics: Melting and reformation of the DNA minor groove, *J. Phys. Chem. B* 111 (2007) 10833.
- [44] R. Prado-Gotor, E. Grueso, A kinetic study of the interaction of DNA with gold nanoparticles: Mechanistic aspects of the interaction, *Phys. Chem. Chem. Phys.* 13 (2011) 1479.

[45] W.R. Algar, U.J. Krull, Adsorption and hybridization of oligonucleotides on mercaptoacetic acid-capped CdSe/ZnS quantum dots and quantum dot–oligonucleotide conjugates, *Langmuir* 22 (2006) 11346.

## Chapter 8

# Novel Synthesis of Biocompatible and Highly Luminescent Metal Cluster and their Characterization

### 8.1. Introduction

Atomically precise metal particles, comprising of only a few atoms with dimensions comparable to the Fermi wavelength of electrons, are called quantum clusters (QCs). The resulting quantum confinement produces unique optical, electronic and chemical properties of QCs that are dramatically different from that of nanoparticles (NPs) which exhibit plasmon absorption. Unusual properties of QCs make them attractive as novel systems of choice for exploring a wide range of phenomena like catalysis, metal ion sensing, bioimaging [1-4]. Several monolayer-protected noble metal QCs have been reported till date and a few crystal structures are also known [5-8]. Current research in this area is mostly limited to noble metals, especially Au and Ag, due to their inertness, stability and ease of synthesis. Particularly, QCs of Au ( $\text{Au}_{\text{QCs}}$ ) have been well studied because of their unusual stability at ambient conditions and wide spectral tunability, yielding diverse optoelectronic properties [9-15]. Efforts to synthesize atomically precise  $\text{Ag}_{\text{QCs}}$  have been limited due to their higher reactivity [16, 17]. Some  $\text{Ag}_{\text{QCs}}$  have also been crystallized [18]. More recently, a growing number of studies have reported  $\text{Cu}_{\text{QCs}}$  and  $\text{Pt}_{\text{QCs}}$  [19, 20]. In addition to the nature of the metal, nature of the ligand can also affect the stability and properties of QCs. Macromolecular templates, where proteins act as ligands, are rather recent entries in the field [21-23]. Several proteins have been used as ligands for such cluster synthesis due to their biocompatibility and high photoluminescence quantum yield. The general synthetic route is to first form a metal-protein adduct followed by reduction at elevated pH where the protein acts as the reducing agent or by reduction using an external reducing agent and confining the newly formed cluster core by the protein scaffold simultaneously. These highly luminescent protein-protected clusters are being used as sensors for environmentally hazardous metal ions and other sensitive molecules such as explosives. A number of groups have used protein-protected luminescent QCs in biolabeling [3, 24]. It is anticipated that noble metal QCs would be less toxic and more

suitable as carriers of biological cargo [25]. However, therapeutic studies have shown that they may not be completely free of side effects [26]. For this field to evolve, it is imperative that newer QCs be explored with characteristics of noble metal QCs but with better biocompatibility and newer properties. Apart from being better biocompatible and cheaper, unique catalytic and magnetic properties of Fe make Fe<sub>QCs</sub> important candidates among the yet to be explored QCs. Since the first example of metallic Fe NPs (~100 nm) [27], several attempts have been made to characterize them [28-30]. Although recipes to synthesize metallic Fe NPs in the 3-100 nm window exist, new approaches are required for synthesizing Fe<sub>QCs</sub>. Nanometer sized Fe<sup>0</sup> inherently suffers from instability because of easy surface oxidation upon exposure to air and in presence of water, making the synthesis of Fe-clusters difficult. Nevertheless, it is important to note that Fe-clusters are known in the gas phase [31-34]. Obviously, suitable chemical procedures and appropriate protection would enable their synthesis in the solution state.

In this chapter, we describe the first efficient synthesis of highly luminescent and water-soluble Fe<sub>QCs</sub>, starting from Hemoglobin (Hb), a Fe-containing metalloprotein which acts as the iron source as well as the protecting agent. We have employed an efficient ligand exchange strategy with a smaller ligand, trioctyl phosphine oxide (TOPO), and subsequent phase transfer of the cluster from water to chloroform for detailed structural characterization. A number of complimentary experimental techniques, including mass spectroscopy, NMR, FT-IR and optical spectroscopy, were used to obtain the precise molecular signature of the clusters in the solution phase. We believe this work will enrich the area further and open a new window to the theoretical as well as the experimental community to understand and evolve this system towards real applications.

## **8.2. Result and Discussion**

### **8.2.1. Atomically Precise Luminescent Iron Clusters in Solution [35]:**

Hemoglobin is a major component of blood that transports oxygen from the respiratory organs (lungs or gills) to the rest of the body. It contains Fe ion, present either as Fe<sup>2+</sup> or Fe<sup>3+</sup>, coordinated by four nitrogen atoms of porphyrin present in the protein. In this study, we used Hb as a source of Fe ion as well as the protecting agent to make luminescent Fe<sub>QCs</sub>. The synthetic approach relies on the extraction of the porphyrin-bound Fe<sup>2+</sup>/Fe<sup>3+</sup> in

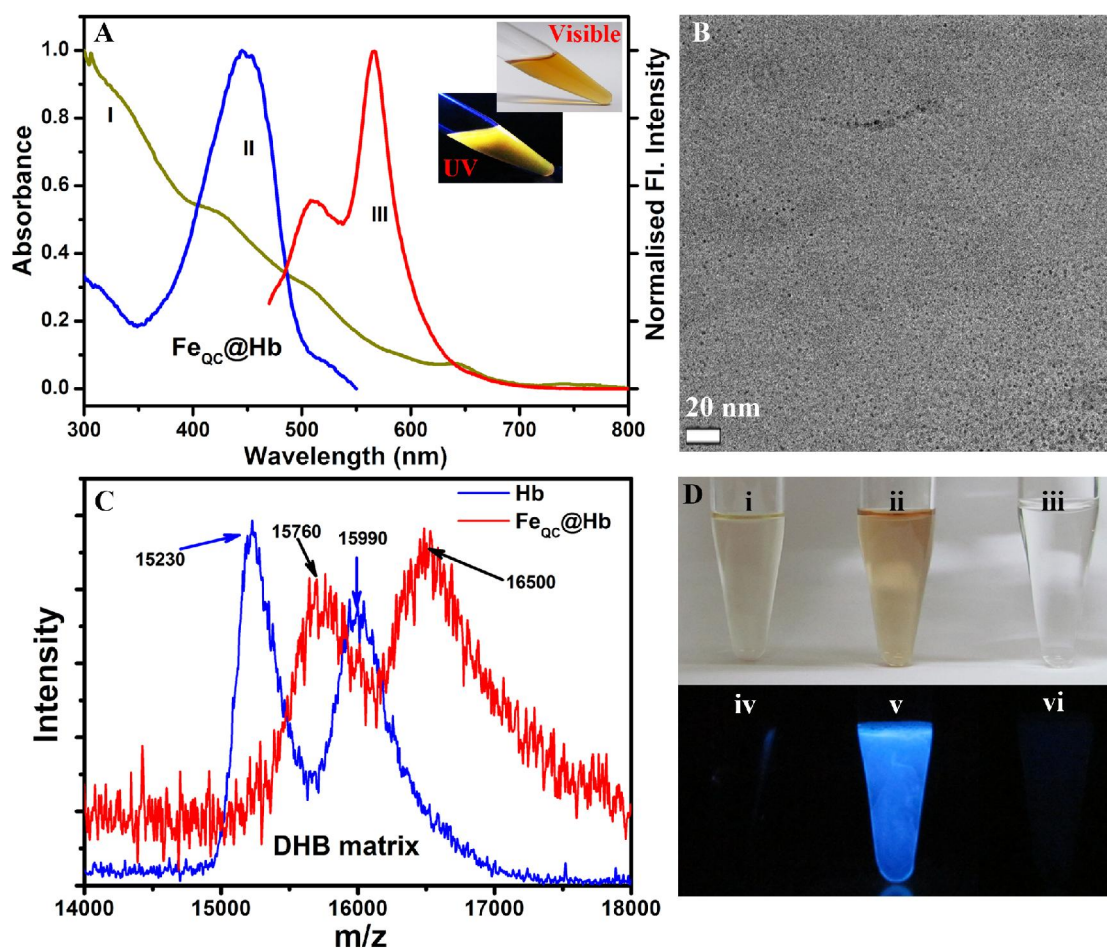


**Figure 8.1.** (A) UV-vis absorption spectrum (yellow) of water soluble cluster indicates the discrete, molecular like bands. Excitation (blue) and PL (red) spectra of Fe<sub>QC</sub>@Hb in water where, excitation wavelength = 530 nm and PL wavelength = 565 nm. (B). TEM image of Fe<sub>QC</sub>@Hb shows a core size of less than 2 nm. Several tiny particles of nearly uniform size are spread over the grid. (C). MALDI-TOF mass spectra of Hb (blue) and Fe<sub>QC</sub>@Hb (red) in the linear positive mode using dihydroxybenzoic acid (DHB) matrix. (D). Upper panel: Bright field photographs of luminol-hydrogen peroxide mixture after the addition of (i) Fe<sub>QC</sub>@Hb (ii) Hb and (iii) water (control). Lower panel: Dark field photograph of luminol-hydrogen peroxide mixture after the addition of (iv) Fe<sub>QC</sub>@Hb (v) Hb and (vi) water (control). Note that, the chemiluminescence observed for luminol-hydrogen peroxide mixture (vi) is very poor; however, increases several fold in presence of Hb (e) because of the presence of Fe<sup>2+</sup> and Fe<sup>3+</sup>. In case of Fe<sub>QC</sub>@Hb, the solution is not showing any chemiluminescence revealing that Fe is in zero oxidation state.

Hb-matrix using piperidine followed by the reduction of Fe<sup>2+</sup>/Fe<sup>3+</sup> with NaBH<sub>4</sub> at room temperature (details in 3.2.9). After ~12 hrs of incubation with NaBH<sub>4</sub>, the solution turned yellowish brown and showed strong yellow luminescence under UV light (Figure 8.2), indicating a change in the oxidation state of Fe atom in Hb-matrix. After

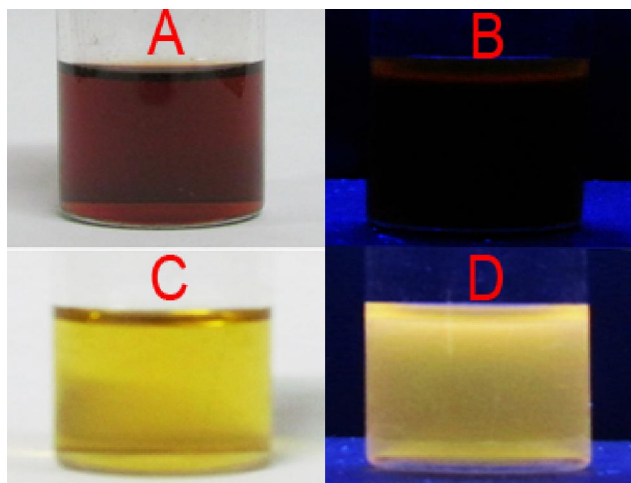


**Figure 8.2.** Photographs of (A) Hb (left upper panel) and (C) Fe<sub>QC</sub>@Hb (left lower panel) in water-piperidine solvent and their corresponding photographs (B) (right upper panel) and (D) (right lower panel) under UV light. Change in colour (A to C i.e., brown to yellow) under visible light indicates the change of Fe oxidation state.

lyophilization and re-suspension of the product in water, the aqueous solution exhibited the same yellow luminescence under UV light (inset of Figure 8.1A). The aqueous phase also showed discrete bands centered at 344 (3.60), 420 (2.95), 507 (2.45) and 639 nm (1.94 eV) (Figure 8.1A). Such molecule-like discrete bands are unique to QCs [6]. The absence of any characteristic band corresponding to Fe NP (at 360 nm) [30] further confirmed that the Fe<sub>QCs</sub> present in the aqueous phase were nearly pure in the as-synthesized form and were mostly free of large NPs. The Fe<sub>QCs</sub> showed luminescence band at 567 nm (2.19 eV) upon photo-excitation at 530 nm (2.34 eV) (Figure 8.1A). The quantum yield (QY) of Fe<sub>QCs</sub> in water (at 565 nm) was determined to be 10%, using Rhodamine 6G (QY = 95% in CH<sub>3</sub>CH<sub>2</sub>OH) as the reference.

It is well known that the intrinsic fluorescence of proteins, due to aromatic amino acids like tryptophan, can show a tail in the blue region. Furthermore, Hb consists of four porphyrin moieties which are well-known to be red emitting. To rule out potential artifacts, we conducted several control experiments by taking account of all potential products that might have formed after the reaction of NaBH<sub>4</sub> and piperidine, in presence of specific proteins (Figure 8.3-8.10). First, we considered apo-myoglobin, as Hb contains four myoglobin units. The observed excitation as well as the emission peaks (Figure 8.3)

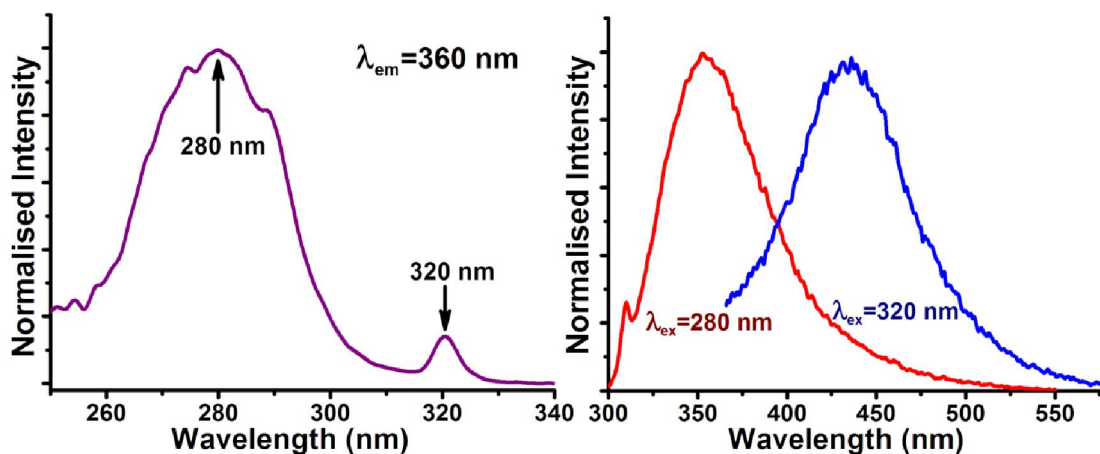


**Figure 8.3.** Excitation (left) and PL (right) spectra of Apo-myoglobin after the addition of piperidine and sodium borohydride indicates that 440 nm emission peak (blue) is originate from protein. Arrows indicate the excitation peaks. The peak at 280 nm is attributed to the tryptophan residues in Apo-myoglobin. The other peak at 320 nm is originated from the protein (Apo-myoglobin), which may be attributed to the photoproducts of some aromatic amino acids.

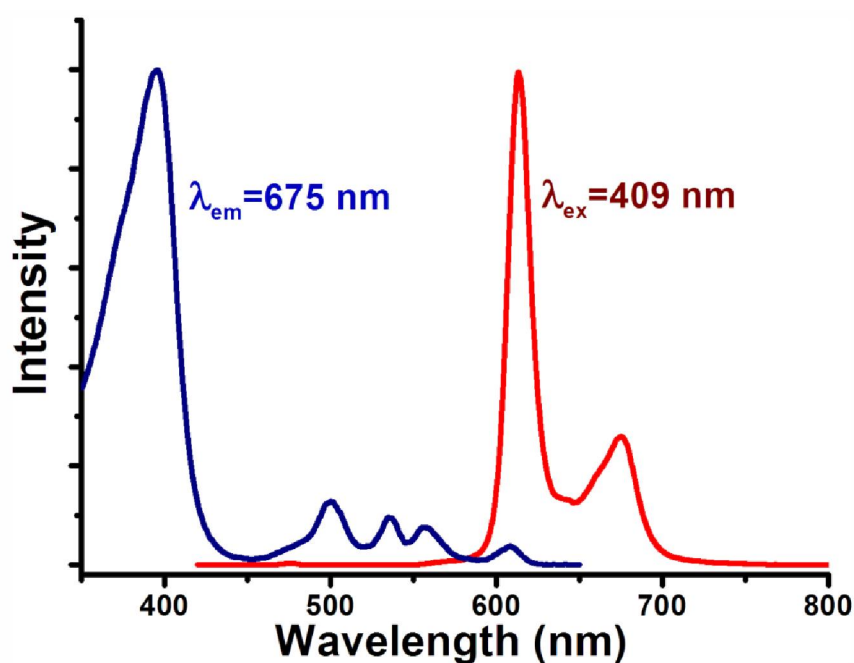
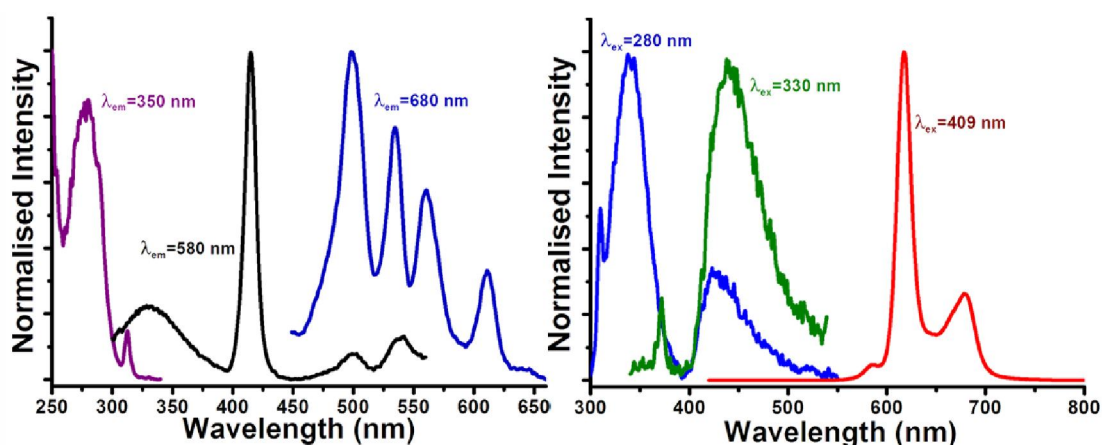


**Figure 8.4.** Excitation (blue) and PL (red) spectra of Hemato-porphyrin after the treatment with piperidine and sodium borohydride.

clearly rule out the possibility of any photoluminescence (PL) due to protein residues peaking at 565 nm. Second, we considered hemato-porphyrin as a prototype of the porphyrin unit present in the protein and performed the same experiment. Upon the

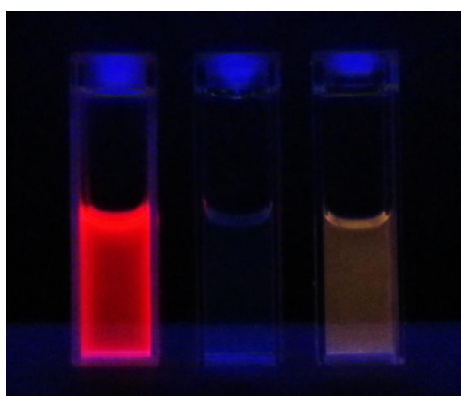
treatment of  $\text{NaBH}_4$  and piperidine, the PL peaks of hemato-porphyrin remained unchanged (Figure 8.4). The observation indicates that porphyrin moiety is not responsible for the 565 nm PL peak. Finally, hemato-porphyrin was attached to apo-myoglobin as a mimic of Hb (without iron) and treated with  $\text{NaBH}_4$  and piperidine. Binding of apo-myoglobin with hemato-porphyrin was checked with lifetime measurements (Figure 8.9). The figure indicates that the decay is slower compared to hemato-porphyrin after the treatment. In Figure 8.5, absence of the 565 nm peak justifies the role of Fe in the yellow luminescence. Our control experiments rule out the possibility of any kind of PL contribution from the protein matrix and support the formation of a new type of material in the protein environment. The occurrence of visible luminescence in a material composed of iron is intriguing. Why should a non-noble metal like Fe show such unique optical properties is still unclear at this time and detailed theoretical studies are needed to establish the precise origin of the optical bands.

Transmission electron microscopic (TEM) images indicated the presence of a large quantity of tiny particles with good uniformity (Figure 8.1B). However, conventional HRTEM is not a reliable technique for evaluating the size distribution of QCs due to electron beam-induced coalescence [36]. Although X-ray crystallography is the best method to understand the structure and composition of any material in detail, till date no



**Figure 8.5.** Excitation (left) and PL (right) spectra of Apo-myoglobin-Hemato-porphyrin complex after the addition of piperidine and sodium borohydride. Absence of any yellow luminescence justifies the role of Fe ions for the generation of 565 nm PL peak.

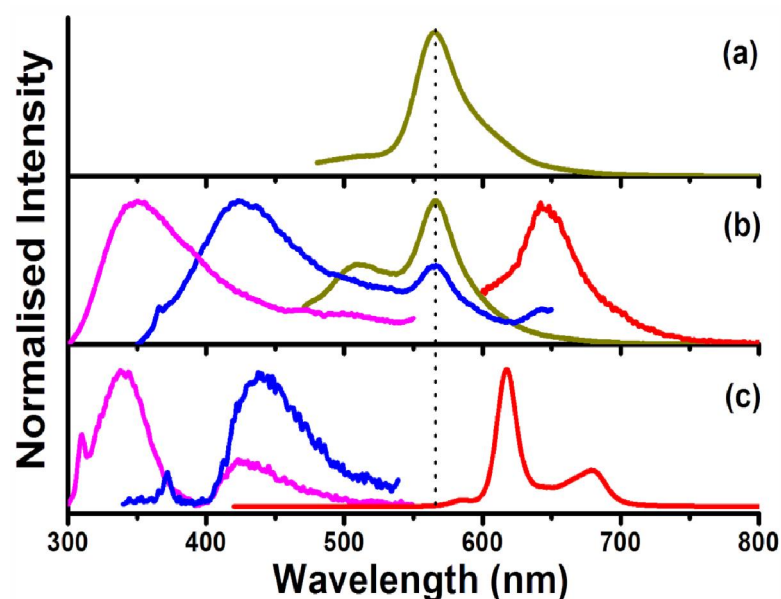
protein-protected clusters could be crystallized. Mass spectroscopy is a robust technique for characterizing proteins and metal clusters. Matrix-assisted laser desorption ionization mass spectrometry (MALDI MS) and electrospray ionization mass spectrometry (ESI MS) are better suited to study the composition of QCs. MALDI MS of Hb, using DHB as matrix, showed two peaks at  $m/z$  15,230 and 15,990 due to  $\alpha$ -globin chain (MW: 15126.4 Da) and  $\beta$ -globin chain (MW: 15867.2 Da) of Hb. These peaks were shifted to  $m/z$  values 15,760 and 16,500, respectively in the case of  $\text{Fe}_{\text{QCs}}\text{@Hb}$  (Figure 8.1C) confirming successful cluster formation. This mass difference corresponds to 7-10 Fe atoms and the composition can be roughly assigned as  $\text{Fe}_{7-10}\text{@Hb}$ . However, due to resolution limitations at higher mass range, exact number of Fe atoms, determined from the mass difference, may not be correct. This problem was circumvented by a ligand-exchange strategy with a small ligand, tri-octylphosphineoxide (TOPO) (see later in the text). The ligand-exchanged clusters were characterized using ESI MS analysis, a more accurate technique for assigning composition of molecules containing multiple isotopes.



**Figure 8.6.** Photographs of Hemato-porphyrin, Apo-myoglobin and Holo-myoglobin (from left to right; after the addition of piperidine and sodium borohydride) under visible (upper panel) and UV light (lower panel). The photographs show the difference of PL under same excitation (365 nm UV light).

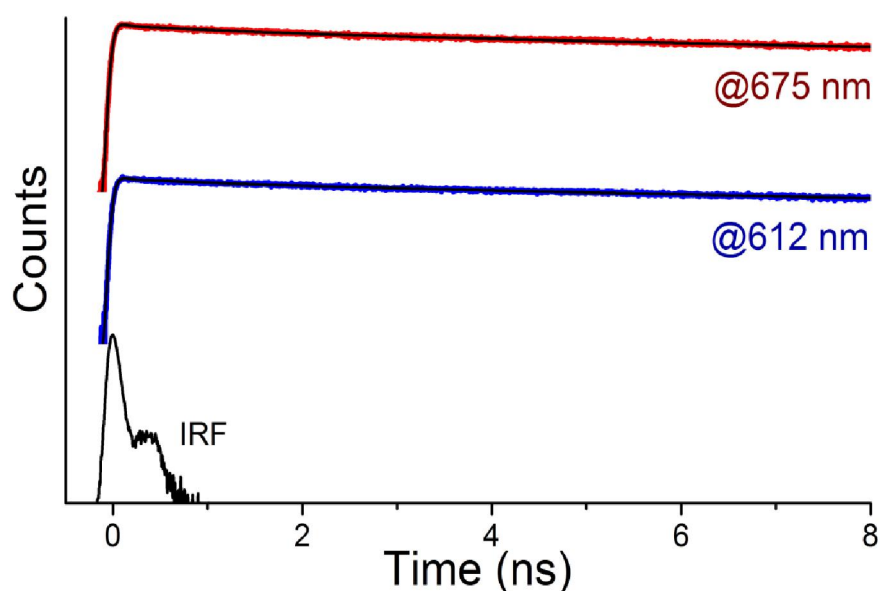
The oxidation state of Fe was investigated by a number of techniques. X-ray photoelectron spectroscopy (XPS) is the most appropriate method to confirm the oxidation state of the core for atomically precise noble metal clusters. In the present study, although we attempted to obtain the XPS spectrum, due to inherent poor signal intensity of Fe 2p in XPS as well as low density of cluster in the protein, we could not establish the oxidation

state of Fe in cluster. Instead, we have performed an indirect method to verify the oxidation state of Fe that we refer as “luminal experiment” (details in 3.2.11). Briefly, Hb-bound  $\text{Fe}^{2+}/\text{Fe}^{3+}$  in blood is a catalyst for the chemiluminescence reaction that causes luminol to intensely glow blue in presence of peroxide [37]. During this reaction,  $\text{Fe}^{2+}/\text{Fe}^{3+}$  is reduced with the concomitant oxidation of  $\text{H}_2\text{O}_2$  to  $\text{O}_2$ . However, if Fe is already in ‘zero’ oxidation state, it cannot catalyze the chemiluminescence reaction. Unlike the case with Hb,  $\text{Fe}_{\text{QC}}@\text{Hb}$  could not induce a blue glow in a mixture of luminol and  $\text{H}_2\text{O}_2$  (Figure 8.1D) suggesting that the as-prepared QCs are in metallic state.

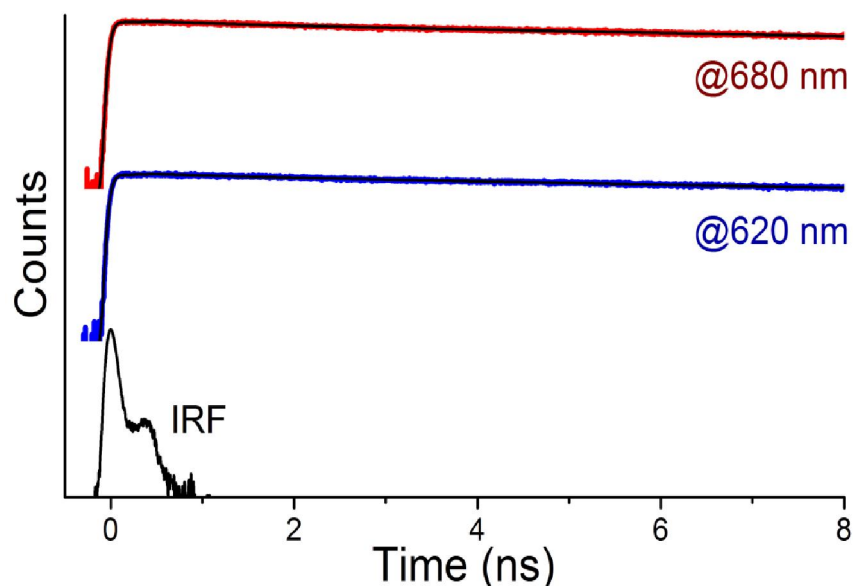


**Figure 8.7.** PL spectra of (a)  $\text{Fe}_{\text{QC}}@\text{TOPO}$  in chloroform, (b)  $\text{Fe}_{\text{QC}}@\text{Hb}$  and (c) Apo-myoglobin-Hemato-porphyrin complex after the addition of piperidine and sodium borohydride. Excitation wavelengths are 280 nm for pink, 330 nm for blue, 450 nm for yellow and 580 nm for red. The spectra clearly notify that 565 nm peak is due to  $\text{Fe}_{\text{QC}}$ s, not from any protein residues.

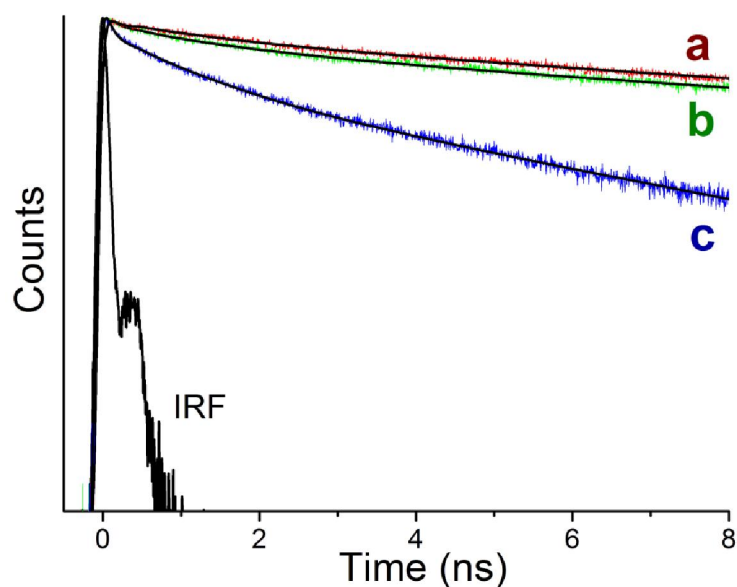
Although water-soluble, protein protected  $\text{Fe}_{\text{QC}}$ s showed evidence of high stability and quantum efficiency, but a major problem was the accurate molecular identification from MALDI MS analysis. To work in a lower mass range, we chose TOPO (tri-octylphosphineoxide), an organic ligand, for ligand exchange as well as for transferring the  $\text{Fe}_{\text{QC}}$ s into chloroform (details in 3.2.10). TOPO-capped  $\text{Fe}_{\text{QC}}$ s ( $\text{Fe}_{\text{QC}}@\text{TOPO}$ ) in chloroform also exhibited discrete, molecule-like bands at 355 (3.49), 402 (3.09), 516 (2.40), and 570 (2.18 eV) (Figure 8.11A).



**Figure 8.8.** Picosecond-resolved fluorescence transients (Y axis is in ln scale) of Hemato-porphyrin, after the addition of piperidine and sodium borohydride, collected at 612 nm (blue) and 675 nm (red) respectively. Excitation wavelength was 375 nm in both cases. Note that the transients of  $\text{Fe}_{\text{QC}}@\text{Hb}$  or  $\text{Fe}_{\text{QC}}@\text{TOPO}$  (See Figure 2c in the manuscript) were faster than these PL decays (Table 8.1) indicating the origin of 565 nm PL from different species in the  $\text{Fe}_{\text{QC}}$  samples apart from porphyrin unit. Base lines are shifted for clarity.

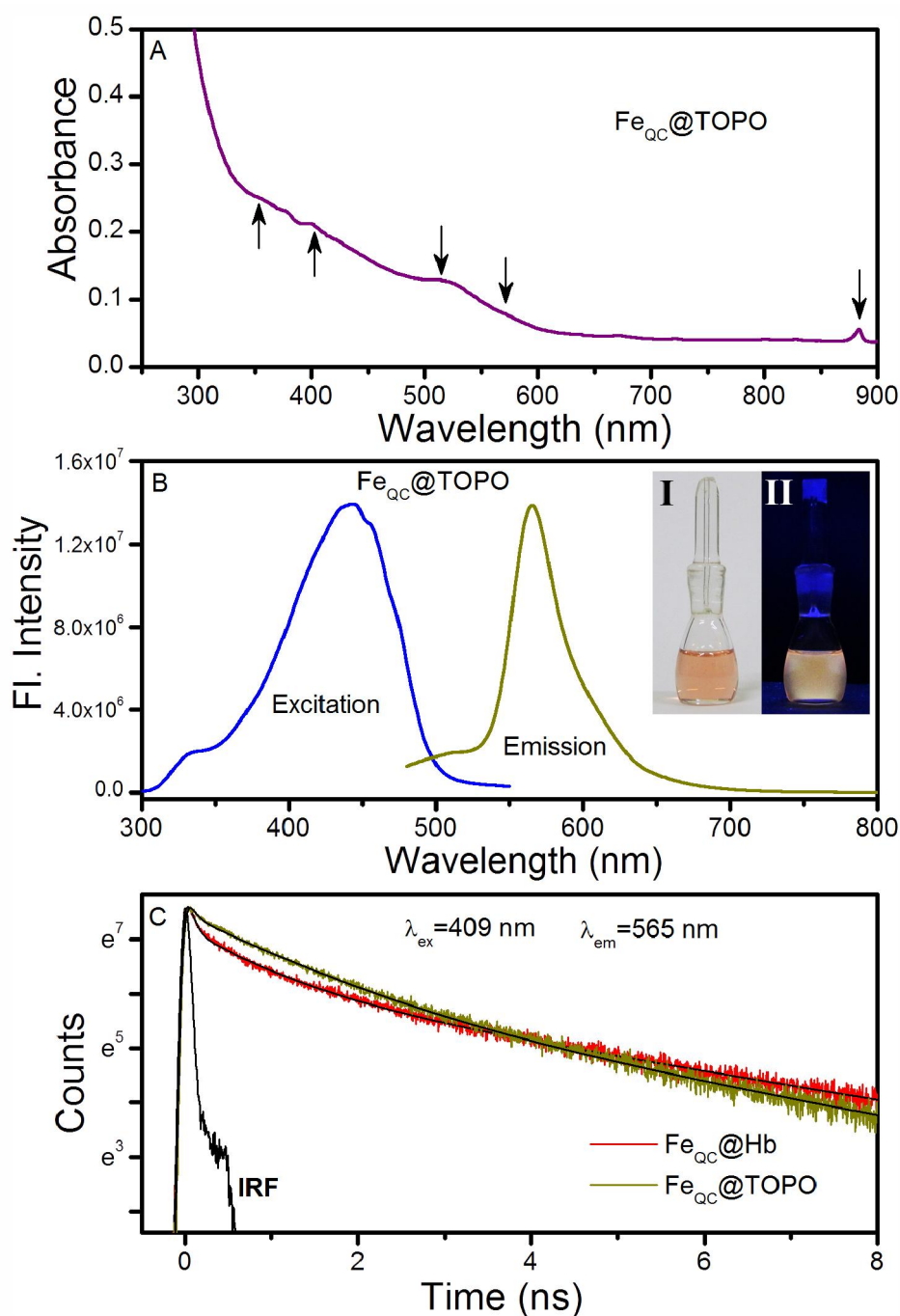


**Figure 8.9.** Picosecond-resolved fluorescence transients (Y axis is in ln scale) of Apo-myoglobin-Hemato-porphyrin complex, after the treatment with piperidine and sodium borohydride, collected at 620 nm (red) and 680 nm (blue), respectively. Excitation wavelength was 375 nm. The decay transients are found to be slower after the treatment compared to Hemato-porphyrin suggesting the binding of Hemato-porphyrin to Apo-myoglobin. Base lines are shifted for clarity.

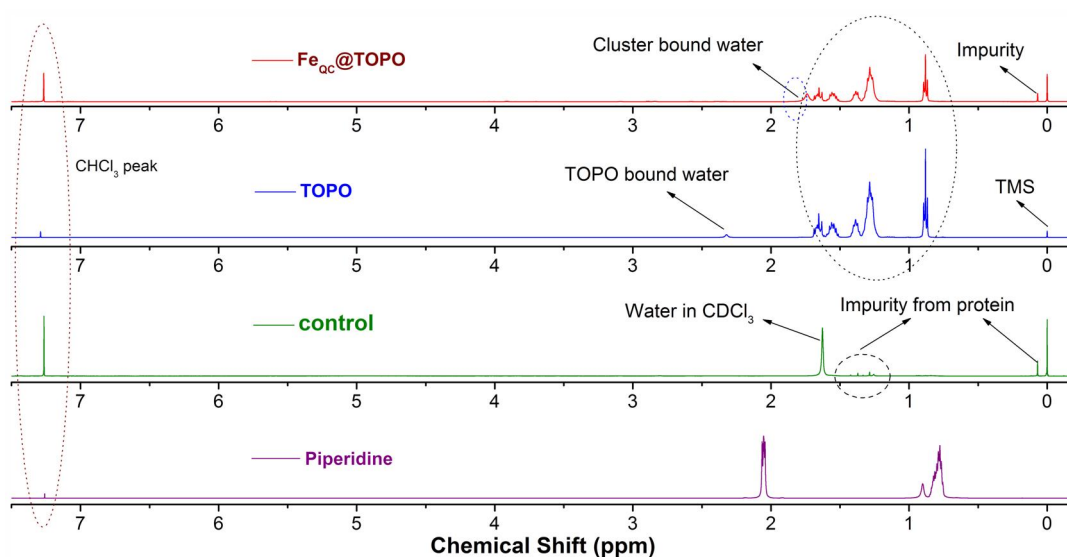


**Figure 8.10.** Picosecond-resolved fluorescence transients (Y axis is in ln scale) of (a) Apo-myoglobin-Hemato-porphyrin complex, (b) Hemato-porphyrin and (c)  $\text{Fe}_{\text{QC}}@\text{Hb}$ , collected at 650 nm respectively. Excitation wavelength was 375 nm. (All the decays have been taken after the treatment of sodium borohydride in water-piperidine mixture). Decay of  $\text{Fe}_{\text{QC}}@\text{Hb}$  is different from treated Hemato-porphyrin and Hemato-porphyrin-Apo myoglobin complex, suggesting that the peak at 647 nm originates from the QC's.

The bands were shifted from the corresponding bands of  $\text{Fe}_{\text{QC}}@\text{Hb}$  in aqueous medium (Figure 8.1A). Note that during ligand exchange, phase transfer was partial which indicated that only a part of the clusters is present in the aqueous phase. Excitation and photoluminescence (PL) spectra of  $\text{Fe}_{\text{QC}}@\text{TOPO}$  in chloroform are shown in Figure 8.11B.  $^1\text{H-NMR}$  experiments showed the chloroform layer, containing TOPO, to be free of Hb or piperidine (Figure 8.12). The presence of tiny  $\text{Fe}_{\text{QC}s}$  in the chloroform layer was verified from TEM images and energy dispersive spectroscopy (Figure 8.13). The clusters aggregated upon long-time electron beam irradiation forming nanoparticles (Figure 8.13), as seen before in the case of Au clusters [36]. Therefore, it is fair to conclude that the 565 nm peak originates solely from  $\text{Fe}_{\text{QC}}@\text{TOPO}$ . We note that the PL peak remained constant during phase transfer while the absorption spectra changed. For Au clusters, Negishi *et al* have shown that when the core size changes from  $\text{Au}_{10}$  to  $\text{Au}_{18}$  the lowest energy absorption peak changes from 330 nm to 570 nm, whereas the PL maximum remains constant at 1.5 eV [14]. Akin to the Au clusters, we anticipate that iron



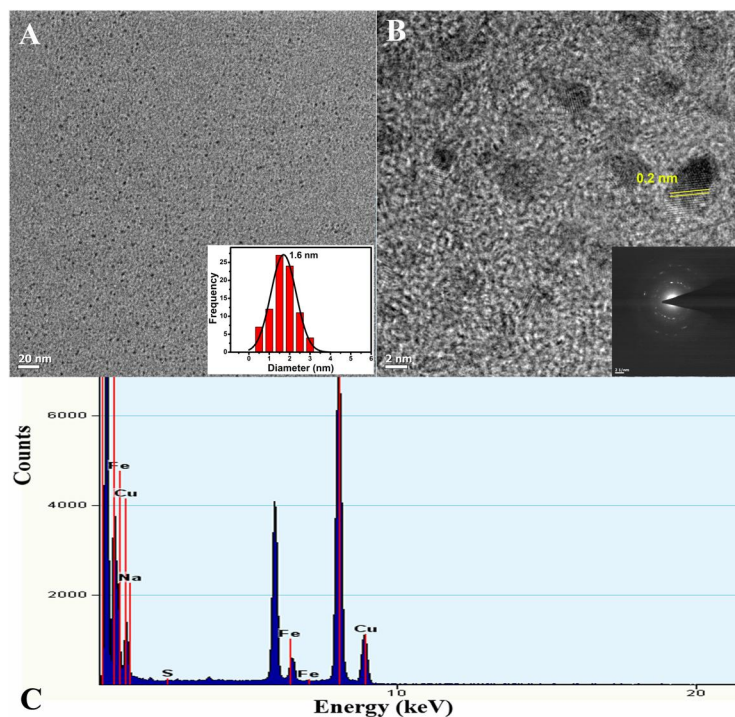
**Figure 8.11.** (A). UV-vis absorption spectrum of  $\text{Fe}_{\text{QC}}@\text{TOPO}$  in chloroform after solvent correction. Arrows indicate the absorption bands. (B). Excitation and PL spectra of  $\text{Fe}_{\text{QC}}@\text{TOPO}$  in chloroform solution. Inset shows the photograph of the cluster solution in chloroform under (I) visible and (II) UV light. (C). Photoluminescence decay of  $\text{Fe}_{\text{QC}}@\text{Hb}$  and  $\text{Fe}_{\text{QC}}@\text{TOPO}$  with instrument response function (IRF)  $\sim 60$  ps. Standard error of decay time components is  $\sim 10\%$ .



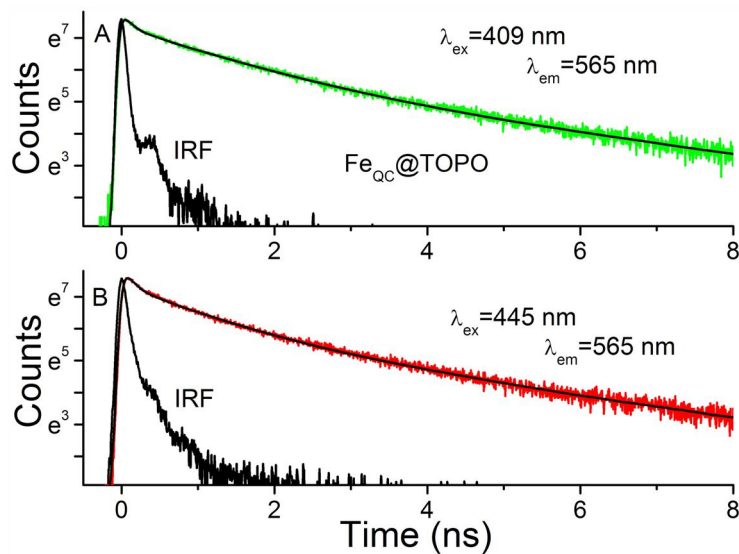
**Figure 8.12.**  $^1\text{H-NMR}$  spectra of piperidine, TOPO,  $\text{Fe}_{\text{QC}}@\text{TOPO}$  and the control sample in  $\text{CDCl}_3$  solution. For control, phase transfer has been performed by taking 3 mL of chloroform on the bottom of 3.0 mL (10 mg/ mL) of aqueous  $\text{Fe}_{\text{QC}}@\text{Hb}$  solution. The mixture was gently stirred for 8-12 hrs at 298 K. Finally, the solution in chloroform was lyophilized and  $\text{CDCl}_3$  was added to perform the NMR experiment. From the figure it is clear that  $\text{Fe}_{\text{QC}}@\text{TOPO}$  is free from piperidine and protein residues.

clusters with different core sizes present in chloroform could have similar luminescence, however, with different extinction compared to the clusters present in water. The solution of  $\text{Fe}_{\text{QC}}@\text{TOPO}$  was brown under visible light but exhibited a bright yellow color when irradiated with a UV light (Figure 8.11B inset). Using Rhodamine 6G as the reference, the QY of the  $\text{Fe}_{\text{QC}}@\text{TOPO}$  was determined to be 12%. Figure 2C shows the decay transients of the  $\text{Fe}_{\text{QC}}\text{s}$  before and after phase transfer. Luminescence lifetime values of the  $\text{Fe}_{\text{QC}}\text{s}$ , obtained from luminescence transients observed at 565 nm were 0.08 (64%), 0.91 (22%), and 3.90 (14%) ns in water and 0.11 (43%) and 1.14 (38%), and 3.60 (19%) ns in chloroform. The observed differences of the transients are not very significant and probably arise due to reduction of the non-radiative decay in non-polar chloroform [38]. The luminescence transients were found to be almost invariant as a function of excitation wavelength (375, 409 and 445 nm), which provided strong evidence that the observed clusters have similar luminescence profile (Figure 8.14).

In order to obtain more definite mass spectral signatures, we performed ESI MS analysis of TOPO capped  $\text{Fe}_{\text{QC}}\text{s}$  in 9:1 chloroform:acetonitrile in positive ion mode, in the  $m/z$  range of 100-4000. TOPO showed an intense peak at  $m/z$  387 due to its molecular ion peak. The



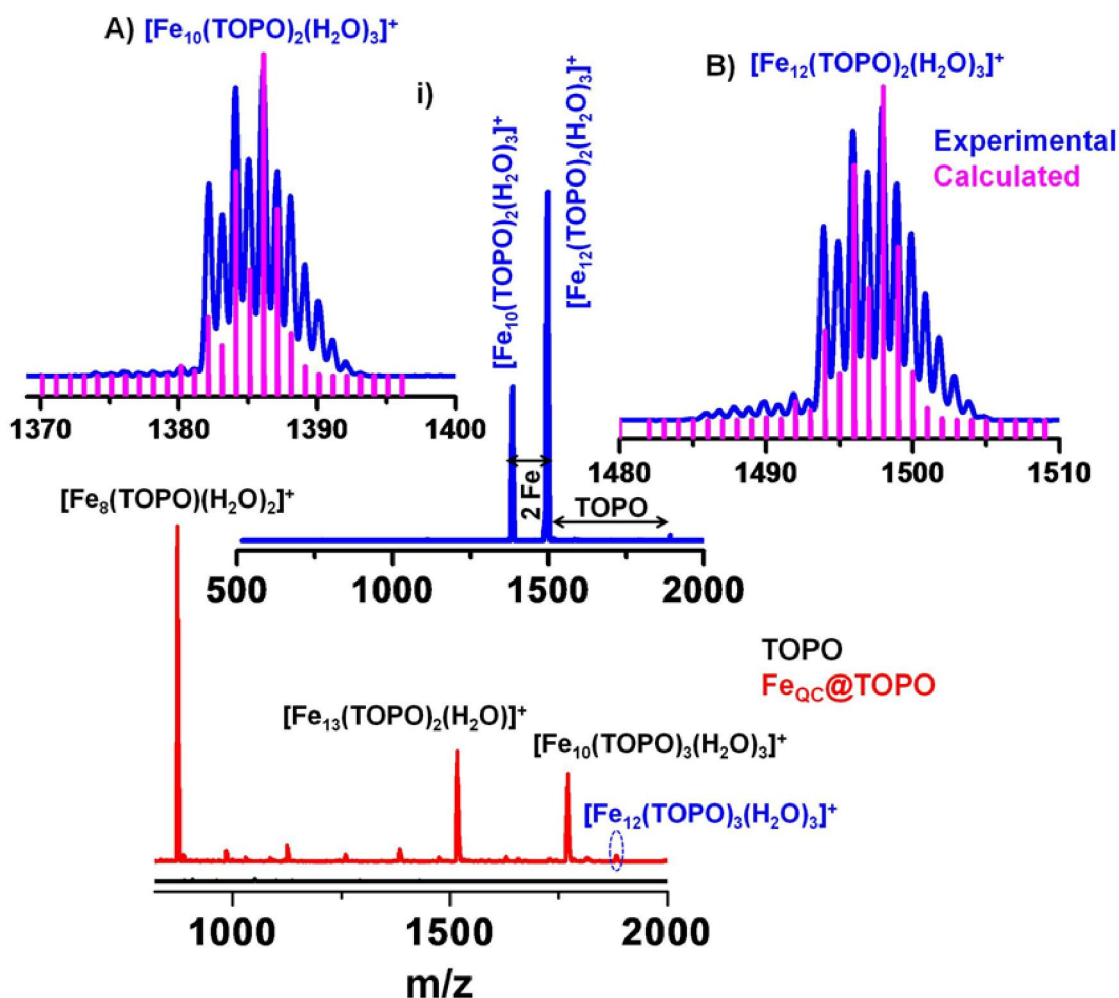
**Figure 8.13.** TEM image (A) of  $\text{Fe}_{\text{QC}}@$ TOPO shows the presence of tiny QCs. Inset shows the size distribution of the QCs. The scale bar in the TEM image is 20 nm. (B) TEM image of iron cluster aggregates upon 20 min electron beam irradiation. Crystal lattice of the one grown particle is shown by lines. Inset shows the corresponding SAED pattern. (C) EDS spectrum shows the presence of iron.



**Figure 8.14.** Picosecond-resolved fluorescence transients of  $\text{Fe}_{\text{QC}}@$ TOPO (A) at 409 nm excitation and (B) 445 nm excitation, show the lifetime profiles are independent of the excitation wavelength.

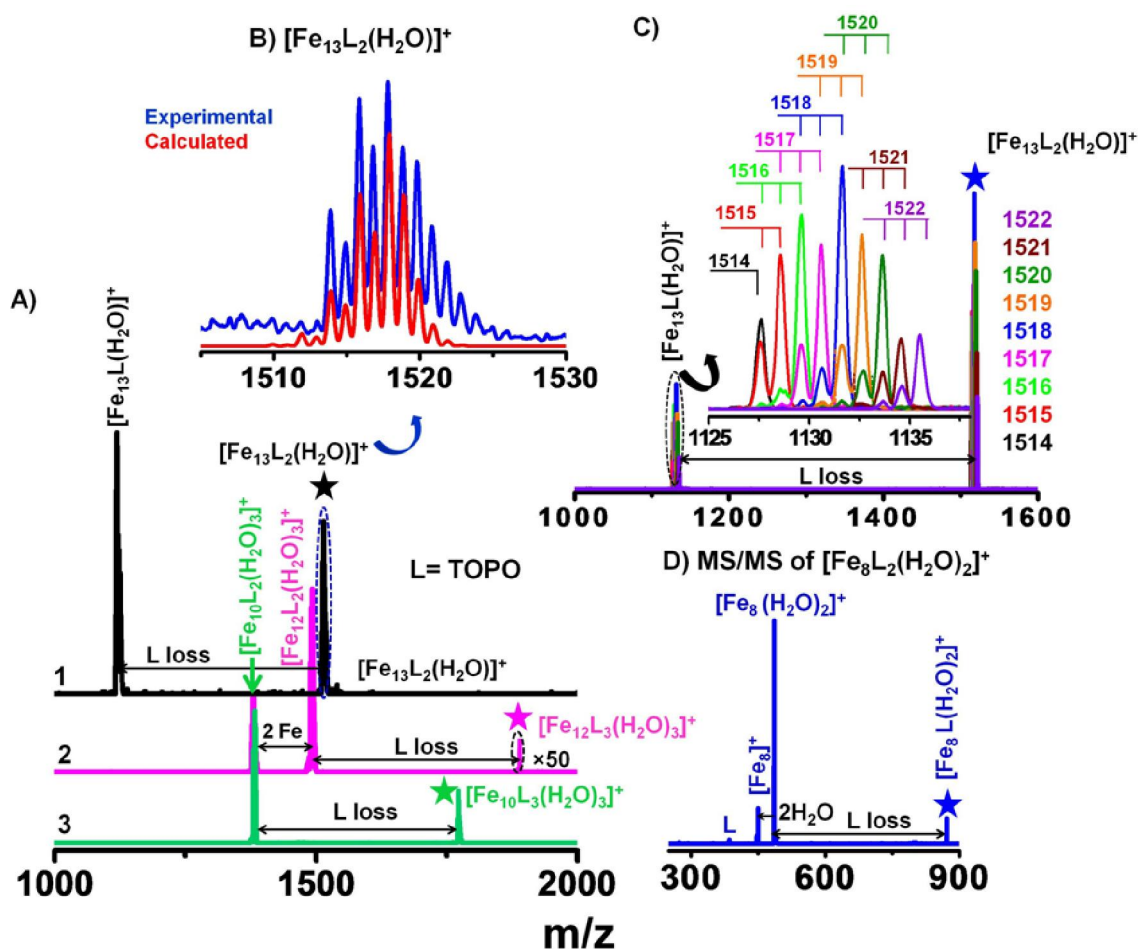
TOPO dimer and other fragments were also observable in the lower mass region ( $m/z < 800$ ). In the region beyond  $m/z 800$ , specific peaks due to clusters appear while the lower mass region is dominated by ligand peaks (Figure 8.15). In this figure, expanded cluster region shows the presence of multiple cores namely,  $[\text{Fe}_8(\text{TOPO})(\text{H}_2\text{O})_2]^+$ ,  $[\text{Fe}_{10}(\text{TOPO})_3(\text{H}_2\text{O})_3]^+$  and  $[\text{Fe}_{13}(\text{TOPO})_2(\text{H}_2\text{O})]^+$ . It is to be noted that, unlike several Au clusters [39], we have not seen any multiple charged species and all the compositions were verified with theoretically calculated isotope patterns. Along with the major peaks observed as discussed above, several small intensity peaks are also visible in the range studied. Most of the peaks are fragments of the above mentioned peaks. One can envisage three different ways of fragmentation, as observed in the present study: a) direct loss of TOPO, b) loss of water (one or multiple) molecule, and c) loss of a TOPO fragment namely, the octyl group. For instance, the peak at  $m/z 1131$  is a TOPO-devoid fragment of  $[\text{Fe}_{13}(\text{TOPO})_2(\text{H}_2\text{O})]^+$ . Similarly, the peak at  $m/z 1386$  corresponds to the TOPO-devoid fragment of  $[\text{Fe}_{10}(\text{TOPO})_3(\text{H}_2\text{O})_3]^+$ . The  $m/z 1257$  peak is assigned as  $[\text{Fe}_8(\text{TOPO})_2(\text{H}_2\text{O})_2]^+$  and hence, the  $m/z 870$  peak is probably due to  $[\text{Fe}_8(\text{TOPO})(\text{H}_2\text{O})_2]^+$ , arising after the loss of one TOPO moiety. These are examples of direct loss of TOPO moiety from the parent cluster. The fragmentations were ascertained by extensive MS/MS studies (see later). Loss as well as of addition of water molecules were also observed in some cases. Two peaks, at  $m/z 1368$  and  $m/z 1404$ , accompanying the  $m/z 1386$  peak (assigned as  $[\text{Fe}_{10}(\text{TOPO})_2(\text{H}_2\text{O})_3]^+$ ), arise due to the loss / gain of one water molecule as  $[\text{Fe}_{10}(\text{TOPO})_3(\text{H}_2\text{O})_2]^+$  and  $[\text{Fe}_{10}(\text{TOPO})_3(\text{H}_2\text{O})_4]^+$  respectively. Water loss was also observed in the case of  $[\text{Fe}_8(\text{TOPO})_2(\text{H}_2\text{O})_2]^+$ , where loss of two water molecules and one ligand lead to bare  $\text{Fe}_8^+$  core (see Figure 8.16). The peak centered around  $m/z 1660$  is due to the loss of an octyl group from TOPO from the parent ion  $[\text{Fe}_{10}(\text{TOPO})_3(\text{H}_2\text{O})_3]^+$ , which confirms the presence of the third type of fragmentation pattern.

Another kind of fragmentation could be the loss of Fe. This fragmentation pattern is seen for  $[\text{Fe}_{12}(\text{TOPO})_3(\text{H}_2\text{O})_3]^+$ . Presence of  $\text{Fe}_{12}$  core was confirmed from the MS/MS data, where the parent peak,  $[\text{Fe}_{12}(\text{TOPO})_3(\text{H}_2\text{O})_3]^+$  shows the loss of two two Fe atoms yielding  $[\text{Fe}_{10}(\text{TOPO})_2(\text{H}_2\text{O})_3]^+$  along with  $[\text{Fe}_{12}(\text{TOPO})_2(\text{H}_2\text{O})_3]^+$  (Figure 8.15i). The same  $[\text{Fe}_{10}(\text{TOPO})_2(\text{H}_2\text{O})_3]^+$  fragment was seen in the MS/MS of  $[\text{Fe}_{10}(\text{TOPO})_3(\text{H}_2\text{O})_3]^+$  (see



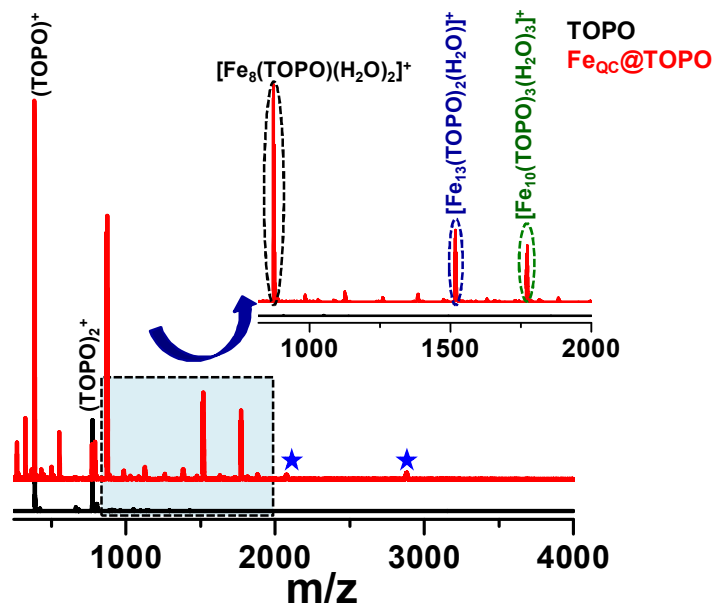
**Figure 8.15.** ESI MS of TOPO and  $\text{Fe}_{\text{QC}}@$ TOPO in the mass range  $m/z$  800-2000 showing the presence of  $[\text{Fe}_8(\text{TOPO})(\text{H}_2\text{O})_2]^+$ ,  $[\text{Fe}_{10}(\text{TOPO})_3(\text{H}_2\text{O})_3]^+$ ,  $[\text{Fe}_{12}(\text{TOPO})_3(\text{H}_2\text{O})_3]^+$  and  $[\text{Fe}_{13}(\text{TOPO})_2(\text{H}_2\text{O})]^+$ . Inset i) is showing MS/MS of  $[\text{Fe}_{12}(\text{TOPO})_3(\text{H}_2\text{O})_3]^+$  where ligand as well as Fe loss is also observable. A) and B)  $[\text{Fe}_{12}(\text{TOPO})_2(\text{H}_2\text{O})_3]^+$  and  $[\text{Fe}_{10}(\text{TOPO})_2(\text{H}_2\text{O})_3]^+$  are compared with the theoretically calculated isotope patterns of these species.

Figure 8.16), where the parent cluster loses one ligand molecule to generate the observed fragment. Figures 8.15A and 8.15B clearly show that the calculated and the experimentally observed isotope patterns match very well. Although the mass of two Fe atoms and that of one octyl group are nearly identical, the mismatch in the observed isotope pattern in the case of  $[\text{Fe}_{10}(\text{TOPO})_2(\text{H}_2\text{O})_3]^+$  rule out the presence of the octyl group. Extensive MS/MS studies were performed to understand the cluster compositions.



**Figure 8.16.** (A) ESI MS/MS of 1)  $[\text{Fe}_{13}(\text{TOPO})_2(\text{H}_2\text{O})]^+$  (black), 2)  $[\text{Fe}_{12}(\text{TOPO})_3(\text{H}_2\text{O})_3]^+$  (magenta) and 3)  $[\text{Fe}_{10}(\text{TOPO})_3(\text{H}_2\text{O})_3]^+$  (green), showing subsequent ligand losses. For all the cases, parent ions are marked with stars and for fragments, the compositions are indicated.  $[\text{Fe}_{12}(\text{TOPO})_3(\text{H}_2\text{O})_3]^+$  shows two Fe losses also. In this case, intensity of the parent peak has been multiplied by 50 to make it visible. (B)  $[\text{Fe}_{13}(\text{TOPO})_2(\text{H}_2\text{O})]^+$  spectrum is compared with the calculated spectrum. Rest of the spectra are compared in supporting information (Figure S25). (C) MS/MS spectra of each peak in the  $[\text{Fe}_{13}(\text{TOPO})_2(\text{H}_2\text{O})]^+$  envelope, with a mass width 1 Da. Fragment peaks after ligand loss are expanded in the inset, showing isotope distribution, principally due to iron. The parent ion chosen for MS/MS is mentioned above the isotope pattern observed. (D) ESI MS/MS of  $[\text{Fe}_8(\text{TOPO})_2(\text{H}_2\text{O})_2]^+$  showing ligand as well as water losses to give bare  $[\text{Fe}_8]^+$  core.

Collision energy dependent MS/MS study of the clusters showed consecutive ligand losses for all the clusters investigated (Figure 8.17-8.21). In Figure 8.16A, MS/MS data for  $[\text{Fe}_{10}(\text{TOPO})_3(\text{H}_2\text{O})_3]^+$ ,  $[\text{Fe}_{12}(\text{TOPO})_3(\text{H}_2\text{O})_3]^+$  and  $[\text{Fe}_{13}(\text{TOPO})_2(\text{H}_2\text{O})]^+$  are shown, keeping all experimental parameters and collision energies identical. In all the cases, ligand



**Figure 8.17.** ESI MS spectra of TOPO and Fe<sub>QC</sub>@TOPO in a larger mass window. The region, m/z 800-2000, marked with dotted rectangle is expanded in the inset. Major peaks are labelled. Other peaks are fragments from these peaks, as confirmed from MS/MS. The peaks labelled \* are unidentified ions.

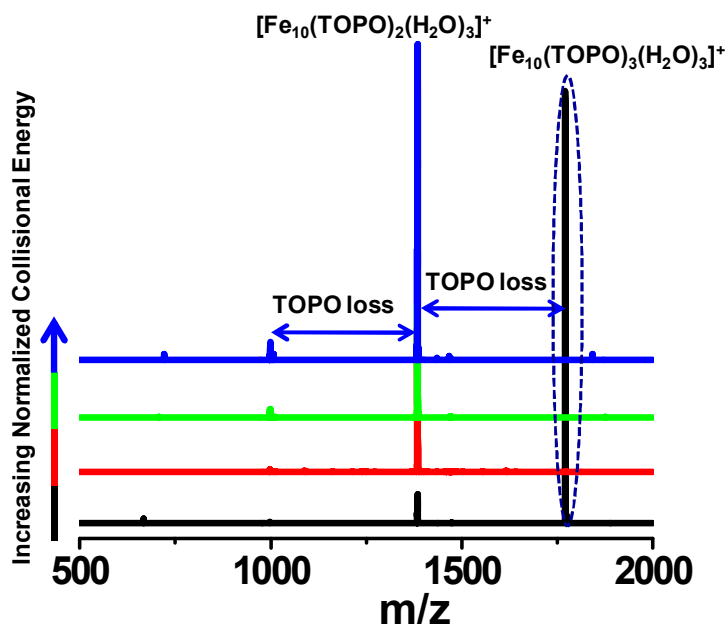


**Figure 8.18.** ESI MS/MS of  $[\text{Fe}_{10}(\text{TOPO})_3(\text{H}_2\text{O})_3]^+$  with increasing collisional energy (CE) showing multiple ligand losses.

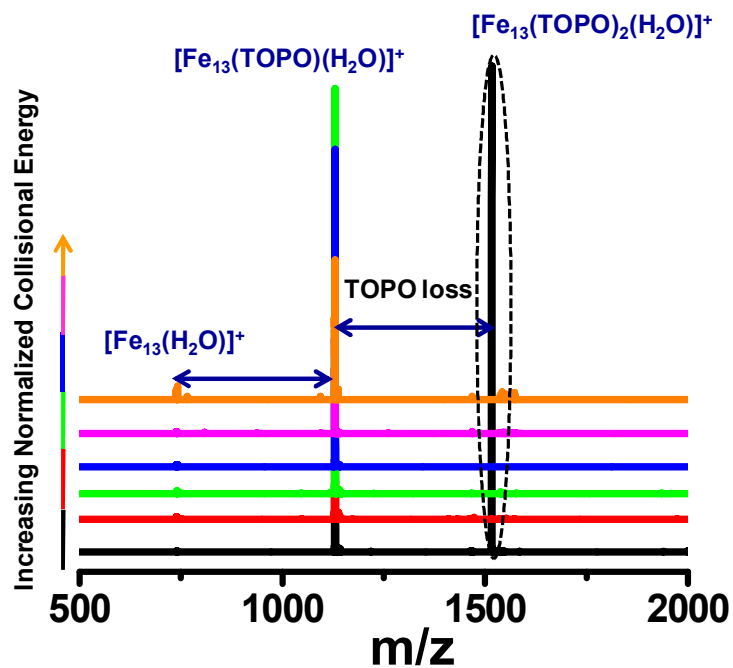


**Figure 8.19.** ESI MS/MS of  $[\text{Fe}_{13}(\text{TOPO})_2(\text{H}_2\text{O})]^+$  with increasing collision energy (CE) showing multiple ligand losses.

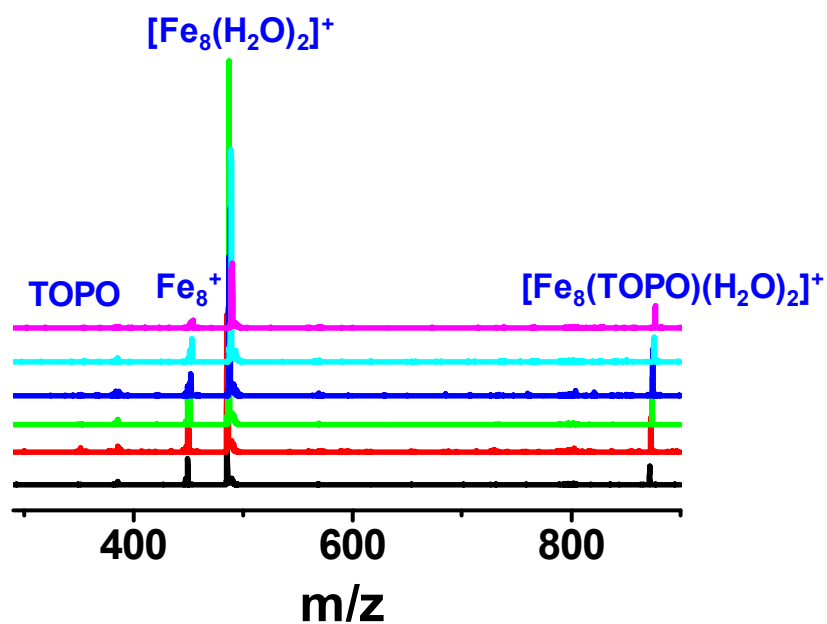


**Figure 8.20.** ESI MS/MS of  $[\text{Fe}_8(\text{TOPO})(\text{H}_2\text{O})_2]^+$  with increasing collision energy (CE) showing ligand as well as water losses.

loss can be seen with good isotope distribution, matching with the calculated spectrum (data for  $[\text{Fe}_{13}(\text{TOPO})_2(\text{H}_2\text{O})]^+$  is shown in Figure 8.16B). Presence of Fe was also confirmed by conducting MS/MS on each peak in a given envelope for the isotopes. For example, in the case of  $[\text{Fe}_{13}(\text{TOPO})_2(\text{H}_2\text{O})]^+$ , peaks in the range  $m/z$  1514-1522 were chosen with an isotope width of 1 Da and MS/MS was performed (Figure 8.16C). Each peak yielded a distribution of peaks that arose principally due to the presence of Fe. For  $[\text{Fe}_8(\text{TOPO})(\text{H}_2\text{O})_2]^+$ , ligand as well as water loss could be observed, producing a bare  $[\text{Fe}_8]^+$  core (Figure 8.16D and Figure 8.20). Presence of water, bound to the cluster core, was also observed in the MS/MS study for  $\text{Fe}_{13}$  core, where, upon higher collision energy,  $[\text{Fe}_{13}(\text{TOPO})_2(\text{H}_2\text{O})]^+$  loses two ligands to yield  $[\text{Fe}_{13}(\text{H}_2\text{O})]^+$  (Figure 8.19). This study proves the presence of attached water to the cluster core, which may act as ligand. We observed the loss of TOPO in most of the cases, which could be a reason behind the less than expected number of observed ligands attached to the core. It is possible that before we could detect the ion in ESI MS, the cluster might have already lost some ligands which was seen in the case of  $[\text{Fe}_8(\text{TOPO})_2(\text{H}_2\text{O})_2]^+$  (Figure 8.21). Another reason for the discrepancy might be that the steric hindrance due to the presence of three octyl chains present in a single TOPO molecule acted as a deterrent to attachment of more TOPO ligands. However, only a detailed theoretical study on the position and conformation of the ligands and structure of the cluster core can sort out this puzzle.

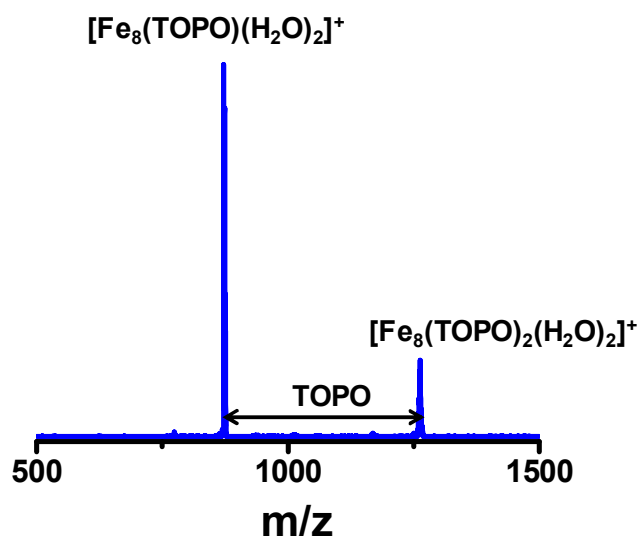


**Figure 8.21.** ESI MS/MS of  $[\text{Fe}_8(\text{TOPO})_2(\text{H}_2\text{O})_2]^+$  showing ligand loss.

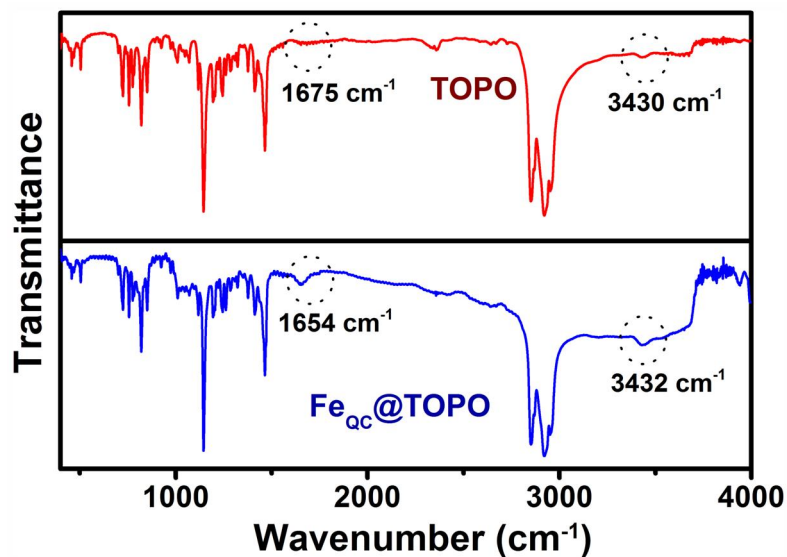


**Figure 8.22.** FT-IR spectra of TOPO and  $\text{Fe}_{\text{QC}}@\text{TOPO}$  show the presence of water vibration bands marked with dotted circles.

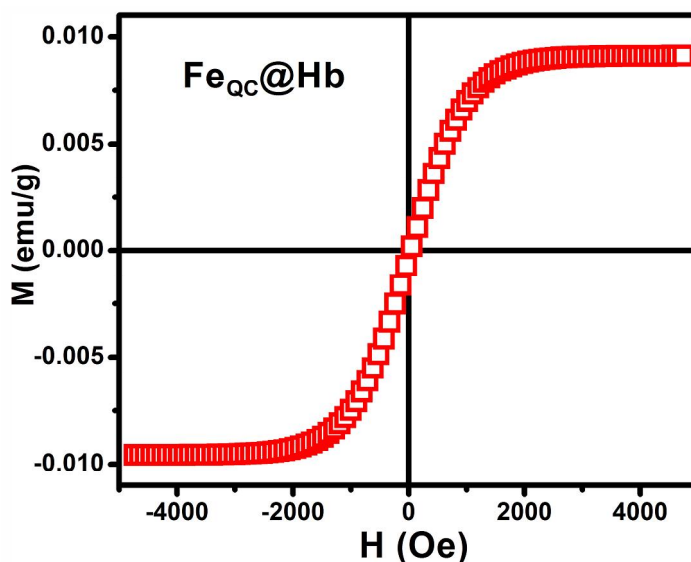


**Figure 8.23.** Vibrating sample magnetometer (VSM) data of  $\text{Fe}_{\text{QC}}\text{s}$  show the super-paramagnetic behaviour of the QCs (plotted after subtracting the diamagnetic background from the sample holder).

Bound water molecules have been reported earlier for dendrimer capped  $\text{Au}_8$  nanodots by Dickson et al [40]. However, the presence of three water molecules bound to Fe, a metal much more reactive than Au, was totally unexpected. The MS data was complemented by the solid-state FT-IR studies of TOPO and  $\text{Fe}_{\text{QC}}@\text{TOPO}$  where it was found that both

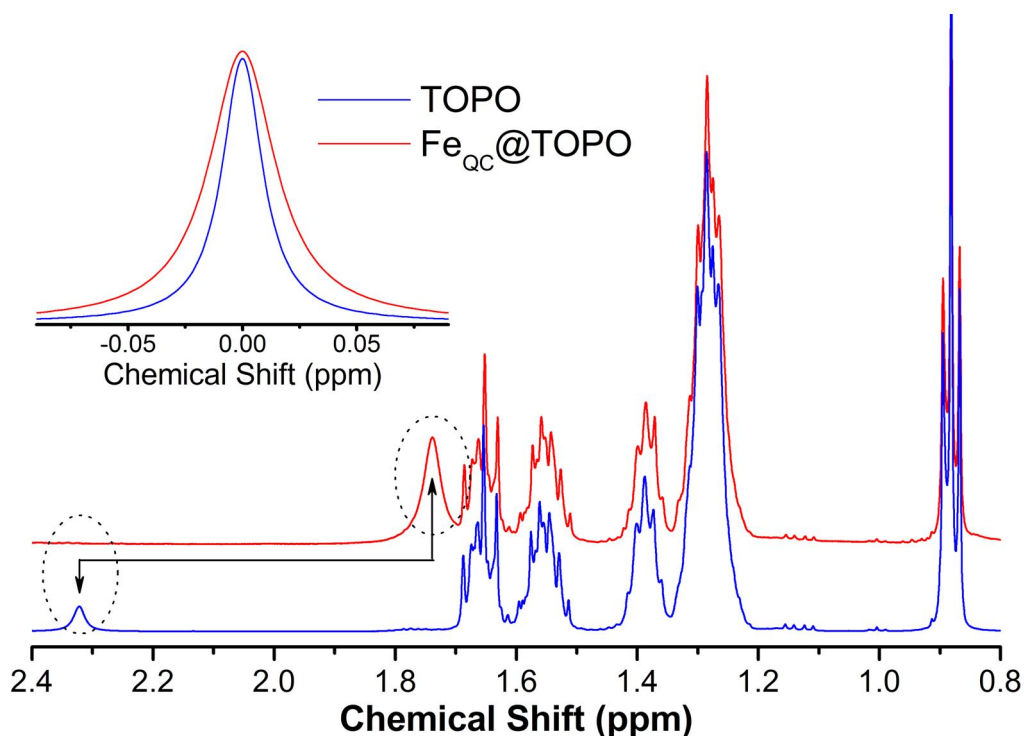


**Figure 8.24.**  $^1\text{H}$ -NMR spectra of TOPO (blue) and  $\text{Fe}_{\text{QC}}@\text{TOPO}$  (red). Bound water resonances for both the samples are marked with dotted circles. Broadening of the  $\text{Fe}_{\text{QC}}@\text{TOPO}$ -bound water resonance is shown in the inset.

the nature of water in TOPO and  $\text{Fe}_{\text{QC}}@\text{TOPO}$ ,  $^1\text{H}$  NMR studies were performed on TOPO and  $\text{Fe}_{\text{QC}}@\text{TOPO}$  in  $\text{CDCl}_3$ . Superimposed  $^1\text{H}$ -NMR spectra of TOPO and  $\text{Fe}_{\text{QC}}@\text{TOPO}$  are shown in Figure 8.24. Except for one singlet resonance (2.32 ppm for TOPO and 1.69 ppm for  $\text{Fe}_{\text{QC}}@\text{TOPO}$  samples), the two spectra are identical and are in agreement with the previously published spectrum of TOPO [41]. The unique singlet peaks in each spectrum, distinct from pure water signal in chloroform (7.24 ppm), could be attributed to TOPO/ $\text{Fe}_{\text{QC}}@\text{TOPO}$  bound water since the peaks disappeared upon addition of  $\text{D}_2\text{O}$ . This is consistent with the presence of bound water molecules associated with  $\text{Fe}_{\text{QC}}@\text{TOPO}$  (from ESI MS and FT-IR) and TOPO (from FT-IR). If the water signal in  $\text{Fe}_{\text{QC}}@\text{TOPO}$  indeed corresponds to molecules bound to  $\text{Fe}_{\text{QC}s}$ , then the superparamagnetic  $\text{Fe}_{\text{QC}}$ -center (Figure 8.23) is expected to induce faster relaxation and an upfield chemical shift of the  $\text{Fe}_{\text{QC}}$ -bound water resonance. Compared to that in TOPO, the water signal in  $\text{Fe}_{\text{QC}}@\text{TOPO}$  showed an upfield shift (0.63 ppm) and faster relaxation, both

**Table 8.1.** Lifetime values (excitation at 375 nm) of the control experiments have provided the evidence of formation of Fe<sub>QC</sub>s in the protein matrix. Values in parentheses represent the relative weight percentage of the time component with a standard error of ~ 10%.

System	Wavelength $\lambda_{\max}$ (nm)	Lifetimes (ns) (Percentage)			Average Lifetime (ns)
Fe <sub>QC</sub> @Hb	450	0.05 (78%)	0.67 (16%)	3.84 (06%)	0.39
	565	0.08 (64%)	0.91 (22%)	3.90 (14%)	0.80
	650	0.07 (49%)	1.02 (25%)	4.79 (26%)	1.53
Hemato- porphyrin	612	0.14 (20%)	1.24 (13%)	14.78 (67%)	10.15
	650	0.16 (24%)	1.4 (20%)	13.77 (56%)	7.98
	675	0.125 (21%)	1.25 (16%)	14.06 (63%)	9.00
Fe <sub>QC</sub> @Holo- Myoglobin	450	0.05 (88%)	0.10 (05%)	4.78 (02%)	0.21
	565	0.17 (52%)	0.84 (39%)	3.04 (09%)	0.70
	650	0.14 (37%)	1.16 (34%)	4.08 (29%)	1.63
Apo- Myoglobin &Hemato- porphyrin complex	620	-	1.13 (09%)	15.29 (91%)	14.06
	650	0.15 (19%)	1.40 (17%)	14.07 (64%)	9.30
	680	-	1.03 (13%)	14.78 (87%)	13.03

in terms of spin-lattice relaxation time  $T_1$  (2.54 s in TOPO and 1.13 s in Fe<sub>QC</sub>@TOPO) and line width or  $1/T_2^*$  (0.019 ppm in TOPO and 0.034 ppm in Fe<sub>QC</sub>@TOPO). Presence of upfield shifted and broadened water peak (Figure 8.24) in the background of all other proton peaks (due to TOPO) establishes a strong interaction of water molecules on the cluster surface.

### 8.3. Conclusion

In summary, we have devised a facile synthetic route for preparing atomically precise and highly luminescent Fe<sub>QC</sub>s. These clusters synthesized in solution have been detected as [Fe<sub>8</sub>(TOPO)(H<sub>2</sub>O)<sub>2</sub>]<sup>+</sup>, [Fe<sub>10</sub>(TOPO)<sub>3</sub>(H<sub>2</sub>O)<sub>3</sub>]<sup>+</sup>, [Fe<sub>12</sub>(TOPO)<sub>2</sub>(H<sub>2</sub>O)<sub>3</sub>]<sup>+</sup> and [Fe<sub>13</sub>(TOPO)<sub>2</sub>(H<sub>2</sub>O)]<sup>+</sup>, with well-defined and unique isotope distribution in ESI MS. The cluster contains water molecules as revealed from our MS/MS analysis which was corroborated by FT-IR and NMR spectroscopic studies. It is anticipated that a theoretical study will provide further insights on the structure, stability and conformation of the cluster. We believe that this new material holds promise for fundamental applications like catalysis, imaging and sensing.

## References

- [1] Z. Wu, M. Wang, J. Yang, X. Zheng, W. Cai, G. Meng, H. Qian, H. Wang, R. Jin, Fluorescent probes: Well-defined nanoclusters as fluorescent nanosensors: A case study on  $\text{Au}_{25}(\text{SG})_{18}$ , *Small* 8 (2012) 2027.
- [2] N. de Silva, J.-M. Ha, A. Solovyov, M.M. Nigra, I. Ogino, S.W. Yeh, K.A. Durkin, A. Katz, A bioinspired approach for controlling accessibility in calix[4]arene-bound metal cluster catalysts, *Nat. Chem.* 2 (2010) 1062.
- [3] C.-A.J. Lin, T.-Y. Yang, C.-H. Lee, S.H. Huang, R.A. Sperling, M. Zanella, J.K. Li, J.-L. Shen, H.-H. Wang, H.-I. Yeh, W.J. Parak, W.H. Chang, Synthesis, characterization, and bioconjugation of fluorescent gold nanoclusters toward biological labeling applications, *ACS Nano* 3 (2009) 395.
- [4] P.L. Xavier, K. Chaudhari, A. Bakshi, T. Pradeep, Protein-protected luminescent noble metal quantum clusters: An emerging trend in atomic cluster nanoscience, *Nano Rev.* 3 (2012) 14767.
- [5] M. Zhu, C.M. Aikens, F.J. Hollander, G.C. Schatz, R. Jin, Correlating the crystal structure of a thiol-protected  $\text{Au}_{25}$  cluster and optical properties, *J. Am. Chem. Soc.* 130 (2008) 5883.
- [6] H. Qian, M. Zhu, Z. Wu, R. Jin, Quantum sized gold nanoclusters with atomic precision, *Acc. Chem. Res.* 45 (2012) 1470.
- [7] P.D. Jadzinsky, G. Calero, C.J. Ackerson, D.A. Bushnell, R.D. Kornberg, Structure of a thiol monolayer-protected gold nanoparticle at 1.1 Å resolution, *Science* 318 (2007) 430.
- [8] M.W. Heaven, A. Dass, P.S. White, K.M. Holt, R.W. Murray, Crystal structure of the gold nanoparticle  $[\text{N}(\text{C}_8\text{H}_{17})_4][\text{Au}_{25}(\text{SCH}_2\text{CH}_2\text{Ph})_{18}]$ , *J. Am. Chem. Soc.* 130 (2008) 3754.
- [9] J. Akola, M. Walter, R.L. Whetten, H. Häkkinen, H. Grönbeck, On the structure of thiolate-protected  $\text{Au}_{25}$ , *J. Am. Chem. Soc.* 130 (2008) 3756.
- [10] P.R. Nimmala, A. Dass,  $\text{Au}_{36}(\text{SPh})_{23}$  nanomolecules, *J. Am. Chem. Soc.* 133 (2011) 9175.
- [11] R.L. Whetten, R.C. Price, Nano-golden order, *Science* 318 (2007) 407.

- [12] I. Dolamic, S. Knoppe, A. Dass, T. Bürgi, First enantioseparation and circular dichroism spectra of Au<sub>38</sub> clusters protected by achiral ligands, *Nat. Commun.* 3 (2012) 798.
- [13] Z.Y. Li, N.P. Young, M. Di Vece, S. Palomba, R.E. Palmer, A.L. Bleloch, B.C. Curley, R.L. Johnston, J. Jiang, J. Yuan, Three-dimensional atomic-scale structure of size-selected gold nanoclusters, *Nature* 451 (2008) 46.
- [14] Y. Negishi, K. Nobusada, T. Tsukuda, Glutathione-protected gold clusters revisited: Bridging the gap between gold(I)-thiolate complexes and thiolate-protected gold nanocrystals, *J. Am. Chem. Soc.* 127 (2005) 5261.
- [15] A. Dass, Mass spectrometric identification of Au<sub>68</sub>(SR)<sub>34</sub> molecular gold nanoclusters with 34-electron shell closing, *J. Am. Chem. Soc.* 131 (2009) 11666.
- [16] T.U.B. Rao, B. Nataraju, T. Pradeep, Ag<sub>9</sub> quantum cluster through a solid-state route, *J. Am. Chem. Soc.* 132 (2010) 16304.
- [17] H. Xu, K.S. Suslick, Water-soluble fluorescent silver nanoclusters, *Adv. Mater.* 22 (2010) 1078.
- [18] H. Yang, Y. Wang, H. Huang, L. Gell, L. Lehtovaara, S. Malola, H. Häkkinen, N. Zheng, All-thiol-stabilized Ag<sub>44</sub> and Au<sub>12</sub>Ag<sub>32</sub> nanoparticles with single-crystal structures, *Nat. Commun.* 4 (2013) 3422.
- [19] S.-I. Tanaka, J. Miyazaki, D.K. Tiwari, T. Jin, Y. Inouye, Fluorescent platinum nanoclusters: Synthesis, purification, characterization, and application to bioimaging, *Angew. Chem. Int. Ed.* 50 (2011) 431.
- [20] N. Goswami, A. Giri, M.S. Bootharaju, P.L. Xavier, T. Pradeep, S.K. Pal, Copper quantum clusters in protein matrix: Potential sensor of Pb<sup>2+</sup> ion, *Anal. Chem.* 83 (2011) 9676.
- [21] A. Baksi, P.L. Xavier, K. Chaudhari, N. Goswami, S.K. Pal, T. Pradeep, Protein-encapsulated gold cluster aggregates: The case of lysozyme, *Nanoscale* 5 (2013) 2009.
- [22] J. Xie, Y. Zheng, J.Y. Ying, Protein-directed synthesis of highly fluorescent gold nanoclusters, *J. Am. Chem. Soc.* 131 (2009) 888.
- [23] K. Chaudhari, P.L. Xavier, T. Pradeep, Understanding the evolution of luminescent gold quantum clusters in protein templates, *ACS Nano* 5 (2011) 8816.

- [24] M.A. Habeeb Muhammed, P.K. Verma, S.K. Pal, A. Retnakumari, M. Koyakutty, S. Nair, T. Pradeep, Luminescent quantum clusters of gold in bulk by albumin-induced core etching of nanoparticles: Metal ion sensing, metal-enhanced luminescence, and biolabeling, *Chem. Eur. J.* 16 (2010) 10103.
- [25] Y. Pan, S. Neuss, A. Leifert, M. Fischler, F. Wen, U. Simon, G. Schmid, W. Brandau, W. Jahnen-Dechent, Size-dependent cytotoxicity of gold nanoparticles, *Small* 3 (2007) 1941.
- [26] R. Bhattacharya, P. Mukherjee, Biological properties of “naked” metal nanoparticles, *Adv. Drug Deliv. Rev.* 60 (2008) 1289.
- [27] K.S. Suslick, S.-B. Choe, A.A. Cichowlas, M.W. Grinstaff, Sonochemical synthesis of amorphous iron, *Nature* 353 (1991) 414.
- [28] T. Ling, L. Xie, J. Zhu, H. Yu, H. Ye, R. Yu, Z. Cheng, L. Liu, G. Yang, Z. Cheng, Y. Wang, X. Ma, Icosahedral face-centered cubic Fe nanoparticles: Facile synthesis and characterization with aberration-corrected TEM, *Nano Lett.* 9 (2009) 1572.
- [29] L.-M. Lacroix, S.b. Lachaize, A. Falqui, M. Respaud, B. Chaudret, Iron nanoparticle growth in organic superstructures, *J. Am. Chem. Soc.* 131 (2008) 549.
- [30] L. Guo, Q. Huang, X.-y. Li, S. Yang, Iron nanoparticles: Synthesis and applications in surface enhanced Raman scattering and electrocatalysis, *Phys. Chem. Chem. Phys.* 3 (2001) 1661.
- [31] D.B. Jacobson, B.S. Freiser, Heteronuclear diatomic transition-metal cluster ions in the gas phase. The bond energy of  $\text{FeCo}^+$ , *J. Am. Chem. Soc.* 106 (1984) 4623.
- [32] A.W. J. Castleman, R.G. Keesee, Clusters: Properties and formation, *Ann. Rev. Phys. Chem.* 37 (1986) 525.
- [33] B.H. Weiller, P.S. Bechthold, E.K. Parks, L.G. Pobo, S.J. Riley, The reactions of iron clusters with water, *J. Chem. Phys.* 91 (1989) 4714.
- [34] S.C. Richtsmeier, E.K. Parks, K. Liu, L.G. Pobo, S.J. Riley, Gas phase reactions of iron clusters with hydrogen, *J. Chem. Phys.* 82 (1985) 3659.
- [35] N. Goswami, A. Bakshi, A. Giri, P.L. Xavier, G. Basu, T. Pradeep, S.K. Pal, Atomically precise luminescent iron clusters in solution, *Nanoscale* (2013) (In press).
- [36] P. Ramasamy, S. Guha, E.S. Shibu, T.S. Sreeprasad, S. Bag, A. Banerjee, T. Pradeep, Size tuning of Au nanoparticles formed by electron beam irradiation of  $\text{Au}_{25}$

- quantum clusters anchored within and outside of dipeptide nanotubes, *J. Mater. Chem.* 19 (2009) 8456.
- [37] A.L. Rose, T.D. Waite, Chemiluminescence of luminol in the presence of iron(II) and oxygen: Oxidation mechanism and implications for its analytical use, *Anal. Chem.* 73 (2001) 5909.
- [38] T. Udayabhaskararao, Y. Sun, N. Goswami, S.K. Pal, K. Balasubramanian, T. Pradeep, Ag<sub>7</sub>Au<sub>6</sub>: A 13-atom alloy quantum cluster, *Angew. Chem. Int. Ed.* 51 (2012) 2155.
- [39] J.B. Tracy, M.C. Crowe, J.F. Parker, O. Hampe, C.A. Fields-Zinna, A. Dass, R.W. Murray, Electrospray ionization mass spectrometry of uniform and mixed monolayer nanoparticles: Au<sub>25</sub>[S(CH<sub>2</sub>)<sub>2</sub>Ph]<sub>18</sub> and Au<sub>25</sub>[S(CH<sub>2</sub>)<sub>2</sub>Ph]<sub>18-x</sub>(SR)<sub>x</sub>, *J. Am. Chem. Soc.* 129 (2007) 16209.
- [40] J. Zheng, J.T. Petty, R.M. Dickson, High quantum yield blue emission from water-soluble Au<sub>8</sub> nanodots, *J. Am. Chem. Soc.* 125 (2003) 7780.
- [41] J. Kříž, J.i. Dybal, E. Makrlík, J. Budka, P. Vaňura, Interaction of hydrated protons with trioctylphosphine oxide: NMR and theoretical study, *J. Phys. Chem. A* 113 (2009) 5896.

## List of Publications

1. **A. Giri**, A. Makhal, B. Ghosh, A. K. Raychaudhuri and S.K. Pal  
“Functionalization of Manganite Nanoparticles and their Interaction with Biologically Relevant Small Ligands: Picosecond Time-Resolved FRET Studies”  
*Nanoscale*, 2010, 2, 2704
2. **A. Giri**, N. Goswami, M. S. Bootharaju, P. L. Xavier, R. John, N. T. K. Thanh, T. Pradeep, B. Ghosh, A. K. Raychaudhuri and S. K. Pal  
“Emergence of Multicolor Photoluminescence in  $\text{La}_{0.67}\text{Sr}_{0.33}\text{MnO}_3$  Nanoparticles”  
*J. Phys. Chem. C* 116 (2012) 25623.
3. **A. Giri**, N. Goswami, M. Pal, M.T. Zar Myint, S. Al-Harhi, A. Singha, B. Ghosh, J. Dutta and S.K. Pal  
“Rational Surface Modification of  $\text{Mn}_3\text{O}_4$  Nanoparticles to Induce Multiple Photoluminescence and Room Temperature Ferromagnetism”  
*J. Mater. Chem. C* 1 (2013) 1885.
4. **A. Giri**, N. Goswami, P. Lemmens and S. K. Pal  
“Preparation of Water Soluble L-Arginine Capped CdSe/Zns QDs and their Interaction with Synthetic DNA: Picosecond-Resolved FRET Study”  
*Mater. Res. Bull.* 47 (2012) 1912. (Cover Article).
5. N. Goswami, A. Baksi, **A. Giri**, P.L. Xavier, G. Basu, T. Pradeep and S.K. Pal  
“Atomically Precise Luminescent Iron Clusters in Solution”  
*Nanoscale* (2013) (In press).

- 6.\* **A. Giri**, N. Goswami, S. Sarkar and S. K. Pal  
 “Bio-Nanomaterials: Understanding Key Biophysics and Their Applications”  
 Book Chapter in “Biomaterials” Edited by J.N. Govil, STUDIUM PRESS LLC, USA, 2013.
- 7.\* N. Goswami, **A. Giri**, S. Kar, M. S. Bootharaju, R. John, P. L. Xavier, T. Pradeep and S. K. Pal  
 “Protein Directed Synthesis of NIR-Emitting, Tunable HgS Quantum Dots and Their Applications in Metal Ion Sensing”  
*Small* 8 (2012) 3175.
- 8.\* N. Goswami, **A. Giri** and S. K. Pal  
 “MoS<sub>2</sub> Nanocrystals Confined in a DNA Matrix Exhibiting Energy Transfer”  
*Langmuir* 29 (2013) 11471.
- 9.\* N. Goswami, **A. Giri**, M.S. Bootharaju, P.L. Xavier, T. Pradeep and S.K. Pal  
 “Copper Quantum Clusters in Protein Matrix: Potential Sensor of Pb<sup>2+</sup> Ion”  
*Anal. Chem.* 83 (2011) 9676.
- 10.\* P. K. Verma, **A. Giri**, N. T. K. Thanh, L. D. Tung, O. Mondal, M. Pal and S. K. Pal  
 “Superparamagnetic Fluorescent Nickel–Enzyme Nanobioconjugates: Synthesis and Characterization of a Novel Multifunctional Biological Probe”  
*J. Mater. Chem.* 2010, 20, 3722.

\* Not included in the thesis.